Heavy-Fermion like Correlations and Crystal-Field Excitations in Copper-Ruthenates with Perovskite-related Structure

Dissertation

zur Erlangung des akademischen Grades
Dr. rer. nat.

eingereicht an der
Mathematisch-Naturwissenschaftlich-Technischen Fakultät
der Universität Augsburg

von
Axel Günther

Augsburg, Mai 2015

1. Gutachter:	Prof. Dr. Alois Loidl
2. Gutachter:	Prof. Dr. Armin Reller
Tag der mündlichen Prüfung:	14. Juli 2015

Contents

List of Figures

List of Tables

Nomenclature

AF	antiferro-
AFM	antiferromagnet(ic)
aka	also known as
arb. units	arbitrary units
BVS	bond valence sum
CEF	crystal electric field
CW	Curie-Weiss
DFT	density functional theory
DOS	density of states
DSC	differential scanning calorimetry
DSP	digital signal processor
e.g.	exempli gratia [latin]: for example
EXAFS	extended x-ray absorption fine structure spectroscopy
FL	Fermi liquid
f.u.	formula unit
GeV	giga electron Volt
HF	heavy fermion
i.e.	id est [latin]: that means
IV	intermediate valence
k_B	Boltzmann constant
LF	longitudinal field
LLW	Lea, Leask, and Wolf
mA	milli ampere
m_e	electron mass
meV	milli electron volt
MeV	mega electron volt

MHz	mega hertz
MPMS	magnetic property measurement system
MR	magneto resistance
ms	milli second
mT	milli tesla
N_A	Avogadro constant
ND	neutron diffraction
NFL	non-Fermi liquid
NMR	nuclear magnetic resonance
NPD	neutron powder diffraction
NQR	nuclear quadrupole resonance
PES	photoelectron spectroscopy
PPMS	physical property measurement system
ps	pico second
QCP	quantum critical point
QPT	quantum phase transition
R	gas constant
RFI	radio-frequency interference
rms	root mean square
RRR	residual resistivity ratio
RT	room temperature
RXES	resonant x-ray emission spectroscopy
SC	superconducting
sGdo	single Gaussian damped oscillator
sGKT	static Gaussian Kubo-Toyabe
SQUID	superconducting quantum interference device
T_c	critical temperature (e.g. Curie temperature)
TF	transverse field
TGA	thermogravimetric analysis
TMO	transition metal oxide
TOF	time-of-flight
T_{SF}	spin fluctuation temperature
vs.	versus

XANES	x-ray absorption near edge structure spectroscopy
XAS	x-ray absorption spectroscopy
XPS	x-ray photoemission spectroscopy
XRD	x-ray diffraction
ZF	zero field
γ_μ	gyromagnetic ratio of the muon
μ_B	Bohr magneton
μ_N	nuclear magneton
μSR	muon spin rotation/relaxation

1 Introduction

The members of the perovskite structural family, named after the Russian mineralogist Lev Aleksevich Perovski, crystallographically all stem from the parent mineral calcium titanate ($CaTiO_3$), also named perovskite.[1] This substance forms an extremely versatile ceramic host with the general formula ABX_3 and a vast variety of compounds and corresponding properties. Here, A and B are cations of very different sizes connected by anions X, which is oxygen in most cases but may also be any other halogen, chalcogen, nitrogen etc. or a mixture of them. By appropriate changes in composition one can modify the material properties, including high dielectric constants and ferroelectricity in $BaTiO_3$ [2, 3], colossal magnetoresistance in doped $LaMnO_3$ [4], multiferroicity in $TbMnO_3$ [5], incipient ferroelectricity dominated by quantum fluctuations at low temperatures in $SrTiO_3$ [6], and of course high-T_c-superconductivity in the perovskite-related systems Ba-La-Cu-O and Y-Ba-Cu-O.[7, 8]

Although not realized in the mineral perovskite, the term perovskite is also eponymous for a structure-type of cubic symmetry (space group $Pm\bar{3}m$, no.221) as realized in $SrTiO_3$ (mineral name: tausonite). Here, the B cations (Ti) are surrounded by anions X (O) in octahedral (6-fold), and the A cations (Sr) by anions X (O) in cuboctahedral (12-fold) coordination (see Fig. 1.1). For the stability of the structure, the relative size of the involved ions is quite important. The Goldschmidt tolerance factor $t = {(r_A+r_X)}/{\sqrt{2}(r_B+r_X)}$ [9] can be used as indicator for the stability and distortion of the perovskite structure where $r_{X,A,B}$ denotes the ionic radius of the anion X and those of the cations A and B. If t is close to 1 then the structure is typically cubic. If t it is well below 1 then the structure tends to buckling and distortion which leads to various lower-symmetry collective tilting schemes.[10, 11, 12, 13]

In the idealized cubic perovskite unit cell, type A atoms occupy the body centered position (½,½,½), type B atoms the cube corner positions (0,0,0), and X atoms the

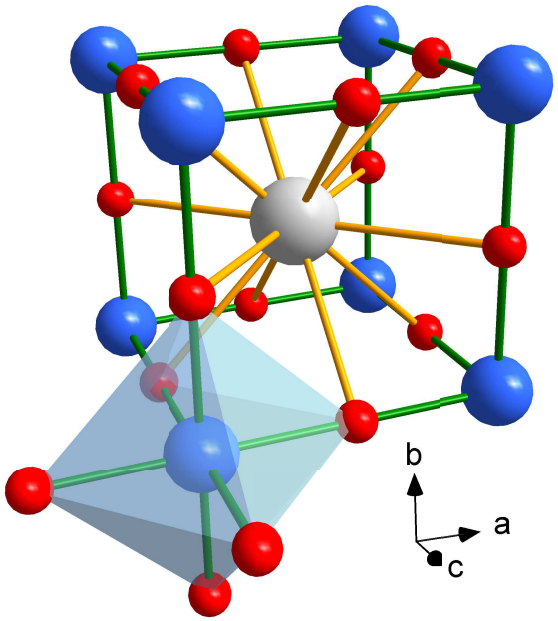

Figure 1.1: The ideal perovskite structure as realized in $SrTiO_3$. The anionic environment (red spheres) of the B cations (blue spheres) is illustrated by the light blue octahedron whereas the cuboctahedral coordination of the A cations (grey spheres) is shown by orange bonds.

face centered positions (½,½,0) (see Fig. 1.1). Substitution of three fourths of the A-site by Jahn-Teller [14] active ions (Cu^{2+}, Mn^{3+}) has two consequences: firstly a 1:3 ordering between the cations of the A-site and secondly a tilting of the BX_6 octahedra which also increases the B-O-Cu(Mn) bond angle from 90° to roughly 110° and reduces the B-O-B bond angle from 180° to a value near 140°. This octahedral tilting represents the smallest energy change, since it allows an adjustment of the A-O distances while leaving the rigid BX_6 octahedra intact and changing mainly the B-O-B bond angle [15] which has to be considered when interpreting electronic and magnetic interactions between the cations.[13] Together, this profound modification of the anionic environment leads to a decomposition of the original A-site and, therefore, to the appearance of a new crystallographic C-site (Cu, Mn) with four close oxygen atoms arranged as an almost square and four oxygens further away arranged as a rectangle perpendicular to the before mentioned square.[16] The new C-site also implies a doubling of the unit cell in all three crystallographic directions while leaving the cubic symmetry intact.[17] All members of this $AC_3B_4O_{12}$ (C = Cu, Mn) family have the same crystal structure, namely a $2 \times 2 \times 2$ supercell of the original perovskite with $a^+a^+a^+$-tilted octahedra [10] and the space group $Im\bar{3}$ (no.204). They can be substituted at the A- and B-site with a vast variety of metal ions including alkalis, alkaline earths, transition metals, lanthanides, and actinides.[18] Beginning in the 1960s they have been characterized structurally [19, 20, 21, 16, 22] and have attracted growing attention in the last years regarding their electronic properties including colossal dielectric constants in $CaCu_3Ti_4O_{12}$ [23, 24, 25], temperature-induced intersite charge transfer in $LaCu_3Fe_4O_{12}$ [26], large low-field magnetoresistance in $CaCu_3Mn_4O_{12}$ [27, 28, 29], and heavy-fermion like behavior in $CaCu_3Ru_4O_{12}$.[30]

Among the large class of A-site ordered perovskites of stoichiometry $AC_3B_4O_{12}$, this work focuses on detailed investigations of the copper-ruthenates $ACu_3Ru_4O_{12}$ (A = Na, Ca, Sr, La, Pr, Nd). They were found to belong to the few examples of purely d-electron based transition-metal compounds showing heavy-fermion properties, LiV_2O_4 being the first among them.[31, 32, 33, 30] It is well established that ruthenates reveal a rather complex and unpredictable behavior [34] and during the last decade experiments on ruthenates have provided a wealth of interesting discoveries.[35] The thesis is especially motivated as compounds within the vast class of heavy-fermion compounds exhibit outstanding properties like superconductivity (Sr_2RuO_4 [36, 37], $CeCu_2Si_2$ [38]), the proximity to a quantum critical point ($La_4Ru_6O_{19}$ [39], $CeCu_{5.9}Au_{0.1}$ [40]), and other exotic ground states. Exper-

iments were carried out utilizing x-ray diffraction, neutron diffraction and spectroscopy, magnetic and resistivity measurements, as well as heat capacity and muon spectroscopy techniques. A broad range of external parameters is scanned and depending on the specific technique, a temperature range from 50 mK to 400 K is covered and external magnetic fields up to 14 T are applied. All compounds investigated are metallic paramagnets with an enhanced Pauli-susceptibility, a T^2 dependence of the low-temperature electrical resistivity and a significantly enhanced Sommerfeld coefficient consistently manifesting a heavy-fermion state. Toward low temperatures, $CaCu_3Ru_4O_{12}$ exhibits non-Fermi liquid properties visible in a logarithmic divergence of the heat capacity and a positive linear T-dependence of the resistivity. Moreover, an intermediate-valence transition in $CaCu_3Ru_4O_{12}$ can be related to an unusual spontaneous structural contraction appearing at 154 K on cooling without affecting the symmetry. It is visible as abrupt change in the lattice constant, a broad feature in the susceptibility, and as tiny peak in the specific heat. The inverse magnetic susceptibility of the Sr and the La compound exhibits an unusual linear decrease over a wide temperature range while the compounds with A = Pr and Nd are dominated by the local moment of the rare earth ions including CEF effects, also clearly visible as Schottky peaks in the heat capacity and as dispersionless inelastic intensities in the dynamic structure factor.

2 Spot Light on the Copper-Ruthenates

In the following, a chronological reference to all papers published on $A\mathrm{Cu_3Ru_4O_{12}}$ (A = Na, Ca, Sr, La, Pr, Nd) including their main findings is given. New results obtained within this work are then described later in the chapter "Results & Discussion".

It first was found that from the copper-ruthenates the following homologues can be synthesized with the before mentioned crystal structure: $A\mathrm{Cu_3Ru_4O_{12}}$ (A = Na, Ca, Sr, La, Pr, Nd).[41, 42] Later on, $\mathrm{NaCu_3Ru_4O_{12}}$, $\mathrm{CaCu_3Ru_4O_{12}}$, and $\mathrm{LaCu_3Ru_4O_{12}}$ were identified as metallic Pauli-paramagnets [41] with the metallic character suggested as being related to valence degeneracy between Cu and Ru.[43] It was also shown that these compounds exhibit heavy-fermion like behavior as evidenced by a quadratic temperature dependence of the resistivity and an enhanced Sommerfeld coefficient of the specific heat.[44, 33, 30] In $\mathrm{CaCu_3Ru_4O_{12}}$ the signature of a heavy-fermion state is strongly supported by a Wilson ratio [45] and a Kadowaki-Woods relation [46, 47] fulfilling the criteria for typical heavy-fermion metals.[30] Furthermore, it was proposed that $\mathrm{CaCu_3Ru_4O_{12}}$ is a d-electron heavy-fermion system equivalent to traditional f-electron heavy-fermion systems in which the states are formed by hybridization between two different electronic subsystems, namely localized f-electrons and band states of mainly s- and p-derived conduction electrons. In that sense, $\mathrm{CaCu_3Ru_4O_{12}}$ was originally interpreted as a heavy fermion system with localized magnetic moments of $\mathrm{Cu^{2+}}$ ions and itinerant Ru-derived d-electrons with a broad peak in the susceptibility at $\approx 175\,\mathrm{K}$ indicating a Kondo resonance.[30]

Detailed structural investigations on $A\mathrm{Cu_3Ru_4O_{12}}$ (A = Na, Ca, Sr, La, Nd) by thermogravimetric experiments revealed that the stoichiometry of these compounds is almost exactly 1:3:4:12. Bond-valence calculations based on EXAFS measurements indicate a Ru valence closer to +4 than expected from the formal charge, an effective Cu valence below

+2, and effectively over-charged A-cations.[48, 49] DFT based [50, 51] electronic structure calculations on ACu$_3$Ru$_4$O$_{12}$ (A = Na, Ca, Sr, La, Nd) show that the electronic properties are strongly influenced by covalent-type bonding between transition metal d- and oxygen p-states and that the tilting of the RuO$_6$ octahedra mainly arises from adjustment of the Cu-O bond lengths in the CuO$_4$ plaquettes.[15] It is also shown that the unusually high effective charge of the A-site cation is due to the failure of the bond-valence approach because the response of the A-site cation to the tilting is small and the structure does not offer the possibility to simultaneously optimize A-O and Cu-O bond lenghts. XPS experiments and cluster model calculations on CaCu$_3$Ru$_4$O$_{12}$ [52] support the picture of localized Cu 3d and itinerant Ru 4d electrons being coupled antiferromagnetically by the Kondo mechanism. First-principles studies on CaCu$_3$Ru$_4$O$_{12}$ [53] confirm the itinerant paramagnetism from a theoretical point of view. However, there is evidence that two conductive channels contribute to the metallic behavior, namely a Ru-O-Ru network via $dp\pi$ coupling of ruthenium and oxygen, and an indirect Ru-O-Cu interaction by hybridization of itinerant Ru 4d and localized Cu 3d electrons through O 2p orbitals which might play a role in the formation of the heavy-mass behavior. The quadrupole parameters and the Knight shift [54] of Cu have been derived from field-sweep NMR in CaCu$_3$Ru$_4$O$_{12}$.[55] Copper NQR studies in CaCu$_3$Ru$_4$O$_{12}$ [56] probe a change in the Cu 3d electron nature represented by a change in the Korringa slope on decreasing temperature without indication of magnetic order. The slope of the spin-lattice relaxation rate $1/T_1$ is T-dependent and shows a Korringa-like behavior characteristic for a metal above 150 K, and again below 20 K with a slightly reduced absolute value as characteristic for several mixed-valence heavy-fermion compounds.

Non-Fermi liquid behavior was found in CaCu$_3$Ru$_4$O$_{12}$ below 2 K [57] evidenced by a logarithmic increase of the heat capacity and deviations from a Korringa law in the spin-lattice relaxation rate probed by NQR for $0.2\,\mathrm{K} < T < 10\,\mathrm{K}$. Additional high-resolution single crystal x-ray diffraction on CaCu$_3$Ru$_4$O$_{12}$ [57] yields lattice parameters very close to the powder data and the stoichiometry very close to the nominal one (1:3:4:12). In contrast to previous results in literature, [43] merohedral twinning domains are found to be present at low temperatures.[57] A more detailed look was taken at the heavy-mass behavior of ACu$_3$Ru$_4$O$_{12}$ (A = Na, Ca, La) and A-site mixtures of them (Na$_{0.5}$Ca$_{0.5}$Cu$_3$Ru$_4$O$_{12}$ and Ca$_{0.5}$La$_{0.5}$Cu$_3$Ru$_4$O$_{12}$) in order to investigate the effects of hetero-valent substitution without introducing disorder at the Cu and Ru site.[58] A comparison of susceptibil-

ity and specific heat with respect to the A-site valence questions the formation of the heavy fermion state by the Kondo effect and correlations among itinerant Ru electrons are proposed as dominant for the mass enhancement. In addition, AC-susceptibility measurements down to 20 mK show no indication for either magnetic order or superconductivity. Extended NMR/NQR measurements on $CaCu_3Ru_4O_{12}$ also raise considerable doubts about the formation of the heavy-fermion state via localized Cu electrons in a dense Kondo model.[59] Here, the spin-lattice relaxation rate shows Korringa laws for $5\,\mathrm{K} < T < 20\,\mathrm{K}$ and $150\,\mathrm{K} < T < 700\,\mathrm{K}$, implying a significant change of the electronic properties between 20 K and 150 K and ruling out the existence of Cu-localized moments. Measurements on more finely graduated A-site mixtures of $ACu_3Ru_4O_{12}$ (A = Na, Ca, La) reveal a suppression of the mass enhancement in compositions close to $CaCu_3Ru_4O_{12}$ although a Kondo-like effect is most pronounced in that compound.[60] It is speculated that a formation of a gap structure at the Fermi energy is responsible for that reduction which is argued to be caused by a many-body effect in the presence of an enhanced Cu DOS in addition to correlated Ru 4d electrons. Such a duality of a simultaneously localized and itinerant nature of the d electrons is different from conventional Kondo lattices with clearly localized f-electrons. Studies of the electronic structure of $ACu_3Ru_4O_{12}$ (A = Na, Ca, La) by XPS and high-resolution photoemission spectroscopy show differences between the compounds.[61] In $CaCu_3Ru_4O_{12}$ the Cu 3d xy orbital is closer to half filling and more Cu 3d electrons are involved in the states close to E_F when compared to $NaCu_3Ru_4O_{12}$ and $LaCu_3Ru_4O_{12}$.

Characteristic properties of an intermediate-valence system were found in $CaCu_3Ru_4O_{12}$ inferred from a small but abrupt volume change at 154 K probed by neutron diffraction and high-resolution heat capacity measurements.[62] While the crystal symmetry is preserved, NMR Knight shift measurements of Ru reveal a crossover from a paramagnetic behavior at high temperatures to itinerant band states at low temperatures. Compared to the respective elemental metal, the Ru spin-lattice relaxation rate is strongly enhanced and that of Cu slightly reduced. This unambiguously points to a HF behavior resulting from correlations within the Ru d-bands independent of the physics at the Cu site. DFT calculations expect some kind of charge transfer taking place at 154 K between Cu and Ru and can relate the structural anomaly with the d-electron number. That is nearly constant below 125 K and has a roughly linear dependence above 150 K. High-field magnetization and magneto-resistance measurements [63, 64] on the solid-solution series $CaCu_3Ru_xTi_{4-x}O_{12}$

[1] support the picture of a localization-itinerancy crossover with an increase of delocalized Cu^{2+} moments (Cu^{2+} holes) with increasing x which is consistent with an earlier study of this series based on susceptibility and heat capacity measurements.[65] XANES measurements [66] on the substitution series $A Cu_3 Ru_x Ti_{4-x} O_{12}$ (A = La, Nd) indicate the oxidation state of Ru close to +4. As the lanthanides (La, Nd) are strictly 3+, a charge transfer from Ru to Cu seems to occur leading to the presence of considerable amounts of Cu^{+}. Additional clues for a NFL behavior in single crystalline $CaCu_3Ru_4O_{12}$ is evidenced by a linear dependence of the resistivity below 2.5 K.[35] Furthermore, HF behavior is reported also for $A Cu_3 Ru_4 O_{12}$ (A = Pr, Nd), represented by enhanced Sommerfeld coefficients. An XAS and RXES study on $A Cu_3 Ru_4 O_{12}$ (A = Na, Ca, La) indicates that the number of O 2p holes decreases when the A-site valence is increased (Na^{+} to Ca^{2+} to La^{3+}).[67] Apparently these holes are responsible for the suppression of the enhancement of the electronic specific heat. In addition, the charge-transfer energy increases when the A-site valence is increased (Na^{+} to Ca^{2+} to La^{3+}) which indicates that the A-site does not only control the Ru 4d and Cu 3d hole numbers but also that of O 2p. That means that the valences of Ru and Cu are affected not only by electron doping (changing the A-site valence) but also by change of the charge-transfer energy. Soft XAS as well as soft x-ray PES experiments together with calculations of band structure and cluster configuration interaction have been carried out especially on $CaCu_3Ru_4O_{12}$.[68] The electronic structure shows a robust 2+ valence of the Cu ions forming localized moments while the Ru electrons have a more itinerant character. In addition, the formation of Zhang-Rice singlets [69] is excluded in $CaCu_3Ru_4O_{12}$ as the first ionization states of Cu are too far from the Fermi level to allow for thermal or virtual excitations, stated also in earlier XPS studies.[52] This is in contrast to findings of the presence of Zhang-Rice singlets in the isostructural metallic compounds $CaCu_3Co_4O_{12}$ and $CaCu_3Cr_4O_{12}$ and demonstrates the importance of a careful choice of the B-site cation.[70, 71, 72]

ESR on Gd-doped $LaCu_3Ru_xTi_{4-x}O_{12}$ reveals an enhanced Korringa relaxation in the pure ruthenate (x = 4) which gradually diminishes on increasing Ti content.[73] Exploratory μSR measurements have been carried out on $A Cu_3 Ru_4 O_{12}$ (A = Ca, Pr, Nd).[74] The root mean square field is determined to 0.15 mT in $CaCu_3Ru_4O_{12}$, independent of temperature. This very low value is attributed to interactions between the muon spin and

1 Note that the system $CaCu_3Ru_xTi_{4-x}O_{12}$ seems to have a miscibility gap approximately for $1.5 < x < 4$ and decomposes preferably into the pure titanate and ruthenate, respectively.[30]

the Cu nuclear moments and its constancy implies that the structural anomaly at 154 K [62] does not affect the atomic positions noticeably. The μSR spectra of ACu$_3$Ru$_4$O$_{12}$ (A = Pr, Nd) are dominated by the interaction with the electronic rare-earth moments. The decay rate follows a simple exponential behavior which is typical for free paramagnetic moments. Its temperature dependence features a smooth increase from 200 K toward 10 K for PrCu$_3$Ru$_4$O$_{12}$ whereas the low temperature data of NdCu$_3$Ru$_4$O$_{12}$ indicates a sudden upturn below 3 K starting from a constant value above. Complex lattice vibrations in ACu$_3$Ru$_4$O$_{12}$ (A = La, Pr, Nd) have been determined by EXAFS measurements revealing that neither a rigid-cage nor a simple reduced-mass approximation are sufficient for describing the behavior of the rattler rare-earth atoms.[75] Resistivity measurements on LaCu$_3$Ru$_4$O$_{12}$ up to 900 K demonstrate a behavior typical for that of a bad metal with a nearly linear T-dependence above 400 K without any sign of saturation.[76] Moreover, the thermoelectric power of ACu$_3$Ru$_4$O$_{12}$ (A = Na, Ca, Ca$_{0.5}$La$_{0.5}$, La) can be directly correlated with the evolution of the Pauli paramagnetic susceptibility. XANES and TGA investigations on the solid-solution series ACu$_3$Ru$_x$Ti$_{4-x}$O$_{12}$ (A = La, Pr, Nd) confirm a constant oxidation state of +4 for Ru which is independent of the grade of substitution.[77] On the other hand, the oxygen valence is reduced from +2 in the pure titanate (x = 0) to a non-integer oxidation state of +1.6 in the pure ruthenate (x = 4). The analysis furthermore suggests a change from a localized to an itinerant character of the Cu electronic states with increasing Ru content, while the Ru electrons themselves remain localized.

In order to clarify the origin of the heavy-fermion formation, the degree of localization and itinerancy of the involved copper and ruthenium magnetic moments, as well as the possible proximity to a quantum critical point, a systematic investigation of the copper-ruthenates including detailed analyses of magnetic and transport properties is in the focus of the present study. Moreover, the influence of magnetic A-site ions on the material properties is studied, with special attention to on-site crystal-field effects of the lanthanide ions and the interplay of f- and d-electron magnetism. The Kramers/non-Kramers type nature of the Nd^{3+}/Pr^{3+} ions allows for comparative experiments unravelling exotic ground state properties such as quadrupolar ordering and quadrupolar Kondo-effects recently found in several intermetallic Pr compounds.

3 Theoretical Background

A central aspect of modern condensed matter research is to understand the coupling between magnetic and electronic properties. Among these are such phenomena as high-temperature superconductivity, colossal magnetoresistance, high dielectric constants, and multiferroicity. Materials with correlated electrons and a high effective electron mass m^*, so-called heavy-fermion systems, typically lie at the edge of magnetic instability, in a regime where quantum fluctuations of magnetic and electronic degrees of freedom are strongly coupled. This makes them highly suitable for research in order to get a deep insight into the electronic and magnetic interactions present within.[78, 79, 80, 81]

Classical heavy-fermion materials contain lanthanides and/or actinides which have strongly localized f-electrons and corresponding magnetic moments. Since the first identification of a HF state in $CeAl_3$ [82] they have attracted great attention among solid state scientists also because of the discovery of superconductivity in the HF compound $CeCu_2Si_2$.[38] Moreover, they have become the focus of interest since it was found that certain AFM ordered intermetallics can be tuned through a quantum phase transition by an external control parameter, which can be pressure, doping, or a magnetic field.[40, 83, 84] The central aspect which also coined the term "heavy fermion" lies within the strong enhancement of the effective electron mass by a factor of $m^*/\mathrm{m_e}$ = 1..1000 when compared to conventional metals like copper. In general, the physics of heavy-fermions arises from the immersion of localized magnetic moments - typically ions close to an empty or filled f-shell (Ce^{3+}, Yb^{3+}) - in a quantum sea of itinerant conduction electrons which results in a highly enhanced density of states at the Fermi level (Abrikosov-Suhl resonance) and a concomitantly quasi-particle renormalization described by an enhanced effective electronic mass m^*. In most f-electron systems, the coupling between the moments leads to AFM order, but in HF metals typically the conduction electrons induce a quantum

mechanical jiggling of the local moments strong enough to prevent magnetic order or to suppress it to lowest temperatures.[78, 79, 80, 81]

Besides the classical heavy-fermion systems, it has been demonstrated that heavy-fermion behavior can also appear in transition-metal oxides (d-electron derived) which do not contain any f-electron element, with LiV_2O_4 being the first and most prominent example.[31, 32] Here, it has been speculated that the d-electrons are partly localized and that heavy-fermion formation results from a strong interaction of localized d-electrons with d-derived band states. As the vanadium ions also constitute a pyrochlore lattice which is strongly frustrated, the heavy fermion properties in LiV_2O_4 have also been explained in terms of magnetic frustration.[85] Later on it has been elucidated that different routes can provide heavy fermions, the closeness of a metal-to-insulator transition being one of those.[86] In contrast to f-electron-based systems, a general picture is still lacking to explain the Kondo like behavior found in a few metallic d-electron systems with strong electron correlations.[86] Moreover, one can also find superconductors among d-electron derived systems, like Sr_2RuO_4.[36, 37, 87, 88]

The mechanism which is responsible for the mass enhancement involves a phenomenon called Kondo effect.[89, 90] It describes how a free magnetic ion (i.e. the f-electron system) with a Curie susceptibility at high temperatures becomes screened by the spins of neighboring conduction electrons. Hereby, a spinless scattering center is formed in a continuous process once the magnetic field or the temperature drops below a certain energy scale which is characterized by the Kondo temperature T_K. The resistivity which would be present due to isolated magnetic ions anyway is additionally increased by these magnetically quenched moments upon cooling. In a highly-correlated electron system this process develops coherence below a certain temperature with a concomitant drop in resistivity upon further cooling. This process does not only have an effect on the resistivity but also on the specific heat, in which the so-called Sommerfeld coefficient γ describing the electronic contribution is enhanced by a factor of m^*/m_e. Even more, the low temperature specific heat often exhibits an unusual dependence and the low-temperature susceptibility is also strongly enhanced.[78, 79, 80, 81]

The low-temperature properties of ordinary metals (i.e. which do not order magnetically and don't become superconducting) can be well described by the phenomenological theory of Fermi liquids.[91, 92, 93] It predicts simple power laws in temperature ascribed

to low-lying excitations of non-magnetic ground states, such as a T-independent Pauli spin-susceptibility χ_0, a linear T-dependence of the electronic specific heat $C_{\mathrm{el}} = \gamma T$, and a power-law behavior of the resistivity according to $\rho = \rho_0 + AT^2$ ($\rho = \rho_0 + AT^5$) in regimes dominated by electron-electron (electron-phonon) scattering. In many cases it is even applicable in the presence of strong electronic correlations, since χ_0, γ, and $\sqrt{A}$ are proportional to the effective (quasiparticle) mass m^*, which is around $\mathrm{m_e}$ in conventional metals but can exceed this value by a factor of several thousand in certain heavy-fermion systems. Sometimes it is possible to fit a broad crossover regime with some effective power laws. One should not confuse this effect with a true generic universal power-law scaling behavior. Namely, an exponent is well defined theoretically, if at least formally a scaling limit exists. This purely formal condition translates to the experimental requirement that an algebraic behavior can be established only if it extends over a considerable range in a regime where no other relevant scale is expected to exist. Note that for the power-law bahavior an extension to absolute zero is still not necessary. In fact, a Fermi liquid is essentially never the true ground state of a metallic system but nevertheless its fixed point can govern the physics over several decades in temperature down to an exponentially small temperature where an order sets in.[78, 79, 80, 94, 81]

Apart from that, a large number of compounds close to a magnetic instability show marked deviations from FL theory which is called non-Fermi-liquid (NFL) behavior. This situation is often realized when the magnetic ordering temperature is suppressed toward absolute zero by tuning competing interactions with an external control parameter, such as magnetic field, pressure, or chemical doping giving rise to a so-called quantum phase transition. Traditionally, such phenomena are observed in correlated f-electron based intermetallic compounds [95, 96] but an increasing number of transition metal compounds also show such kind of behavior, like $CaRuO_3$ [97, 98], $Sr_3Ru_2O_7$ [99, 100, 101], and $La_4Ru_6O_{19}$.[39] It manifests itself in power laws of physical quantities with exponents different from that of a Fermi liquid. Especially the heat capacity often shows a logarithmic divergence toward absolute zero ($C/T \propto -\ln T$) over up to two decades in temperature.[102, 94, 103]

A phenomenon regularly encountered in correlated electron systems is that of mixed valence. In such compounds, the electronic occupation of the (mostly) $4f$ or $5f$ shell of rare earth or actinide atoms may change either continuously or discontinuously as

temperature, pressure, or chemical composition is varied. Associated with such a transition, changes in the electrical resistivity, crystal volume, elastic stiffness, specific heat, optical reflectivity, color, and magnetic properties may occur. Traditionally, the term "valence" in RE/actinide containing compounds applies to the number of localized f-electrons and the term "mixed valence" refers to a situation where the respective ion exists in two different configurations, namely $4f^n/5f^n$ and $4f^{n-1}/5f^{n-1}$. The static mixed valence type arises from a distribution of two distinct species within a crystal, e.g. Fe_3O_4, sometimes exhibiting phonon induced valence fluctuations at high temperatures.[104, 105] In the cases, where the energy required to excite a localized f-electron from the atomic shell to the conduction band at the Fermi level is small or zero, the ion exhibits a quantum mechanical fluctuation between different electronic configurations. The average electronic occupation and (therefore) the atomic valence is then non-integral and is called "homogeneous mixed valence", "intermediate valence", or "interconfigurational fluctuation".[106, 107, 108, 109]

Common classification tools among HF systems are the Wilson- [45] and the Kadowaki-Woods-ratio.[46, 47] The Wilson ratio R_W serves as dimensionless quantity and provides insight into the type of interaction present within the respective material. It includes the zero-temperature magnetic susceptibility χ_0 and the coefficient of the electronic contribution to the specific heat γ. In the original definition calculated within the renormalization group approach [45] it is defined by $R_\mathrm{W} = \pi^2 \mathrm{k}_\mathrm{B}^2 \chi(0)/g^2 \mu_\mathrm{B}^2 s(s+1)\gamma$ (cgs-units, k_B: Boltzmann constant, g: Landé g-factor, s: spin, μ_B: Bohr magneton). For a free electron gas ($g = 2$, $s = 1/2$) $R_\mathrm{W} = 1$ whereas in the strong correlation limit for local Fermi liquids $R_\mathrm{W} = 2$. Mind that different theoretical approaches for the modeling of magnetic impurities in metals have been made resulting in a variation of the universal value of R_W.[110, 111, 112, 113, 114, 115, 116] For the calculation of the Wilson ratio often the susceptibility at around 10 K is used as approximation for the zero-temperature limit.[58] The Kadowaki-Woods-ratio R_KW is defined by $R_\mathrm{KW} = A/\gamma^2$ and compares the temperature dependence of a metal's low-temperature resistivity $\rho(T) = \rho_0 + AT^2$ to that of its electronic heat capacity $C(T) = \gamma T$ - both predicted by Fermi-liquid theory - in order to examine the relationship between the electron-electron scattering rate and the renormalization of the electron mass. Its remarkable property is that it exhibits a constant universal value, at least within a certain class of materials: It was found that in a number of transition metals [46] (see empty upside down triangles in Fig. 5.21) R_KW takes the universal value

of $4{\cdot}10^{-7}\,\mu\Omega\mathrm{cmK^2mol^2/mJ^2}$. Later, many f-electron heavy-fermion compounds were identified to have an enhanced universal value of $R_{\mathrm{KW}} = 10^{-5}\,\mu\Omega\mathrm{cmK^2mol^2/mJ^2}$ even though γ varies by more than one order of magnitude in these materials (see empty circles in Fig. 5.21). Similarly to the above mentioned transition metals, many Yb-based compounds [117] also show up with a universal value of $R_{\mathrm{KW}} = 4 \cdot 10^{-7}\,\mu\Omega\mathrm{cmK^2mol^2/mJ^2}$ (see empty squares in Fig. 5.21). Several efforts have been made to define more universal versions of the Kadowaki-Woods ratio in order to include different material classes in a single consistent model.[118, 119, 120]

3.1 Thermal Expansion

For a modeling of the thermal expansion, it is assumed to be proportional to the internal energy of a quantum mechanical oscillator. Two approaches can be used to calculate the frequency spectra of the phonons in the distribution function, the Einstein model and the Debye model.[121] The first one assumes optical phonons which build up a narrow frequency band and describes the behavior especially at high temperatures. In terms of the temperature-dependent lattice constant $a(T)$, this leads to

$$a(T) = a_0 \left[1 + \alpha\theta_{\mathrm{E}}/(e^{\theta_{\mathrm{E}}/T} - 1)\right] \tag{3.1.1}$$

with the zero-temperature lattice constant a_0, the high-temperature thermal expansion coefficient α, and the Einstein temperature θ_{E}. The second model assumes acoustic phonons which are mainly excited at lower temperatures and show a dispersion up to an upper frequency limit ω_{D}. It best describes the behavior at low temperatures and for $a(T)$ has the form

$$a(T) = a_0 \left[1 + 3\alpha\theta_{\mathrm{D}} \left[\int_0^1 t^3/(e^{tx} - 1)\,\mathrm{d}t\right]_{x=\theta_{\mathrm{D}}/T}\right] \tag{3.1.2}$$

with the zero-temperature lattice constant a_0, the high-temperature thermal expansion coefficient α, and the Debye temperature θ_{D}.

3.2 Specific Heat

3.2.1 Lattice Specific Heat

In a crystalline solid, the mean positions of the atoms are regularly arranged on a crystal lattice, where they are held by interatomic forces. At moderate temperatures, i.e. well below the melting point, the thermally induced vibrations around the mean position are small and can be considered as simple harmonic such that a model of a set of independently oscillating masses connected by elastic springs can be applied. However, the treatment of such harmonic oscillators in terms of classical statistical mechanics fails to describe the observed temperature dependence of the specific heat C and requires treatment by quantum statistics.

The discrete energy levels of a quantum-mechanical harmonic oscillator are given by

$$\epsilon_n = (n + 1/2)\hbar\omega. \tag{3.2.1}$$

The probability of finding an oscillator in the quantum state n with corresponding energy ϵ_n is

$$p_n = \frac{\mathrm{e}^{-\epsilon_n/\mathrm{k_B}T}}{\sum\limits_n \mathrm{e}^{-\epsilon_n/\mathrm{k_B}T}}. \tag{3.2.2}$$

The zero-point energy $\hbar\omega/2$ is common to both the nominator and denominator of equation 3.2.2 such that the mean value of n in thermal equilibrium can be written as

$$\langle n \rangle = \sum_n n p_n = \frac{\mathrm{e}^{-\epsilon_n/\mathrm{k_B}T}}{1 - \mathrm{e}^{-\epsilon_n/\mathrm{k_B}T}} = \frac{1}{\mathrm{e}^{\epsilon_n/\mathrm{k_B}T} - 1}. \tag{3.2.3}$$

The underlying statistics of the distribution of n is of Bose-Einstein type which leads us to the first model of the lattice specific heat, the Einstein model.[122] Here, the lattice is considered as a collection of independently vibrating oscillators, all with the same frequency ω_E. The distribution of vibrational modes then is a delta function and for a

collection of N oscillators with three translational degrees of freedom, the average internal energy E amounts

$$E = 3N \int \left(\langle n \rangle + 1/2\right) \hbar\omega \delta(\omega - \omega_\mathrm{E}) \, \mathrm{d}\omega = 3N\hbar\omega_\mathrm{E} \left(\frac{1}{\mathrm{e}^{\hbar\omega_\mathrm{E}/\mathrm{k_B}T} - 1} + 1/2 \right). \tag{3.2.4}$$

With the Einstein temperature $\theta_\mathrm{E} = \hbar\omega_\mathrm{E}/\mathrm{k_B}$, the specific heat C can be calculated to

$$C = \partial E/\partial T = 3N \left(\frac{\theta_\mathrm{E}}{T}\right)^2 \frac{\mathrm{e}^{\theta_\mathrm{E}/T}}{\left(\mathrm{e}^{\theta_\mathrm{E}/T} - 1\right)^2}. \tag{3.2.5}$$

The Einstein model correctly predicts the Dulong-Petit [123] limit $C(T \to \infty) = 3N\mathrm{k_B}$ at high temperatures which is equal to $3\mathrm{N_A k_B} = 3\mathrm{R} \approx 24.9\,\mathrm{Jmol^{-1}K^{-1}}$ in the case of one mol of substance and it describes the dependence of C over a wide T-range very well. However, at low temperatures it predicts an exponential decrease which is not observed experimentally. The central argument criticizing the Einstein model is the assumption that all atoms vibrate with the same frequency. Starting from that point, this leads us to the Debye model.[124]

In contrast to the Einstein model, it treats the vibrations of the atomic lattice in terms of a collective phenomena, namely as acoustic modes. This approach is motivated because due to the quantization of the lattice vibrations only low-frequency modes are excited at low temperatures. In a typical solid, the wavelengths of these modes are much longer than the interatomic distances such that they can be treated as an elastic, isotropic continuum.

The Debye model starts with the picture of a plane wave travelling through a finite cube of side length L with the speed of sound c_s:

$$\nabla^2\psi = \frac{1}{c_s^2} \frac{\partial^2\psi}{\partial t^2}. \tag{3.2.6}$$

With the boundary conditions $\psi = 0$ at $x, y, z = 0$ and $x, y, z = L$, the solution of this differential equation are standing waves of the form

$$\psi(x,y,z,t) = A \sin k_x x \sin k_y y \sin k_z z \sin \omega t. \tag{3.2.7}$$

Here, A is the amplitude, ω is the frequency, and $k_{x,y,z} = 2\pi/\lambda_{x,y,z}$ denote the wavevectors with wavelengths $\lambda_{x,y,z}$ which are related to the order of the overtones $n_{x,y,z}$ by $k_{x,y,z} = n_{x,y,z}\pi/L$. The number of allowed values of $n_{x,y,z}$ in n-space in the range $n_{x,y,z} + dn_{x,y,z}$ is then equal to

$$\Delta n_x \Delta n_y \Delta n_z = \frac{L^3}{\pi^3} \Delta k_x \Delta k_y \Delta k_z = \frac{V}{\pi^3} \Delta k_x \Delta k_y \Delta k_z, \tag{3.2.8}$$

where V is the volume of the cube. $\Delta k_x \Delta k_y \Delta k_z$ refers to the volume element in the first octant of k-space according to

$$\Delta k_x \Delta k_y \Delta k_z = \frac{1}{8} 4\pi k^2 \mathrm{d}k, \tag{3.2.9}$$

such that the number of allowed states $\mathrm{d}n$ the following equation applies:

$$\mathrm{d}n = \frac{V}{2\pi^2} k^2 \mathrm{d}k. \tag{3.2.10}$$

Using as approximation the dispersion relation $c_s = \lambda\nu$, then the density D of phonon modes for each polarization direction is

$$D(\omega) = \frac{\mathrm{d}n}{\mathrm{d}\omega} = \frac{V}{2\pi^2} \frac{\omega^2}{c_s^3}. \tag{3.2.11}$$

Since the sound velocity c_s in a solid generally depends on the direction of propagation, it should be considered as an average over all directions. Moreover, the dispersion relation of acoustic modes decomposes into three branches, a longitudinal one and two equivalent transversal ones with corresponding sound velocities $c_{l,t1,t2}$ such that with the identity $3\left\langle c_s^{-3} \right\rangle = c_l^{-3} + 2c_t^{-3}$ the density of modes changes to

$$D(\omega) = \frac{V}{6\pi^2} \left(c_l^{-3} + 2c_t^{-3} \right) \omega^2. \tag{3.2.12}$$

To account for the discrete nature of a solid in terms of the crystal lattice, only wavelengths longer than two lattice constants ($\lambda > 2a$) are considered. This is applicable, since high frequency vibrations can still be described by long wavelengths. This leads to a cut-off frequency ω_D defined by

$$\int_0^{\omega_\mathrm{D}} 3D(\omega)\mathrm{d}\omega. \tag{3.2.13}$$

Calculation of the integral leads to

$$\omega_\mathrm{D} = \left(\frac{6\pi^2 N}{V}\right)^{1/3} \left(\frac{1}{c_l^3} + \frac{2}{c_t^3}\right)^{-1/3}. \tag{3.2.14}$$

With this identity, the density takes the simple form

$$D(\omega) = \frac{3N}{\omega_\mathrm{D}^3}\omega^2 \tag{3.2.15}$$

with the characteristic Debye temperature defined by $\theta_\mathrm{D} = \hbar\omega_\mathrm{D}/\mathrm{k_B}$. The average internal energy E can the be calculated to

$$E = 3\int_0^{\omega_\mathrm{D}} D(\omega)\left(\langle n\rangle + 1/2\right)\hbar\omega\mathrm{d}\omega = E_0 + 9N\mathrm{k_B}T\left(\frac{T}{\theta_\mathrm{D}}\right)^3 \int_0^{x_\mathrm{D}} \frac{x^3}{\mathrm{e}^x - 1}\mathrm{d}x \tag{3.2.16}$$

with $x = \hbar\omega/\mathrm{k_B}T$ and $x_\mathrm{D} = \hbar\omega_\mathrm{D}/\mathrm{k_B}T$ and the specific heat C then amounts

$$C = \partial E/\partial T = 9\mathrm{R}\left(\frac{T}{\theta_\mathrm{D}}\right)^3 \int_0^{x_\mathrm{D}} \frac{x^4\,\mathrm{e}^x}{\left(\mathrm{e}^x - 1\right)^2}\mathrm{d}x. \tag{3.2.17}$$

As the Einstein model, the Debye model correctly predicts the Dulong-Petit [123] limit. It furthermore describes the T-dependence of the lattice heat capacity at low temperature very well, which can there be approximated by the power law $C = \beta T^3$ with $\beta = 12\mathrm{R}\pi^4/5\theta_\mathrm{D}^3$. Due to simplifying assumptions, namely that the frequency is inversely proportional to

the wavelength (meaning a constant speed of sound), its accuracy suffers at intermediate temperatures.

In practice, both Debye and Einstein terms are used to model the lattice specific heat of a solid. Usually, one Debye term is utilized to account for the low temperature contribution of acoustic phonons (one longitudinal and two transversal modes) and several Einstein terms (typically 1-3) describe the optical phonons at intermediate temperatures.[125, 126]

3.2.2 Electronic Specific Heat

According to classic statistical mechanics, the equipartition law leads to a contribution to the specific heat of $1/2 k_B T$ for one electron moving freely through a metal and for each translational degree of freedom. For one mol of monovalent metal this would lead to an electronic specific heat of $3/2$R. Together with the lattice specific heat this would result in $9/2$R at high temperatures which is not observed experimentally. The solution of this problem is to treat it quantum-mechanically by obeying the Pauli exclusion principle in using Fermi-Dirac statistics for the distribution of electronic states.

In a metal the inner shell electrons are tightly bound in contrast to the outer electrons within unfilled shells. But even they cannot move freely as they are subject to the periodic potential of the lattice. This causes the electronic states to form bands which are separated by energy gaps and it is these bands which represent all possible states into which electrons can be exited. For ordinary temperatures, the number of electrons being excited into higher energy states can be approximated by the number of electrons in the vicinity of the Fermi level. The average energy E of N electrons can be written as

$$E = \int_0^\infty \epsilon f(\epsilon)\eta(\epsilon)\mathrm{d}\epsilon = \int_0^\infty (\epsilon - \mu) f(\epsilon)\eta(\epsilon)\mathrm{d}\epsilon + N\mu \tag{3.2.18}$$

with the electron energy ϵ, the Fermi-Dirac function $f(\epsilon) = \left(\mathrm{e}^{(\epsilon-\mu)/k_B T} + 1\right)^{-1}$, and the density $\eta(\epsilon)$ of states for both spin directions. The specific heat C is then given as

$$C = \partial E/\partial T = \int_0^\infty (\epsilon - \mu) \frac{\mathrm{d}f(\epsilon)}{\mathrm{d}T} \eta(\epsilon) \mathrm{d}\epsilon. \tag{3.2.19}$$

If we use now $x = (\epsilon - \mu(T))/\mathrm{k_B}T$, then we get

$$\frac{\mathrm{d}f(\epsilon)}{\mathrm{d}T} = \frac{\mathrm{d}f}{\mathrm{d}x}\frac{\mathrm{d}x}{\mathrm{d}T} = (-)\frac{\mathrm{e}^x}{(\mathrm{e}^x+1)^2}\left(\frac{\mu'}{\mathrm{k_B}T} + \frac{x}{T}\right). \tag{3.2.20}$$

By changing the variable of integration with the identity $\mathrm{d}\epsilon/\mathrm{d}x = \mathrm{k_B}T$ and changing the lower integration limit from $\epsilon = 0 \Leftrightarrow x = -\mu/\mathrm{k_B}T$ to $-\infty$ which is justified for sufficiently low temperatures, the specific heat C will amount

$$C = (\mathrm{k_B}T)^2 \int_{-\infty}^{+\infty} \frac{x\,\mathrm{e}^x}{(\mathrm{e}^x+1)^2}\left(\frac{\mu'}{\mathrm{k_B}T} + \frac{x}{T}\right)\eta(\mu + \mathrm{k_B}Tx)\,\mathrm{d}x. \tag{3.2.21}$$

Since we are interested only in the low temperature results, we will expand $\eta(\mu + \mathrm{k_B}Tx)$ in a Taylor series and ignore terms higher than linear in T. Furthermore, $\mathrm{e}^x/(\mathrm{e}^x+1)^2$ is an even function, so that only even powers of x contribute to the integral and by replacing $\eta(\mu)$ with $\eta(\epsilon_\mathrm{F})$ one can write

$$C = (\mathrm{k_B}T)^2 \frac{\eta(\epsilon_\mathrm{F})}{T} 2\int_0^\infty \frac{x^2\,\mathrm{e}^x}{(\mathrm{e}^x+1)}\mathrm{d}x = \frac{\pi^2\mathrm{k_B^2}}{3}\eta(\epsilon_\mathrm{F})\,T = \gamma T. \tag{3.2.22}$$

We now see that with the Sommerfeld coefficient γ [44] the electronic specific heat is linear in T. It is also generally applicable to all electrons irrespective of the nature of the band and requires only the determination of the density of states at the Fermi level.[125, 126]

3.2.3 Schottky Anomalies from Crystal-Electric Fields

The static charge distribution represented by the regularly arranged ions within a crystal structure causes an electric field with certain local symmetries at the respective lattice sites, the so called crystal-electric field (aka: crystal field). Depending on this symmetry,

the degeneracy of the free-ion ground state of a magnetic ion ($J \neq 0$) is lifted and the population of these gets temperature dependent. This results in a contribution to the specific heat C of which the molar one for a system with n discrete energy levels (ground state included) and degeneracies g_i, which are separated from the ground state by energies ϵ_i (ground state: $\epsilon_0 = 0$ by definition), amounts

$$C = \partial E/\partial T = \partial/\partial T \left(\mathrm{N_A} \sum_{i=0}^{n-1} \epsilon_i g_i \exp(-\epsilon_i/\mathrm{k_B}T) / \sum_{i=0}^{n-1} g_i \exp(-\epsilon_i/\mathrm{k_B}T) \right). [125,\ 126] \quad (3.2.23)$$

The corresponding (absolute) molar entropy S of such a system is

$$S = \mathrm{N_A}/T \left(\sum_{i=0}^{n-1} \epsilon_i g_i \exp(-\epsilon_i/\mathrm{k_B}T) / \sum_{i=0}^{n-1} g_i \exp(-\epsilon_i/\mathrm{k_B}T) + \right. \\ \left. + \mathrm{k_B}T \ln\left(\sum_{i=0}^{n-1} g_i \exp(-\epsilon_i/\mathrm{k_B}T) \right) \right). [125,\ 126] \quad (3.2.24)$$

Note that the low-temperature limit of the absolute entropy is proportional to the logarithm of the ground-state degeneracy: $\lim_{T\to 0} S = \mathrm{R} \ln g_0$. That means that it only starts at $S = 0$ in the case of a singlet ground state. The high-temperature limit for a $(2J+1)$-fold degenerate system is $\lim_{T\to\infty} S = \mathrm{R}\ln(2J+1)$. For the evaluation of the experimental data of such Schottky contributions it is of importance to look at the entropy difference ΔS which accumulates while increasing the temperature and simultaneously changing the population of the corresponding levels of the system. For example, consider the Kramers ion Nd^{3+} ($4f^3$, $J = 9/2$) in a CEF of cubic symmetry. According to LLW,[127] the 10-fold $(2J+1)$ degenerate Nd^{3+} free ion ground state ${}^4I_{9/2}$ is split into one doublet Γ_6 and two quartets $\Gamma_8^{(1,2)}$. The possible term schemes for this case are depicted in Fig. 3.1. The absolute entropy S and the entropy difference ΔS are listed at the right side of each term scheme. That means, e.g., for the experimentally observable transition from a doublet ground state to an excited quartet state, the entropy changes by $\mathrm{R}\ln 3$ (rightmost scheme).

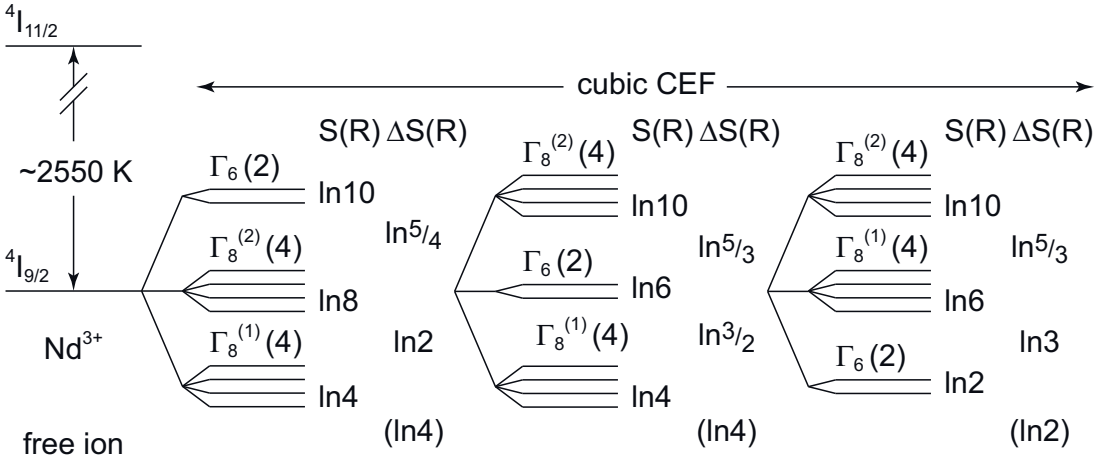

Figure 3.1: Level schemes of Nd^{3+} as a free ion and in a CEF of cubic symmetry. The degeneracy of the respective CEF level labeled Γ_i is given in brackets, the absolute entropy S and the entropy difference ΔS are written on the right side of each of the possible level sequences. The entropy difference in brackets is that which is hidden in the ground state and is therefore not accessible experimentally. See text for details.

3.2.4 Nuclear Schottky Anomalies

The temperature dependent molar specific heat C arising from an axially symmetric quadrupole interaction of a nuclei with nuclear spin I and $2I+1$ (non-degenerate) energy levels E_i ($i = 0..2I$) amounts

$$C = \mathrm{R}/T^2 \left[\left(1/Z \sum_{i=0}^{2I} E_i^2 e^{-E_i/T} \right) - \left(1/Z \sum_{i=0}^{2I} E_i e^{-E_i/T} \right)^2 \right] .[125] \tag{3.2.25}$$

E_i itself is dependent on the global and local magnetic field B_g and B_l, the magnetic and quadrupole moment of the nuclei μ and Q as well as on the global and local electric field gradients $V_{zz,\mathrm{g}}$ and $V_{zz,\mathrm{l}}$ according to

$$E_i = \begin{cases} [\mu(i-I)(B_\mathrm{g}+B_\mathrm{l})/(\mathrm{k_B}I)] & \Leftrightarrow I < 1 \\ [\mu(i-I)(B_\mathrm{g}+B_\mathrm{l})/(\mathrm{k_B}I)] + & \\ + \{3eQ(V_{zz,\mathrm{g}}+V_{zz,\mathrm{l}})/[4I(2I-1)\mathrm{k_B}]\}\,[(i-I)^2 - I(I+1)/3] & \Leftrightarrow I > 1. \end{cases} \tag{3.2.26}$$

If interested only on its high-temperature side, such a Schottky anomaly can also be simplified by expansion in inverse powers of T according to

$$C = \frac{R}{80}\frac{(2I+2)(2I+3)}{2I(2I-1)}\left(\frac{e^2qQ}{\mathrm{k_B}}\right)^2 T^{-2} - \\ -\frac{R}{1120}\frac{(2I-3)(2I+2)(2I+3)(2I+5)}{4I^2(2I-1)^2}\left(\frac{e^2qQ}{\mathrm{k_B}}\right)^3 T^{-3}.[128] \tag{3.2.27}$$

4 Methods & Experimental Details

4.1 Sample Preparation

Polycrystalline samples of $A\mathrm{Cu_3Ru_4O_{12}}$ (A = Na, Ca, La, Pr, Nd) were synthesized by solid-state reaction.[48, 41] Stoichiometric amounts of high purity anhydrous $\mathrm{NaCO_3}$, $\mathrm{CaCO_3}$, $\mathrm{La_2O_3}$, $\mathrm{Pr_2O_3}$, $\mathrm{Nd_2O_3}$ (99.9%), CuO (99.99%), and $\mathrm{RuO_2}$ (99.95%) were ground in an agate mortar and pestle and pressed into pellets. Placed in alumina crucibles, they were fired in air at ambient pressure in a muffle oven at 1040°C for 24 h. To assure complete chemical reaction and to achieve single-phase material with good homogeneity, the sintering process at 1040°C was repeated several times with subsequent regrinding, pressing and firing. Care has to be taken not to exceed 1050°C otherwise Na an Cu are likely to evaporate, leading to distorted stoichiometry or even to decomposition of the desired material. There is also experimental evidence that the application of high pressures in the range of 2-3.5 GPa is harmful with regard to the stabilization of Ru-containing perovskites, leading to the segregation of $\mathrm{RuO_2}$.[129] For the synthesis of $\mathrm{SrCu_3Ru_4O_{12}}$ an enhanced route was chosen in order to minimize the formation of the impurity phase $\mathrm{SrRuO_3}$. Here, stoichiometric amounts of $\mathrm{SrCO_3}$ (99.9%), CuO (99.99%), and $\mathrm{RuO_2}$ (99.95%) were hand-mixed in a mortar and pestle. Per gram of starting material an additional amount of 0.3 g of CuO was added as flux. The mixture was fired in air as described above at a temperature of 1040°C at which a eutectic mixture of CuO and $\mathrm{Cu_2O}$ forms with respect to the partial pressure of oxygen in the oven atmosphere.[130, 131] After cooling, the product was extracted by dissolving the flux with diluted hydrochloric acid. The resulting crystals are perfect cubes with a size of $\approx 80\,\mu$m which were ground back to powder for further investigations .

For the preparation of single crystals from the batch "CaCRHC2", polycrystalline material was prepared in a first step from anhydrous $\mathrm{CaCO_3}$, CuO, and $\mathrm{RuO_2}$ with the stoi-

chiometric proportion 1:2.94:4.40. The material was thoroughly ground under 2-propanol in an agate mortar and calcined in air in an alumina crucible at 1050°C for 24 h after drying. The product has been x-ray checked without indications of impurities. Single crystal growth was realized on the basis of Ref. [42] in a 1:2 mass proportion flux of $CuO:Cu_2O$. Therefore 2 g of flux were mixed with 0.3 g of polycrystalline $CaCu_3Ru_4O_{12}$ (batch "CaCRH") in a platinum crucible and heated to 1200°C with a ramp of 240°C/h. After a holding time of 3 h the mixture was cooled to 1000°C with a rate of 5°C/h. Finally, the oven was switched off and after cooling to room temperature the flux was removed with diluted hydrochloric acid.

The preparation of the batch "Flux1" was done similar to the method described above. Here, 0.3163 g of a 1:4.54 molar mixture of anhydrous $CaCO_3$ and RuO_2 was directly mixed with 2 g of a 1:2 mass proportion flux $CuO:Cu_2O$ in an agate mortar. The mixture was heated to 1200°C with a ramp of 300°C/h in an undocumented crucible (probably alumina) where it stayed for 3 h before it was cooled at a rate of 5°C/h to 900°C. After cooling to room temperature the product was extracted with diluted hydrochloric acid yielding 0.243 g of $CaCu_3Ru_4O_{12}$ (59% of the theoretical value).

4.2 X-ray Powder Diffraction

X-ray powder diffraction is used as an analytical technique to reveal information about the crystallographic structure of polycrystalline materials. It is based on the observation of the angular dependent intensity of a x-ray beam scattered by a sample and its identification by comparing the diffraction data against a crystal structure database or by computer-aided calculation assuming a certain structure, commonly known as Rietveld refinement.[132] The refinement results may also be used to characterize sample parameters such as chemical composition, crystallite size, preferred orientation of grains, strain, and to quantify the fraction of phases within heterogeneous materials.

Fig. 4.1 shows the schematics of the transmission mode diffractometer Stadi P (STOE & Cie., Darmstadt) used in this work. In order to acquire a diffraction pattern, a monochromatic x-ray beam has to be generated in a special electron tube in which a cathode (usually made of tungsten) is heated to 1200-1800°C (see Fig. 4.1). Electrons forced to leave the

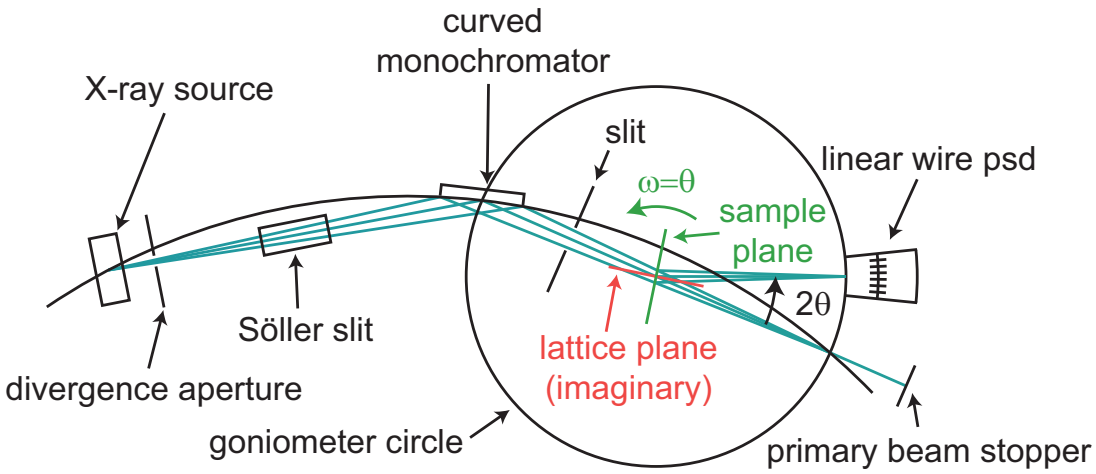

Figure 4.1: Schematic diagram of the path of x-rays of the transmission mode diffractometer Stadi P (STOE & Cie., Darmstadt). X-rays are drawn in dark cyan, sample plane in green, imaginary lattice plane fulfilling the Bragg condition in red. See text for details. (Diagram based on [133]).

cathode by the heat are accelerated by a high voltage (20 – 60 kV) applied between cathode and an anode made of some other pure metal (in this case copper). When striking the anode, the electrons both emit continuous x-ray radiation by being decelerated in the anode metal and discrete (monoenergetic) high intensity x-rays by ejecting other electrons bound to an anode (copper) atom. The so produced x-ray beam is limited in size by an aperture and collimated by a so called Söller slit. One of the discrete x-ray energies (in this case the $K_{\alpha 1}$ line of copper, λ = 1.540598 Å) is then filtered out with a curved germanium monochromator by using its (111) lattice plane and directed to the sample being investigated.

As mentioned above, the scattered x-ray intensity has an angular dependence which originates from the interaction of the incident electromagnetic x-ray wave with the electron cloud of the sample atoms, known as Rayleigh scattering. This means that in general, the method of x-ray diffraction exhibits sensitivity for the electron density and is therefore hardly suitable for the detection of light elements such as hydrogen. The process of Rayleigh scattering is elastic (non-absorbing) and occurs when radiation interacts with particles much smaller than its corresponding wavelength. It can be described as follows:[1] Electrons of the sample atoms underlie an accelerated movement

1 Note that effects of the scattering process such as absorption, extinction, polarization, atomic scattering factor, structure factor, etc. also influence the diffracted intensity.

caused by the oscillating electromagnetic field of the incident x-rays which forces them to move in the same manner. This results in a dynamic dipole which re-radiates x-rays of the same frequency/wavelength. Scattered x-rays of neighboring elementary dipoles (i.e. atoms) within a certain coherence volume interfere with each other leading to extinction/amplification of the scattering amplitude by overlapping waves (destructive/constructive interference) and effecting a stationary interference pattern. The situation of individual scattering atoms can be reduced to a much simpler picture by looking at equivalent (parallel) planes of the sample's crystal lattice. Here maxima in the interference pattern arise at scattering angles (2θ) which fulfill the Bragg [134] condition for constructive interference[2]

$$n\lambda = 2d_{hkl}\sin\theta_{hkl} \tag{4.2.1}$$

with

- λ ... X-ray wavelength
- d_{hkl} ... distance between equivalent lattice planes with Miller index hkl [136]
- θ_{hkl} ... angle between incident ray and the scattering lattice planes.
- n ... maximum of the n^{th} order.

The recording of the diffracted intensity is carried out in a way such that the sample plane (green line in Fig. 4.1) is rotated out of the perpendicular position with respect to the incident beam (starting typically at $\omega = \theta = 5°$). The scattered beam forms the same angle with the lattice plane (red line in Fig. 4.1) as the incident one such that the total deflection angle is 2θ with respect to the unscattered (primary) beam. In any position of $\omega = \theta$ only those lattice planes of the sample crystallites are relevant for intensity that are perpendicular to the sample plane and fulfill the Bragg condition. The intensity is recorded by a linear wire position-sensitive detector at position 2θ which covers a 2θ range of a few degrees for high angular resolution and to improve statistics. Both sample and detector rotation are synchronized such that the detector always forms twice the angle with respect to the primary beam as the sample over the full 2θ range (typically up

2 Note that in crystallography $n := 1$ and reflexes of higher order ($n > 1$) are indicated by Miller indices containing a common factor. For example $(hkl) = (222)$ represents the second order spectrum of $(hkl) = (111)$.[135]

to 2θ = 160°). Further statistical improvement of the scattered intensity is achieved by continuous rotation of the sample around its plane normal throughout the measurement. For a detailed description on (powder) diffraction and structure determination see also Refs. [133, 137, 135, 138, 139, 140].

For $A\mathrm{Cu_3Ru_4O_{12}}$ (A = Na, Ca, Sr, La, Pr, Nd) studied in this work, the diffraction patterns were recorded at room temperature with the machine described above. A few milligram of the powdered material were placed between two acetate foils with some silicon grease as adhesive and then fixed in a holder ring. The crystallographic data were analyzed by Rietveld refinement [132] using the FullProf program suite.[141] The parameters for zero point shift (*zero*), scale factor (*scale*), lattice constants (*a, b, c*), profile shape (*shape*), overall isotropic displacement (b_{iso}), resolution parameters (*u, v, w*) and the x-y-coordinates of oxygen were determined.

4.3 Neutron Scattering

Structural aspects of condensed matter are not only accessible with x-rays (photons) but also with massive particles as probe featuring a de Broglie wavelength [142] of the same order as interatomic distances. For neutrons this corresponds to energies in the meV range which is related to an energy spectrum with a characteristic temperature close to room temperature. Thus, such neutrons are called thermal neutrons.

Two possible layouts are used for the production of neutrons: first is the fission of heavy nuclei (mostly uranium-235) by slow neutrons carried out in a nuclear reactor optimized not for energy output (as in a nuclear power plant) but for high neutron flux. This process is self-sustaining as more neutrons are released during fission than consumed for initiation; second is a spallation source in which an accelerator is used to create a proton beam with a current of about 1 mA and a particle energy in the GeV range. It is guided to a target made of some special heavy-metal alloy (e.g. uranium, lead-bismuth) releasing neutrons from the nuclei by intra- and inter-nuclear cascade reactions describable as an evaporation process.

As both methods primarily produce fast neutrons with typical energies of 1 MeV and above, they have to be slowed down. This energy shift is accomplished by inelastic

collisions of the high-energy neutrons with nuclei of a so-called moderator which usually consists of heavy water or liquefied deuterium surrounding the neutron source. The transportation of the neutrons from the source to the scientific instrumentation arranged outside the radiation shielding of the core is carried out by beam tubes. To reduce unwanted radiation such as fast neutrons, they are directed tangentially to the core an thus ending within the moderator which radiates the neutrons isotropically. Since the intensity of the neutron flux falls of with the distance r from the core as $1/r^2$, so-called neutron guides are used to reduce this loss in luminosity. They consist of tubes with a usually rectangular cross section of which the inner walls (glass or silicon as substrate) are coated with alternating nickel/titanium multilayers which are optimized to reflect the neutrons from the guide wall.

For x-rays, the effective area that governs the probability of a scattering or absorption event - the cross section - is mainly represented by the electron shell of an atom due to the strong interaction between photon and electron via the electromagnetic fundamental force. This means that x-rays cannot penetrate very deep into matter, especially in materials consisting of heavier elements with a correspondingly large number of electrons. In contrast, a neutron interacts with matter in other ways which makes it so advantageous for experimentalists as probe: Firstly, it is uncharged and therefore does not underlie the Coulomb interaction. Hence, it can deeply penetrate into the sample close to the nucleus being scattered there by nuclear forces. These nuclear scattering processes are isotope-dependent, making it easy to distinguish between them. This especially helps to identify light atoms such as hydrogen which are merely invisible with x-rays. Secondly, not only the wavelength of thermal neutrons is in the range of interatomic distances but also their energy is of the same order as that of many excitations in condensed matter (e.g. phonons, crystal field splittings etc.). During inelastic scattering processes (creation/annihilation of excitations) this leads to a measurable change in the energy of a neutron carrying valuable information about static or dynamic aspects within the material being investigated. Thirdly, a neutron carries a magnetic moment and can therefore interact with other magnetic moments such as an unpaired electron in a magnetic atom. With this property of the neutron, light can be thrown on magnetic ordering phenomena and spin correlations.

Detailed information with a view from the theoretical and experimental as well as from

the engineering side on all aspects of neutron scattering can be found in Refs. [143, 144, 145, 146].

4.3.1 Powder Diffraction

Neutron powder diffraction (NPD) basically works the same way as with x-rays (see chapter 4.2). Fig. 4.2 shows such a neutron powder diffractometer setup (to be more specific: the diffractometer "HRPT" from the Swiss spallation source SINQ of the Paul-Scherrer-Institute) with the neutron beam being extracted from the core with an above mentioned beam tube (top right). In order to reduce residual background radiation such as high-energy neutrons and gamma quanta, the neutrons are guided via several filters, collimators and reductions before striking the monochromator crystal (lower right). It allows a flexible choice of the neutron wavelength (0.94 – 2.96 Å) by taking different (hkk) planes of germanium wafers and different resolutions/intensities by adjusting appropriate primary/secondary collimators and by choosing the beam take-off-angle (90° or 120°). A shutter can be closed to prevent the neutron beam from exiting the neutron guide/heavy concrete shielding when working in the beam path, e.g. during sample change or maintenance. Before reaching the sample, the neutron beam passes a so-called monitor which allows to observe the actual beam intensity. This is important because the neutron flux has an occasionally high fluctuation due to instability of the proton beam forming the basis of the neutron source. During acquisition and analysis of the diffraction patterns it gives the possibility to normalize data and hence to be able to better compare different data sets, e.g. diffraction patterns for one and the same sample but at different temperatures. The sample is centered in the detector assembly, usually within a cylindrical vanadium can placed in a cryostat, a cryomagnet or an oven offering different sample conditions. A beam stop behind the sample (outside the sample environment) prevents machinery/persons being hit by the primary neutron beam. At the respective vertical position at which the sample is mounted within the cryostat, it is made of aluminum, a material easily penetrable for neutrons. Neutrons being scattered by the sample get a radial distribution according to the crystal structure of the sample (see also chapter 4.2). This pattern is recorded with a position sensitive detector covering scattering angles from 5° to 160°. It consists of 1600 gold-plated tungsten wires with an angular separation of 0.1° running in a detector gas atmosphere of He-3 (3.6 bar) and CF_4 (1.1 bar). A collimator

is positioned between sample and detector with radially separated (1°) mylar foils coated with Gd_2O_3 to eliminate Bragg peaks from sample environment (cryostat or furnace) and to reduce background radiation. The detector bank is mounted on air cushions making fine rotation possible for resolutions higher than 0.1°.

Structural investigations on $ACu_3Ru_4O_{12}$ (A = Na, Ca, Sr, La, Pr, Nd) were performed by NPD on the machine described above with a wavelength of $\lambda = 1.1545$ Å (monochromator: Ge-822). The samples (few gram each, half a gram in the case of $NaCu_3Ru_4O_{12}$) were filled in cylindrical vanadium cans and mounted in a cryostat which allows cooling the sample from room temperature (RT) down to 1.6 K. The data were analyzed by Rietveld refinement [132] using the FullProf program suite.[141] The parameters for zero point shift (*zero*), scale factor (*scale*), sample transparency coefficient (*sysin*), lattice constants (*a, b, c*), anisotropic displacement parameters (B_{ij}) for all lattice sites, resolution parameters (*u, v, w*) and the x-y-coordinates of oxygen were determined.

4.3.2 Time-Of-Flight Spectroscopy

Thermal neutrons used in scattering experiments have velocities according to their kinetic energy ($v = \sqrt{2E/m}$) which is of the order km/s. Loss or gain in energy by interactions of the neutrons with the sample can then easily be measured by determination of their change in velocity (time-of-flight over a certain distance). However, detecting a neutron (e.g. at a starting point) can only be performed once as they are only visible in nuclear reactions in which the original neutron itself is lost. Therefore, TOF techniques can only be used once, either for the measurement of the incoming or the scattered wavevector. In most setups the latter method is used which is called direct TOF.

The instrument IN4 at the Institut Laue-Langevin (ILL), Grenoble, France is such a direct TOF spectrometer (see Fig. 4.3). It is a high-flux instrument used for the study of excitations in condensed matter and works in the energy range 10-100 meV. A polychromatic (white) neutron beam extracted from the moderator tank is partially monochromatized by two counter-rotating disc choppers (up to 5000 rpm). By that most of the undesired background radiation (high energy neutrons and gamma rays) is cut off and packets of low energy neutrons are generated falling upon a monochromator which allows the selection of a suitable energy/wavelength from the thermal neutron spectrum. The

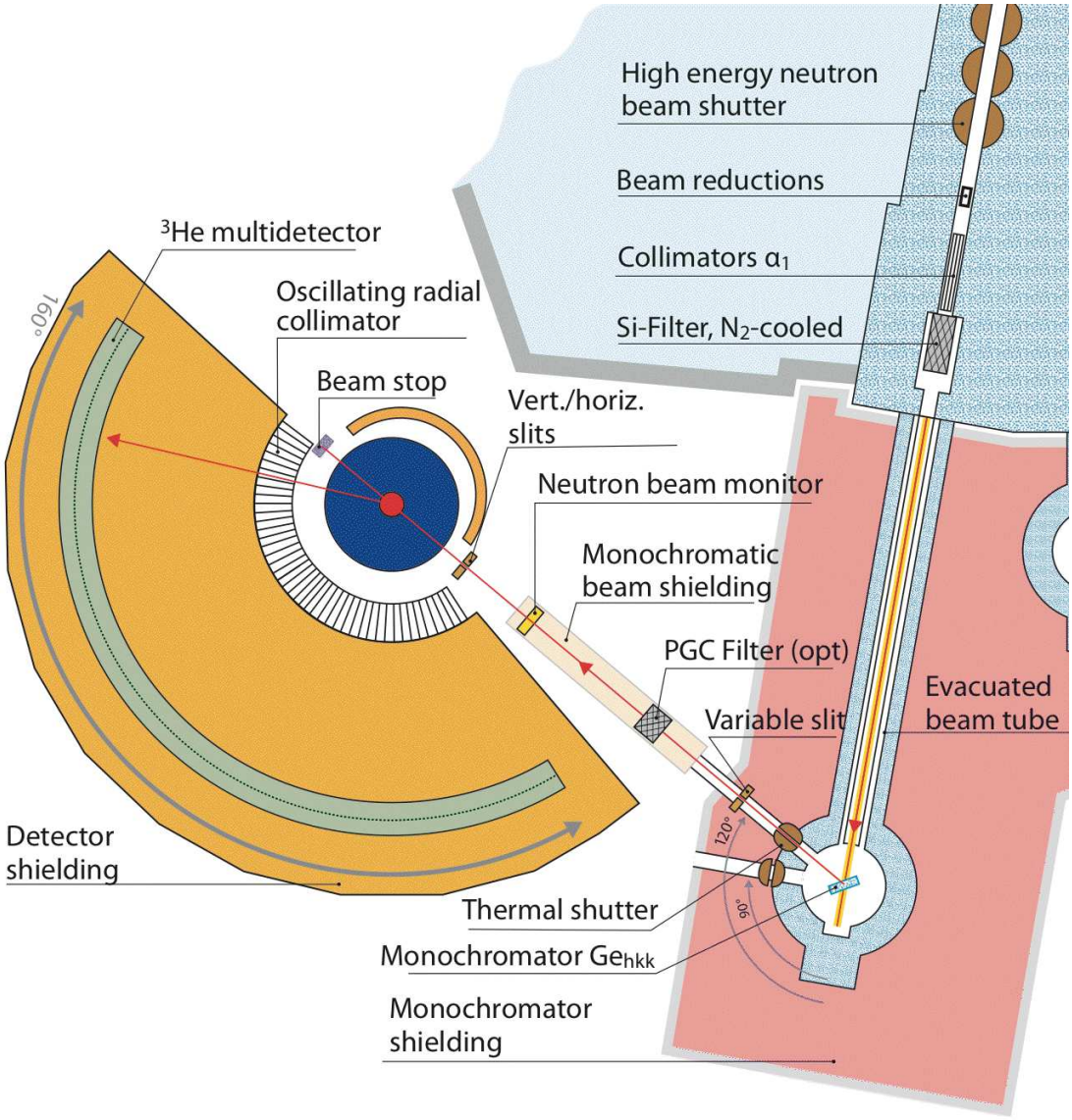

Figure 4.2: Beam line and detector setup of the high-resolution powder diffractometer for thermal neutrons (HRPT) at the Swiss spallation neutron source (SINQ) of the Paul-Scherrer-Institute (PSI), Villigen, Switzerland. See text for details. Courtesy of PSI.

monochromator consists of an assembly of 55 crystal pieces which concentrate the divergent incident beam onto a small area at the sample position for best flux performance. The variable curvature of the monochromator is essential in controlling the time and space focussing conditions for optimal performance.[147] The reflected monochromatic beam then passes to the Fermi chopper, effectively a rapidly rotating collimator (up to 40000 rpm) only transmitting neutrons when the neutron path is parallel to the slits. It also chops the already packeted beam into very short pulses ($10 - 50\,\mu s$) which are then guided to the sample. Various sample environments (cryostats, furnaces, cryomagnets, etc.) are available to study materials with respect to external parameters. A collimator arranged radially around the sample eliminates scattering from the sample environment before the scattered neutron beam enters the detector covering scattering angles up to 120°. The time-of-flight raw data $I(2\theta, t)$ are further treated in order to obtain the dynamic structure factor $S(Q, \omega)$ that is characteristic of the dynamical and structural properties of the sample.

Inelastic neutron-scattering experiments were performed in a temperature range of $1.6\,K < T < 200\,K$ with the TOF instrument described above and with an incident neutron wavelength of 2.181 Å corresponding to 17.19 meV. The powdered samples (15 g $CaCu_3Ru_4O_{12}$, 20 g $PrCu_3Ru_4O_{12}$) were folded in aluminum foil and fixed in a cadmium frame. An empty foil and a vanadium standard have been additionally measured to account for background and detector efficiency, respectively. The raw data have been corrected in a standard way employing the LAMP program package [148] converting TOF to energy transfer and a constant wavevector (Q) or energy-transfer (ω) mapping finally resulting in the dynamic structure factor $S(Q, \omega)$. The large-angle detector bank of the spectrometer covers a range of wave vector transfers of $0.75\,Å^{-1} \leq Q \leq 5.2\,Å^{-1}$ in the elastic channel for the selected wavelength. At the time of the experiment the small-angle detector usually covering Q values below $0.75\,Å^{-1}$ was not available.

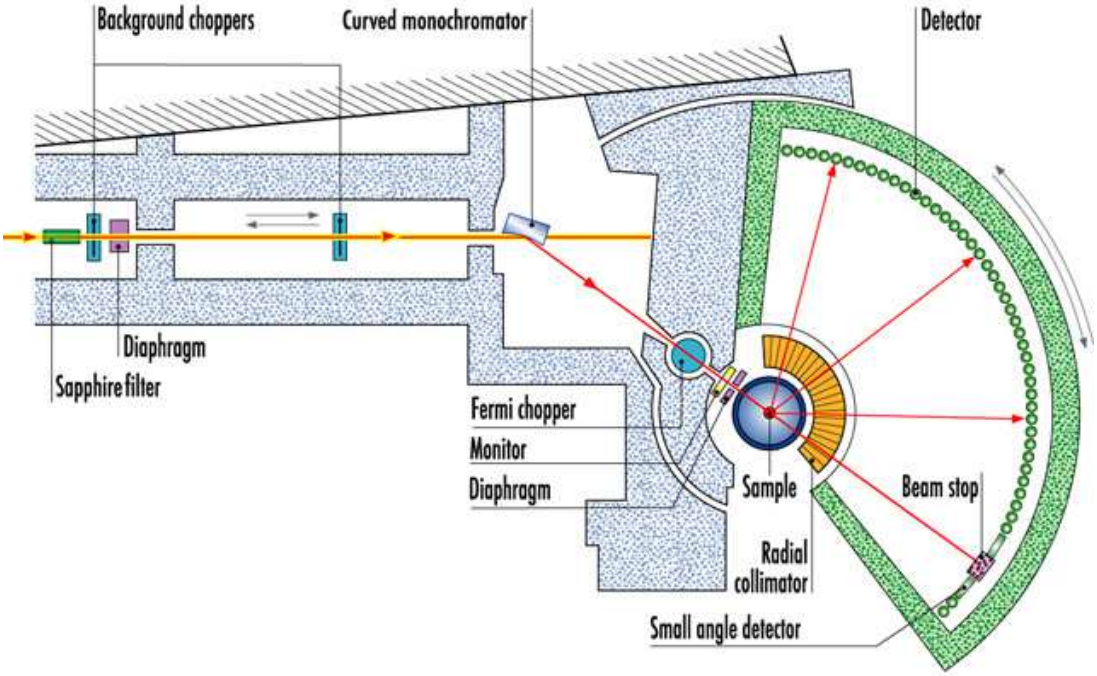

Figure 4.3: Beam line and detector setup of the thermal neutron time-of-flight spectrometer IN4C at the Institut Laue-Langevin (ILL), Grenoble, France. See text for details. Courtesy of ILL.

4.4 Physical Property Measurement System

The physical property measurement system (PPMS) is a commercial (Quantum Design) highly automated multiple purpose device for measuring temperature and magnetic field dependent physical quantities such as resistivity, heat capacity, thermal transport or dielectric response, for example. It consists firstly of a controller unit including field and temperature control as well as the measurement equipment for the various physical quantities and secondly of a cylindrical cryostat with a cylindrical sample chamber of about 26 mm diameter in which different insets (so-called sample pucks as well as custom-made sample rods) can be put, each designed for a specific physical property. The cryostat is nitrogen-jacketed (for lower helium consumption) and filled with liquid helium as cooling agent allowing for temperatures from 400 K down to 2 K. A superconducting coil made of Nb_3Ti embedded in copper within the helium dewar can produce magnetic fields up to 9 T. The sample chamber is not designed as in a classic flow cryostat in which the helium directly passes the sample within the chamber. In fact, the helium passes the lower end of the sample chamber through the so-called cooling annulus, thus cooling the sample chamber from outside.[149]

4.4.1 Heat Capacity

Similar to other techniques (e.g. DSC), the PPMS option for measuring the heat capacity controls the heat added to and removed from the sample while monitoring the resulting change in temperature. During the measurement, the sample is cooled/heated to a certain temperature at which the specific heat is to be measured. A known amount of heat is then applied at constant power for a fixed time depending on sample mass and temperature (between a fraction of a second up to minutes) and then this heating period is followed by a cooling period of the same duration. For this a sample with a mass of 1-200 mg (ideally 10-20 mg) and a maximum size of 3×3 mm is put on a platform which is suspended with four double-wires in a gold-plated brass/copper-beryllium frame. The wires also provide the thermal connection for the platform and the electrical connection to the heater and thermometer which are attached at the lower side of the platform. The sample itself is fixed on the platform with a well-defined amount of grease (Apiezon

N/H) which ensures good thermal coupling between sample and platform. The so-called puck (assembly consisting of frame and electrical contact socket) is then inserted into the sample chamber with a special rod-like tool while flooding it continuously with helium to avoid air/moisture entering the chamber. For the heat capacity measurement it must be guaranteed that the heat flow only occurs between sample and platform. That is why the whole sample chamber has to be evacuated to about 10^{-3} mbar with a cryopump so that the thermal conductance between the sample platform and the thermal bath (puck) is totally dominated by the conductance of the suspension wires. This gives a reproducible heat link to the bath with a corresponding time constant large enough to allow both the platform and sample to achieve sufficient thermal equilibrium during the measurement.

The specific heat option of the PPMS measures the heat capacity at constant pressure $C_p = \frac{\partial Q}{\partial T}\big|_p$. It uses a relaxation technique which determines the heat capacity of a sample by fitting the temperature response of the wire-suspended platform including sample and contact grease as caused by the applied heat pulse. This method is an adiabatic method which describes the temperature response of the sample as a function of time. It assumes that the sample is in good thermal contact with the platform such that both are at the same temperature during the measurement. It is presumed that the temperature T as a function of time t obeys the equation $C_{\mathrm{tot}}{}^{dT}\!/_{dt} = -K_{\mathrm{w}}\left[T - T_{\mathrm{b}}\right] + P(t)$ where C_{tot} is the total heat capacity of the sample and platform, K_{w} is the thermal conductance of the supporting wires, T_{b} is the temperature of the thermal bath, and $P(t)$ is the power applied by the heater. The heater power $P(t)$ is equal to P_0 during the heating portion of the measurement and equal to zero during the cooling portion. The solution of this equation is given by exponential functions with a characteristic time constant $\tau = C_{\mathrm{tot}}/K$. For poor thermal contacts between sample and platform, there is a more sophisticated model using two time constants. It simulates a heat flow between sample and platform and between platform and puck: $C_{\mathrm{platform}}{}^{dT_{\mathrm{p}}}\!/_{dt} = P(t) - K_{\mathrm{w}}\left[T_{\mathrm{p}}(t) - T_{\mathrm{b}}\right] + K_{\mathrm{g}}\left[T_{\mathrm{s}}(t) - T_{\mathrm{p}}(t)\right]$ and $C_{\mathrm{sample}}{}^{dT_{\mathrm{s}}}\!/_{dt} = -K_{\mathrm{g}}\left[T_{\mathrm{s}}(t) - T_{\mathrm{p}}(t)\right]$ where K_{g} is the thermal conductance between sample and platform due to the grease and $T_{\mathrm{p}}(t)$ and $T_{\mathrm{s}}(t)$ the respective temperatures of platform and sample. To separate the specific heat of the sample from the contribution of platform and grease, their (temperature dependent) heat capacity is measured in advance and saved in a so-called addenda table. This allows the subtraction of these parts from the total specific heat to obtain the pure quantity of the sample.[150]

In the present case of the copper-ruthenates, the samples have to be placed carefully onto the platform with a generous amount of contact grease as their fragile and porous nature leads to a reduced thermal coupling. In the case of $SrCu_3Ru_4O_{12}$ the formation of impurity phases has to be avoided which form during sintering according to experience. Instead of sintering, the pressed pellet for the heat capacity measurement is stabilized with cellulose (Sigmacell Type 20) as binder during pressing at room temperature without further firing in an oven. An addenda table has been created in advance for the cellulose, likewise that of the thermal grease Apiezon. The contribution of the binder is then automatically subtracted from the raw data.

4.4.2 DC Resistivity

The DC resistivity option of the PPMS uses a configurable resistance bridge capable of performing four-wire resistance measurements in the range $1\,\Omega < R < 1\,\mathrm{M}\Omega$. Up to three samples may be mounted on a resistivity puck to be measured at one time, each sample interfaced with one separate four-wire channel: two leads for current and two leads for voltage (positive and negative, respectively). The advantage of using four wires is that this greatly reduces the contributions of leads and joints to the resistance measurement. In the standard mode (AC mode) a DC current excitation in the form of a square waveform is passed through a sample via the current leads while the voltage leads measure the potential difference across the sample. The utilization of a waveform eliminates errors from DC offset voltages and, when additionally synchronized to the AC line frequency, it greatly reduces noise from the power line. The voltmeter has a very high impedance so the voltage leads draw very little current, and by using Ohm's law, it is therefore possible to determine the resistance with a high accuracy. Small cuboid rods ($\approx 2 \times 2 \times 13\,\mathrm{mm}^3$) of $A\mathrm{Cu}_3\mathrm{Ru}_4\mathrm{O}_{12}$ (A = Na, Ca, Sr, La, Pr, Nd) were pressed from powder with a special pressing tool and sintered for stability. The rods were contacted with thin copper wires with the aid of silver paint: two leads at the small (end) faces of the cuboid for the injection of the current and two leads in between for the measurement of the voltage drop. For the determination of the resistivity, the distance between the two innermost (voltage) contacts and the cross-section of the rod has to be quantified which is done under a scaled binocular. For the measurement the maximum possible current of 5 mA was applied in order to have the maximum voltage drop and accordingly the lowest noise.[151]

4.4.3 AC Resistivity

The AC transport option of the PPMS supports different types of electrical transport current measurements, namely AC resistivity, Hall coefficient, I-V curve, and critical current by using a precision current source and a precision voltmeter. The source has a current resolution of 2 µA with a maximum current of 2 A and uses a DSP-generated sinusoidal current excitation and a phase sensitive voltage detection with a frequency range of 1 Hz < f < 1 kHz. It therefore provides greater sensitivity (1 nΩ < R < 1 kΩ) than the DC option as frequency-dependent noise, DC offset, and instrumental drift can be eliminated by digital filtering of the signal. This is possible due to the fact that the quantity of interest has a form similar to the driving form with a known frequency.[152] Contacting of the sample works the same way as with the DC method (see subsection 4.4.2). AC resistivity measurements were performed on $LaCu_3Ru_4O_{12}$ and $PrCu_3Ru_4O_{12}$ with an excitation of 50 mA and a frequency of 1 Hz.

4.5 Magnetic Property Measurement System (SQUID)

The magnetic property measurement system (MPMS) is a commercial (Quantum Design) highly automated and sophisticated analytical instrument for studying magnetic properties of small samples in magnetic fields up to 5 T and in a (standard) temperature range of 2 K < T < 400 K. Very similar to the PPMS (see section 4.4) it consists of a controller unit including field and temperature control as well as the measurement equipment and of a cylindrical cryostat with a cylindrical sample chamber in which the sample is inserted fixed to a plastic straw on a special rod. Within the cryostat a superconducting coil provides the magnetic field and a SQUID detection system is responsible for the measurement of the magnetic moment of the sample. Here also, the sample is cooled by the evaporation of liquid helium from outside through the cooling annulus (see section 4.4). The SQUID detection system comprises the sensing loops, a RFI-shielded superconducting isolation transformer, and the SQUID sensor. The sensing loops are designed as highly balanced second-derivative coil set to reject the uniform field produced by the SC magnet to a precision of 0.1 %. The (sample) signal detected by these loops is coupled into the SQUID sensor through the above mentioned transformer which includes a heater winding

enabling to drive the input circuit (both sides) to a normal (dissipative) state in order to eliminate persistent currents induced in the pickup coils when changing the magnetic field. This heater is turned on during all magnet (dis)charging operations as well as at the beginning of a sample measurement sequence. [153] The heart of the SQUID sensor (the actual magnetometer) is a superconducting ring containing so-called Josephson junctions [154] which weaken the superconductivity at the point of contact by some kind of barrier: a physical constriction or a thin insulating/normal-conducting layer. The junctions show the correspondent Josephson effect which is an interference mechanism of macroscopic wave functions by quantum tunneling of cooper pairs. The detailed physics are described elsewhere in literature.[155]

4.6 Continuous-Flow Cryostat

A continuous-flow cryostat (see Fig. 4.4) is a multi-purpose device delivering a low-temperature and high magnetic field environment for samples under investigation. It is a robust cylindrical high-vacuum shielded helium dewar including a superconducting magnet and a likewise cylindrical insert in which the sample itself is put in a top-loading manner. Customized sample holders designed for different kinds of measurements (resistivity, thermal expansion, heat capacity, etc.) can be used. A computer controls the cryostat electronics (helium level meter, temperature controller, magnet power supply) and measurement equipment via interface bus. The magnet consists of a number of coaxial solenoid sections wound using multi-filamentary superconducting wires which give a both physically and thermally stable structure under the large Lorentz forces generated during operation. An additional so-called lambda-stage can be used to increase the maximum possible field of the SC magnet by cooling its surrounding helium to a lower temperature than the normal pressure boiling point of helium ($T < 4.2\,\mathrm{K}$).[156]

DC-resistivity measurements were performed in a commercial continuous-flow cryomagnet system (Teslatron, Oxford Instruments) in a temperature range of $1.6\,\mathrm{K} < T < 290\,\mathrm{K}$ and in magnetic fields up to 14 T with a DC-current source (Keithley 2400) and a sensitive digital voltmeter (Keithley 182). The excitation current was in the range $1\,\mathrm{mA} < I < 100\,\mathrm{mA}$ depending on the sample.

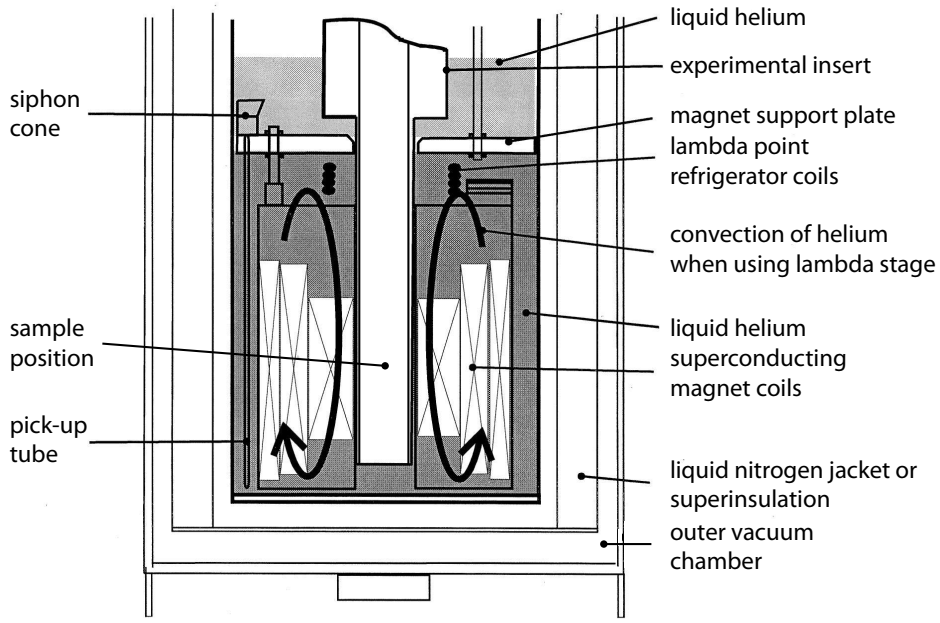

Figure 4.4: Schematic cross-section of the lower part of a continuous flow cryostat including a superconducting magnet (diagram based on Ref. [156]).

DC-magnetization measurements were performed in an identical system (Teslatron, Oxford Instruments) in a temperature range of $1.6\,\mathrm{K} < T < 80\,\mathrm{K}$ and in magnetic fields up to 14 T. The susceptometer equipment comprises a pick-up coil set embedded in a hollow rod-shaped cryostat insert and an above mounted extraction head containing a motor with a reciprocating mechanical assembly. The sample is fixed at the lower end of a fiber glass rod which itself is inserted into the above mentioned insert in a top-loading manner and fixed to the leverage of the extraction head. A motor-drive unit is used to control the extraction head in order to move the sample at selectable speeds up and down through the pick-up coils while simultaneously capturing the coil signal with a fast sensitive digital voltmeter (Keithley 182). The recorded waveform is computer-analyzed and evaluated to derive the magnetic moment by comparison with a calibration sample (usually palladium).[157]

4.7 Dilution Refrigerator

A dilution refrigerator is a cryogenic device of which the cooling effect is based on the heat of mixing of the two helium isotopes He-3 and He-4. It provides continuous cooling from typically 20 K down to the mK range and consists of a vacuum-superinsulation or liquid nitrogen jacketed vessel with the actual cooling stage designed as an insert. The insert itself is immersed in liquid He-4 and separates its internal components by an additional vacuum chamber (see Fig. 4.5).

Starting with a gaseous mixture of He-3 and He-4 (≈ 11.9 vol.% He-3) at room temperature, the cooling agent is pumped from the storage dumps into the cold traps to remove oil vapor (from the pumps), oxygen, nitrogen, and other spurious contaminants. The traps consist of cans filled with activated carbon (or similar material) and are immersed in liquid nitrogen. From the nitrogen cold traps the gas is guided to another cold trap which is part of the cryostat and therefore immersed in liquid He-4. Its purpose is precooling the gas to approximately 4.2 K and removing low-boiling gases such as neon and hydrogen which could freeze and block the capillaries within the cryostat. The liquification of the purified helium gas mixture is carried out by the condenser (or "1K pot") which is immersed in a small He-4 bath. By pumping the He-4 bath of the condenser it can be cooled to roughly 1.2 K which is cold enough to liquefy He-3 and He-4. Several sophisticated impedance/heat-exchanger combinations form the way down to the mixing chamber in which the so-far homogenous liquefied mixture accumulates. Reducing the vapor pressure of the mixture via pumping at the so-called still it can be cooled further down to temperatures where a separation into a light top-floating He-3-rich (concentrated) phase and a dense low-floating He-3-poor (diluted) phase occurs. The amount of mixture has to be chosen correctly such that it fits the dimensions of the mixing chamber, the still and also the conduct from the mixing chamber to the still, so that the phase boundary lies withing the mixing chamber, the liquid surface within the still and the inlet of the conduct within the He-3-poor phase. The temperature of the still is adjusted to approximately 0.6 K since there the vapor pressure of He-3 is roughly 1000 times higher than that of He-4 and therefore effectively pure He-3 is removed from the cryostat an recondensed into the mixing chamber. By pumping away almost pure He-3 vapor from the still, the He-3 concentration in the dilute phase of the mixing chamber decreases and He-3

from the concentrated phase is forced to compensate the loss by diffusion. The effects of this diffusion are of quantum-mechanical nature but can be considered equivalent to an adiabatic expansion of He-3 and therefore providing refrigeration. This circulation of He-3 establishes a dynamic equilibrium within the mixing chamber of which the cooling power can be used to chill samples mounted outside the mixing chamber in high vacuum or alternatively immersed within the dilute phase. For a deeper insight into physics and technical details of a dilution refrigerator see also Refs. [158, 155, 159].

Specific-heat measurements were performed in a custom-made dilution refrigerator using a relaxation method.[160] For $CaCu_3Ru_4O_{12}$ the heat capacity was measured in a temperature range of $65\,\mathrm{mK} < T < 2.5\,\mathrm{K}$ and for $PrCu_3Ru_4O_{12}$ $100\,\mathrm{mK} < T < 20.1\,\mathrm{K}$. Resistivity measurements on selected $CaCu_3Ru_4O_{12}$ single crystals as well as on polycrystalline $PrCu_3Ru_4O_{12}$ were carried out in a temperature range of $50\,\mathrm{mK} < T < 2.5\,\mathrm{K}$ in the same device using a low-dissipation four-wire AC-resistance bridge (Linear Research LR700).

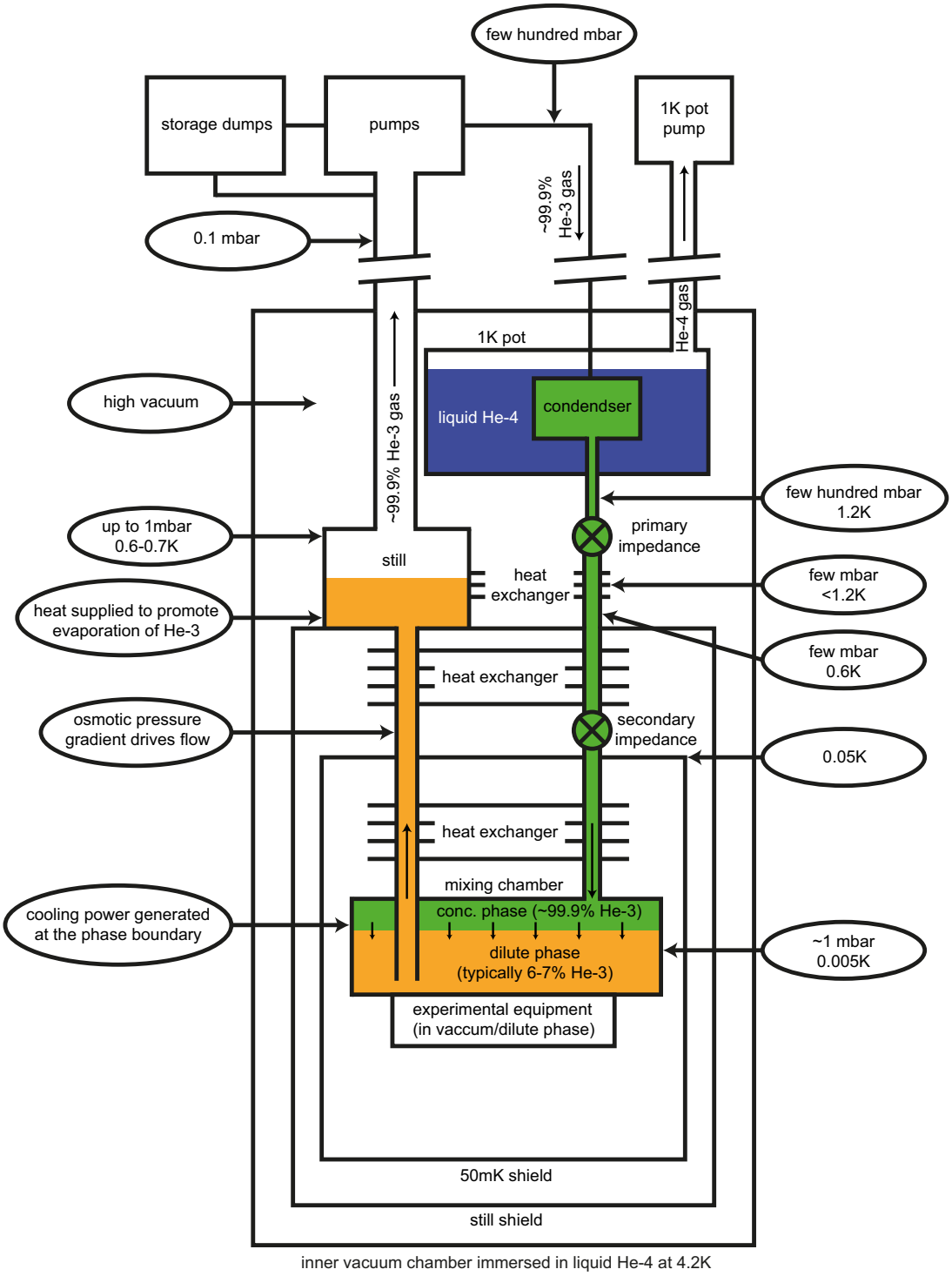

Figure 4.5: Schematic diagram of the internal components of a dilution refrigerator during circulation in the dynamic equilibrium (not including valve system). Liquid phases are drawn as colored areas (diagram based on Ref. [161]).

4.8 Muon Spin Rotation (μSR)

Muons are highly unstable elementary particles and are members of the family of leptons to which also electrons belong. When being implanted into condensed matter by a high-energy beam they can serve as microscopic probe and give valuable information about their atomic, molecular or crystalline surrounding. There exist two types of muons which are the corresponding antiparticles to each other: a negatively charged one (μ^-) and a positively charged one (μ^+). In a solid the negative muon behaves similar to an electron and is captured by a nucleus which forces it to a low lying electron-like orbit. In contrast, the behavior of the positively charged muon is comparable to a proton. Repulsing electrostatic forces from the nuclei in the solid typically compels the incoming μ^+ to interstitial sites at which it also stops and remains there until it decays. This makes it the preferable muon for solid state research. The production of the μ^+ is carried out in a high-energy particle accelerator in which a pion precursor beam is generated by collision of a proton beam (several 100 MeV) with the nuclei of a production target (typically beryllium): $p + p \rightarrow p + n + \pi^+$ and $p + n \rightarrow n + n + \pi^+$. The pions have a very short lifetime ($\tau = 26$ ns) and positive muons (μ^+) are formed via the weak decay $\pi^+ \rightarrow \mu^+ + \nu_\mu$. One type of muon beam is obtained like this: part of the pions are stopped still within the target and due to conservation of momentum and angular momentum the decay mechanism of these resting pions is such that the spin of the produced muon is antiparallel to its flight path which makes the muon beam a polarized one. Muons produced near the surface of the target are able to exit it without being absorbed and are collimated and guided to the sample with the aid of deflection magnets. This beam type is therefore called surface beam, is nearly 100% polarized and ideally monochromatic with a kinetic energy of 4.1 MeV and a muon lifetime of $\tau = 2.2\,\mu$s (much longer than the pions). When hitting the sample under investigation, they fortunately lose their energy very quickly (within 100 ps) without disturbing the μSR experiment. In addition, all the processes involved during the deceleration are of coulombic origin (ionization, electron scattering/capture) and do not interact with the muon spin, so that the muon is thermalized without any significant loss of polarization. The internal magnetic field B_μ of the solid experienced by the muon at the stopping site affects the muon spin which begins to precess around the direction of the field with a frequency ν_μ directly related to the magnitude of the field: $\nu_\mu = \gamma_\mu B_\mu / 2\pi$ (with the gyromagnetic ratio: $\gamma_\mu = e/m_\mu = 850.6$ MHz/T). Now another important property of

the muon comes into play: its decay into a positron ($\mu^+ \rightarrow e^+ + \nu_e + \bar{\nu}_\mu$) is anisotropic, i.e. that the positrons are emitted preferably in the direction of the muon spin. Hence, the intensity I of the emitted positrons exhibits an angular and time dependence as $I(\phi, t) = 1 + A\cos(\phi - 2\pi\nu_\mu t)$ (ϕ is the angle between initial polarization and observation angle; A is the asymmetry factor, which amounts +1/3 when averaging the intensity over all positron energies). The evaluation of the angular distribution of the positrons from the muon decay allows the determination of the muon spin at the time of the decay or even its evolution in time within the solid from which then conclusions about the nature of internal magnetic fields can be drawn.[162, 163]

Muon spin rotation/relaxation experiments were performed on $A\mathrm{Cu_3Ru_4O_{12}}$ (A = Ca, Pr, Nd) at the swiss muon source (SμS) of the Paul Scherrer Institute (PSI), Switzerland. For the measurements the powders were put into an envelope made of thin aluminized Mylar tape and then mounted with similar tape on the forks of the cryostat stick. The surface beam facility Dolly ($E_\mu = 4.1\,\mathrm{MeV}$) was used with a vertical variable temperature cryostat (Variox, Oxford Instruments). Zero field and transverse field measurements were carried out between 2 K and 200 K. The sample was large compared to the beam spot and also the VETO was enabled, so no background signal was to be expected. This was verified by transverse field measurements which were restricted to 5 mT to avoid beam bending and with it a change of the spectral baseline (alpha-parameter). The asymmetry spectra were fitted using the WKM program (TU Braunschweig).

5 Results & Discussion

5.1 Structure

$A\mathrm{Cu_3Ru_4O_{12}}$ (A = Na, Ca, Sr, La, Pr, Nd) crystallizes in the cubic space group $Im\bar{3}$ (T_h^5) (No.204).[41, 164] The structure (see Fig. 5.1) can be considered as a $2 \times 2 \times 2$ supercell of the parent perovskite $AB\mathrm{O_3}$ ($Pm\bar{3}m$, O_h^1, No.221) which is formed by simultaneous A-site ordering (1:3 type) and counter-rotation of the $\mathrm{RuO_6}$ octahedra around the $\langle 111 \rangle$ axes.[165] The occupied Wyckoff positions [166] are $2a$: A at $(0, 0, 0)$, $6b$: Cu at $(1/2, 0, 0)$, $8c$: Ru at $(1/4, 1/4, 1/4)$, and $24g$: O at $(x, y, 0)$. Fig. 5.1 shows the unit cell[1] of $\mathrm{PrCu_3Ru_4O_{12}}$ at room temperature derived from NPD including plots of the thermal ellipsoids (99.9% probability level). The octahedra depict the tilted $\mathrm{RuO_6}$ units. On the right cell face, the $\mathrm{CuO_4}$ plaquettes are indicated by yellow/green planes. In the other investigated compounds the Pr-site is occupied by Na, Ca, Sr, La, or Nd, respectively. Other candidates for the occupation of the A-site with comparable ionic radii [48, 169] would be $\mathrm{Cd^{2+}}$ (95 pm) [41], $\mathrm{Ce^{3+}}$ (101 pm), and $\mathrm{Sm^{3+}}$ (96 pm). However, these ions turn out to be already too small to form a stable structure, at least under ambient pressure reaction conditions. Especially $\mathrm{Ce^{3+}}$, which would have a radius between that of Na and Ca is oxidized to $\mathrm{Ce^{4+}}$ (87 pm) during preparation. Therefore, the lower limit for the A-site ionic radius must be close to that of $\mathrm{Nd^{3+}}$ (98 pm).

5.1.1 X-Ray Diffraction

Powder XRD at room temperature reveals high purity material for $A\mathrm{Cu_3Ru_4O_{12}}$ (A = Na, Ca, Sr, La, Pr, Nd) with minor indications of impurities in the case of $\mathrm{NaCu_3Ru_4O_{12}}$

1 Another possible description of the structure of $A\mathrm{Cu_3Ru_4O_{12}}$ (A = Na, Ca, Sr, La, Pr, Nd) is one in terms of a filled skutterudite $\mathrm{RT_4X_{12}}$ which crystallizes in the same space group.[167, 168, 75]

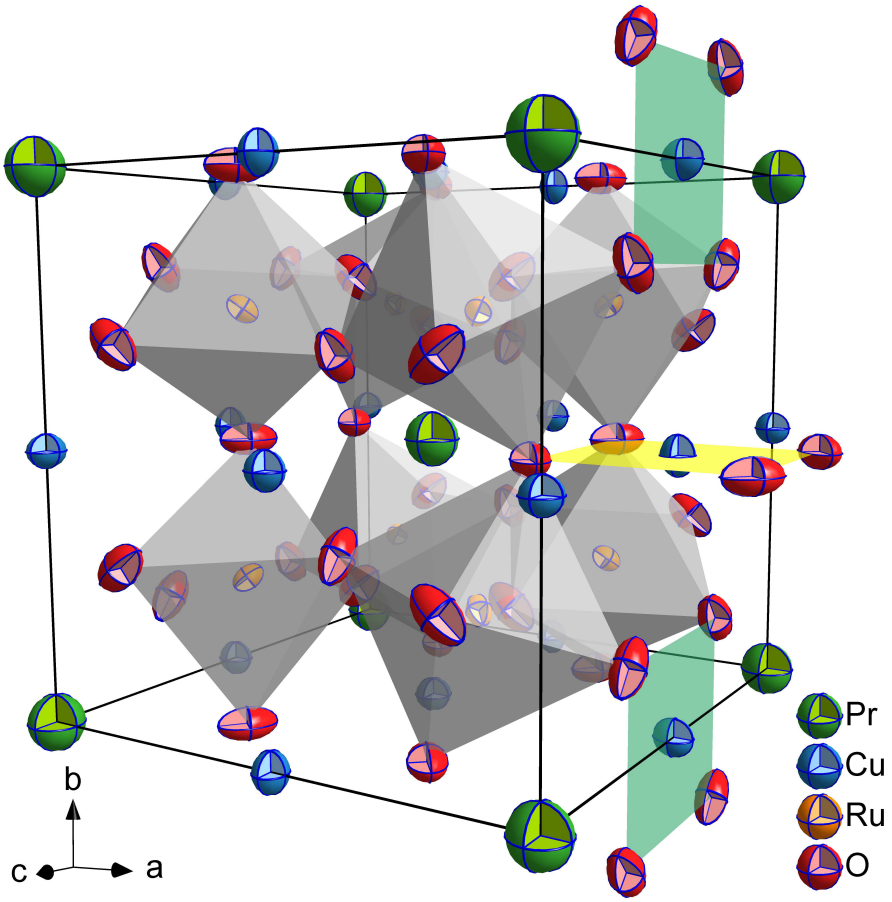

Figure 5.1: Unit cell of $PrCu_3Ru_4O_{12}$ at room temperature derived from NPD including plots of the thermal ellipsoids (99.9% probability level). The octahedra depict the tilted RuO_6 units. On the right cell face, the CuO_4 plaquettes are indicated by yellow/green planes. In the other investigated compounds the Pr-site is occupied by Na, Ca, Sr, La, or Nd.

A	a (Å)	x	y	R_{Bragg} (%)	R_{p} (%)	R_{wp} (%)	R_{exp} (%)	χ^2 (%)
Na	7.37109(4)	0.17935(82)	0.30987(75)	9.58	20.20	23.00	10.69	4.64
Ca	7.40812(4)	0.17674(85)	0.30509(92)	6.53	22.20	24.30	13.60	3.19
Sr	7.45342(5)	0.19199(136)	0.30288(136)	9.91	24.90	22.30	13.32	2.81
La	7.48340(4)	0.17177(110)	0.30228(91)	9.37	29.60	22.60	15.29	2.19
Pr	7.45203(6)	0.17264(114)	0.30310(88)	4.63	29.10	23.90	18.68	1.63
Nd	7.46001(6)	0.17829(169)	0.30821(177)	4.74	35.20	26.60	19.30	1.90

Table 5.1: Lattice constant a, oxygen positional parameters (x, y), and reliability factors (R_{Bragg}, R_{p}, R_{wp}, R_{exp}, χ^2) of $A\text{Cu}_3\text{Ru}_4\text{O}_{12}$ (A = Na, Ca, Sr, La, Pr, Nd) as resulting from the XRD-Rietveld refinements at room temperature.

(0.8% CuO) and $\text{SrCu}_3\text{Ru}_4\text{O}_{12}$ (0.35% SrRuO_3, 0.95% CuO). During preparation of $\text{SrCu}_3\text{Ru}_4\text{O}_{12}$ parts of the reactants inevitably form the thermodynamically favored phase SrRuO_3.[170] Figs. 5.2, 5.3, and 5.4 show the corresponding XRD diffraction patterns with excellent agreement between observed and calculated intensities. In Table 5.1 the lattice constant a, oxygen positional parameters (x, y), and reliability factors (R_{Bragg}, R_{p}, R_{wp}, R_{exp}, χ^2) of $A\text{Cu}_3\text{Ru}_4\text{O}_{12}$ (A = Na, Ca, Sr, La, Pr, Nd) are listed as derived from the XRD-Rietveld refinements at room temperature. Generally, the values for the lattice constants and the oxygen positional parameters correspond reasonably well with results given in literature.[41, 42, 48] Surprisingly, the lattice constant of the Nd compound is slightly higher than that of $\text{PrCu}_3\text{Ru}_4\text{O}_{12}$, but should be lower due the the lanthanide contraction. A reasonable explanation for this could be problems with the diffractometer (misalignment) as neutron data (see chapter 5.1.2) shows the opposite result. The variation of the oxygen positional parameters (x, y) with the A-site ion is in the range of a few % apart from a higher x value of $\text{SrCu}_3\text{Ru}_4\text{O}_{12}$ which is most probably an artifact (compare with results of Ref. [48]). This means that the Ru-O-Ru and the Cu-O-Ru bond angles remain almost the same in all compounds.

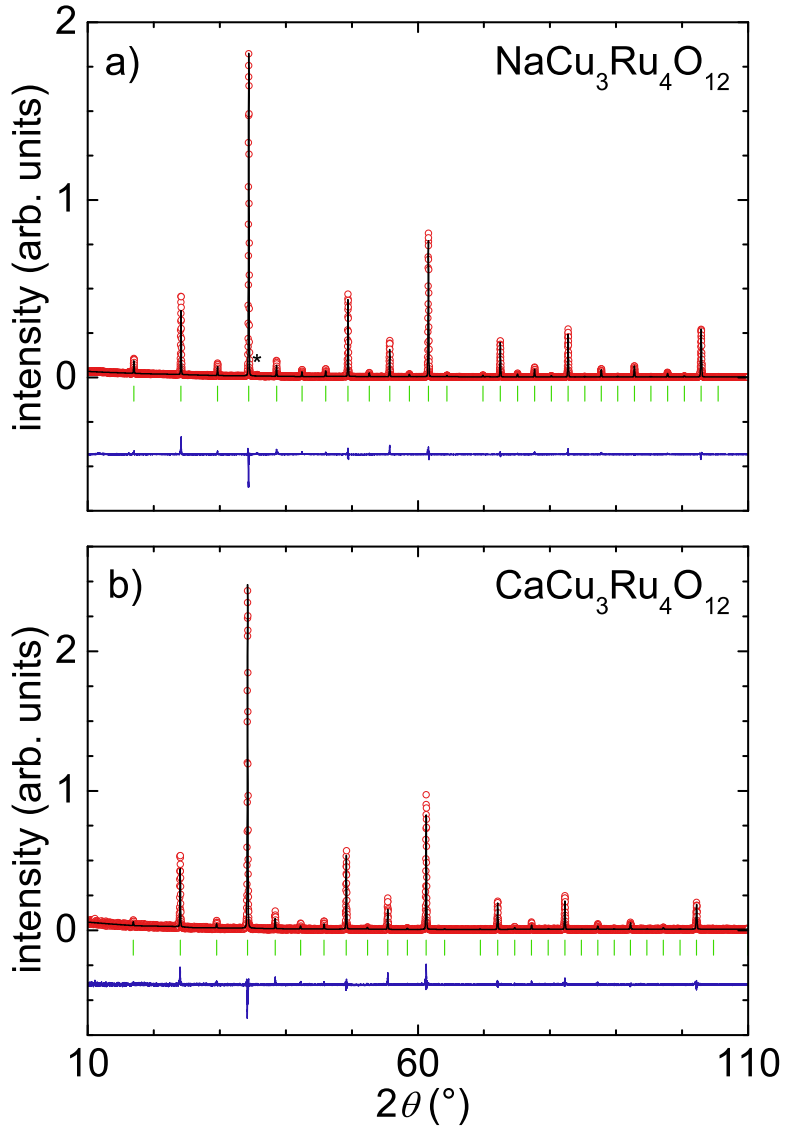

Figure 5.2: Room temperature powder x-ray diffraction pattern of $NaCu_3Ru_4O_{12}$ (frame a) and $CaCu_3Ru_4O_{12}$ (frame b). Measured and calculated intensities (empty red circles and black line), as well as their difference pattern (blue line at the bottom, shifted to negative values for clear depiction) and corresponding Bragg-peak positions (green vertical bars) are shown. The asterisk marks the main peak of a CuO impurity phase in $NaCu_3Ru_4O_{12}$.

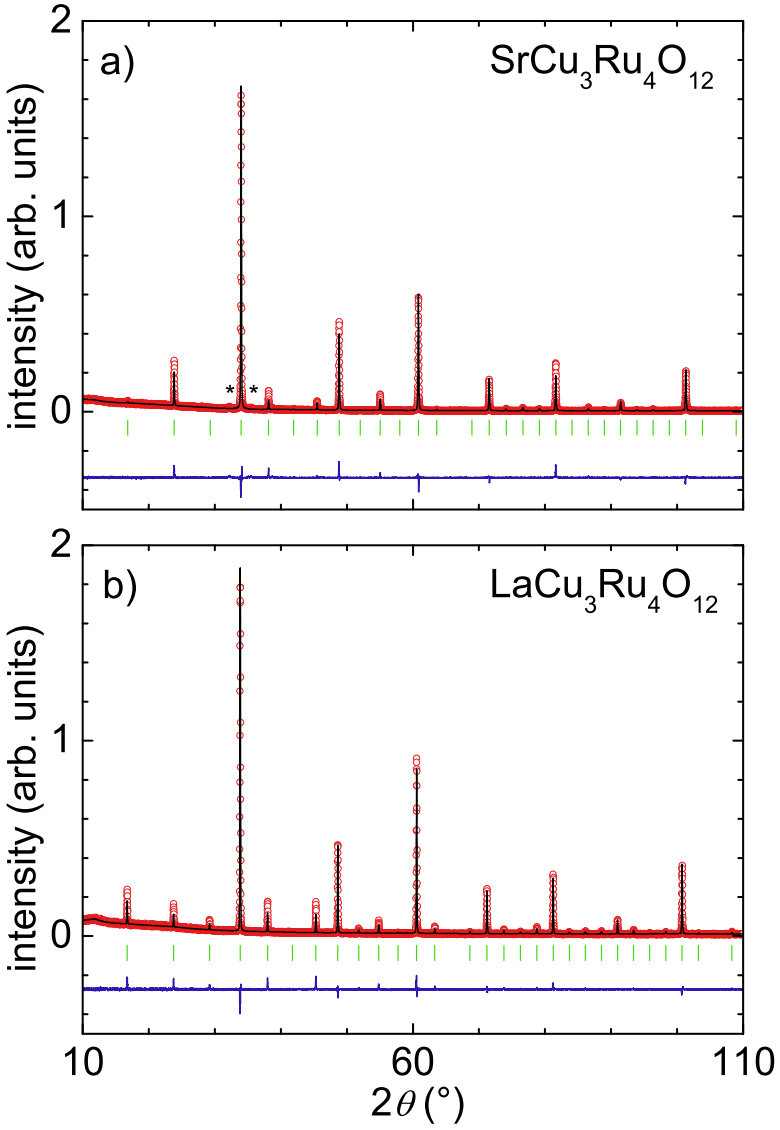

Figure 5.3: Room temperature powder x-ray diffraction pattern of $SrCu_3Ru_4O_{12}$ (frame a) and $LaCu_3Ru_4O_{12}$ (frame b). Measured and calculated intensities (empty red circles and black line), as well as their difference pattern (blue line at the bottom, shifted to negative values for clear depiction) and corresponding Bragg-peak positions (green vertical bars) are shown. The asterisks mark the main peaks of a $SrRuO_3$ (left asterisk) and a CuO (right asterisk) impurity phase in $SrCu_3Ru_4O_{12}$.

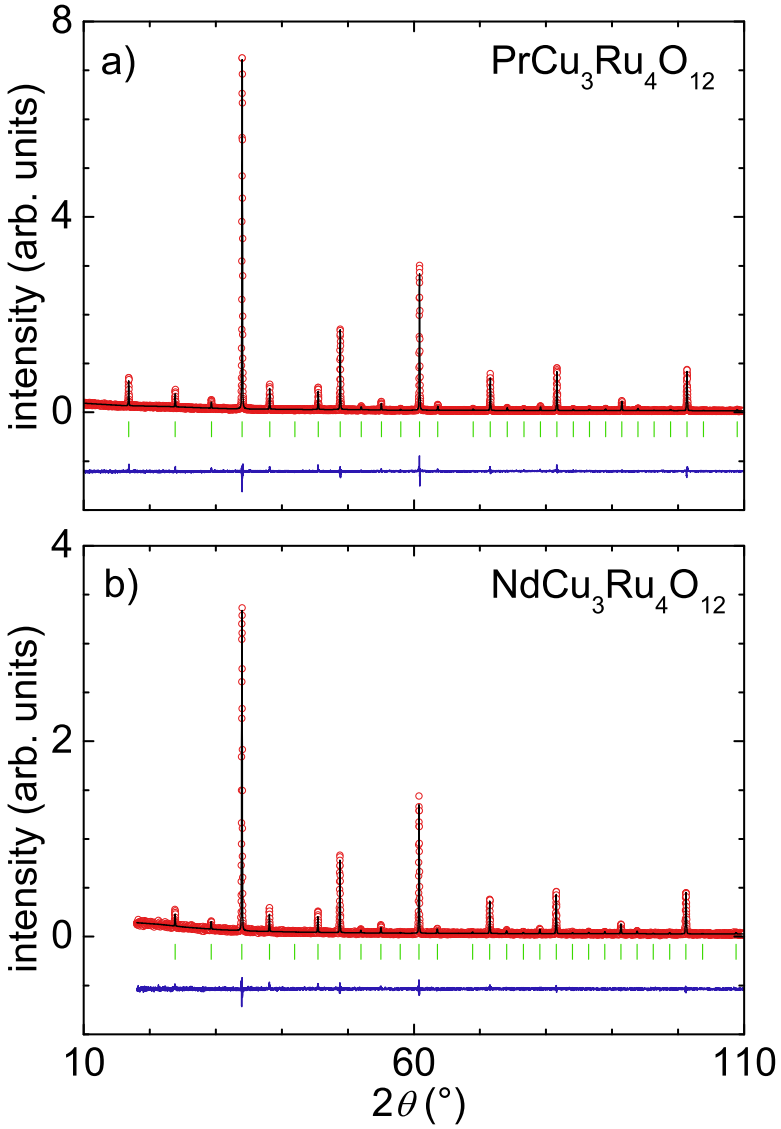

Figure 5.4: Room temperature powder x-ray diffraction pattern of $PrCu_3Ru_4O_{12}$ (frame a) and $NdCu_3Ru_4O_{12}$ (frame b). Measured and calculated intensities (empty red circles and black line), as well as their difference pattern (blue line at the bottom, shifted to negative values for clear depiction) and corresponding Bragg-peak positions (green vertical bars) are shown.

5.1.2 Neutron Diffraction

NPD measurements were performed in the temperature range $1.6\,\mathrm{K} \leq T \leq 292\,\mathrm{K}$. Figs. 5.5, 5.6, and 5.7 exemplarily show the NPD patterns of $A\mathrm{Cu_3Ru_4O_{12}}$ (A = Na, Ca, La, Pr, Nd) at 175 K. They (and all other patterns) were analyzed by Rietveld refinement [132] and demonstrate good agreement between observed and calculated intensities. Note that in the case of $\mathrm{NaCu_3Ru_4O_{12}}$ only few material was available leading to poor statistics which includes a broad background covering nearly the full 2θ range. The refined lattice constants a, oxygen positional parameters (x, y), and reliability factors (R_{Bragg}, R_{p}, R_{wp}, R_{exp}, χ^2) for the patterns at 175 K are listed in Table 5.2. The structural data corresponds well with data reported in literature.[171, 42, 48]

Temperature dependent measurements do not reveal any magnetic Bragg peaks implying the absence of long-range magnetic order down to 1.6 K. For the Na, La, Pr, and Nd compound also no structural phase transitions can be detected (see Figs. 5.8 and 5.9) corroborated by the fractional positions of oxygen (corresponding to a Ru-O-Ru bond angle of $\approx 140^\circ$) which does not show any notable temperature dependence (see insets of Figs. 5.8 and 5.9). However, in the case of $\mathrm{CaCu_3Ru_4O_{12}}$ at $\approx 154\,\mathrm{K}$ a small but sharp drop in the lattice constant of about 0.012% occurs during cooling.[62] Cycling the temperature reveals full reversibility without evidence for hysteresis (see Fig. 5.8b). When analyzing the patterns it turns out that there is no change in the symmetry especially also no significant T-dependence of the fractional positions of oxygen (see inset of Fig. 5.8b). Such a behavior can be explained by valence fluctuations but which seem to have only a small influence on the electronic structure. This is confirmed by the calculation of the variations of the d-electron occupancies which amount roughly 10^{-3}, thus, being two orders of magnitude smaller than in f-electron based intermediate-valence systems.[62]

The temperature dependent lattice constant (see Figs. 5.8 and 5.9) can be described with an anharmonic behavior according to the Einstein model (see chapter 3.1). A good description of the thermal expansion is achieved for $\mathrm{PrCu_3Ru_4O_{12}}$ for which data between 2 K and room temperature is available, resulting in an Einstein temperature $\theta_{\mathrm{E}} = 389\,\mathrm{K}$. Due to the lack of high temperature data for the other investigated compounds, θ_{E} is fixed to a value comparable to that of $\mathrm{PrCu_3Ru_4O_{12}}$. This is a convenient assumption because the materials are isostructural and have comparable masses. For $\mathrm{NaCu_3Ru_4O_{12}}$,

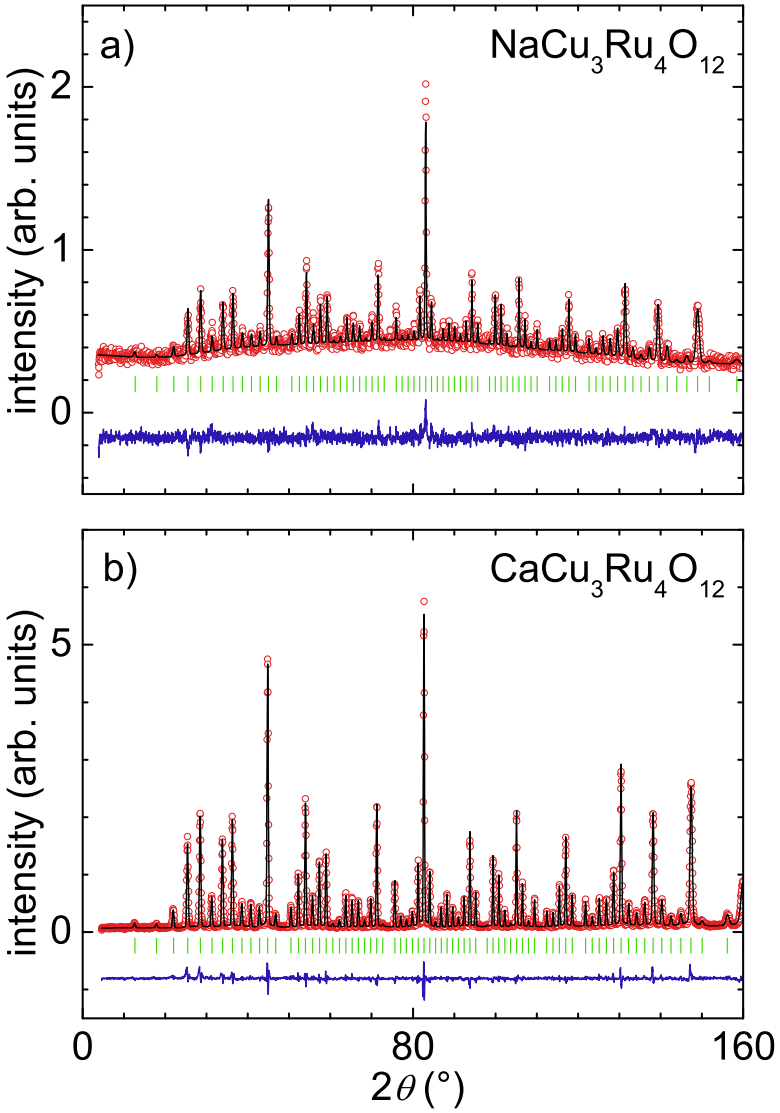

Figure 5.5: Neutron powder diffraction pattern of $NaCu_3Ru_4O_{12}$ (frame a) and $CaCu_3Ru_4O_{12}$ (frame b) at 175 K. Measured and calculated intensities (empty red circles and black line), as well as their difference pattern (blue line at the bottom, shifted to negative values for clear depiction) and corresponding Bragg-peak positions (green vertical bars) are shown.

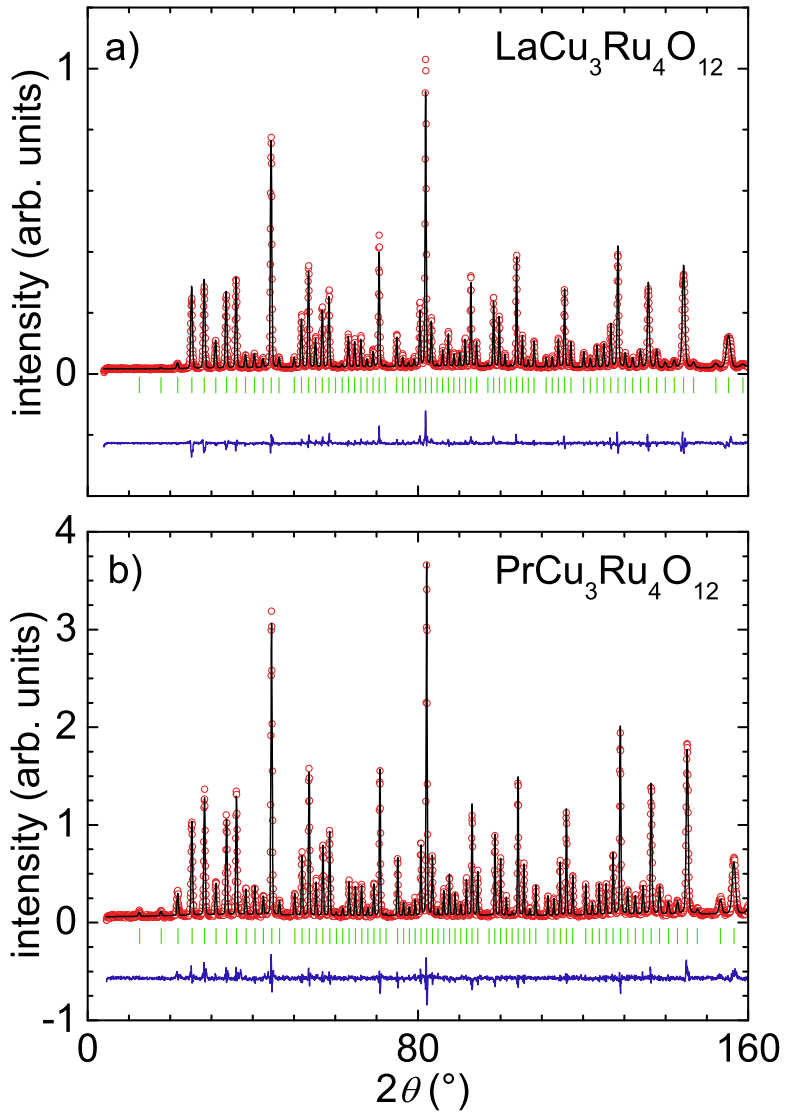

Figure 5.6: Neutron powder diffraction pattern of $LaCu_3Ru_4O_{12}$ (frame a) and $PrCu_3Ru_4O_{12}$ (frame b) at 175 K. Measured and calculated intensities (empty red circles and black line), as well as their difference pattern (blue line at the bottom, shifted to negative values for clear depiction) and corresponding Bragg-peak positions (green vertical bars) are shown.

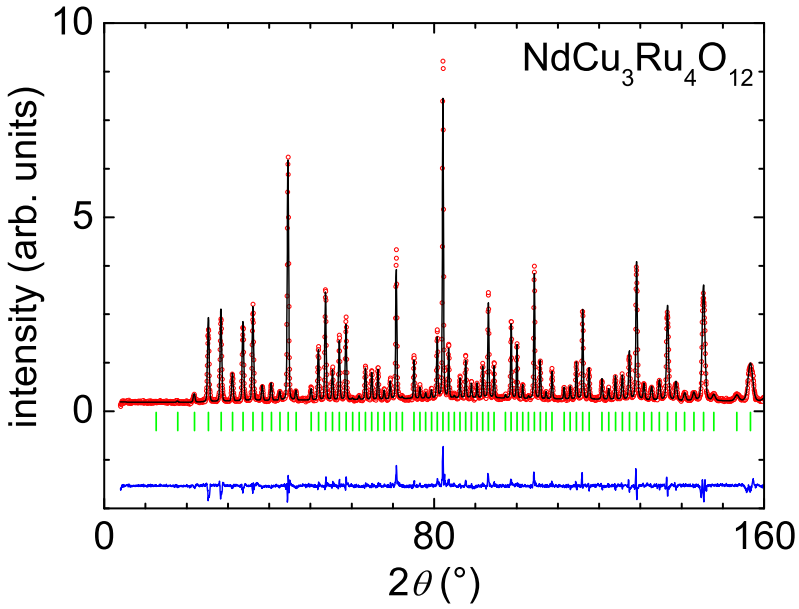

Figure 5.7: Neutron powder diffraction pattern of $NdCu_3Ru_4O_{12}$ at 175 K. Measured and calculated intensities (empty red circles and black line), as well as their difference pattern (blue line at the bottom, shifted to negative values for clear depiction) and corresponding Bragg-peak positions (green vertical bars) are shown.

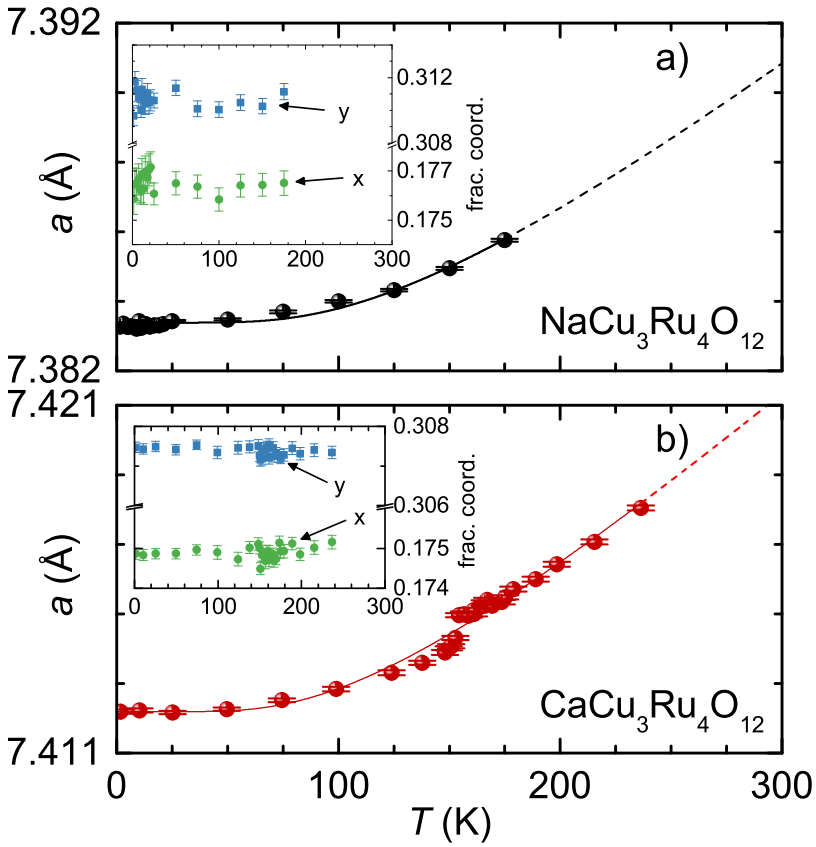

Figure 5.8: Temperature dependent lattice parameter a of $NaCu_3Ru_4O_{12}$ (frame a) and $CaCu_3Ru_4O_{12}$ (frame b) as resulting from the Rietveld refinement of the NPD measurements (error bars smaller than the symbol size). The solid lines (dashed where no data is available/data is not included in fitting) are fits to the thermal expansion. The insets show the refined oxygen positions expressed in fractional coordinates (x and y). See text for details.

$LaCu_3Ru_4O_{12}$, and $NdCu_3Ru_4O_{12}$, θ_E is fixed to 390 K whereas in the special case of $CaCu_3Ru_4O_{12}$ with its structural anomaly, θ_E is fixed to 340 K. For all these compounds, data and fit correlate reasonably well and the corresponding parameters are listed in Table 5.4.

The anisotropic displacement factors U^{ij}_{cif} have been refined for $ACu_3Ru_4O_{12}$ (A = Na, Ca, La, Pr, Nd) at T = 175 K and are listed in Table 5.3. In general, it has to be admitted that the refinement of these parameters within powder measurements is not an ideal method, it may be even unreliable. However, for $PrCu_3Ru_4O_{12}$ at room temperature it shows reasonable results (see Fig. 5.1). Here, the oxygen atoms feature a preferred

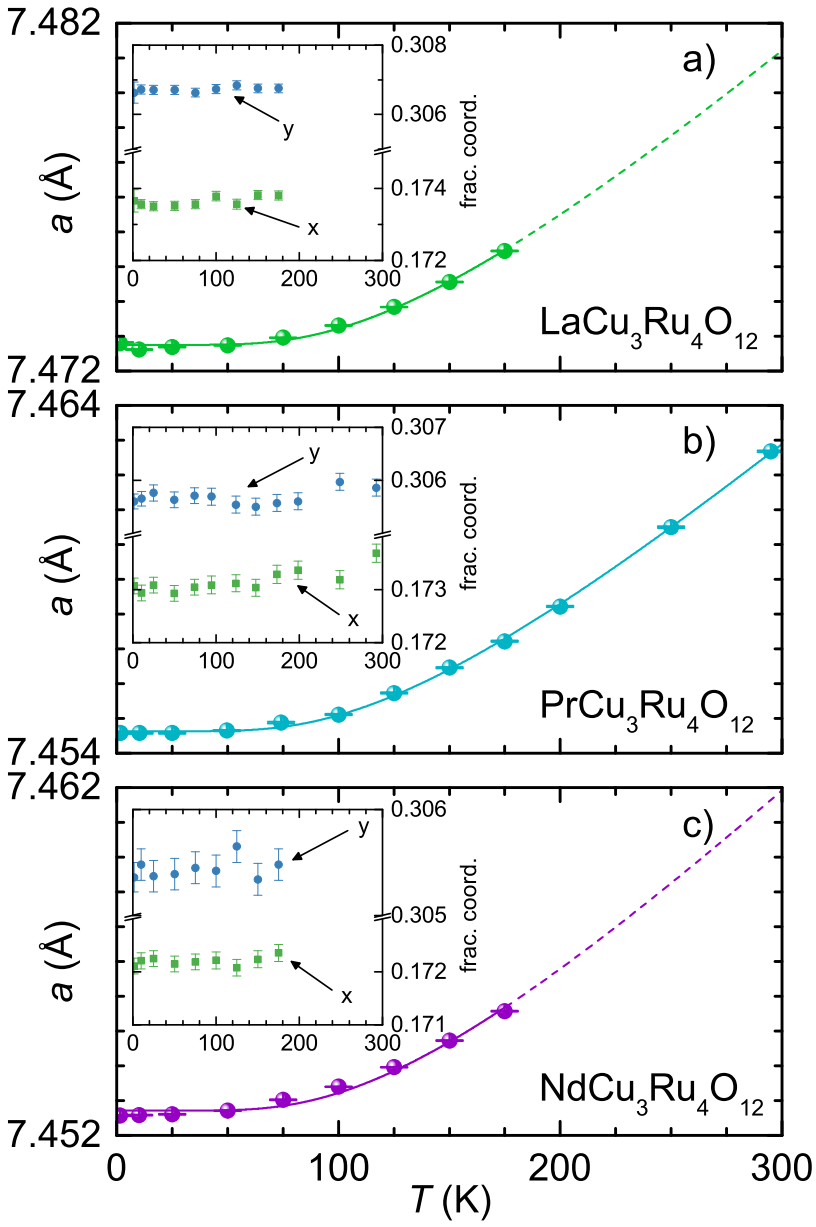

Figure 5.9: Temperature dependent lattice parameter a of $LaCu_3Ru_4O_{12}$ (frame a), $PrCu_3Ru_4O_{12}$ (frame b), and $NdCu_3Ru_4O_{12}$ (frame c) as resulting from the Rietveld refinement of the NPD measurements (error bars smaller than the symbol size). The solid lines (dashed where no data is available) are fits to the thermal expansion. The insets show the refined oxygen positions expressed in fractional coordinates (x and y). See text for details.

vibrational direction within the faces of the unit cell demonstrating the rotation of the RuO_6-octahedra around the ⟨111⟩ axes. Ru mainly vibrates along the cell diagonal ⟨111⟩ (out of the octahedral faces) and Cu along the main cell axes ⟨100⟩ (along the surface normal to the CuO_4 plaquettes) although it is almost isotropic. On the contrary, Pr (i.e. the *A*-site in general) is confined to an isotropic displacement due to local symmetry restrictions.[172, 164] Both in $LaCu_3Ru_4O_{12}$ and $NdCu_3Ru_4O_{12}$ the situation seems a little bit different: The vibration of the octahedra is still around ⟨111⟩ but with a significantly smaller amplitude. Ru features an almost isotropic oscillation within the octahedra while the movement of Cu is clearly out of the plaquette plane (see Figs. 7.2 and 7.2 in chapter 7). The behavior of oxygen and ruthenium in $CaCu_3Ru_4O_{12}$ is pretty much the same as in $PrCu_3Ru_4O_{12}$ whereas Cu has a strong anisotropic displacement: it is flattened to a very thin lense-like shape demonstrating a strong vibration out of and, paradoxically, in one direction within the CuO_4 plaquettes (see Fig. 7.1 in chapter 7). The anisotropic displacement factors derived from XRD single crystal data of $NdCu_3Ru_4O_{12}$ at room temperature by Muller *et al.* [42] have been converted from the β^{ij} to the U^{ij}_{cif} nomenclature for comparison according to Refs. [173, 174] and are also listed in Table 5.3. In contrast to the NPD data,[2] the octahedra exhibit a more pronounced vibration around the ⟨111⟩ axis whereas copper displays an almost isotropic behavior.

The temperature dependence of the anisotropic displacement factors of $ACu_3Ru_4O_{12}$ (*A* = Na, Ca, La, Pr, Nd) is shown in Figs. 7.5, 7.6, and 7.7. In general, the behavior is relatively smooth with an increasing displacement toward high temperatures as expected. Minor spikes occur in $PrCu_3Ru_4O_{12}$ and $CaCu_3Ru_4O_{12}$ but are probably of statistical origin. Especially in $CaCu_3Ru_4O_{12}$ also no anomaly in the displacement occurs when crossing the lattice constant anomaly at 154 K. The quite noisy data of $NaCu_3Ru_4O_{12}$ is owed to bad statistics of the diffraction patterns as a consequence of the low amount of material available in the experiment.

2 Note that NPD data was recorded at 175 K and x-ray data at room temperature.

A	a (Å)	x	y	R_{Bragg} (%)	R_{p} (%)	R_{wp} (%)	R_{exp} (%)	χ^2 (%)
Na	7.38576(4)	0.17651(50)	0.31115(50)	12.10	51.00	32.80	28.27	1.35
Ca	7.41831(8)	0.17512(19)	0.30745(17)	13.60	15.60	8.40	3.44	4.28
La	7.47545(1)	0.17381(13)	0.30675(13)	10.90	11.90	6.68	4.23	3.16
Pr	7.45736(1)	0.17329(17)	0.30557(16)	4.59	13.20	14.60	10.40	1.98
Nd	7.45557(1)	0.17236(16)	0.30548(15)	5.38	13.30	13.80	7.44	3.42

Table 5.2: Lattice constant a, oxygen positional parameters (x, y), and reliability factors (R_{Bragg}, R_{p}, R_{wp}, R_{exp}, χ^2) of $A\mathrm{Cu_3Ru_4O_{12}}$ (A = Na, Ca, La, Pr, Nd) as resulting from the NPD-Rietveld refinements at 175 K.

	Atom	*site*	*symmetry*	U^{11} (10^{-4}Å^2)	U^{22} (10^{-4}Å^2)	U^{33} (10^{-4}Å^2)	U^{12} (10^{-4}Å^2)	U^{13} (10^{-4}Å^2)	U^{23} (10^{-4}Å^2)
own work	Na	2a	$m\bar{3}.$	0(30)	U^{11}	U^{11}	0	0	0
	Cu	6b	*mmm.*.	60(30)	60(30)	-10(20)	0	0	0
	Ru	8c	$.\bar{3}.$	19(6)	U^{11}	U^{11}	-6(9)	U^{12}	U^{12}
	O	24g	*m*..	-5(13)	45(15)	59(13)	-5(10)	0	0
	Ca	2a	$m\bar{3}.$	78(11)	U^{11}	U^{11}	0	0	0
	Cu	6b	*mmm.*.	-9(7)	39(7)	50(8)	0	0	0
	Ru	8c	$.\bar{3}.$	13.5(1.7)	U^{11}	U^{11}	6(3)	U^{12}	U^{12}
	O	24g	*m*..	64(6)	55(5)	16(4)	28(4)	0	0
	La	2a	$m\bar{3}.$	26(4)	U^{11}	U^{11}	0	0	0
	Cu	6b	*mmm.*.	29(6)	59(6)	16(6)	0	0	0
	Ru	8c	$.\bar{3}.$	23.6(1.6)	U^{11}	U^{11}	-2(3)	U^{12}	U^{12}
	O	24g	*m*..	37(3)	42(4)	45(4)	6(3)	0	0
	Pr	2a	$m\bar{3}.$	58(10)	U^{11}	U^{11}	0	0	0
	Cu	6b	*mmm.*.	20(8)	25(7)	19(8)	0	0	0
	Ru	8c	$.\bar{3}.$	13.2(1.8)	U^{11}	U^{11}	1(2)	U^{12}	U^{12}
	O	24g	*m*..	54(5)	47(4)	20(4)	22(4)	0	0
	Nd	2a	$m\bar{3}.$	14(5)	U^{11}	U^{11}	0	0	0
	Cu	6b	*mmm.*.	16(7)	39(7)	4(7)	0	0	0
	Ru	8c	$.\bar{3}.$	13(2)	U^{11}	U^{11}	-2(3)	U^{12}	U^{12}
	O	24g	*m*..	24(4)	28(4)	30(5)	3(4)	0	0
Muller *et al.*	Nd	2a	$m\bar{3}.$	73.2	U^{11}	U^{11}	0	0	0
	Cu	6b	*mmm.*.	53.5	67.6	53.5	0	0	0
	Ru	8c	$.\bar{3}.$	59.1	U^{11}	U^{11}	-1.1	U^{12}	U^{12}
	O	24g	*m*..	112.6	107.0	73.2	25.3	0	0

Table 5.3: Anisotropic displacement factors U_{cif}^{ij} of $A\mathrm{Cu_3Ru_4O_{12}}$ (A = Na, Ca, La, Pr, Nd) according to the conventions given by Grosse-Kunstleve *et al.* [174] Values were derived from the refinement of the NPD patterns at 175 K for each constituent atom with corresponding crystallographic site and local symmetry (own work).[172, 164] XRD single crystal data of $\mathrm{NdCu_3Ru_4O_{12}}$ at room temperature [42] are listed for comparison.

A	a_0 (Å)	α (10^{-6} K^{-1})	θ_E (K)
Na	7.38339(3)	6.923(256)	390
Ca	7.41219(8)	7.647(205)	340
La	7.47275(3)	7.744(205)	390
Pr	7.45463(3)	7.558(51)	389
Nd	7.45271(6)	8.462(385)	390

Table 5.4: Zero-temperature lattice constant a_0, high-temperature thermal expansion coefficient α, and Einstein temperature θ_E of ACu$_3$Ru$_4$O$_{12}$ (A = Na, Ca, La, Pr, Nd) as resulting from the fit to the temperature dependent lattice constant according to the Einstein model (see chapter 3.1, Figs. 5.8 and 5.9, and text for details).

5.2 Magnetism

Fig. 5.10 shows the magnetic susceptibility (upper frame, logarithmic plot) and its inverse (lower frame, linear plot) of ACu$_3$Ru$_4$O$_{12}$ (A = Na, Ca, Sr, La, Pr, Nd) in an external field of 1 T. In terms of a coarse classification the compounds can be categorized in two groups: the first one with the non-magnetic A-site ions (A = Na, Ca, Sr, La) featuring a weak temperature-dependence of the susceptibility and the second one with the magnetic rare-earth ions at the A-site (A = Pr, Nd) of which the susceptibility is strongly temperature dependent as it is dominated by the rare-earth ion and its behavior due to crystal-field effects. All compounds exhibit an enhanced Pauli-paramagnetism roughly two orders of magnitude larger than that of free electrons [30] and a Curie-Weiss dependence of the susceptibility at high temperatures but with substantial differences regarding their low-temperature behavior. Fits to the high-temperature inverse susceptibility according to a Curie-Weiss law (two CW laws for LaCu$_3$Ru$_4$O$_{12}$) are represented by dark grey lines (dark grey curve) in the lower frame of Fig. 5.10. The corresponding results are listed in Table 5.5. One has to admit that for CaCu$_3$Ru$_4$O$_{12}$ and even more for NaCu$_3$Ru$_4$O$_{12}$ more reliable fits could be achieved when using susceptibility data above 400 K as in both compounds a very broad maximum below superimposes the CW behavior. An estimate of the impurity content is made by fitting the low temperature Curie tail for ACu$_3$Ru$_4$O$_{12}$ (A = Na, Ca, Sr, La) with a Curie-Weiss law (see following paragraphs). For ACu$_3$Ru$_4$O$_{12}$ (A = Pr, Nd) this cannot be done due to strong magnetic effects of the rare-earth ions. When leaving aside these impurities including ferromagnetic SrRuO$_3$, then

for the Na, Ca, and Sr compound, an additional temperature independent component of the susceptibility is evident from Figs. 7.9, 7.10, and 7.11. This contribution shows up as constant shift to lower susceptibilities with increasing field. Evidently, it is present up to 400 K which implies a ferromagnetic character with an ordering temperature above. A possible explanation are iron impurities incorporated during preparation, either coming from steel pressing tools or from the starting material (especially from RuO_2). However, then it is a little bit mysterious why the other compounds (La, Pr, and Nd) - which are prepared in the same way - do not show such a behavior (see Figs. 7.12, 7.13, and 7.14).

$NaCu_3Ru_4O_{12}$ exhibits a nearly temperature-independent susceptibility for 100 K < T < 400 K with a defect contribution of 0.253 μ_B/f.u. (≈ one free spin (s = 1/2) per 7 f.u.) derived from a fit to the Curie tail below 10 K (not shown). For T > 350 K the inverse data can be described with a Curie-Weiss law but resulting in an extremely high absolute value of the AFM CW temperature (θ_{CW} = −6728 K) and also with an unexplainable high effective moment of 12.86 μ_B/f.u. A possible explanation for this could be a behavior similar to that of $CaCu_3Ru_4O_{12}$ (following paragraph), namely a very broad peak in the susceptibility attributed to a Kondo resonance.[30] Compared to the Ca compound, the peak is smaller and its maximum temperature is higher (at around 300 K), but still prevents an evaluation of the data in terms of a CW law, at least below 400 K. Approximately between 30 K and 50 K the susceptibility changes its curvature twice, explicitly visible by means of the inverse data. This is consistent with data published in ref. [58], however the reason for this remains unclear.

In $CaCu_3Ru_4O_{12}$ again a weak temperature dependence of an enhanced Pauli-susceptibility is observed but with a broad maximum around 180 K which is also consistent with the temperature-dependent Cu-63 NMR Knight shift, similarly revealing a broad maximum at that temperature.[62] This behavior is analog to that of $CeSn_3$ [176] where the maximum of the susceptibility was identified with the Kondo temperature.[30] Generally, a high Kondo temperature indicates a strong hybridization that enables charge fluctuations putting these systems into the class of mixed-valent compounds of which $CeSn_3$ is considered as a prototypical representative. Below room temperature, the susceptibility of mixed-valent compounds can vary considerably depending on the characteristic spin-fluctuation temperature T_{SF}. For example, $CeSn_3$ reveals a high-temperature Curie-Weiss law above 200 K, followed by a broad maximum around 150 K, and turns into an enhanced

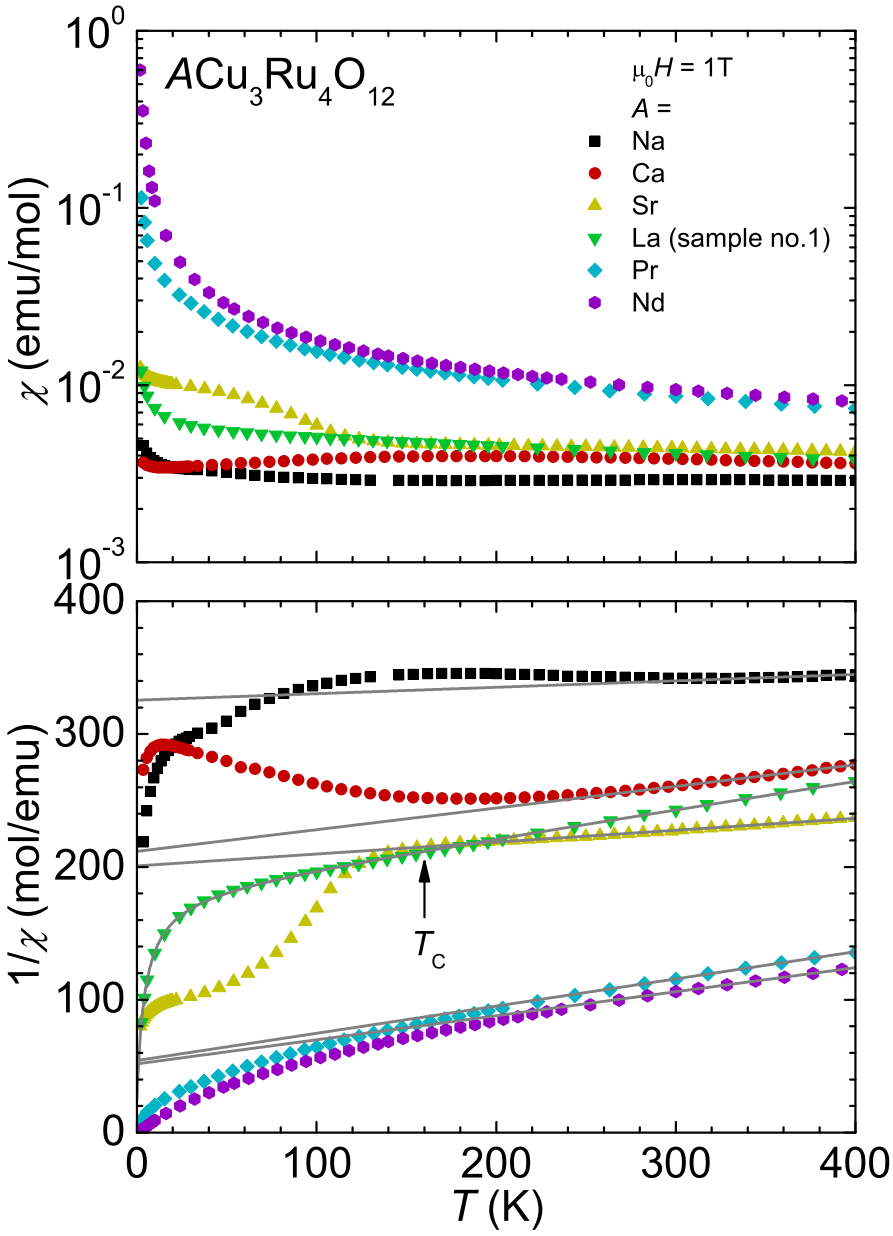

Figure 5.10: Temperature dependent magnetic susceptibility (upper frame, semi-logarithmic plot) and its inverse (lower frame, linear plot) of $ACu_3Ru_4O_{12}$ (A = Na, Ca, Sr, La, Pr, Nd) in an external field of 1 T. The grey solid lines (curve for $LaCu_3Ru_4O_{12}$) are fits according to a Curie-Weiss law (see text and Table 5.5 for details). The arrow indicates the Curie temperature T_C of $SrRuO_3$.[175]

A	θ_{CW} (K)	μ_{eff} (μ_B/f.u.)	R_W
Na	-6728	12.86	2.9
Ca	-1299	7.00	2.4
Sr	-2243	9.45	2.6
La	-875	6.17	1.7
Pr	-265	6.25	1.0
Nd	-286	6.65	1.8

Table 5.5: Curie-Weiss temperature θ_{CW} and effective magnetic moment μ_{eff} as resulting from the fits to the inverse magnetic susceptibility of $A Cu_3Ru_4O_{12}$ (A = Na, Ca, Sr, La, Pr, Nd) (see Fig. 5.10). The evaluation of the Wilson ratio R_W is described in the text. Note that the itinerant character of the magnetism suspends the classical meaning of a Curie-Weiss temperature and must be seen as a pure fitting parameter, at least for $A Cu_3Ru_4O_{12}$ (A = Na, Ca, Sr). In the case of $A Cu_3Ru_4O_{12}$ (A = Pr, Nd), θ_{CW} adopts a meaning as a parameter of the CEF.

Pauli-susceptibility below 40 K.[177] In general, a Curie behavior due to localized paramagnetic moments is expected well above T_{SF} whereas an enhanced Pauli-susceptibility is expected well below T_{SF}. At high temperatures the data of $CaCu_3Ru_4O_{12}$ can also be fitted to a Curie-Weiss law leading to a high absolute value of the AFM CW temperature ($\theta_{CW} = -1299$ K) and to an effective moment of 7.0 μ_B/f.u. which is higher than expected. A model with localized moments with straightforward valences (3× Cu^{2+}: $S = 1/2$ and 4× Ru^{4+}: low spin state, $S = 1$) would lead to an effective moment of 6.4 μ_B/f.u. It is clear that the magnetic moments of the metal ions depend on the density of states and assuming fully itinerant d-electrons, it can acquire any non-integer value. But at sufficiently high temperatures (i.e. above 400 K) a Curie-Weiss law should be observable with a moment corresponding to the expected paramagnetic ones. The impurity concentration deduced from the low temperature Curie tail is approximately two times lower than that in $NaCu_3Ru_4O_{12}$ (0.112 μ_B/f.u.) corresponding to one free spin per 15 f.u. In contrast to the susceptibility data shown in Fig. 5.10, a Curie-type upturn of the Knight shift is not observed at low temperatures, confirming its origin to be due to local magnetic defects.

The inverse susceptibility of $SrCu_3Ru_4O_{12}$, although formally isoelectronic to the Ca compound, follows a totally different dependence. Here, a perfect linear behavior down to approximately 150 K is evident below which it begins to deviate significantly. This drop-off is due to the contribution of the impurity phase $SrRuO_3$ (see chapter 5.1) which is an

itinerant ferromagnet with a Curie temperature of 160 K.[175] Unlike in $NaCu_3Ru_4O_{12}$ and $CaCu_3Ru_4O_{12}$, where the abnormal values of the AFM CW temperature can be ascribed to a broad peak in the relevant fitting range, the susceptibility of $SrCu_3Ru_4O_{12}$ more resembles that of $LaCu_3Ru_4O_{12}$ (following paragraph). For both compounds, there is no signature for a deviation from the linear dependence toward higher temperatures such that an explanation of the unusually high CW temperature (-2243 K) fails. In contrast to $LaCu_3Ru_4O_{12}$, where the effective moment can be well identified with the paramagnetic constituents, it is unexplainable high in the case of $SrCu_3Ru_4O_{12}$ (9.45 μ_B/f.u.). The defect contribution is calculated to 0.326 μ_B/f.u. by fitting the low temperature Curie tail, corresponding to roughly one free spin per 5 f.u.

At first sight the susceptibility of $LaCu_3Ru_4O_{12}$ might also reveal an itinerant paramagnet with local magnetic impurities dominating at low temperatures. In fact, it has been interpreted in this way, previously.[33] However, on the basis of a continuously decreasing susceptibility with increasing temperature and a corresponding inverse susceptibility revealing a perfect linearity for 80 K < T < 400 K a phenomenological description by two Curie-Weiss laws[3] suggests itself. A comparison with $SrCu_3Ru_4O_{12}$ and to a smaller extent also with $CaCu_3Ru_4O_{12}$ shows a similar high-temperature behavior. For the comparison with the Sr homologue it would be of great advantage having material free of $SrRuO_3$ as it greatly superimposes the intrinsic behavior of the host compound, at least below the ferromagnetic ordering temperature of 160 K. But, although coming with an unrealistically high effective moment, $SrCu_3Ru_4O_{12}$ seems to have a similar temperature dependence as $LaCu_3Ru_4O_{12}$. In contrast to the Ca compound which exhibits a cusp-like maximum in the magnetic DC-susceptibility, the CW law of $LaCu_3Ru_4O_{12}$ holds down to much lower temperatures and then is hidden by an impurity-caused Curie tail. The dominating high temperature behavior can be described by a paramagnetic moment of 6.17 μ_B/f.u. and a CW temperature of θ_{CW1} = −875 K followed by a defect contribution with a paramagnetic moment of 0.41 μ_B/f.u. and a CW temperature of θ_{CW2} = −0.6 K. The Curie tail roughly implies one free spin (S = 1/2) per four formula units, probably located in grain boundaries and/or close to the surface. A model with local moments seems to be applicable in the case of $LaCu_3Ru_4O_{12}$ but it is not straightforward to calculate an effective moment since the adoption of a formal integer valence of either Cu or Ru does not come out even when presuming La^{3+} and O^{2-} rigidly. The assumption of two Cu^{2+} (S = 1/2), one Cu^{+} (S = 0),

3 $\chi = C_1/(T-\theta_{CW1}) + C_2/(T-\theta_{CW2})$, C_1/C_2: Curie constants, $\theta_{CW1}/\theta_{CW2}$: CW temperatures

and four Ru^{4+} (low spin state, $S = 1$) leads to a paramagnetic moment of $6.17\,\mu_B$/f.u., perfectly matching the experimental value. However, a similar theoretical moment of $6.0\,\mu_B$/f.u. is achieved when adopting three Cu^{2+} ($S = 1/2$), three Ru^{4+} (low spin, $S = 1$) and one Ru^{3+} (low spin, $S = 1/2$). Hence, the presence of Cu^{+} and/or Ru^{3+} species has been proposed by Labeau *et al.* [41] who first encountered the formation of the trivalent compounds $ACu_3Ru_4O_{12}$ (A = La, Pr, Nd). In fact, bond-valence sum calculations based on EXAFS [48] and XANES [66, 77] measurements indicate the oxidation state of Ru close to +4 implying the presence of considerable amounts of Cu^{+} and, therefore, point to the scenario with four Ru^{4+}. While the paramagnetic moment seems to be reasonable, the absolute value of the AFM CW temperature is astonishingly high. Taken $\theta_{CW} = -875\,K$ for granted and taking into account that $LaCu_3Ru_4O_{12}$ does not undergo magnetic order at any temperature, such a CW temperature would indicate very strong magnetic frustration or complete moment compensation with a characteristic spin-fluctuation temperature of the order of $T^* = \theta_{CW}/4 = 220\,K$ often found experimentally.[116] This is in very good agreement with the characteristic temperature of $CaCu_3Ru_4O_{12}$ which amounts approximately 200 K [30] supporting strong spin fluctuations as the reason for the suppression of the magnetic order in $LaCu_3Ru_4O_{12}$. However, it seems to be unclear why the susceptibility still increases well below the characteristic temperature instead of a broad maximum as observed in $CaCu_3Ru_4O_{12}$. And besides, when having in mind the moderately enhanced Sommerfeld coefficient of $CaCu_3Ru_4O_{12}$ and now solely compare the susceptibility of $CaCu_3Ru_4O_{12}$ with that of $CeSn_3$ [176] it could be argued that the broad maximum around 180 K is related to a Kondo effect between localized Ru 4*d* and itinerant Cu 3*d* electrons.[4] However, why is such a maximum not visible in the susceptibility of $LaCu_3Ru_4O_{12}$ although it possesses an even higher effective electronic mass. This clearly weakens the argument of a Kondo scenario as exclusive or main origin of the mass enhancement in $ACu_3Ru_4O_{12}$ (A = Na, Ca, Sr, La, Pr, Nd).

Turning now to the compounds with magnetic rare-earth ions at the A-site, namely $ACu_3Ru_4O_{12}$ (A = Pr, Nd), it is clear that their susceptibility is dominated by their local magnetic moment which itself underlies the influence of the crystal field. A Curie-Weiss fit to the raw data of the inverse magnetic susceptibility in the range $300\,K < T < 400\,K$ reveals a CW temperature of $\theta_{CW} = -265\,K$ ($\theta_{CW} = -286\,K$) and an effective moment

4 Note that it was also argued in the opposite way, namely that the electrons of Cu are localized and those of Ru itinerant.[30]

of 6.25 μ_B/f.u. (6.65 μ_B/f.u.) for $PrCu_3Ru_4O_{12}$ ($NdCu_3Ru_4O_{12}$), respectively. In a localized model, the expected effective moment is 7.16 μ_B/f.u. (7.18 μ_B/f.u.) for $PrCu_3Ru_4O_{12}$ ($NdCu_3Ru_4O_{12}$) when calculating with Pr^{3+} (Nd^{3+}), 2× Cu^{2+}, 4× Ru^{4+} (low spin, $S = 1$). These values do not go well together but are still in reasonable agreement and indeed, according to Refs. [48, 66] the Ru valence in $NdCu_3Ru_4O_{12}$ is also very close to 4+ as it is the case in $LaCu_3Ru_4O_{12}$. This means that Cu^+ is likely to be present here, too. Note that the resulting CW temperatures have no significance in the original sense but partially stem from details of the rare-earth CEF levels [178] which will be also shown in an extended analysis in the following. More important for the general understanding of the susceptibility is the fact that the RE spins are only weakly coupled to the *d*-electron system of Ru and Cu. Thus it is not possible to find a common CW law including both *d*- and *f*-magnetic moments but one is able to separate both contributions using a purely *d*-electron reference system.

Hence, to arrive at some definite conclusions for the susceptibility of the rare-earth ion, the temperature dependent susceptibility of the La compound (which describes the influence of the *d*-electrons of Cu and Ru ions) is subtracted from the data of $PrCu_3Ru_4O_{12}$ and $NdCu_3Ru_4O_{12}$, respectively. The remaining contribution is attributed to the susceptibility of the rare earth. In Fig. 5.11 the inverse of the difference susceptibility $\Delta\chi = \chi(ACu_3Ru_4O_{12}) - \chi(LaCu_3Ru_4O_{12})$ (A = Pr, Nd) is shown. A CW fit for $T > 200$ K reveals paramagnetic moments of 3.66 μ_B/Pr^{3+} and 4.07 μ_B/Nd^{3+}, which are close to the free-ion values of 3.58 μ_B (Pr^{3+}) and 3.63 μ_B (Nd^{3+}). With decreasing temperature the data begin to deviate from a linear dependence which is attributed to CEF effects of the rare-earth ions.[179] This implies an overall splitting of the CEF levels of at least 150 K and 200 K for Pr^{3+} and Nd^{3+}, respectively. At very low temperatures ($T < 10$ K), the slope of the inverse susceptibility of $PrCu_3Ru_4O_{12}$ increases significantly which can be ascribed to a decreasing effective magnetic moment to roughly 1.8 μ_B/Pr^{3+} and implying a non-magnetic ground state or a ground state bearing a small magnetic moment. This can also be seen in the high-field susceptibility of $PrCu_3Ru_4O_{12}$ (up to 14 T) in Fig. 5.12 on a semi-logarithmic scale. Here, χ begins to spread from a uniform dependence below ≈ 20 K and from that temperature downwards χ continuously decreases upon increasing field while simultaneously developing a more and more pronounced saturation toward lowest temperatures. In the case of Nd^{3+} the magnetic moment is reduced to 2.8 μ_B/Nd^{3+}, pointing to a magnetic ground state. As a matter of fact, the magnetic matrix elements

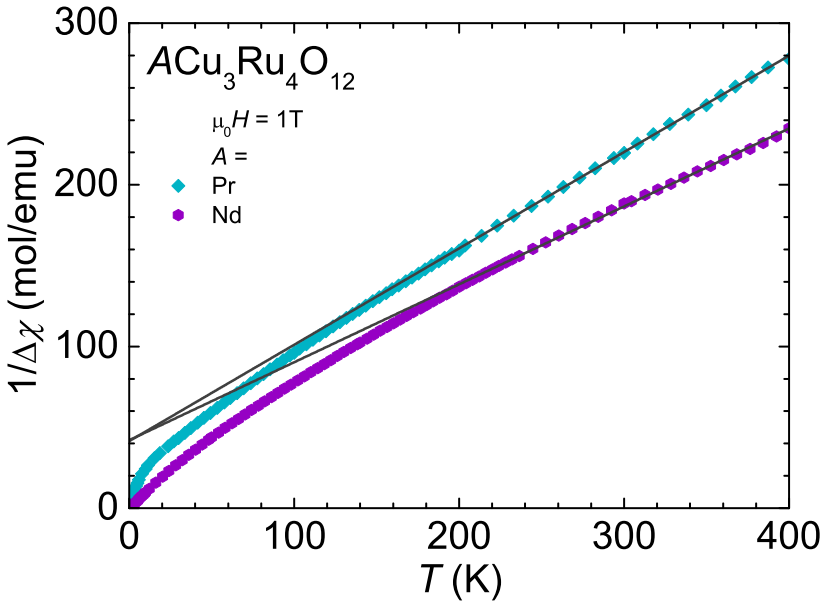

Figure 5.11: Temperature dependent inverse magnetic susceptibility of ACu$_3$Ru$_4$O$_{12}$ (A = Pr, Nd) in an external field of 1 T. The data of the reference compound LaCu$_3$Ru$_4$O$_{12}$ are subtracted from PrCu$_3$Ru$_4$O$_{12}$ and NdCu$_3$Ru$_4$O$_{12}$, respectively. The solid lines are fits according to a Curie-Weiss law (see text for details).

of the eigenstates of Pr^{3+} and Nd^{3+} in a crystal field of cubic symmetry are consistent with the above mentioned findings.[180]

The magnetization of ACu$_3$Ru$_4$O$_{12}$ (A = Na, Ca, Sr, La, Pr, Nd) at 2 K is shown in Fig. 5.13 for fields up to 5 T. For the Na and the Ca compound a saturation of impurities is observable up to ≈ 25 kOe above which it follows a linear dependence. High-field magnetization data of CaCu$_3$Ru$_4$O$_{12}$ show that this linearity holds on up to fields of 52 T.[63, 64] The magnetization curve of SrCu$_3$Ru$_4$O$_{12}$ clearly shows a ferromagnetic signature as represented by a remanence of 49.5 emu/mol. Assuming localized low-spin Ru^{4+} (2.83 μ_B) in the impurity phase SrRuO$_3$ as origin [175] then the content of SrRuO$_3$ in the sample is approximately 0.3% which is in excellent agreement with the XRD results (chapter 5.1.1). However, the spontaneous magnetization of SrRuO$_3$ in the experimental zero-temperature limit in the bulk is 1.6 μ_B/f.u.[175] The assumption of this - probably more trustworthy - value leads to a higher content of SrRuO$_3$, namely 0.55%. At fields above 25 kOe the magnetization of SrCu$_3$Ru$_4$O$_{12}$ turns into a linearity up to highest accessible fields. Inter-

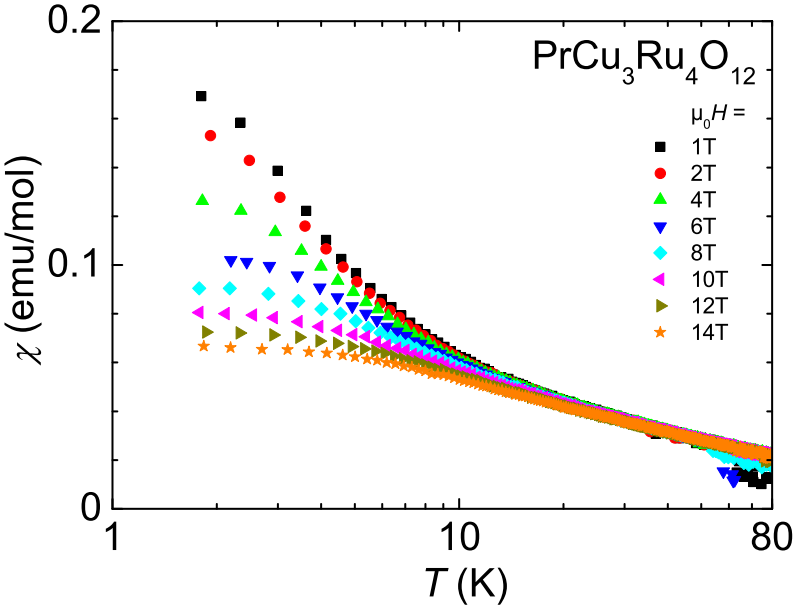

Figure 5.12: Temperature dependent magnetic susceptibility of $PrCu_3Ru_4O_{12}$ in various external fields up to 14 T in a semi-logarithmic representation.

estingly, the magnetization data of $LaCu_3Ru_4O_{12}$ follow the virgin curve of $SrCu_3Ru_4O_{12}$ very closely up to a field of 20 kOe at which it turns into a continuing linear dependence but with a somewhat steeper slope than $SrCu_3Ru_4O_{12}$. However, in contrast to the Sr compound no evidence for a hysteresis loop is visible, such that an unknown ferromagnetic phase can be excluded. Still, below ≈ 50 K, sample no.2 of $LaCu_3Ru_4O_{12}$ shows a suppression of the susceptibility with increasing field which is not present in other La samples (see Fig. 7.12) and which might be related to some unknown impurity phase. Compared to the latter compounds, the magnetization of $ACu_3Ru_4O_{12}$ (A = Pr, Nd) strongly increases even at low fields and shows a saturating tendency toward higher fields (see Figs. 5.13 and 5.14). This clearly shows the strong influence of the $4f$ ground state of the corresponding rare-earth ion.

In traditional correlated f-electron systems, the Wilson ratio serves as dimensionless quantity which provides insight into the type of interaction present within the respective material. It includes the zero-temperature magnetic susceptibility χ_0 and the coefficient of the electronic contribution to the specific heat γ. In the original definition calculated within the renormalization group approach [45] it is defined by R_W =

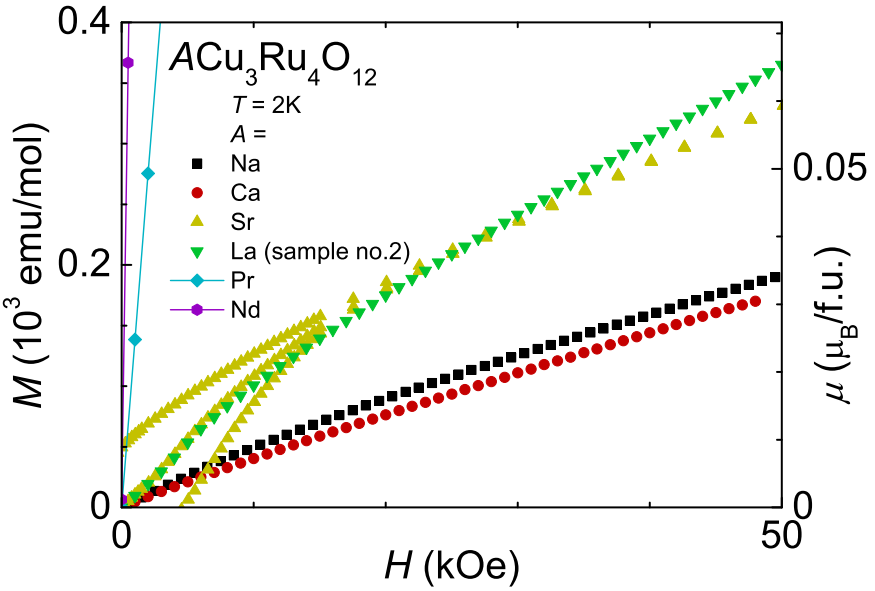

Figure 5.13: Field dependent magnetization $M(T)$ of $A\mathrm{Cu_3Ru_4O_{12}}$ (A = Na, Ca, Sr, La, Pr, Nd) at 2 K in units of emu/mol (left scale) and μ_B/f.u. (right scale).

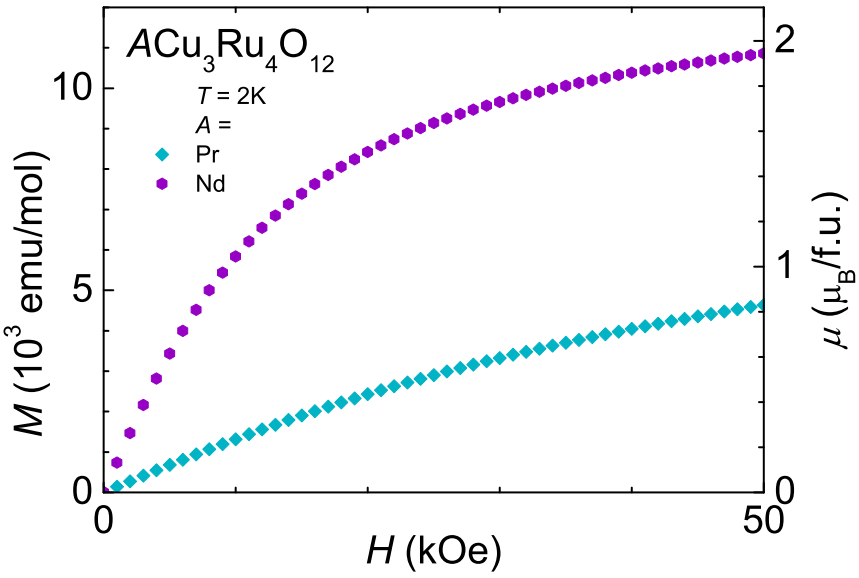

Figure 5.14: Field dependent magnetization of $A\mathrm{Cu_3Ru_4O_{12}}$ (A = Pr, Nd) at 2 K in units of emu/mol (left scale) and μ_B/f.u. (right scale).

$\pi^2 k_B^2 \chi(0)/g^2 \mu_B^2 s(s+1)\gamma$ (cgs-units, k_B: Boltzmann constant, g: Landé g-factor, s: spin, μ_B: Bohr magneton). For a free electron gas ($g = 2$, $s = 1/2$) $R_W = 1$ whereas in the strong correlation limit for local Fermi liquids $R_W = 2$. Mind that different theoretical approaches for the modeling of magnetic impurities in metals have been made resulting in a variation of the universal value of R_W.[110, 111, 112, 113, 114, 115, 116] For the calculation of the Wilson ratio often the susceptibility at around 10 K is used as approximation for the zero-temperature limit.[58] In the case of $A Cu_3Ru_4O_{12}$ (A = Na, Ca, Sr, La, Pr, Nd) this leads to unreasonably high values, especially for $A Cu_3Ru_4O_{12}$ (A = Pr, Nd) (R_W = 10, and 34). More credible results are obtained when fitting the high temperature regime of the susceptibility with $\chi(T) = \chi_0 + C/(T - \theta)$ ($\theta \equiv 0$) and using χ_0 for the calculations. The resulting Wilson ratios are between 1 and 2 for the lanthanide samples and between 2 and 3 for $A Cu_3Ru_4O_{12}$ (A = Na, Ca, Sr) (see also Table 5.5). A double-logarithmic plot of the Sommerfeld coefficient γ vs. zero-temperature susceptibility χ_0 (Wilson ratio R_W) for various heavy-fermion compounds including $A Cu_3Ru_4O_{12}$ (A = Na, Ca, Sr, La, Pr, Nd) is shown in Fig. 5.15. The copper-ruthenates $A Cu_3Ru_4O_{12}$ (A = Na, Ca, Sr, La, Pr, Nd) are situated well between classical f-electron compounds as most of them possess Wilson ratios between 1 and 3 as obvious from the straight lines corresponding to Wilson ratios $R_W = 1, 2$, and 3.

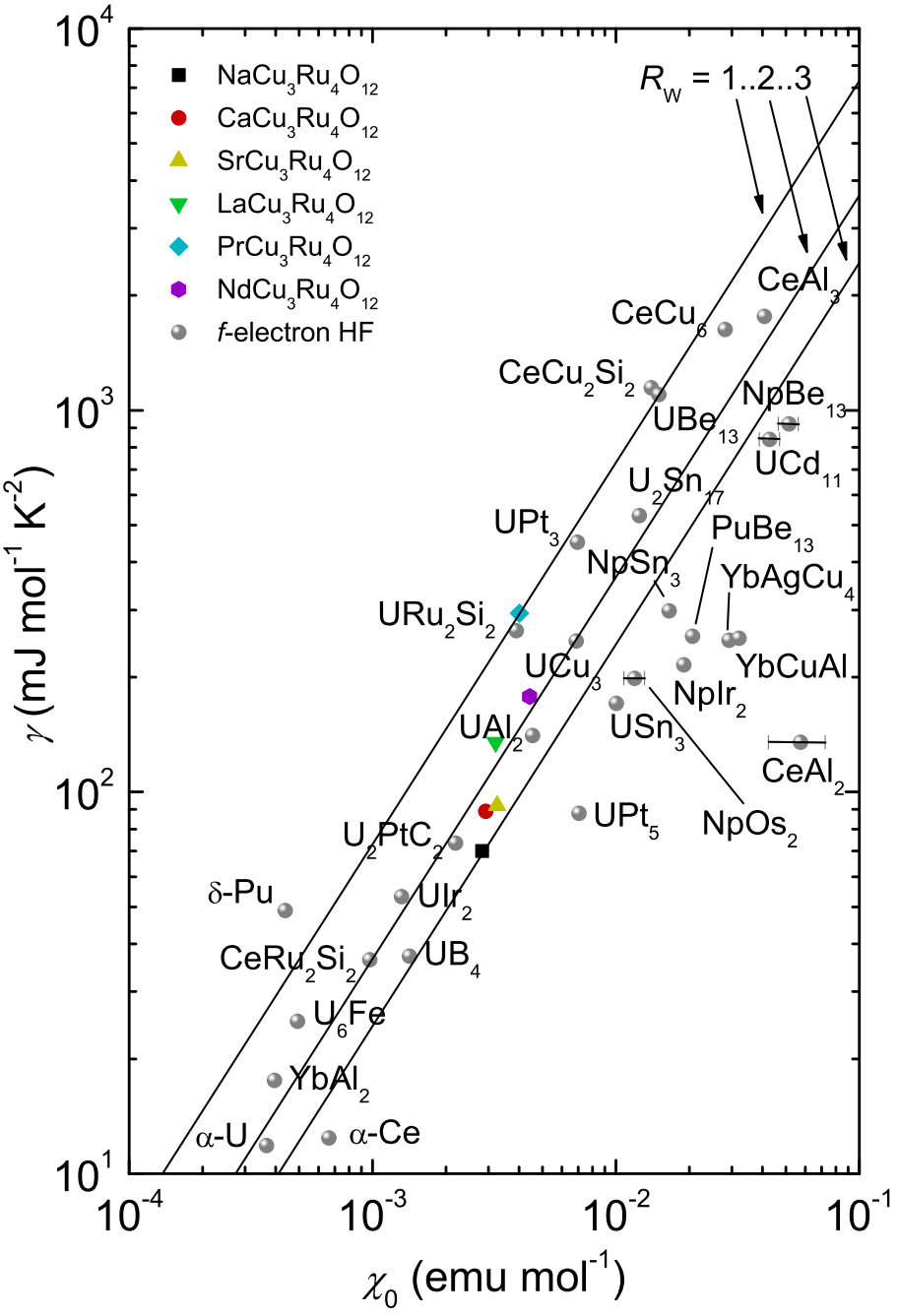

Figure 5.15: Double-logarithmic plot of the Sommerfeld coefficient γ vs. zero-temperature susceptibility χ_0 (Wilson ratio R_W) [45] for various heavy-fermion compounds including $A Cu_3 Ru_4 O_{12}$ (A = Na, Ca, Sr, La, Pr, Nd). The straight lines correspond to Wilson ratios $R_W = 1, 2$, and 3. Diagram based on Refs. [181, 116].

5.3 Resistivity

In Fig. 5.16 the temperature dependent electrical resistivity in zero magnetic field is plotted for polycrystalline $A\mathrm{Cu_3Ru_4O_{12}}$ (A = Na, Ca, Sr, La, Pr, Nd). Metallic conductivity ($d\rho/dT > 0$) is observed for all compounds in the entire temperature range. Evidently, both the residual resistivity ρ_0 and the residual resistance ratio RRR vary largely and can be used to classify the compounds phenomenologically: For the Na, Ca, and Sr compound, ρ_0 is relatively low, as it amounts 25 $\mu\Omega$cm, 44 $\mu\Omega$cm, and 37 $\mu\Omega$cm, while the lanthanide compounds possess roughly 10 times larger values with 273 $\mu\Omega$cm ($\mathrm{LaCu_3Ru_4O_{12}}$), 364 $\mu\Omega$cm ($\mathrm{PrCu_3Ru_4O_{12}}$), and 474 $\mu\Omega$cm ($\mathrm{NdCu_3Ru_4O_{12}}$). The comparingly large value of ρ_0 for the lanthanide compounds involves a low residual resistance ratio ($RRR \approx 2$). On the contrary, the values for the RRR of the alkali/alkaline earth homologues are larger by approximately one order of magnitude: $RRR = 55$ ($\mathrm{NaCu_3Ru_4O_{12}}$), $RRR = 19$ ($\mathrm{CaCu_3Ru_4O_{12}}$), and $RRR = 15$ ($\mathrm{SrCu_3Ru_4O_{12}}$). Apparently the valence of the A-site ion correlates with the value of the RRR. It is largest for monovalent Na, lowest for the trivalent lanthanides, and in between for divalent alkaline earth. The results for $A\mathrm{Cu_3Ru_4O_{12}}$ (A = Na, Ca, La) are in very good agreement with earlier measurements by Labeau *et al.* [41] and Muller *et al.* [42]. In general, the absolute values of the resistivity of $A\mathrm{Cu_3Ru_4O_{12}}$ (A = Na, Ca, La) reported in further publications [30, 33, 58, 76] vary up to a factor of 3, whereas the qualitative characteristics as represented by the residual resistance ratio RRR remain nearly the same for different samples/measurements of one and the same compound. This indicates that the bigger part of the discrepancies is attributed to variations of compactness occurring during pressing/sintering of the powders and to difficulties in determining the exact geometry factors of the samples when converting resistance to resistivity.

In a plot of $\rho - \rho_0$ vs. T^2 (see Fig. 5.17), the resistivity data of polycrystalline $A\mathrm{Cu_3Ru_4O_{12}}$ (A = Na, Ca, Sr, La, Pr, Nd) is fitted according to a quadratic temperature dependence ($\rho(T) = \rho_0 + AT^2$) for $T < 30$ K, which is characteristic for a Fermi liquid. All compounds follow a T^2 law, at least in a certain temperature range. $\mathrm{NaCu_3Ru_4O_{12}}$ exhibits a perfect quadratic dependence (straight line) over the full temperature range under consideration, while in the Ca, Sr, and La compound (dashed and dash-dotted lines) slight deviations occur below ≈ 25 K. For the Ca and Sr compound a detailed analysis is

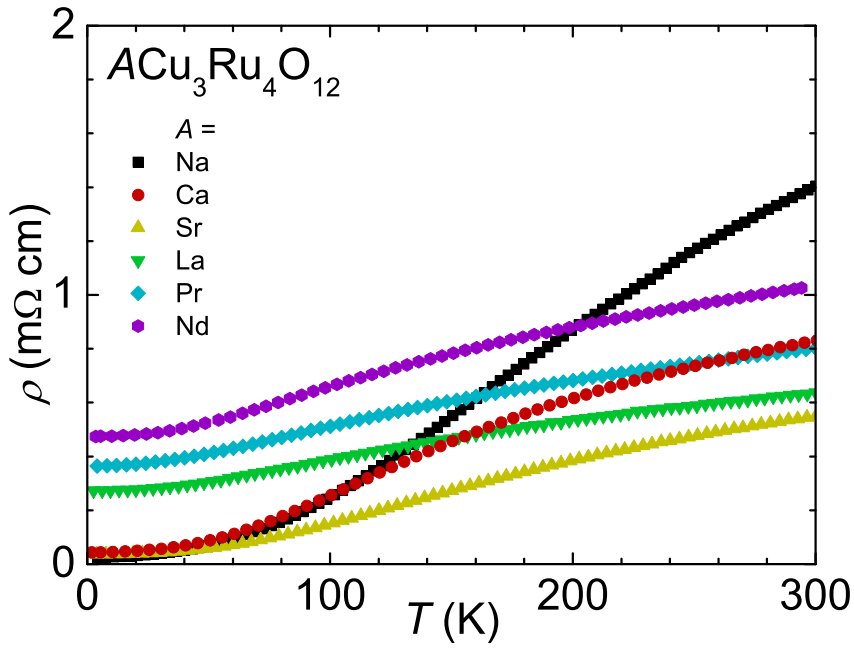

Figure 5.16: Temperature dependent resistivity of polycrystalline $A\mathrm{Cu_3Ru_4O_{12}}$ (A = Na, Ca, Sr, La, Pr, Nd) in zero magnetic field (see text for measurement details).

provided later in this chapter, while the data of $\mathrm{LaCu_3Ru_4O_{12}}$ turn out to be too noisy for profound conclusions. For the compounds with magnetic A-site ions also deviations occur which are pronounced in the Nd compound below 25 K and only weakly show up in $\mathrm{PrCu_3Ru_4O_{12}}$ below 5 K. A more detailed analysis is given later in this chapter also for these two compounds. The fitting parameter A as well as the residual resistivity ρ_0 and the residual resistance ratio RRR are listed in Table 5.6.

A detailed analysis of the low temperature behavior of polycrystalline $\mathrm{CaCu_3Ru_4O_{12}}$ in an external transversal magnetic field ($H \perp I$) is provided in Fig. 5.18. The main frame shows how the temperature dependent resistivity changes with increasing magnetic field (up to 14 T). A positive magneto-resistive effect is present with the magneto-resistance ratio $(\rho_H - \rho_0)/\rho_0$ (see inset of Fig. 5.18) being a monotonically diminishing function of temperature.[5] The T-dependence of the resistivity in different magnetic fields can be excellently described for $2\,\mathrm{K} < T < 30\,\mathrm{K}$ by a power law according to $\rho(T) = \rho_0 + AT^n$ (see solid/dashed/dash-dotted curves in the upper frame of Fig. 5.18). The evaluated

5 ρ_H and ρ_0 denote the temperature dependent resistivity in a certain constant field and in zero field, respectively.

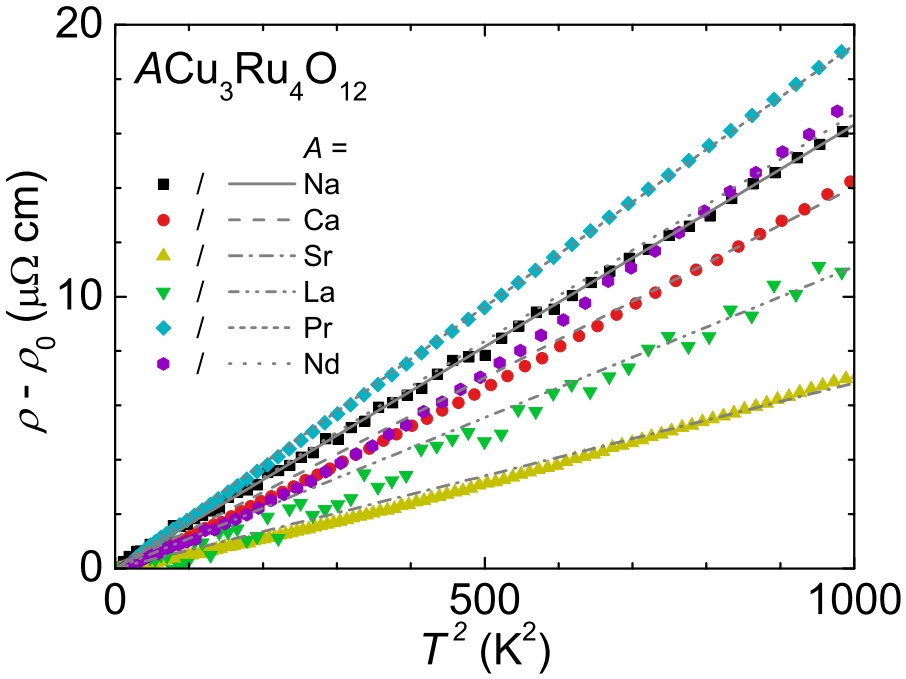

Figure 5.17: Temperature dependent resistivity of ACu$_3$Ru$_4$O$_{12}$ (A = Na, Ca, Sr, La, Pr, Nd) in the representation $\rho - \rho_0$ vs. T^2 including fits to a Fermi liquid (grey lines, see text for details).

A	ρ_0 (μΩcm)	A (10^{-9} Ωcm/K^2)	RRR	R_{KW} (10^{-5} μΩcm mol^2 K^2/mJ^2)
Na	24.8	16.31	55.3	0.333
Ca	43.7	14.18	18.9	0.179
Sr	36.5	7.01	15.0	0.083
La	272.9	11.61	2.3	0.064
Pr	363.5	19.63	2.2	0.023
Nd	473.8	16.85	2.2	0.053
Ca (crystal)	232.0	28.40	5.5	0.357

Table 5.6: Residual resistivity ρ_0 and the coefficient A resulting from the fit to the low temperature resistivity of polycrystalline ACu$_3$Ru$_4$O$_{12}$ (A = Na, Ca, Sr, La, Pr, Nd) according to $\rho(T) = \rho_0 + AT^2$ (see Fig. 5.17) as well as the residual resistance ratio RRR and the Kadowaki-Woods ratio $R_{KW} = A/\gamma^2$.[47] The values of a CaCu$_3$Ru$_4$O$_{12}$ single crystal "Flux1-linear" is also included (lowest row).

power n is almost constant at 2.18 ± 0.01 except for 14 T ($n = 2.10$) whereas $A = 7.50 \pm 0.15\,\mathrm{n\Omega cmK^{-n}}$ except for 14 T ($A = 8.77\,\mathrm{n\Omega cmK^{-n}}$). Furthermore a plot of ρ vs. H for various temperatures (see Fig. 5.18) reveals a perfect quadratic dependence as illustrated by fits according to $\rho(T) = \rho_0 + \alpha H^2$ (solid curves) as expected for a conventional metal obeying Kohler's rule.[182, 183].

Interestingly, the low temperature resistivity of polycrystalline $SrCu_3Ru_4O_{12}$ in an external transversal magnetic field, as plotted in Fig. 5.19, features a different behavior than that of $CaCu_3Ru_4O_{12}$. Although its T-dependence can also be fitted with a power law according to $\rho(T) = \rho_0 + AT^n$ ($n = 2.4$, $A = 1.80 \pm 0.20\,\mathrm{n\Omega cmK^{-n}}$) for all applied magnetic fields, this only holds for $T > 10\,\mathrm{K}$ (see solid/dashed/dash-dotted curves in the upper main frame of Fig. 5.19). For temperatures below and also independent of the applied field, the resistivity looses its power law dependence with a remaining power lower than 2.4. In fact, $\rho(T)$ in zero field decreases linearly with decreasing temperature as evident from a fit from $\approx 7\,\mathrm{K}$ down to lowest accessible temperatures (solid line in the inset of Fig. 5.19). As far as can be assessed from the available T-range, the onset of this linearity is slightly shifted to lower temperatures upon increasing magnetic field (dashed/dash-dotted lines in the inset of Fig. 5.19). A positive linear T-dependence of the resistivity is also observed in a $CaCu_3Ru_4O_{12}$ single crystal as will be shown later in this chapter. As in the above described $CaCu_3Ru_4O_{12}$, a typical quadratic behavior of the field dependence of ρ at constant temperature is observed in $SrCu_3Ru_4O_{12}$, too (see lower frame of Fig. 5.19 with corresponding fits).

For $PrCu_3Ru_4O_{12}$ (upper frame of Fig. 5.20) no shift of the resistivity could be detected for $T > 15\,\mathrm{K}$ when applying magnetic fields up to 9 T. Below that temperature the quadratic dependence in zero field as predicted by Fermi-liquid theory is lost at $\approx 7\,\mathrm{K}$ where the data begins to deviate visibly from a respective fit (grey dashed curve) with a power law lower than two. Here also, the resistivity changes its curvature and once again at $\approx 1.5\,\mathrm{K}$ resulting in a step-like decrease of $\rho(T)$ below 2 K finally leading to a residual resistivity of $\approx 361\,\mu\Omega\mathrm{cm}$ which is roughly 0.8% lower than ρ_0 derived from the fit as Fermi liquid. This anomaly might reflect a change in the temperature-dependent probability of the conduction electrons to be scattered from the crystal-field-split $4f$ levels of the Pr^{3+} ions by elastic as well as inelastic processes. The drop in resistivity is then partly a result of the thermal depopulation of the first excited CEF level to a non-magnetic ground state

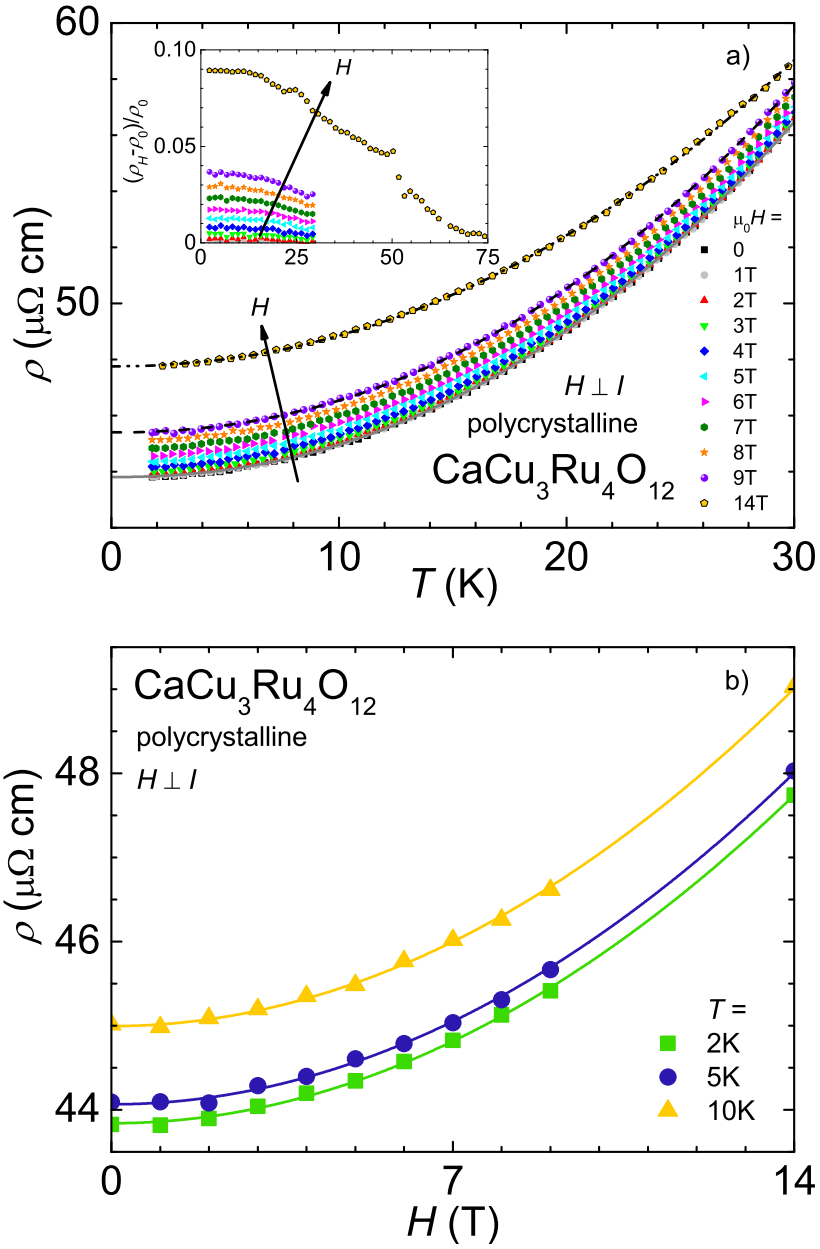

Figure 5.18: Frame a: Temperature dependent resistivity and magneto-resistivity (inset) of polycrystalline $CaCu_3Ru_4O_{12}$ for various transversal magnetic fields. The curves are fits according to a T^n power law (solid: zero field, dashed: 9 T, dash-dotted: 14 T). Arrows indicate the development with increasing magnetic field H. Frame b: Field dependent resistivity of polycrystalline $CaCu_3Ru_4O_{12}$ for various temperatures. Fits according to a parabolic field dependence are shown as solid curves. See text for details.

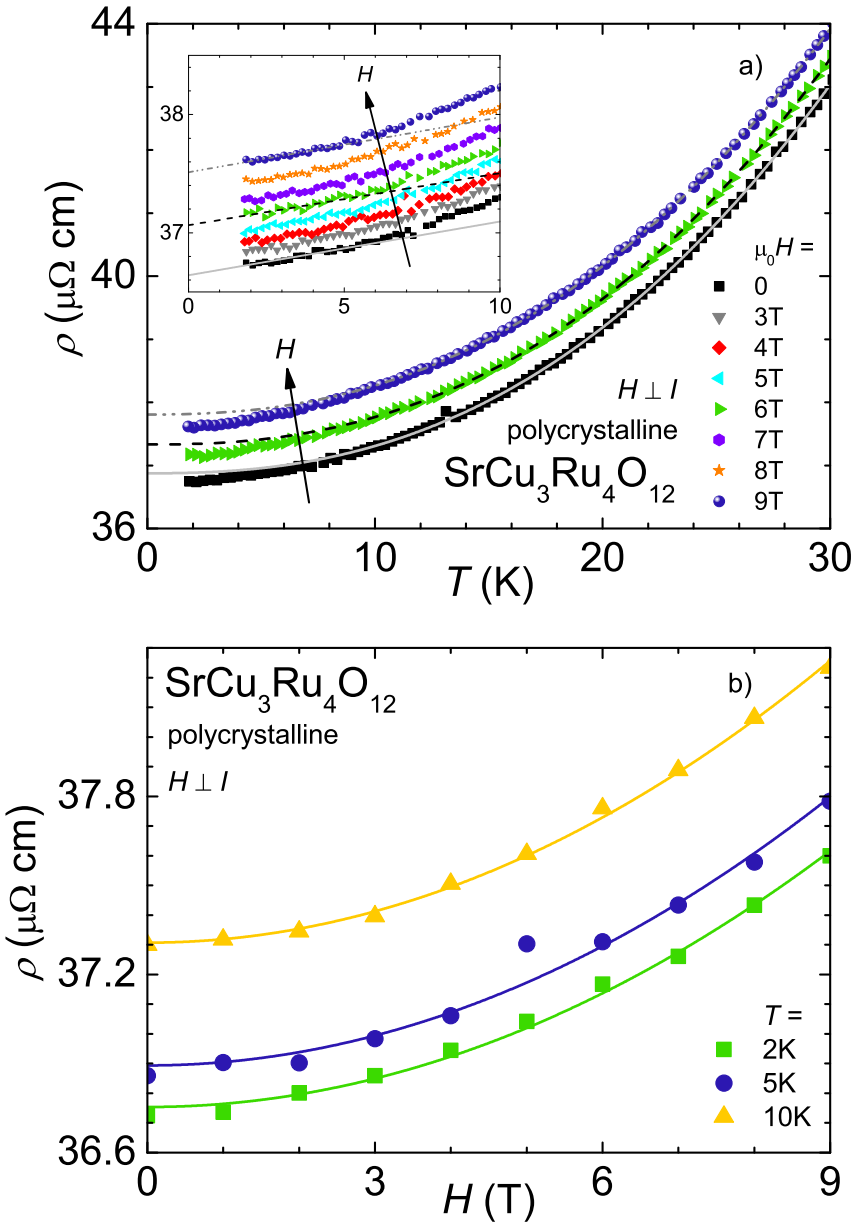

Figure 5.19: Frame a: Temperature dependent resistivity of polycrystalline $SrCu_3Ru_4O_{12}$ for various transversal magnetic fields. The curves are fits according to a T^n power law (solid: zero field, dashed: 6 T, dotted: 9 T). Inset: Temperature dependent resistivity on an enhanced scale for various magnetic fields including fits according to a linear dependence (solid: zero field, dashed: 6 T, dash-dotted: 9 T). Frame b: Field dependent resistivity of polycrystalline $SrCu_3Ru_4O_{12}$ for various temperatures. Fits according to a parabolic field dependence are shown as solid curves. See text for details.

or one with a small magnetic scattering cross section.[184, 185, 186] Looking at the eigenstates of the $J = 4$ split Pr^{3+} ion in a crystal field of cubic symmetry $Im\bar{3}$ (T_h^5) (No.204) [127, 187],[6] then such a behavior is compatible as both the singlet Γ_1 and the doublet Γ_3 have vanishing matrix elements $|\langle\Gamma_i|J_z|\Gamma_j\rangle|$.[180] Something that also attracts attention is the fact that between the low temperature data set (grey full squares, $T < 2.5\,\mathrm{K}$) measured in a dilution refrigerator and the data above 2 K measured in a PPMS (black full squares), a noticeable mismatch regarding their slope is present. The reason for this is not quite clear, although naturally, the two data sets had to be adapted with a factor due to inevitable deviations occurring when contacting samples anew for measurements in different equipment. When looking at the resistivity, how it develops in a magnetic field, it is obvious from Fig. 5.20 (upper frame) that a smooth negative magneto-resistive effect is present for temperatures lower than $\approx 15\,\mathrm{K}$ which decreases the resistivity with increasing field to a nearly linear dependence at 9 T. For a more detailed analysis of this effect, the fit to the zero-field data according to Fermi-liquid theory has been subtracted from all data sets and is shown in Fig. 7.19. The remaining (negative) contribution $\Delta\rho$ features a small and broad maximum in zero field and moderate magnetic fields which vanishes in a field of $\approx 4\,\mathrm{T}$. Simultaneously, $\Delta\rho$ develops a more and more linear dependence for both a high temperature ($T > 10\,\mathrm{K}$) and a low temperature regime ($T < 6\,\mathrm{K}$). This effect is attributed to the Zeeman splitting [188] of the CEF levels of the Pr^{3+} ion.

The behavior is quite similar in the Nd compound (lower frame of Fig. 5.20). Here, no shift of the resistivity in magnetic fields (up to 14 T) could be detected down to $\approx 30\,\mathrm{K}$. Below, a negative MR effect is present as in $PrCu_3Ru_4O_{12}$, yet being much stronger. It amounts $\approx 2.8\%$ at 2.5 K between zero field and 8 T with no significant further change at higher fields (up to 14 T). When fitting the zero-field resistivity with a T^2 power law (grey dashed curve) the fit underestimates the data below $\approx 18\,\mathrm{K}$ indicating a power law stronger than two and leading to a weak, almost linear dependence below 10 K. From the zero-field data it is not quite clear if $NdCu_3Ru_4O_{12}$ also exhibits a step-like decrease in $\rho(T)$. But when looking at the resistivity data in moderate external fields a step-like drop evolves from low temperatures and - similarly to $PrCu_3Ru_4O_{12}$ - becomes almost fully smeared out to a nearly linear behavior in external fields of 14 T. The drop in resistivity which is particularly observable in the 2 T data might resemble the behavior of $PrCu_3Ru_4O_{12}$. However, none of the $J = 9/2$ multiplets of the Nd^{3+} ion in a cubic

6 Note that the notation of the eigenstates Γ_i here is that of Ref. [127].

crystal field is non-magnetic [127, 180, 187] so that an explanation in terms of a reduced scattering probability of the conduction electrons has to be questioned in $NdCu_3Ru_4O_{12}$. Fig. 7.20 shows the resistivity difference $\Delta\rho$ which remains after subtraction of the Fermi-liquid fit to the zero-field data. For magnetic fields smaller than 6 T it exhibits a small and broad maximum as it is the case for $PrCu_3Ru_4O_{12}$. The maximum vanishes in a field of ≈ 6 T and simultaneously, $\Delta\rho$ develops a linear dependence for both a high temperature ($T > 15$ K) and a low temperature regime ($T < 8$ K). As in $PrCu_3Ru_4O_{12}$ this effect is attributed to the Zeeman splitting of the CEF levels of the Nd^{3+} ion.

A well-established way to classify (correlated) metals is to calculate their Kadowaki-Woods ratio $R_{KW}(=A/\gamma^2)$.[46, 47] It compares the coefficient A due to electron-electron scattering of a metal's low-temperature resistivity ($\rho(T) = \rho_0 + AT^2$) to the Sommerfeld coefficient γ of its electronic heat capacity $C(T) = \gamma T$ - both predicted by Fermi-liquid theory - in order to examine the relationship between the electron-electron scattering rate and the renormalization of the electron mass. Notably, it exhibits a constant universal value, at least within a certain class of materials: It was found that in a number of transition metals [46] (see empty upside down triangles in Fig. 5.21) R_{KW} takes the universal value of $4 \cdot 10^{-7}\,\mu\Omega\mathrm{cmK^2mol^2/mJ^2}$. Later, many f-electron heavy-fermion compounds were identified to have an enhanced universal value of $R_{KW} = 10^{-5}\,\mu\Omega\mathrm{cmK^2mol^2/mJ^2}$ even though γ varies by more than one order of magnitude in these materials (see empty circles in Fig. 5.21). Similarly to the above mentioned transition metals, many Yb-based compounds [117] also show up with a universal value of $R_{KW} = 4 \cdot 10^{-7}\,\mu\Omega\mathrm{cmK^2mol^2/mJ^2}$ (see empty squares in Fig. 5.21). Several efforts have been made to define more universal versions of the Kadowaki-Woods ratio in order to include different material classes in a single consistent model [118, 119, 120], however, the original definition is used here to classify the copper-ruthenates. The calculated ratios[7] R_{KW} of $ACu_3Ru_4O_{12}$ (A = Na, Ca, Sr, La, Pr, Nd) are listed in Table 5.21 and manifest values lower than in classic f-electron systems and (except for $PrCu_3Ru_4O_{12}$) slightly higher than in d-electron metals. All compounds are well concentrated in the center of the Kadowaki-Woods plot (see full symbols in Fig. 5.21) with $A \approx 10^{-2}\,\mu\Omega\mathrm{cm/K^2}$ and $\gamma \approx 10^2\,\mathrm{mJ/molK^2}$. Other prominent examples of d-electron based HF metals (see empty upright triangles in Fig. 5.21) exhibit significantly higher Kadowaki-Woods ratios and also vary strongly regarding the values of A and γ. It seems noteworthy that in the filled skutterudites [168] which are structurally

7 Note that the values of γ are derived from fits to the low-temperature specific heat (see chapter 5.4).

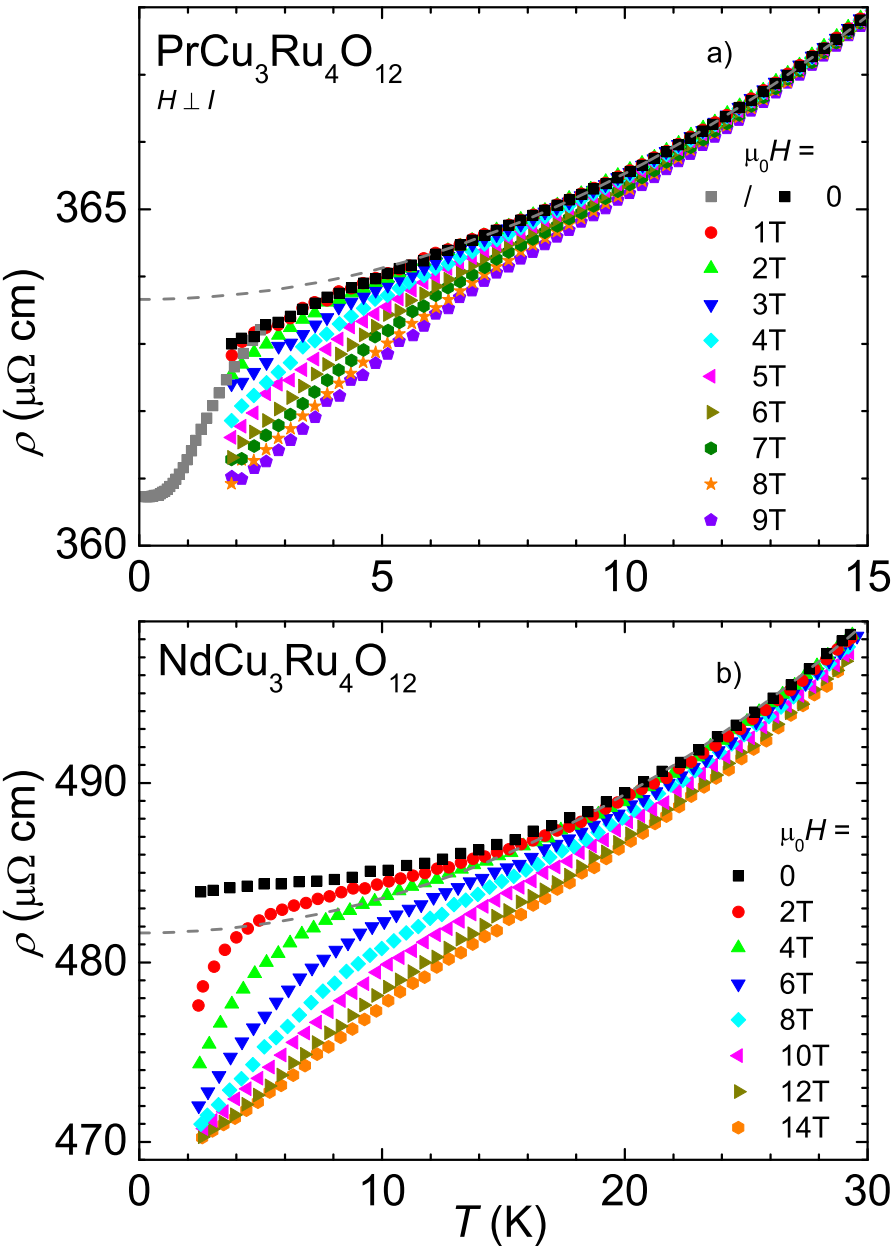

Figure 5.20: Low-temperature resistivity of polycrystalline $PrCu_3Ru_4O_{12}$ (frame a) and $NdCu_3Ru_4O_{12}$ (frame b) in various magnetic fields. The grey dashed curves are fits to the zero field data according to Fermi-liquid theory: $\rho(T) = \rho_0 + AT^2$.

closely related to $A Cu_3Ru_4O_{12}$ (A = Na, Ca, Sr, La, Pr, Nd) and also show heavy-fermion behavior,[189, 190] the Kadowaki-Woods ratio A/γ^2 is reduced [191] from the universal value by roughly one order of magnitude.

Additional resistivity measurements on three $CaCu_3Ru_4O_{12}$ single crystals (see Figs. 5.22 and 5.23) from two different batches (named "Flux1" and "CaCRHC2") reveal that the dependence of the resistivity of $CaCu_3Ru_4O_{12}$ seems to vary not only from batch to batch but also within a batch.[8]

Fig. 5.22 (upper frame) shows an exemplar (named "Flux1-Kondo") with a linear metallic dependence between RT and 50 K and a roughly ten times lower residual resistance ratio (RRR = 1.5) than that of the polycrystalline sample. At 10 K a Kondo-like resistance minimum with a logarithmic increase toward low temperatures is observed, as predicted for dilute magnetic alloys.[90] In the respective inset the resistivity is plotted on a semi-logarithmic scale with a corresponding fit (dashed line) according to $\rho(T) = \rho_0 - A \ln T$ (ρ_0 = 15.0 mΩcm, $A = 6.97 \cdot 10^{-2}$ mΩcm). The logarithmic dependence holds for one decade between 2 K and 0.2 K whereas at its lower limit the resistivity begins to saturate to a value of 15.1 mΩcm. The behavior at lowest temperatures can be described by a negative parabolic dependence $\rho(T) = \rho_0 - AT^2$ (dotted curve) with $A = -8.57 \cdot 10^{-4}\,\Omega\mathrm{cm/K^2}$ as observed in CuFe alloys [192, 193] and explained in terms of a quasi-bound state between the conduction-electron spin and the localized spin.[194] In a variational Kondo picture similar results were found.[195] The resistivity has also been measured in a magnetic field of 14 T revealing no significant deviation from the zero-field data from RT down to 10 K. At this temperature also the 14 T data shows a minimum but with a much stronger logarithmic increase toward low temperatures.

Another specimen from the batch "CaCRHC2" also shows metallic behavior down to 20 K (see lower frame of Fig. 5.22) though with a more complex temperature dependence involving several changes in curvature and an even lower residual resistance ratio (RRR = 1.35). At least four jump discontinuities might indicate residual stress within the sample leading to abrupt changes in resistivity. As depicted in the inset, a broad Kondo-like minimum of the resistivity also arises here but at a slightly higher temperature (T = 17 K).

8 Note that the determination of the geometry for conversion from resistance to resistivity is difficult for an irregularly shaped and not perfectly grown crystal. Thus, the absolute values of the resistivity may vary extensively.

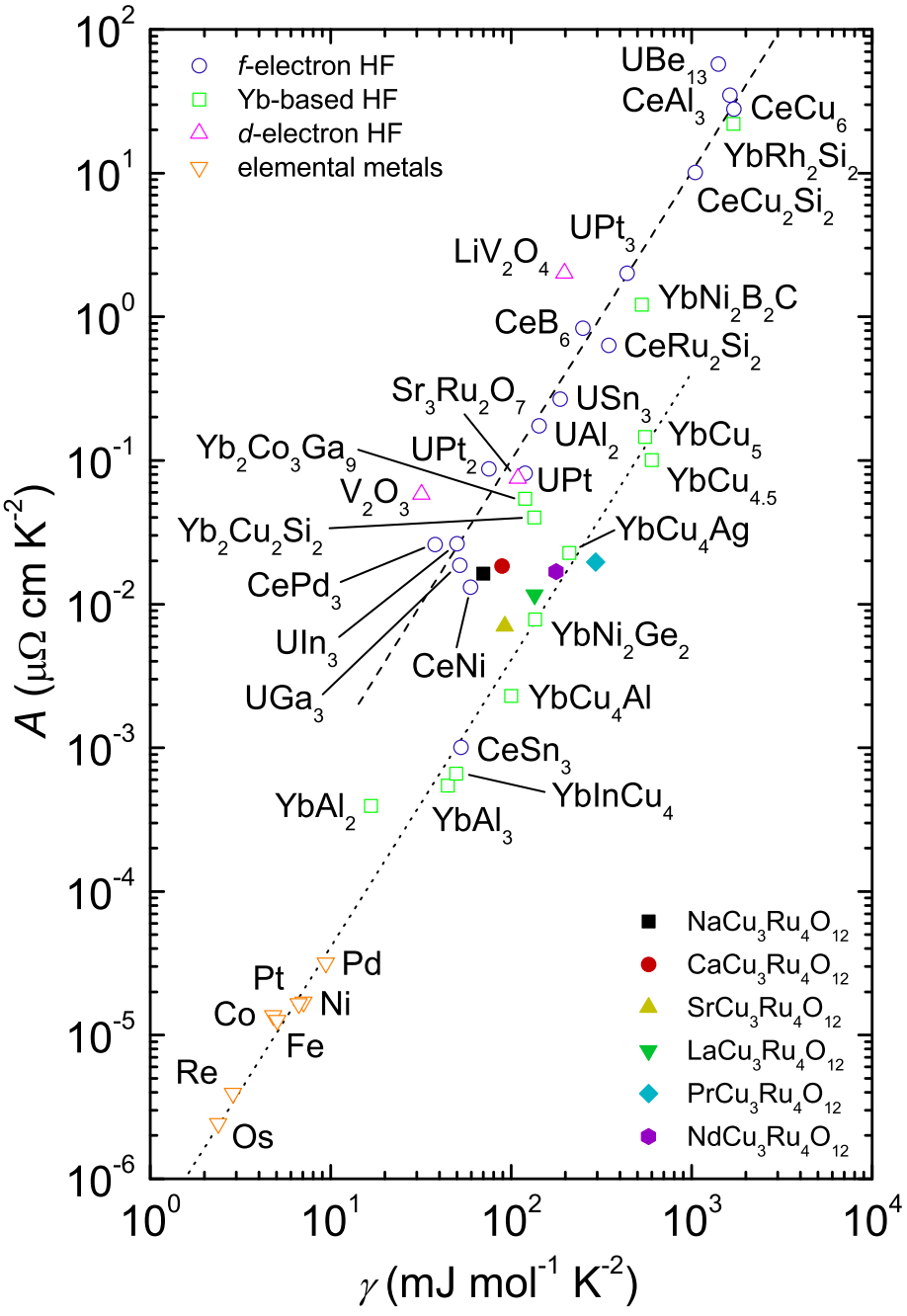

Figure 5.21: Double-logarithmic plot of the coefficient A of the quadratic contribution to the resistivity vs. Sommerfeld coefficient γ (Kadowaki-Woods ratio R_{KW}) for various heavy-fermion compounds including $A\mathrm{Cu_3Ru_4O_{12}}$ (A = Na, Ca, Sr, La, Pr, Nd). The straight lines correspond to Kadowaki-Woods ratios $R_{\mathrm{KW}}(=A/\gamma^2)$ [47] of $10^{-5}\,\mu\Omega\mathrm{cmK^2mol^2/mJ^2}$ (dashed line) and $4{\cdot}10^{-7}\,\mu\Omega\mathrm{cmK^2mol^2/mJ^2}$ (dotted line). Diagram based on Refs. [46, 47, 117].

As demonstrated by a fit according to $\rho(T) = \rho_0 - A \ln T$ ($\rho_0 = 107\,\mathrm{m\Omega cm}$, $A = 0.501\,\mathrm{m\Omega cm}$) a logarithmic divergence is present as in the crystal mentioned above, albeit within a narrower temperature range ($6\,\mathrm{K} < T < 12\,\mathrm{K}$).

A second crystal from the batch Flux1 (named "Flux1-linear") strongly resembles the polycrystalline sample in temperature dependence (see inset of the upper frame of Fig. 5.23, compare to Fig. 5.16). It features the largest residual resistance ratio ($RRR = 5.3$) and the lowest absolute value ($\rho_0 = 234\,\mu\Omega\mathrm{cm}$) among the single crystals. Fig. 5.23 (upper main frame) shows zero-field data as well as data in fields of 6 T and 9 T. Evidently, a positive MR effect occurs as in the polycrystalline sample and for $10\,\mathrm{K} < T < 30\,\mathrm{K}$ all data sets can be fitted according to a power law $\rho(T) = \rho_0 + AT^n$ (solid curve: zero-field, dashed curve: 6 T, dotted curve: 9 T) revealing a nearly quadratic behavior as predicted by Fermi-liquid theory ($n = 2.15 \pm 0.05$, $A = 14.5 \pm 2.5\,\mathrm{n\Omega cm/K^{2.15}}$). A closer look to lower temperatures is provided in the lower frame of Fig. 5.23. Here, data is plotted below 10 K from zero-field up to 9 T in steps of 1 T including the above mentioned fits. Significant deviations from the polycrystalline data and therefore from a Fermi liquid behavior (T^2 power law) are found for the zero-field data below $\approx 7\,\mathrm{K}$. Actually, for $T < 2.5\,\mathrm{K}$ the ZF resistivity shows a positive linear dependence over almost two decades as illustrated by a corresponding fit (dash-dotted line, lower frame) according to $\rho(T) = \rho_0 + AT$ with $A = 183\,\mathrm{n\Omega cm/K}$. Such a behavior was also found in the heavy-fermion f-electron systems $CeCu_{5.9}Au_{0.1}$ [40], $U_{0.9}Th_{0.1}Be_{13}$ [196], $YbRh_2Si_2$ [197], and $U_{0.2}Y_{0.8}Pd_2Al_3$ [198]. The temperature range for which this linearity of the resistivity holds also encompasses the temperature range over which NFL behavior is observed in NQR measurements revealing deviations from a Korringa behavior of the spin-lattice relaxation rate [57] and in specific-heat measurement of polycrystalline $CaCu_3Ru_4O_{12}$ (see chapter 5.4). Moreover, the application of a magnetic field leads to a gradual recovery of a T^2 law as obvious from a comparison of the 6 T and 9 T data to their respective Fermi-liquid fits (dashed/dotted curves, lower frame). Apparently, the data more and more approaches the Fermi-liquid dependence from below as the magnetic field is increased resulting in an almost full recovery for $\mu_0 H = 9\,\mathrm{T}$. Such a behavior was also observed in $CeCu_{5.9}Au_{0.1}$ [40] and in $YbRh_2Si_2$ [197], the former compound with a somewhat different evolution of the T-dependence.

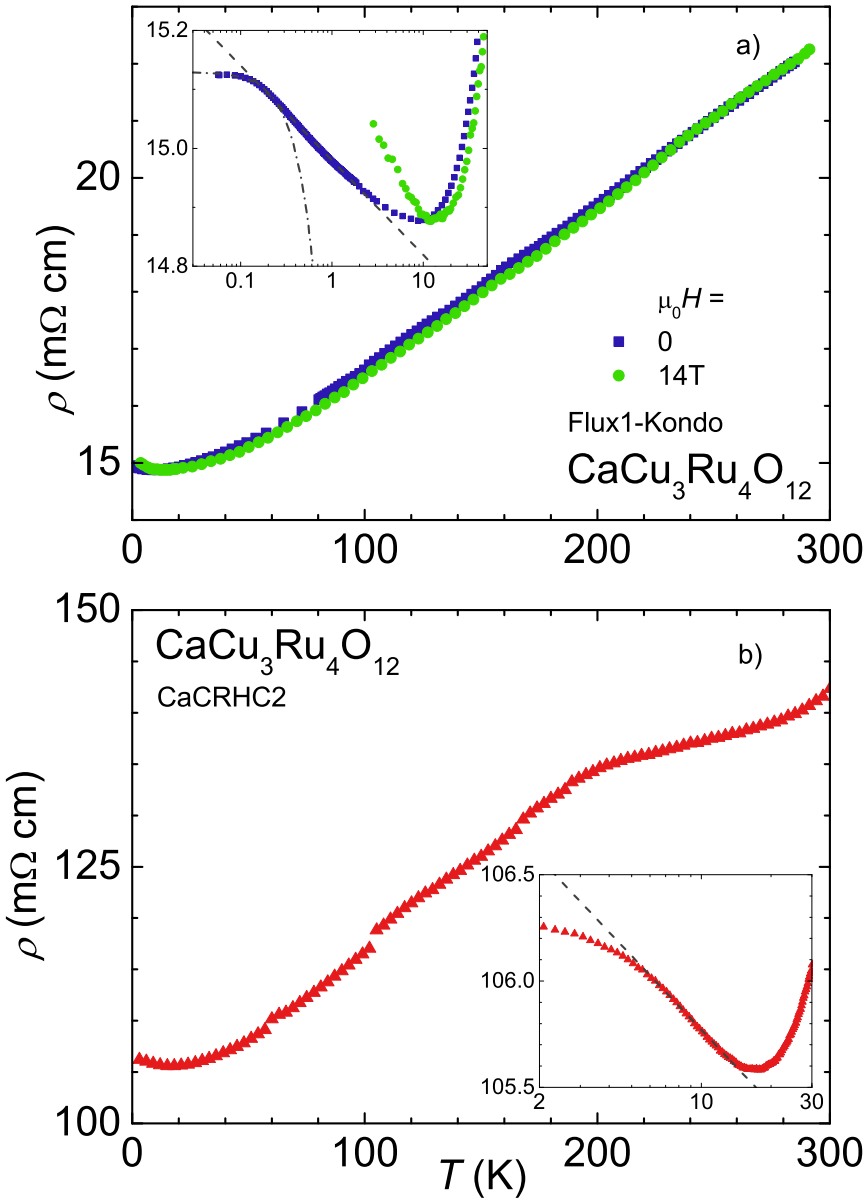

Figure 5.22: Temperature dependent resistivity $\rho(T)$ of two different $CaCu_3Ru_4O_{12}$ single crystals named "Flux1-Kondo" (frame a) and "CaCRHC2" (frame b). The insets show data on an enhanced semi-logarithmic scale. The dashed/dash-dotted curves are fits described in the text.

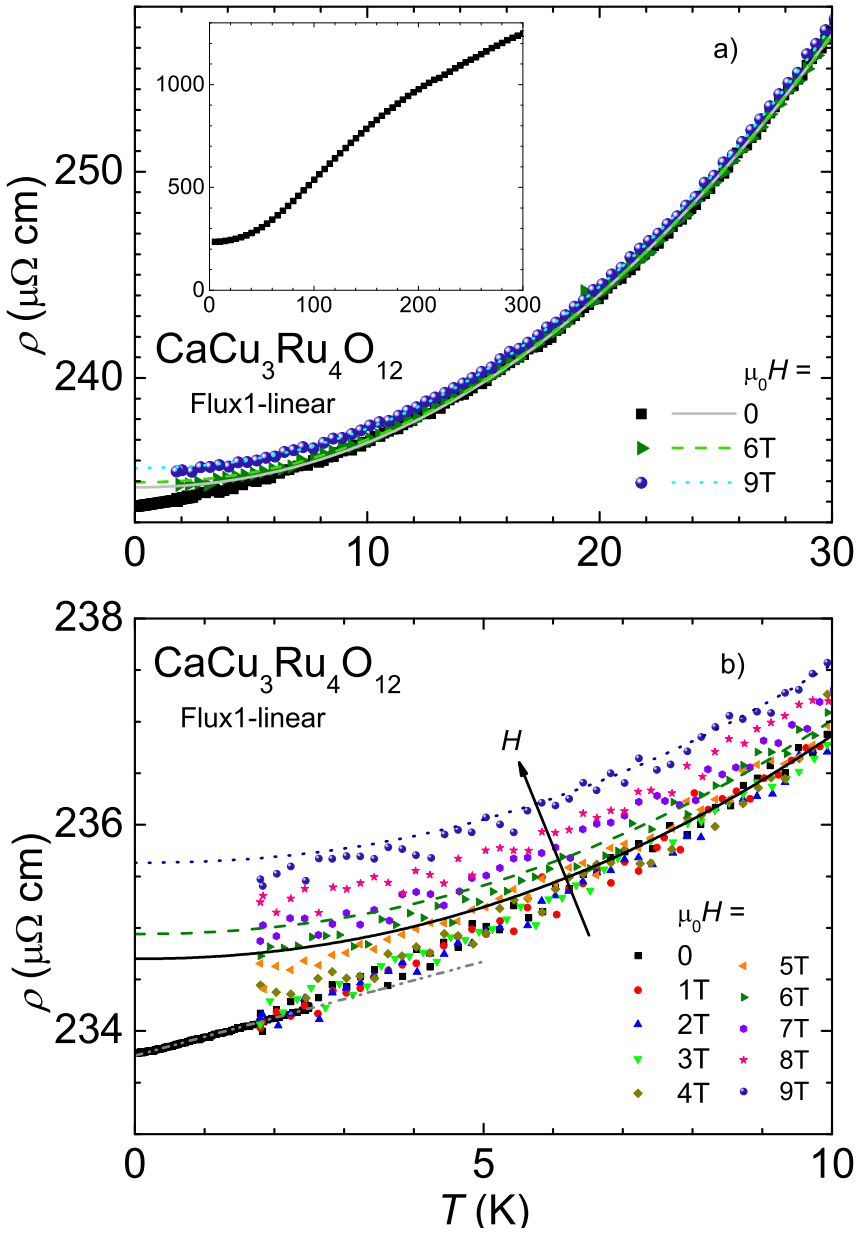

Figure 5.23: Temperature dependent resistivity $\rho(T)$ of a $CaCu_3Ru_4O_{12}$ single crystal named "Flux1-linear" on different temperature scales for various magnetic fields. In frame a data is plotted on an enhanced scale and on a full scale (inset). Frame b shows data below 10 K. Both main frames include fits according to Fermi-liquid theory (solid curve: zero field, dashed curve: 6 T, dotted curve: 9 T) and a fit to a linear dependence (dash-dotted line, lower frame). The arrow in the lower frame indicates the development of the resistivity with increasing magnetic field H. See text for details.

5.4 Specific Heat

The heat capacity of ACu$_3$Ru$_4$O$_{12}$ (A = Na, Ca, Sr, La, Pr, Nd) in the representation C/T vs. T is plotted in Fig. 5.24 for $2\,\mathrm{K} < T < 300\,\mathrm{K}$. In the compounds with non-magnetic A-site ions, ACu$_3$Ru$_4$O$_{12}$ (A = Na, Ca, Sr, La), it exhibits a conventional behavior of metallic Fermi liquids with no anomalies occurring on a full T scale. In the $4f$-electron systems, ACu$_3$Ru$_4$O$_{12}$ (A = Pr, Nd), the same statement holds except for a pronounced upturn at low temperatures which is indicative of a change in the population of the crystal-field-split $4f$ states of Pr^{3+} and Nd^{3+}. Such a contribution is visible in this representation because the electronic term ($C_{\mathrm{el}} = \gamma T$) is reduced to a constant value and the phonons are almost frozen out at such low temperatures. A detailed analysis of the CEF properties will be given later in this chapter. The Fermi-liquid state is explicitly visible in a plot of C/T vs. T^2 with corresponding fits for $T < 25\,\mathrm{K}$ according to $C/T = \gamma + \beta T^2$ (see Fig. 5.25). The resulting electronic contribution described by the Sommerfeld coefficient γ and the phononic contribution β implicitly containing the Debye temperature θ_{D} are listed in Table 5.7. The electronic specific heat and hence also the effective electron mass m^* are enhanced - compared to conventional metals - with values of γ between $72\,\mathrm{mJmol^{-1}K^{-2}}$ (NaCu$_3$Ru$_4$O$_{12}$) and $294\,\mathrm{mJmol^{-1}K^{-2}}$ (PrCu$_3$Ru$_4$O$_{12}$). These moderately enhanced values are characteristic for a correlated metal and in agreement with previous reports.[30, 33, 58, 65, 60] Note that the enhanced Sommerfeld coefficients of the Pr and the Nd compound may partly result from contributions of low-lying CEF levels. The Debye temperatures vary only slightly ($162\,\mathrm{K} < \theta_{\mathrm{D}} < 188\,\mathrm{K}$) and are used in a numerical fit to the specific heat including a fixed Debye term[9], a fixed electronic contribution with the γ coefficient determined above, as well as various Einstein terms, each with an associated Einstein temperature and corresponding degrees of freedom. The results are shown as solid curves in Fig. 5.24 with the fitting parameters listed in Table 5.7. For all compounds a good description of the specific heat is achieved with a fixed electronic term, a fixed Debye term, and two Einstein terms. In total, the degrees of freedom should amount $3 \cdot 20 = 60$ per f.u., but reach only slightly more than 50 ($= a+b+c$). All compounds possess one Einstein term with θ_{E} around 250 K and roughly 20 degrees of freedom and a further one with θ_{E} around 600 K and roughly 30 degrees of freedom. These values agree

9 Note that the degrees of freedom for the Debye term is fixed to three, corresponding to three acoustic phonon modes.

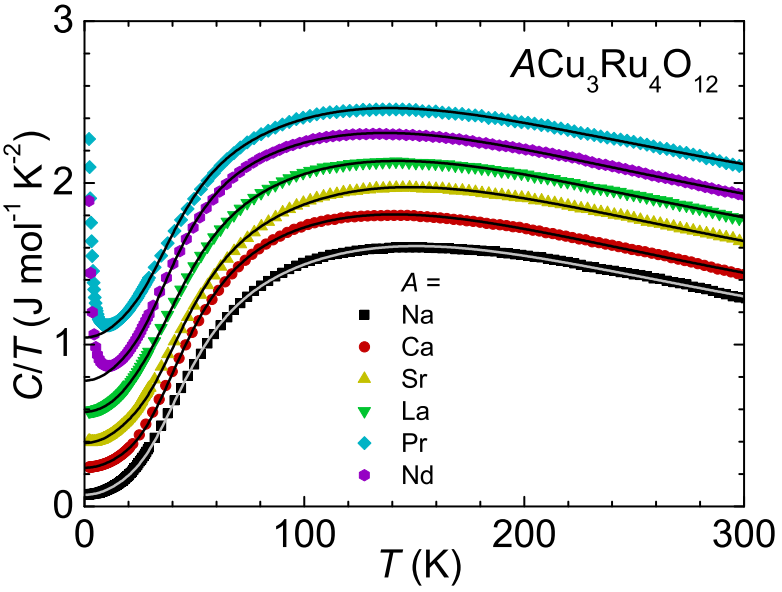

Figure 5.24: Temperature dependent specific heat of polycrystalline $A\mathrm{Cu_3Ru_4O_{12}}$ (A = Na, Ca, Sr, La, Pr, Nd) in the representation C/T vs. T. The data are shifted for clarity (Ca: +0.15, Sr: +0.3, La: +0.45, Nd: +0.6, Pr: +0.75, in units of $\mathrm{Jmol^{-1}K^{-2}}$). The solid curves are fits including an electronic as well as Debye- and Einstein-contributions. See text for details.

reasonably well with the results from the measurements of the temperature dependent lattice constant by neutron diffraction where average Einstein temperatures of ≈ 390 K have been derived (see chapter 5.1.2). Regarding the behavior of the specific heat in an external magnetic field, measurements on $A\mathrm{Cu_3Ru_4O_{12}}$ (A = Na, Ca, Sr, La) do not show any shift for $2\,\mathrm{K} < T < 20\,\mathrm{K}$ in fields up to 9 T (5 T in the case of $\mathrm{NaCu_3Ru_4O_{12}}$).

Looking closer at the specific heat of $\mathrm{CaCu_3Ru_4O_{12}}$ below 20 K, the Fermi-liquid behavior with a dependence according to $C/T = \gamma + \beta T^2$ (see dashed curve in Fig. 5.26) is lost at ≈ 2 K. Below, a logarithmic divergence ($C/T \propto -\ln T$) is visible as a linear increase toward absolute zero on a logarithmic T-scale (green spheres in Fig. 5.26). To account for nuclear contributions C_{nuc} to the specific heat, the corresponding nuclear Schottky anomalies (see chapter 3.2.4) for all relevant isotopes are calculated using the parameters listed in Table 5.8. The accurate values of the electric field gradients V_{zz} at the Cu and Ru sites have been established by NQR previously [57] whereas V_{zz} of Ca-43 is fixed to the value at the Ru site. NQR experiments also show neither a significant

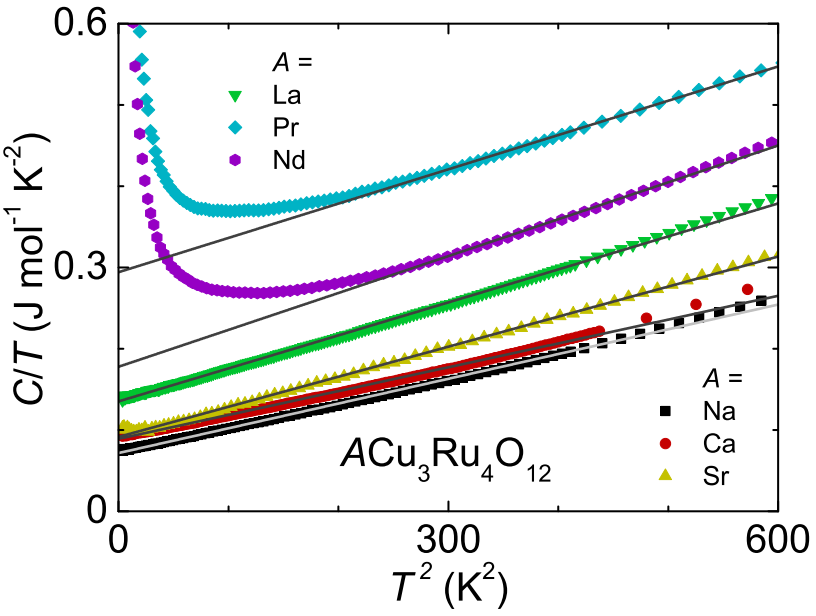

Figure 5.25: Temperature dependent specific heat of polycrystalline $A\mathrm{Cu_3Ru_4O_{12}}$ (A = Na, Ca, Sr, La, Pr, Nd) in the representation C/T vs. T^2. The solid lines are fits according to $C/T = \gamma + \beta T^2$ for conventional Fermi-liquid behavior (see Table 5.7).

A	γ (mJmol^{-1}K^{-2})	β (10^{-4} Jmol^{-1}K^{-4})	$a \cdot \theta_D$ (K)	$b \cdot \theta_{E1}$ (K)	$c \cdot \theta_{E2}$ (K)
Na	72	3.05	3·186	20.1·255	31.2·616
Ca	89	2.93	3·188	21.0·250	28.5·601
Sr	92	3.70	3·174	21.0·255	31.2·610
La	135	4.06	3·169	19.5·257	28.8·605
Pr	294	4.22	3·166	16.5·234	26.7·563
Nd	178	4.54	3·162	18.3·231	28.5·572

Table 5.7: Sommerfeld coefficient γ, Debye coefficient β, and corresponding Debye temperature θ_D resulting from fits to the specific heat of polycrystalline $A\mathrm{Cu_3Ru_4O_{12}}$ (A = Na, Ca, Sr, La, Pr, Nd) below 25 K according to Fermi-liquid behavior: $C/T = \gamma + \beta T^2$ (see Fig. 5.25). The Debye temperature is used as constant value in a fit extended to the full T scale for the determination of further phononic contributions in terms of Einstein temperatures θ_E. The prefactors a, b, and c represent the degrees of freedom which in total amount 60 theoretically, namely three translatory directions of motion times 20 atoms/f.u.

Isotope	x (%)	c (1/f.u.)	I (ħ)	μ (μ_N)	Q (10^{-28} m^2)	V_{zz} (10^{22} V/m^2)
Ca-43	0.135	0.135	7/2	-1.4941	0.0408	0.73
Cu-63	69.170	2.076	3/2	2.8750	-0.2200	0.73
Cu-65	30.830	0.924	3/2	3.0747	-0.2040	0.73
Ru-99	12.760	0.510	5/2	-0.7588	0.0790	0.43
Ru-101	17.060	0.682	5/2	-0.8505	0.4570	0.43

Table 5.8: Natural abundance x in % of all occurrent isotopes of the respective element, concentration c within $CaCu_3Ru_4O_{12}$, nuclear spin I, nuclear magnetic moment μ, quadrupole moment Q, and internal electric field gradient V_{zz} for all isotopes in $CaCu_3Ru_4O_{12}$ relevant for the calculation of the nuclear specific heat. The parameters x, I, μ, and Q are isotope-specific literature values from Ref. [203] (see also Ref. [204]), c and V_{zz} are compound-specific.

line broadening nor a temperature-dependent line shift, such that residual internal fields can be excluded and are set to zero for the calculations. C_{nuc} is then subtracted from the raw data of $CaCu_3Ru_4O_{12}$ resulting in the dataset represented by blue squares in Fig. 5.26. Within the corrected data, a logarithmic dependence is obvious in C/T from a fit according to $C/T = -\alpha \ln(T/T_0) + \gamma + \beta T^2$ with the parameters γ and β being fixed to the values listed in Table 5.7. The resulting fit parameters are correlated and amount $\alpha = 16.4\,\mathrm{mJmol^{-1}K^{-2}}$ and $T_0 = 2.0\,\mathrm{K}$. Usually, the presence of such a behavior over at least one temperature decade - which is fulfilled here from 2 K down to 0.2 K - is regarded as a hallmark for non-Fermi liquid behavior. This temperature range also roughly covers the range over which NFL behavior is observed in NQR measurements on powder revealing deviations from a Korringa behavior of the spin-lattice relaxation rate [57] and in resistivity measurements on a single crystal (see chapter 5.3). However, below 0.1 K, the values of the corrected heat capacity still lie above the expected logarithmic increase. Such unexplained upturns in C/T have been observed in a number of other heavy-fermion compounds, too.[199, 200, 201, 202, 197]

An almost identical behavior can be observed in $SrCu_3Ru_4O_{12}$ (see Fig. 5.27), although the measurement is relatively noisy. For both the measurement in the PPMS (yellow triangles) and in the dilution refrigerator (blue squares), powdered $SrCu_3Ru_4O_{12}$ was pressed into pellets with cellulose as binder (see chapter 4.1). The contribution of the cellulose is automatically subtracted as addenda from the PPMS data (see chapter 4.4) while for the subtraction from the data obtained in the dilution refrigerator the specific

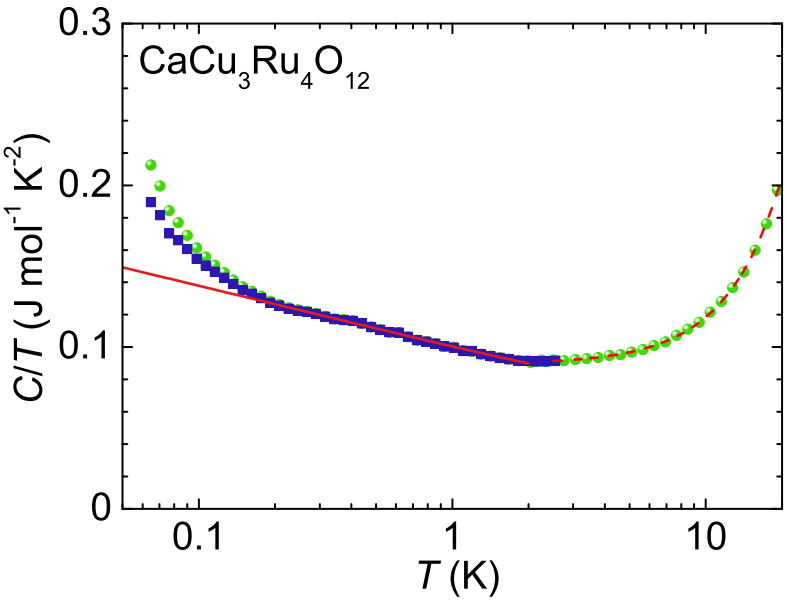

Figure 5.26: Temperature dependent specific heat of polycrystalline $CaCu_3Ru_4O_{12}$ in the representation C/T vs. T on a semi-logarithmic plot (green spheres). The nuclear contribution to the specific heat has been subtracted from the measured data with the remaining part shown as blue squares. The dashed curve represents a fit to $C/T = \gamma + \beta T^2$ with the parameters γ and β as listed in Table 5.7. The solid line is a NFL fit according to $C/T = -\alpha \ln(T/T_0) + \gamma + \beta T^2$ with the above mentioned parameters γ and β being fixed.

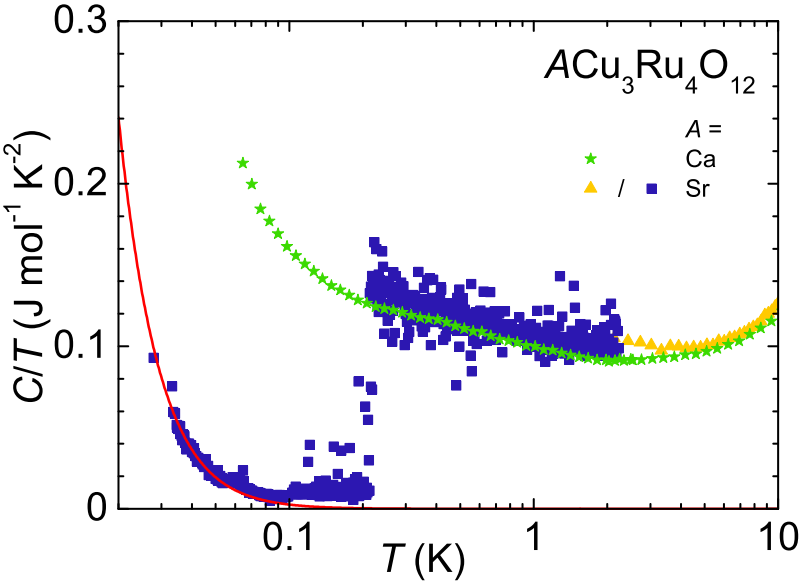

Figure 5.27: Temperature dependent specific heat in the representation C/T vs. T of polycrystalline $ACu_3Ru_4O_{12}$ (A = Ca, Sr) on a semi-logarithmic plot. The data of $SrCu_3Ru_4O_{12}$ is obtained from measurements in a PPMS (yellow triangles) and in a dilution refrigerator (blue squares). The data of $CaCu_3Ru_4O_{12}$ (green stars, see also Fig. 5.26) is shown for comparison. In $SrCu_3Ru_4O_{12}$, a sharp drop at 200 mK is observed both in C as well as C/T but its origin remains unclear.

heat of the cellulose is extrapolated to absolute zero by fitting its available data to a T^3 law between 2 K and 5 K. The specific heat of $SrCu_3Ru_4O_{12}$ nearly follows that of $CaCu_3Ru_4O_{12}$ (green stars, shown as reference material) down to 0.2 K including the same logarithmic divergence for 0.2 K < T < 2 K. Below 0.2 K a sharp drop both in C as well as C/T is present, however, an intrinsic origin is somewhat questionable and is more likely related to the measurement apparatus with the exact cause remaining unknown. Following C/T further below 0.2 K then - in principle - a reasonable dependence (except for the magnitude) is visible with an increase which can be described with a power law according to $C/T \propto T^{-2}$ characteristic for the high-temperature shoulder of a Schottky peak originating from nuclear contributions (red solid curve). Due to the problematic data situation a detailed evaluation of the low-temperature specific heat of $SrCu_3Ru_4O_{12}$ is omitted.

Regarding the structural anomaly discovered in the temperature dependent lattice constant (see chapter 5.1.2), a detailed investigation of the specific heat has been performed in the related temperature range. In Fig. 5.28 data obtained on heating (red upright triangles) is shown on a full scale in the representation C/T vs. T including a numerical fit (black solid curve) which comprises an electronic contribution as well as Debye- and Einstein terms as described before in this chapter. This fit is then subtracted from the specific heat data obtained both on heating (red upright triangles) and cooling (blue upside down triangles) runs. The resulting difference is shown on an expanded scale in a restricted T-range in the inset of Fig. 5.28 revealing a small but significant peak at around 145 K and a width of roughly 15 K. As observed in the NPD experiments, no significant hysteresis effects are visible resulting in an associated entropy of $S \approx 70\,\mathrm{mJmol^{-1}K^{-1}}$ for both data sets and thus pointing toward a second order phase transition. As mentioned in chapter 5.1.2 this again confirms the small size of the effect associated with that entropy.

As mentioned in sections 5.1.1 and 5.1.2, $A\mathrm{Cu_3Ru_4O_{12}}$ (A = Na, Ca, Sr, La, Pr, Nd) crystallizes in a body-centered cubic lattice with space group $Im\bar{3}$ (T_h^5) and a local symmetry of the A-site (and thus the CEF symmetry for this site) represented by the cubic point group $m\bar{3}$ (T_h). According to calculations by LLW,[127] the Hund's rule ground state of Pr^{3+} ($^3H_4$) in a cubic CEF is split into a non-magnetic singlet Γ_1, a non-magnetic doublet Γ_3, and two magnetic triplets $\Gamma_{4,5}$. For the Kramers ion Nd^{3+} ($^4I_{9/2}$) the presence of such a CEF causes its eigenstates to split into an evenly degenerate manner (i.e. at least doubly): into one magnetic doublet Γ_6 and two magnetic quartets $\Gamma_8^{(1,2)}$. For both Pr^{3+} and Nd^{3+} the CEF potential is affected by three parameters: an unbounded stretching factor W which expands the ladder of the CEF levels, and two bounded weighting factors x, y ($|x|$, $|y| \leq 1$).[205, 187] The appropriate J-manifold diagrams of LLW can then be used as a guide to determine the possible ground state/term scheme for $\mathrm{PrCu_3Ru_4O_{12}}$ and $\mathrm{NdCu_3Ru_4O_{12}}$.[10] In the following a closer look is taken at the specific heat of $\mathrm{PrCu_3Ru_4O_{12}}$ and $\mathrm{NdCu_3Ru_4O_{12}}$ in terms of such effects.

A detailed analysis of the specific heat of $\mathrm{PrCu_3Ru_4O_{12}}$ is provided in Fig. 5.29. Frame a shows the zero-field data on a logarithmic T-scale including three data sets: 1. raw data (grey squares); 2. data corrected for an electronic C_{el}, a phononic C_{phonon}, and a nuclear

10Note that the J-manifold diagrams of LLW do not include the CEF parameter y (Ref. [187]) but correspond to the limit of $y \to 0$.

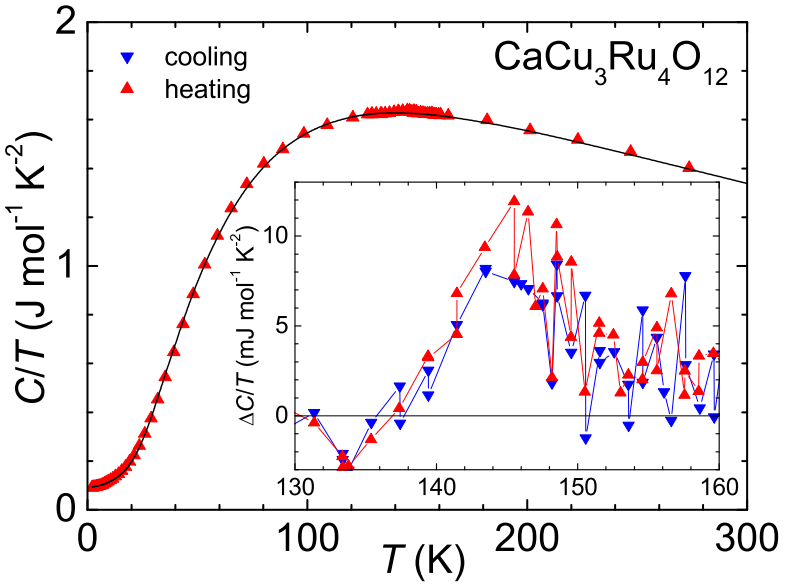

Figure 5.28: Temperature dependent specific heat of polycrystalline $CaCu_3Ru_4O_{12}$ in the representation C/T vs. T obtained on heating (red upright triangles). A numerical fit including an electronic contribution as well as Debye- and Einstein terms is shown as black solid curve and subtracted from the raw data. The resulting difference is shown in the inset for data obtained on heating (red upright triangles) and cooling (blue upside down triangles) runs including lines to guide the eye and a straight line at $C/T = 0$.

term C_{nuc} (green circles); 3. data corrected for the non-magnetic reference compound $LaCu_3Ru_4O_{12}$ (blue triangles). Set 1 combines data acquired in a PPMS ($T > 2\,\mathrm{K}$) and in a dilution refrigerator ($T < 2\,\mathrm{K}$) clearly revealing a Schottky-like anomaly at around 2 K. Such a phenomenon is visible here even in the raw data as both the electronic and the lattice contribution are comparably small at this temperature. Still, for a substantiated evaluation, the electronic and lattice contribution as determined by a fit according to $C/T = \gamma + \beta T^2$ (see Fig. 5.25 and Table 5.7) as well as the nuclear contribution C_{nuc} have been subtracted from the raw data resulting in data set 2. The nuclear term C_{nuc} is determined by calculating the corresponding nuclear Schottky anomalies (see chapter 3.2.4) for all relevant isotopes using the parameters listed in Table 5.9 including a global internal magnetic field $B_{\mathrm{g}} = 11.3\,\mathrm{T}$. The values of the electric field gradients V_{zz} at the Cu and Ru sites have been established in the Ca homologue by NQR previously [57] and serve here as an upper bound. V_{zz} at the Pr site is set to that at the Cu site, as carried out for Ca in $CaCu_3Ru_4O_{12}$. C_{nuc} turns out to be significant only well below 0.4 K such that the procedure of extracting data set 2 is valid up to temperatures of $\approx 20\,\mathrm{K}$ at which the low-temperature approximation $C_{\mathrm{phonon}} = \beta T^3$ looses its validity and the corrected data turns to negative C values. The third data set is generated by subtracting the specific heat of the non-magnetic reference compound $LaCu_3Ru_4O_{12}$ from that of $PrCu_3Ru_4O_{12}$ which is expected to cancel out both electronic and lattice contributions and to carve out further suspected contributions at higher temperatures. Here, the data is limited to the PPMS temperature range and data above 200 K is omitted due to strong noise. As can be seen from Fig. 5.29a, the progression of data set 2 is substantially different from that of set 3, at least for $2\,\mathrm{K} < T < 20\,\mathrm{K}$. Generally speaking, both methods are best practice, and obviously both methods produce smooth and plausible data such that it is not 100% clear if different contributions of the conduction electrons and/or the lattice between $LaCu_3Ru_4O_{12}$ and $PrCu_3Ru_4O_{12}$ can be used to explain the discrepancies. Nonetheless, an attempt is being made to involve all facts within the evaluation.

The lowest visible peak with a maximum at 1.5 K in the corrected data is obviously related to the transition from the lowest to the first excited CEF level of the Pr^{3+} multiplet. When applying magnetic fields this peak is continuously shifted to higher temperatures with increasing field, a consequence of the Zeeman splitting of the $4f$ multiplet which is nicely illustrated in Fig. 5.29b. The corresponding entropy S is calculated by integration of the corrected experimental data (data set 2) divided by temperature with respect to

temperature: $S = \int_{T_1}^{T_2} C/T \, \mathrm{d}T$. Fig. 5.30 shows that S reaches a plateau of $\mathrm{R}\ln 2$ at 4 K in zero field (green dashed curve). Due to the lack of data below 2 K in magnetic fields and in order to get comparable quantities, the specific heat is extrapolated with a straight line from the lowest available data point to absolute zero. For the 9 T data this means that S reaches $\mathrm{R}\ln 2$ at 20 K (red dotted curve). Independently, the zero-field data corrected for the specific heat of $LaCu_3Ru_4O_{12}$ has also been used to calculate the entropy. Here, an extrapolation of the specific heat with a straight line to absolute zero has been included, too. As already obvious from the specific heat (see Fig. 5.29a), and despite the just mentioned correction, this entropy shows a different progression (solid blue curve in Fig. 5.30). It does not show a distinct plateau-like feature and reaches $\mathrm{R}\ln 2$ only at ≈ 14 K but still changes its curvature once more which might indicate corresponding changes in the population of the CEF states. As far as can be stated from the available data, the entropy associated with the CEF begins to level off slightly below $\mathrm{R}\ln 9$ at around 200 K which is also the high-temperature limit for the 9-fold degenerate Pr^{3+} system. This might lead to the assumption that the total splitting of the CEF is roughly of that order.

As already mentioned, the experimental entropy associated with the lowest transition amounts $\mathrm{R}\ln 2$. This means that both the ground state and the first excited state must have the same degeneracy ($g_1/g_0 = 1$). In the present case of Pr^{3+}, i.e. for the cubic point group T_h, there are two sublevels with the same degeneracy, namely the triplets $\Gamma_{4,5}$. When assuming now those two levels to be the lowest ones with a splitting of $\Delta = 3.3$ K, then a corresponding fit/simulation of the specific heat turns out to describe the lowest peak very well (see Fig. 5.29a) although the experimental data is obviously broadened toward low temperatures when compared to the fit. However, it fails for the high temperature data (corrected for $LaCu_3Ru_4O_{12}$) which are considerably underestimated although both remaining multiplets (Γ_1 and Γ_3) are manually set to a splitting of 120 K in order to get all entropy close to that temperature (see Fig. 5.29a). For that reason it is not clear if the correction for the specific heat of $LaCu_3Ru_4O_{12}$ is precise enough or if it produces artifacts interpretable as Schottky anomalies. One has to admit that the correction of the low temperature data (set 2) is the more credible one which can be supposed to be valid up to 20 K. Another argument against the approach of correcting the data by subtraction of $LaCu_3Ru_4O_{12}$ is that the experimental entropy does not go well together with the calculated one using standard theory and the same term scheme as mentioned above (see grey dash-dotted curve in Fig. 5.30). It shows reasonable agreement with the

low temperature data (green dashed curve), however, levels off already at $R \ln 3$ and fails to explain the high temperature data (blue solid curve).

Regarding the above described scenario, one has to bear in mind that the J-manifold diagram given by LLW [127] does not allow for such a level scheme, i.e. both triplets as the lowest sublevels. Even newer calculations of the CEF properties for the respective symmetry [187] - which take into account an additional CEF parameter y - do not change the CEF levels in such a way that both triplets could lie lowest. Then a much more plausible explanation for the entropy ($S = R \ln 2$) is an unusual splitting of the levels due to some effect which could be realized by, e.g., a perturbative influence on a doublet Γ_3 ground state. Such phenomena in terms of quadrupolar order have been found in several cubic Pr compounds recently.[206, 207, 208, 209, 210, 211, 212, 213]

Such an effect is substantiated by the evolution of the splitting upon increasing magnetic field. In Figs. 5.29b and 5.32b, the above mentioned fit is repeated for the specific heat of $PrCu_3Ru_4O_{12}$ and $NdCu_3Ru_4O_{12}$ in zero field (red solid curve) and for data in magnetic fields (shown only for 9 T, dashed curve) which show reasonable agreement with the experimental data. Both the parameter Δ representing the splitting of the Schottky anomaly and the manually determined temperature of the maximum T_{max} have been extracted and are shown in Fig. 5.31. While in the Pr compound, T_{max} increases weakly quadratically over the full available field range (open squares), it exhibits a regular (linear) Zeeman effect in $NdCu_3Ru_4O_{12}$ (open triangles). In the Pr compound, the splitting Δ increases quadratically only up to 2 T and changes to a linear behavior above, whereas that of the Nd compound follows a linear dependence as does T_{max}. The different field dependence of Δ and T_{max} is not quite clear, but a deviation from a regular (linear) Zeeman effect ($NdCu_3Ru_4O_{12}$, full/open triangles) toward a quadratic one ($PrCu_3Ru_4O_{12}$, full/open squares) might suspect a quadrupolar ordering as the driving force behind.

A similar behavior of the (CEF) specific heat can be observed in $NdCu_3Ru_4O_{12}$ although low-temperature data are missing and only the onset of a low-temperature peak in the experimental zero-field data can be seen (see Fig. 5.32a). Due to the fact that this peak apparently also shifts to higher temperatures with increasing fields (see data sets for 1, 3, 6, and 9 T, frame b) one can extrapolate its maximum to roughly 1 K. In the same manner as in $PrCu_3Ru_4O_{12}$, also here two corrected data sets are generated: no.1 - corrected for an electronic C_{el} and a phononic C_{phonon} contribution (green circles), no.2 -

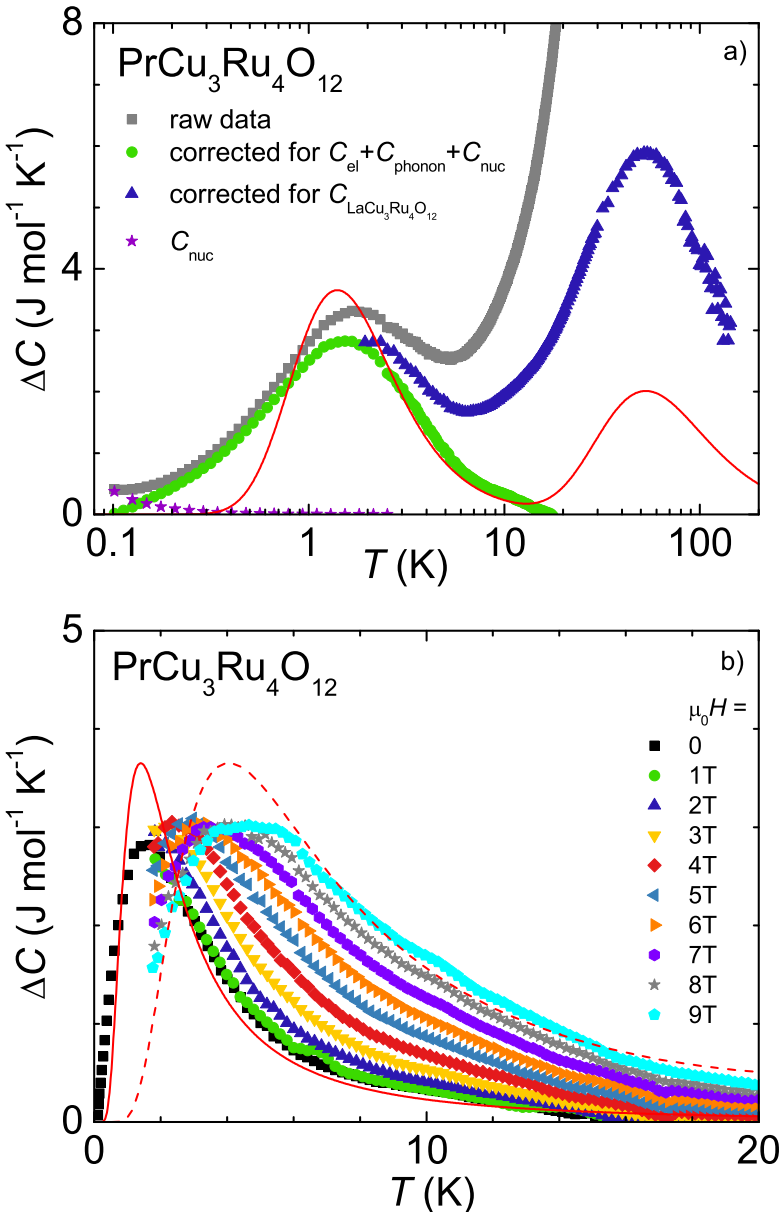

Figure 5.29: Frame a: Specific heat ΔC of $PrCu_3Ru_4O_{12}$ in zero field on a semi-logarithmic scale shown as raw data (grey squares), corrected for phononic $C_{\mathrm{phonon}} = \beta T^3$, electronic $C_{\mathrm{el}} = \gamma T$, and nuclear C_{nuc} contributions (green circles), and corrected for the non-magnetic reference compound $LaCu_3Ru_4O_{12}$ (blue triangles, limited T-range). The curves are fits/simulations according to appropriate CEF level schemes. Frame b: Specific heat ΔC of $PrCu_3Ru_4O_{12}$ corrected for phononic, electronic and nuclear contributions in various magnetic fields. The red solid/dashed curves are fits to the data set of 0/9 T representing the contribution of the lowest CEF excitation. See text for details.

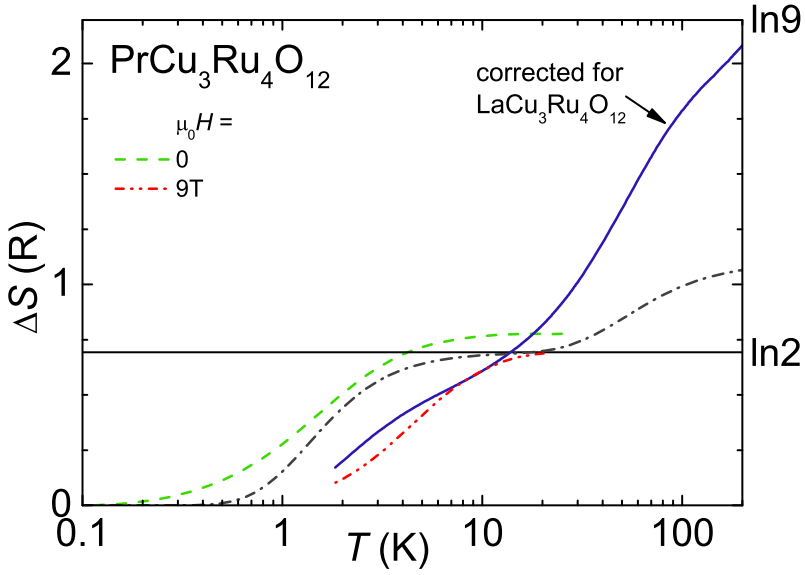

Figure 5.30: Entropy ΔS of $PrCu_3Ru_4O_{12}$ calculated by integration of the specific heat divided by temperature (C/T) after subtraction of electronic, phononic, and nuclear contributions (dashed/dotted curves) and after subtraction of the specific heat of $LaCu_3Ru_4O_{12}$ and adding an offset to account for contributions below 2 K (blue solid curve). The straight solid line stands for an entropy of $R\ln 2$ representing a transition from a ground state to an excited state with degeneracies $g_1/g_0 = 1$. The grey dash-dotted curve is a simulation of the entropy in zero field according to the term scheme derived from a fit to the specific heat (data set 2). See text for details.

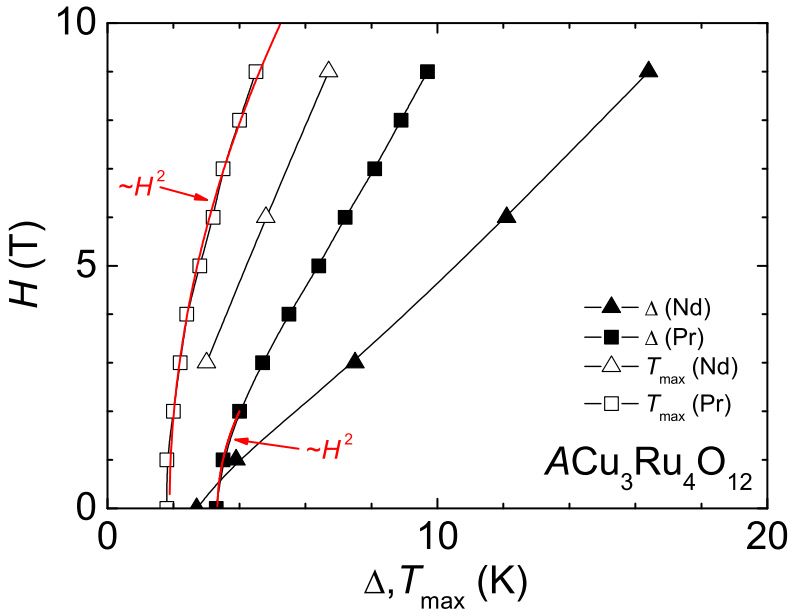

Figure 5.31: Field-dependence of the splitting from the ground state to the first excited state in $A\mathrm{Cu_3Ru_4O_{12}}$ (A = Pr, Nd). Δ is the splitting derived from fits to the corrected specific heat according to a Schottky anomaly. T_{max} denotes the manually extracted maximum of the corresponding Schottky peak of the corrected specific heat. See text for details.

data corrected for the non-magnetic reference compound $LaCu_3Ru_4O_{12}$ (blue triangles). Despite the fact that the zero-field peak is not visible completely, one can use the peak of the data in magnetic fields to calculate the associated entropy. For all data sets a correction as performed for the Pr compound in terms of an offset has been carried out, namely the extrapolation of the specific heat toward absolute zero with a straight line from the lowest available data point. The integration of C/T results in an entropy as plotted in Fig. 5.33. Obviously, the offset is underestimated for the zero-field and the 1 T data but reaches a plateau at $R \ln 3$ slightly above 10 K for data in fields of 3, 6, and 9 T which is comprehensible as the peaks here are almost fully covered experimentally. A value of $R \ln 3$ occurs when the excited state has twice the degeneracy of the ground state (see also chapter 3.2.3). In the case of $NdCu_3Ru_4O_{12}$ this leads to only one possible term scheme, namely a doublet ground state Γ_6 and excited quartet states $\Gamma_8^{(1,2)}$. A corresponding fit/simulation to the zero-field data is plotted in Fig. 5.32a (red solid curve, respectively). It shows a maximum at roughly 1 K and fairly describes the experimental data for $2\,\mathrm{K} < T < 10\,\mathrm{K}$ although a significant broadening is present as it is in $PrCu_3Ru_4O_{12}$. The splitting to the second quartet is manually set to 150 K in order to best match the data corrected for $LaCu_3Ru_4O_{12}$. Also here, the contribution is far below the experimental data such that again the quality of the method of subtracting the reference compound has to be questioned. The same fit is repeated in Fig. 5.32b for the zero-field data (red solid curve) as well as for the data in magnetic fields (shown only for 9 T, black dashed curve). In contrast to the zero-field data, the fit to the 9 T data seems to be much better even though a broadening is present here, too. The splittings have been extracted from the specific heat for all fields. Both the parameter Δ representing the splitting of the Schottky anomaly and the manually determined temperature of the maximum $T_{\max}$ are shown in Fig. 5.31. Δ and $T_{\max}$ increase linearly upon increasing field and have an almost constant ratio of ≈ 0.4. When looking at the entropy of the data corrected for $LaCu_3Ru_4O_{12}$ (blue solid curve in Fig. 5.33), it shows a different behavior as it does not level off at any temperature but only changes its curvature. Furthermore, when having in mind that the calculated offset is underestimated and one would shift the data by an additional offset of roughly $0.6\,R$ which would also rise the plateau of the zero-field data (green dashed curve) to $R \ln 3$, then it would accumulate too much entropy when the temperature is increased.

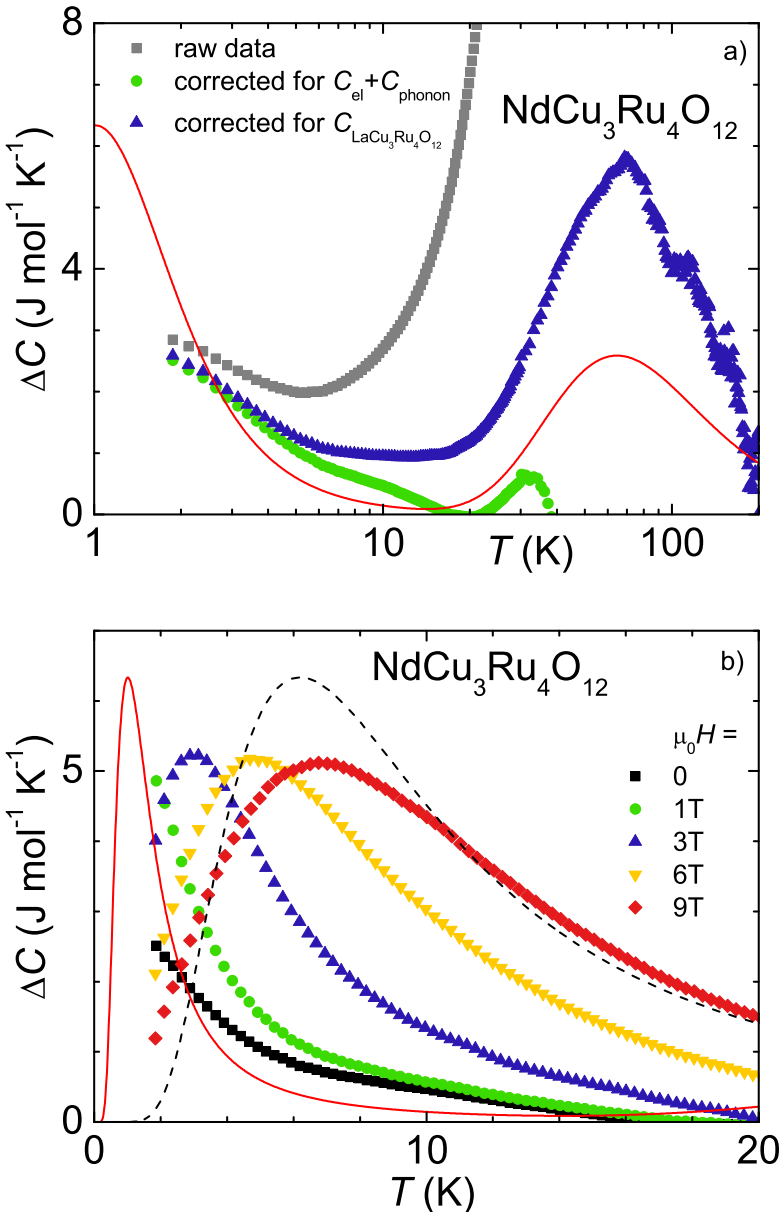

Figure 5.32: Frame a: Specific heat ΔC of $NdCu_3Ru_4O_{12}$ in zero field on a semi-logarithmic scale shown as raw data (grey squares), corrected for phononic $C_{\text{phonon}} = \beta T^3$ and electronic $C_{\text{el}} = \gamma T$ contributions (green circles), and corrected for the non-magnetic reference compound $LaCu_3Ru_4O_{12}$ (blue triangles). The red solid curves is a fit according to an appropriate CEF level scheme. Frame b: Specific heat ΔC of $NdCu_3Ru_4O_{12}$ corrected for phononic and electronic contributions in various magnetic fields. The red solid/black dashed curves are fits to the data set of 0/9 T representing the contribution of the lowest CEF excitation. See text for details.

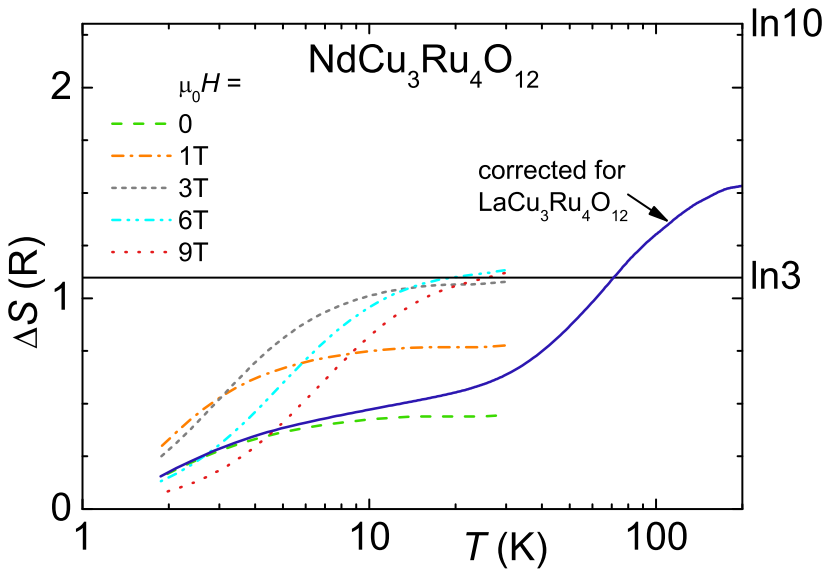

Figure 5.33: Entropy ΔS of $NdCu_3Ru_4O_{12}$ calculated by integration of the specific heat divided by temperature (C/T) after subtraction of electronic and phononic contributions (broken curves) and after subtraction of the specific heat of $LaCu_3Ru_4O_{12}$ (blue solid curve). All data sets have been corrected for an offset to account for contributions below 2 K. The straight solid line stands for an entropy of R ln 3 representing a transition from a doublet ground state to an excited quartet state. See text for details.

Isotope	x (%)	c (1/f.u.)	I (ħ)	μ (μ_N)	Q (10^{-28} m^2)	V_{zz} (10^{22} V/m^2)
Pr-141	100.00	1.000	5/2	5.0587	-0.0589	0.73
Cu-63	69.17	2.076	3/2	2.8750	-0.2200	0.73
Cu-65	30.83	0.924	3/2	3.0747	-0.2040	0.73
Ru-99	12.76	0.510	5/2	-0.7588	0.0790	0.43
Ru-101	17.06	0.682	5/2	-0.8505	0.4570	0.43

Table 5.9: Natural abundance x in % of all occurrent isotopes of the respective element, concentration c within $PrCu_3Ru_4O_{12}$, nuclear spin I, nuclear magnetic moment μ, quadrupole moment Q, and internal electric field gradient V_{zz} for all isotopes in $PrCu_3Ru_4O_{12}$ relevant for the calculation of the nuclear specific heat. The parameters x, I, μ, and Q are isotope-specific literature values from Ref. [203] (see also Ref. [204]), c and V_{zz} are compound-specific.

5.5 Neutron Spectroscopy

Time-of-flight experiments on $CaCu_3Ru_4O_{12}$ and $PrCu_3Ru_4O_{12}$ powder samples were intended to investigate magnetic excitations related to NFL, IV, and CEF properties. The following contour plots in this chapter show the scattering intensity of the dynamic structure factor $S(Q,\omega)$ which is rainbow-color coded on a logarithmic scale indicating increasing intensities from green via yellow and orange to light red above the background level shown in blue. Elastic incoherent scattering is represented by the red riff around $\hbar\omega \approx 0$ including nuclear Bragg reflections (dark red spots) of which some are indicated by their Miller indices.

Fig. 5.34 shows $S(Q,\omega)$ of $CaCu_3Ru_4O_{12}$ at 1.5 K (frame a) and 120 K (frame b). The only significant inelastic intensity is located at the limit of the accessible energy range: for 1.5 K around +13 meV and for 120 K at both +13 meV and +15 meV (yellow coded intensity). When looking at the evolution with temperature of this intensity, then an increase with increasing temperature can be traced for the contour plots of 1.5 and 120 K. The data set of 25 and 50 K (see Fig. 7.23) only partially fit into this picture. A possible reason for this might be a simplified data processing as the correction of the background is done with one and the same data set acquired at 50 K. Usually, magnetic scattering on powder samples is identified by its Q-dependence with a characteristic decrease for increasing Q according to the neutron magnetic form factor. Energy strips at constant $\hbar\omega$ = +12.75 meV and $\hbar\omega$ = +14.9 meV are depicted in Fig. 5.35 which have been derived by accumulating the intensity at constant $\hbar\omega$ with an energy width dE = 0.1 meV and a wavevector width dQ = 0.01 Å^{-1}. Evidently, no magnetic intensity can be identified as there is no corresponding Q-dependence. The intensity increase upon increasing temperature rather suggests an origin related to optical phonons as the associated temperature roughly correlates with the Einstein temperature derived from heat capacity measurements (see Table 5.7). The absence of any appreciable magnetic intensity implies that the magnetic response is weak and spread out in energy. A further feature of the intensity shown in Fig. 5.35 is that apparently the weight of optical phonons changes significantly between 1.5 K and 120 K, especially regarding wavevector transfers around 2 Å^{-1}.

In Fig. 5.36 $S(Q,\omega)$ of $PrCu_3Ru_4O_{12}$ is plotted for T = 1.5 K (frame a) and 100 K (frame b). First of all, almost the same inelastic intensity as present in $CaCu_3Ru_4O_{12}$

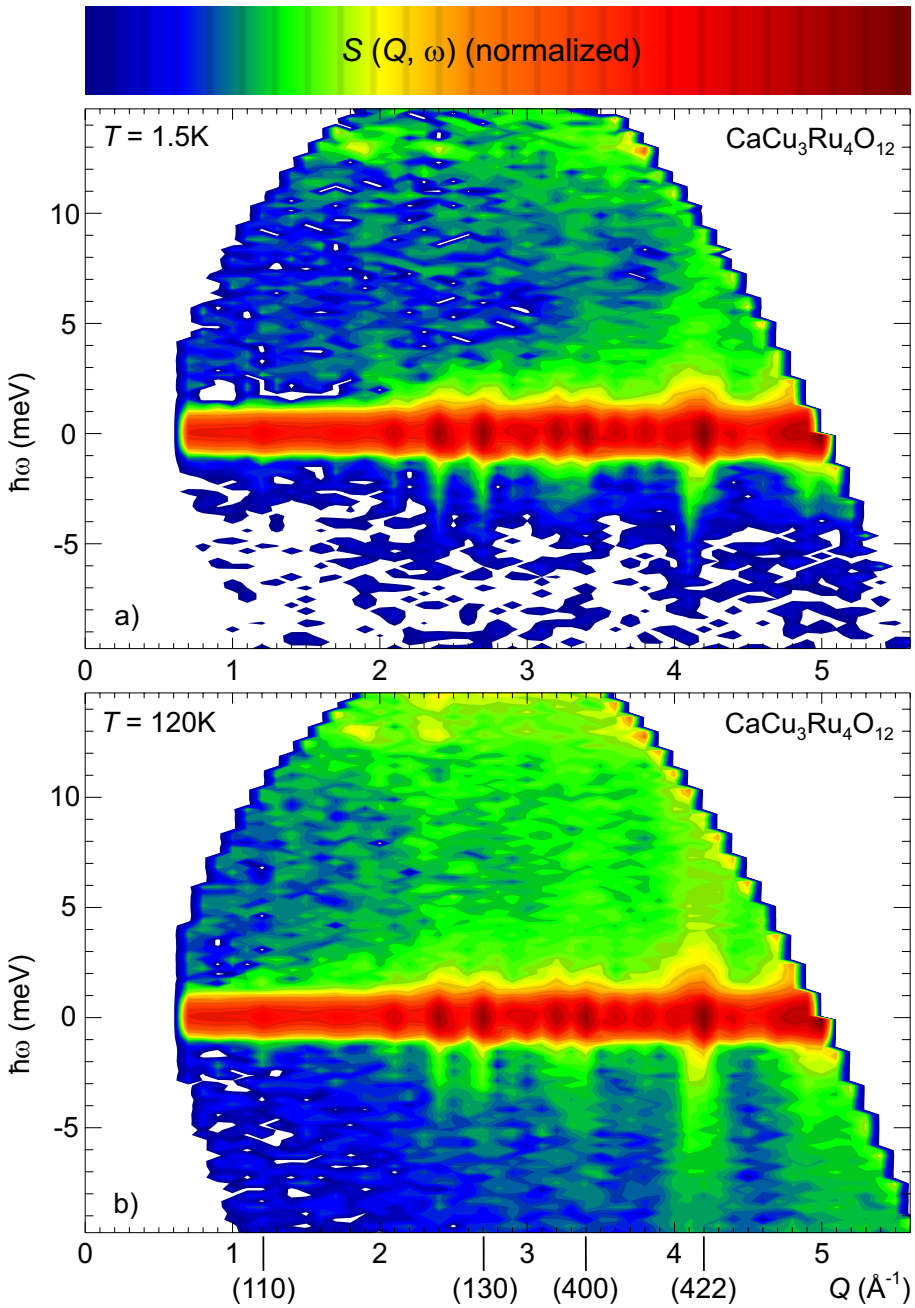

Figure 5.34: Contour plot of the dynamic structure factor $S(Q,\omega)$ of $CaCu_3Ru_4O_{12}$ at 1.5 K (frame a) and 120 K (frame b). Intensities are shown by a rainbow-color coding on a logarithmic scale to indicate increasing intensities from green via yellow and orange to light red above the background level shown in blue. The red riff around $\hbar\omega \approx 0$ represents elastic incoherent scattering including nuclear Bragg reflections (dark red spots) of which some are indicated by their Miller indices. The area with positive $\hbar\omega$ stands for neutrons loosing energy, negative $\hbar\omega$ means energy gain for neutrons.

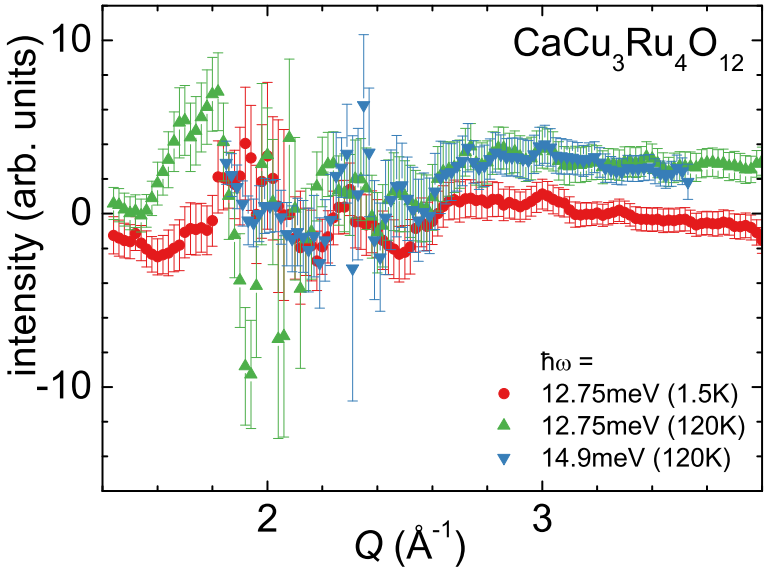

Figure 5.35: Energy strips of the dynamic structure factor $S(Q,\omega)$ of $CaCu_3Ru_4O_{12}$ at 1.5 and 120 K derived by binning the intensity at constant $\hbar\omega$ with an energy width $dE = 0.1$ meV and a wavevector width $dQ = 0.01$ Å^{-1}.

can be identified at both +13 meV and +15 meV (yellow coded intensity). This might be another strong evidence for phononic origin of this feature. Secondly, and more striking are several dispersionless excitations (marked by dashed lines) appearing or vanishing as temperature is changed (see also Figs. 7.24, 7.25, and 7.26). A representative wavevector strip derived by accumulating the intensity at fixed momentum transfer $Q = 1.5\,\text{Å}^{-1}$ and momentum width $\mathrm{d}Q = 0.1\,\text{Å}^{-1}$ is depicted in Fig. 5.37 which is split up into two graphs showing different temperature ranges. Frame a identifies a small maximum at ≈ 3.5 meV which is most pronounced at 1.5 K, continuously loosing intensity upon increasing temperature and is not visible any more above 50 K. The most intense and well defined excitation is located slightly below 8 meV and also decreases with increasing temperature but without being depleted completely. At the high energy edge of this peak some asymmetry/shoulder is visible at ≈ 9.5 meV and is possibly related to another excitation as it concomitantly diminishes with the intensity at 3.5 meV upon increasing temperature. Above 75 K only the excitation centered at 8 meV remains, which can also be observed at the energy gain side (negative $\hbar\omega$). The obvious explanation for the observed inelastic (dispersionless) intensities can be found in terms of excitations due to crystal-field effects. In a crystal field of the cubic site symmetry $m\bar{3}$ (T_h) the 9-fold degeneracy of the single-ion ground state of Pr^{3+} ($J = 4$) is lifted resulting in the formation of a singlet Γ_1, a doublet Γ_3, and two triplets Γ_4/Γ_5.[127] According to Ref. [180] the magnetic matrix elements $\langle \Gamma_i | J_z | \Gamma_j \rangle$ and thus the transition probabilities for $J = 4$ which occur only once in the decomposition of J are independent of the crystal-field parameter x. Trying now to identify the three observed transitions with the calculated magnitudes of $\langle \Gamma_i | J_z | \Gamma_j \rangle$ ($i \neq j$) then one quickly gets to a dead end. For example, assume the transition at 8 meV with the highest magnitude to be that of $\Gamma_3 \leftrightarrow \Gamma_4$ ($\langle \Gamma_3 | J_z | \Gamma_4 \rangle = 9.33$), then the transition at 9.5 meV (which is roughly 3 times lower) could be that of $\Gamma_4 \leftrightarrow \Gamma_5$ ($\langle \Gamma_4 | J_z | \Gamma_5 \rangle = 3.50$). But now we still have a transition at 3.5 meV which is at least two times lower than that at 9.5 meV and we can't relate it to any other theoretical transition as there is none with a lower magnitude any more. Apart from these problems, the situation seems to get even more complicated as a reexamination of the CEF study by LLW [127] resulted in different findings.[187] Though the new calculations don't affect the degeneracy of each sublevel, they do for some eigenfunctions and eigenvalues and thus also the selection rules and transition probabilities.[11] The evolution of the intensity of the respective transitions with temperature

11Note that the J-manifold diagrams of LLW do not include the CEF parameter y but correspond to

is shown in Fig. 5.38. Having in mind the temperature-dependent population of the CEF levels, then the slow and nearly linear decrease (at least up to 150 K) of the 7.9 meV-transition in contrast to the abrupt drop of the transitions at 3.5 meV and 9.5 meV (-25% and -39% when increasing T from 1.5 K to 25 K) might indicate that the 3.5 meV- and 9.5 meV-excitations start from the ground state while the 7.9 meV-transition is located at elevated temperatures. Additionally, the splitting of the ground state to the first excited state was identified by specific heat measurements (see chapter 5.4) to roughly 3.3 K. It is clear that this excitation lies invisible beneath the elastic line. In summary, one has to admit that from the present stock of inelastic neutron data it seems to be impossible to get to some definite conclusion for the CEF level scheme in $PrCu_3Ru_4O_{12}$.

the limit of $y \to 0$.[187]

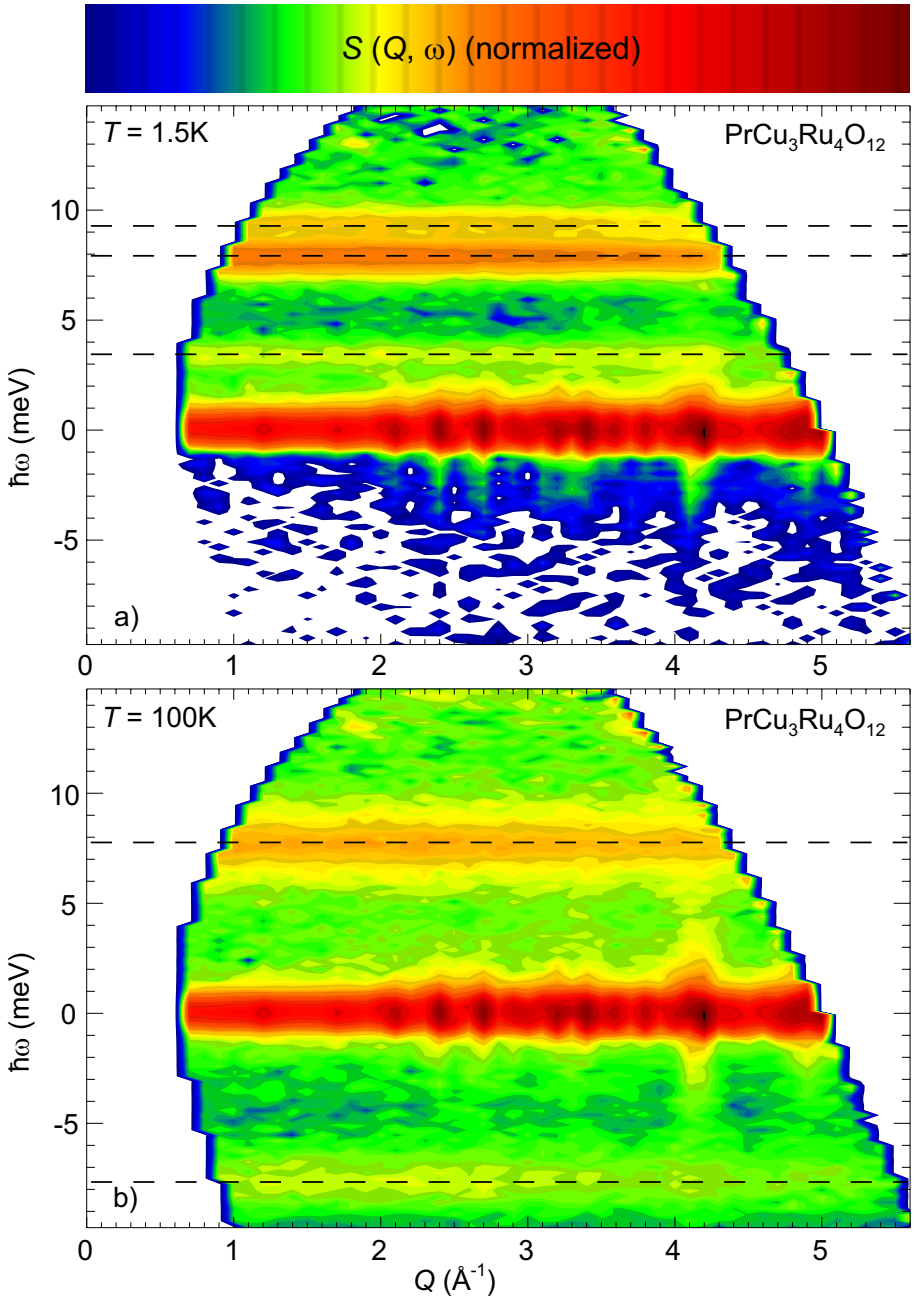

Figure 5.36: Contour plot of the dynamic structure factor $S(Q,\omega)$ of $PrCu_3Ru_4O_{12}$ at 1.5 K (frame a) and 100 K (frame b). Intensities are shown by a rainbow-color coding on a logarithmic scale to indicate increasing intensities from green via yellow and orange to light red above the background level shown in blue. The red riff around $\hbar\omega \approx 0$ represents elastic incoherent scattering including nuclear Bragg reflections (dark red spots) of which some are indicated by their Miller indices. The dashed lines mark the dispersionless intensities as described in the text. The area with positive $\hbar\omega$ stands for neutrons loosing energy, negative $\hbar\omega$ means energy gain for neutrons.

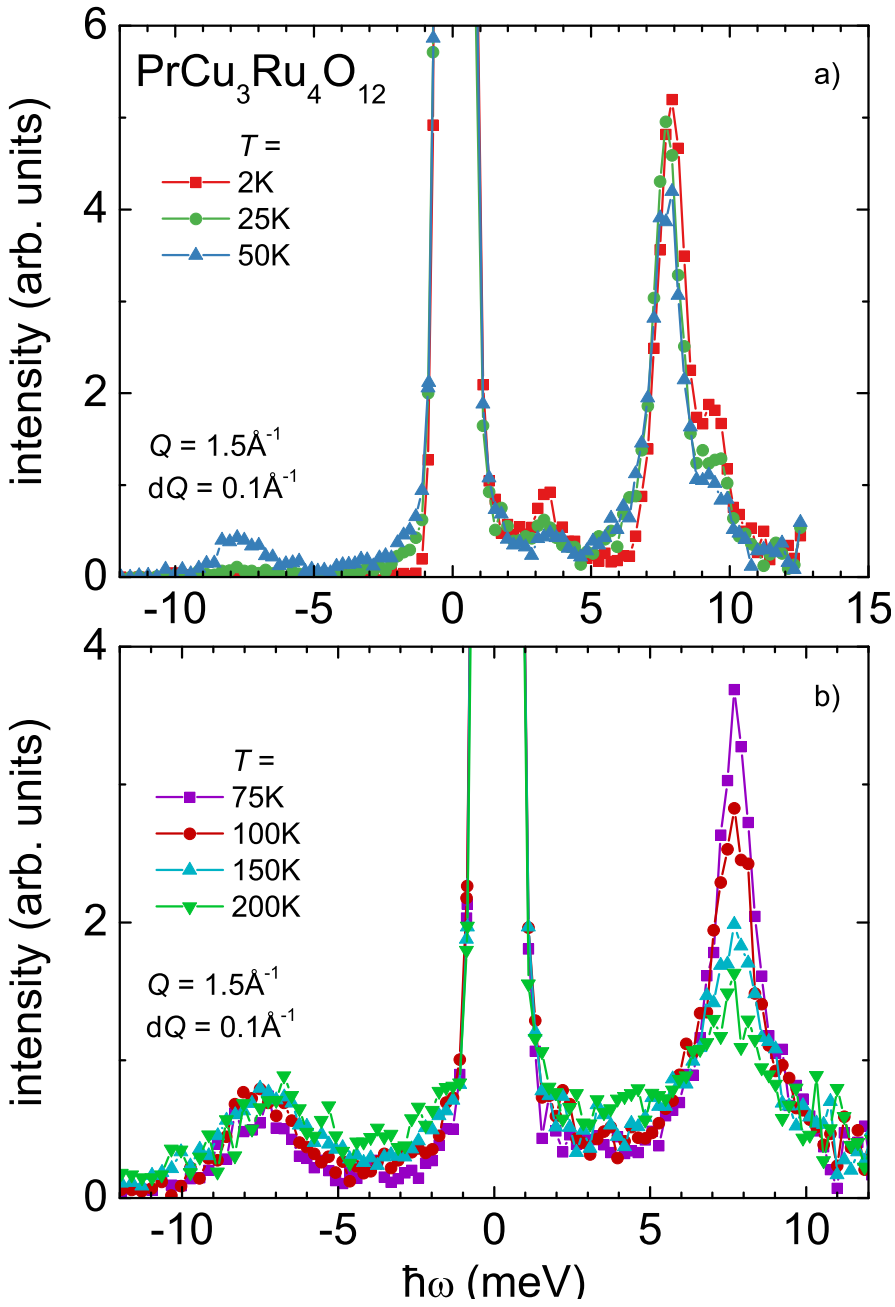

Figure 5.37: Wavevector strips of the dynamic structure factor $S(Q,\omega)$ of $PrCu_3Ru_4O_{12}$ for $1.5\,\mathrm{K} \leq T \leq 50\,\mathrm{K}$ (frame a) and $75\,\mathrm{K} \leq T \leq 200\,\mathrm{K}$ (frame b) derived by binning the intensity at fixed momentum transfer $Q = 1.5\,\mathrm{\AA}^{-1}$ and momentum width $\mathrm{d}Q = 0.1\,\mathrm{\AA}^{-1}$.

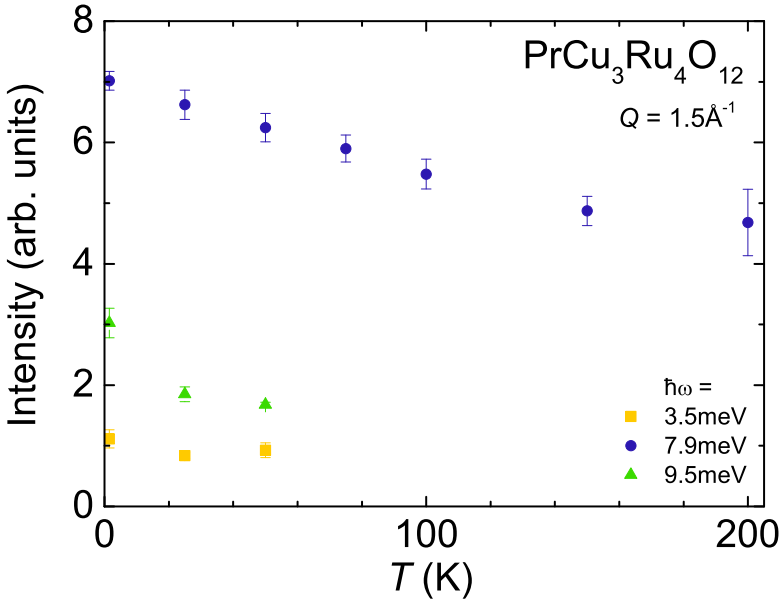

Figure 5.38: Temperature-dependent intensity of the CEF transitions in $PrCu_3Ru_4O_{12}$ induced by neutrons which are fitted with Gaussian-shaped lines (see also Fig. 5.37).

5.6 Muon Spin Rotation (μSR)

Exploratory muon experiments on $ACu_3Ru_4O_{12}$ (A = Ca, Pr, Nd) were carried out in zero field and weak transverse field to get their basic μSR signature. Fig. 5.39 exemplarily shows the weak transverse field (5 mT) data of $CaCu_3Ru_4O_{12}$ at 50 K (left frame) and that of $PrCu_3Ru_4O_{12}$ at 190 K (right frame). A single pattern with full asymmetry ($A_0 = 0.237$) is observed for both compounds which can be described with a single Gaussian damped oscillator (sGdo): $A(t) = A_0 \exp(-\sigma^2 t^2) \cos(2\pi\nu_\mu t + \phi)$.

For $CaCu_3Ru_4O_{12}$ the phase shift ϕ is close to zero and the damping is purely Gaussian, meaning that the local field at the muon site is static on the μSR timescale. The precession frequency ν_μ of the muon corresponds within the limits of error to the applied TF indicating a unique muon stopping site. A temperature independent initial asymmetry A_0 and a nearly constant relaxation rate $\sigma = 0.085\,\mu s^{-1}$ (see Fig. 5.41, blue triangles) suggest that the muon rests stationary at its single stopping site.

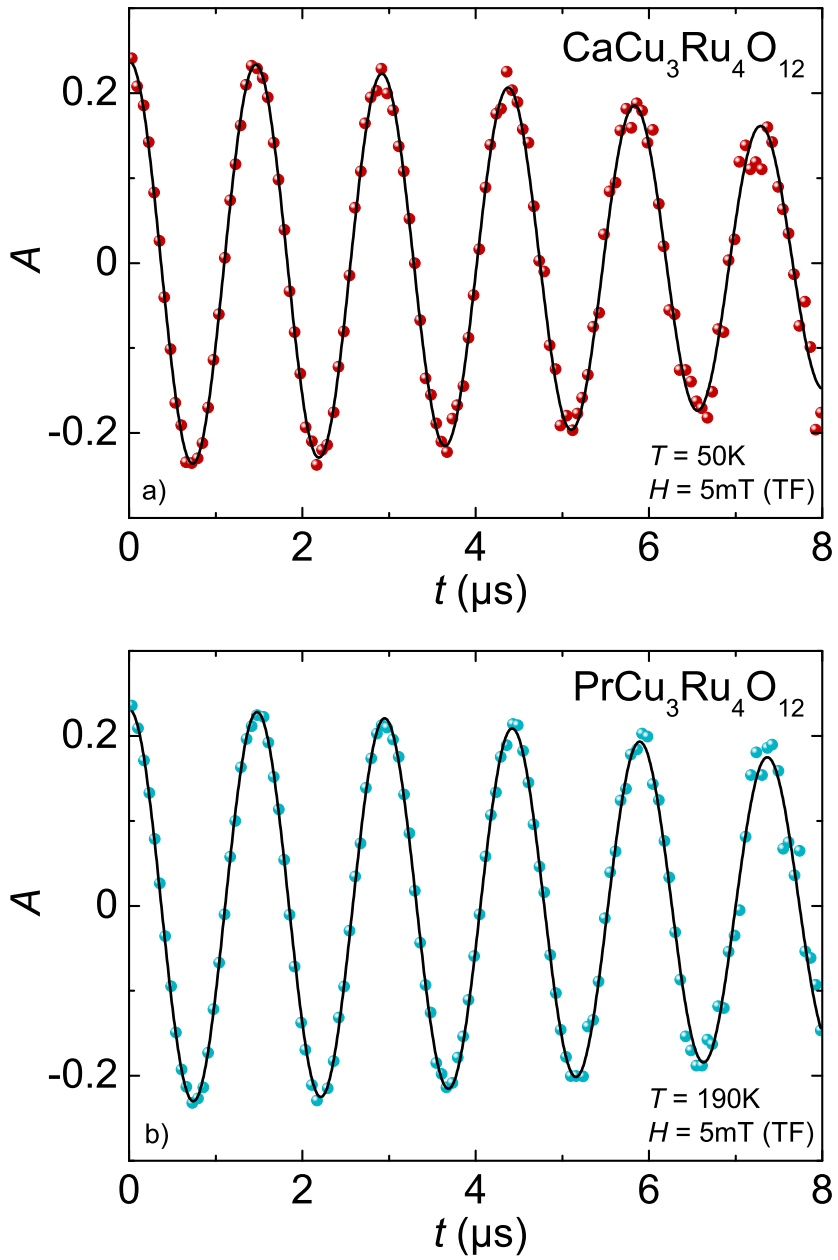

Figure 5.39: Time dependent transverse-field (5 mT) asymmetry A of $CaCu_3Ru_4O_{12}$ at 50 K (frame a) and of $PrCu_3Ru_4O_{12}$ at 190 K (frame b). The solid lines are fits according to a single Gaussian damped oscillator. See text for details.

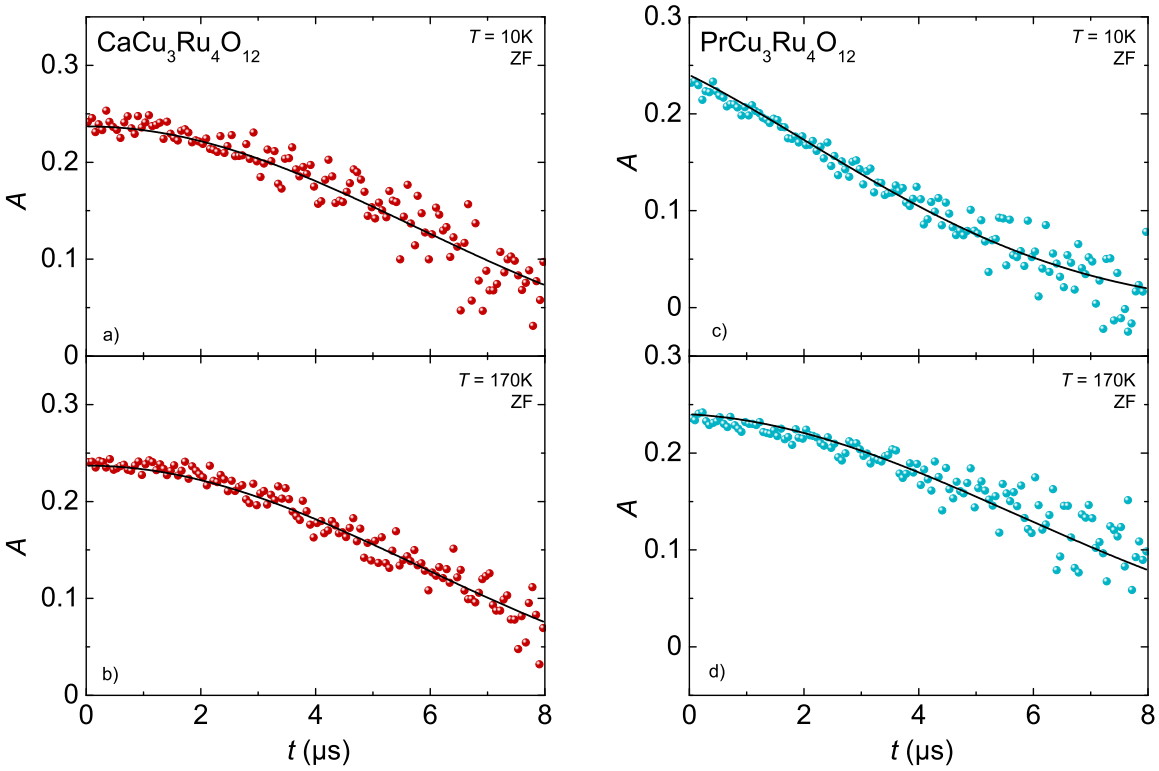

Figure 5.40: Time dependent zero-field asymmetry A of $CaCu_3Ru_4O_{12}$ at 10 K (frame a) and 170 K (frame b) and of $PrCu_3Ru_4O_{12}$ at 10 K (frame c) and 170 K (frame d). The solid lines are fits according to a static Gaussian Kubo-Toyabe relaxation ($CaCu_3Ru_4O_{12}$) and an electron-nuclear double relaxation ($PrCu_3Ru_4O_{12}$). See text for details.

The situation in $PrCu_3Ru_4O_{12}$ is quite similar to that in $CaCu_3Ru_4O_{12}$. At high temperatures, the spectra can also be fitted with Gaussian damping apart from of a somewhat smaller relaxation rate. At low temperatures, the Gaussian damping is unsatisfactory and better - but not perfect - results are achieved with an exponential decay. In addition, the damping rate increases when the temperature is reduced. The likely cause for this is an increasing influence on the spectral shape by an additional interaction with the magnetic moment of Pr^{3+}. This means we have to consider here an electron-nuclear double relaxation. Since this aspect is better pursued in ZF, a detailed discussion of the weak TF results is not attempted. In $PrCu_3Ru_4O_{12}$ both the signal amplitude (initial asymmetry $A_0 \approx 0.236$) and the spectral baseline ($\alpha \approx 0.437$) show no relevant temperature dependence.

The ZF data of $CaCu_3Ru_4O_{12}$ is depicted in Fig. 5.40 (left frame) at 10 K and 170 K. It is consistent with the TF data and exhibits a Gaussian decay indicative of a static Gaussian Kubo-Toyabe (sGKT) relaxation [214]: $A(t) = A_0\,[2/3\,(1-\Delta^2 t^2)\exp(-\sigma^2 t^2/2) + 1/3]$. The parameter of physical relevance is the relaxation rate Δ with $\Delta/\gamma_\mu = B_{\mathrm{rms}}$ being the rms width of the Gaussian distribution of each Cartesian component of the magnetic field B at the muon site. As evident from the latter equation, the sGKT function in total is not a decay of asymmetry with solely Gaussian character. After an initial Gaussian type decay, $A(t)$ reaches a minimum around $t \approx 1.7/\Delta$ and then recovers to a time independent value $A_0/3$. As no minimum is visible in the time dependent asymmetry, this means that this feature of the sGKT function is already outside the time window of the μSR spectrometer leading to problems during fitting: when leaving the parameters A_0 and Δ unrestricted, the system is unable to find the baseline so the initial asymmetry has to be fixed to the value obtained from the TF spectra ($A_0 = 0.237$). Fig. 5.41 shows the resulting ZF relaxation rate Δ (green squares) which is virtually constant at a small value of $\Delta = 0.13\,\mu s^{-1}$ corresponding to $B_{\mathrm{rms}} = 0.15\,\mathrm{mT}$. Such a low value points to nuclear dipole moments as the origin of the local field. Nuclear dipole moments are of course not really static, but their fluctuation rate is rather slow (often in the ms regime) and thus they appear static on the μSR time scale. For a static interaction with nuclear dipoles (meaning a static muon) the ratio of the TF damping rate to the ZF relaxation rate is $\sigma/\Delta = 1/\sqrt{2} \approx 0.7$. Indeed, in the present case $\sigma/\Delta = 0.085/0.13 \approx 0.65$ which justifies the treatment of the ZF and weak TF spectra in the static limit. When looking at the constituents, the only isotope of Ca having a nuclear moment ($-1.5\,\mu_N$) is Ca-43, however with a very low abundance (0.13%). Oxygen is nearly 100% O-16 which has no magnetic dipole moment. Ru has two isotopes of interest (Ru-99 and Ru-101) with moderate abundances (13% and 17%) but with low moment magnitudes ($-0.8\,\mu_N$ and $-0.9\,\mu_N$). Sizeable nuclear moments possess only the isotopes Cu-63 and Cu-65 ($2.9\,\mu_N$ and $3.1\,\mu_N$) with a natural abundance of 69% and 31%.[203] (see also Ref. [204]) Hence, the dominant source of the sGKT relaxation is the coupling between the muon spin and the nuclear moments of Cu. The pure sGKT spectra imply that the influence of localized electronic magnetic moments of the constituents of $CaCu_3Ru_4O_{12}$ on the muon relaxation is negligible. The constancy of $B_{\mathrm{rms}}(T)$ points to the fact that the μ^+-Cu distance is not affected significantly by temperature. In particular in the range of the transition region around 150 K this means that the lattice symmetry is preserved and that the source of the transition

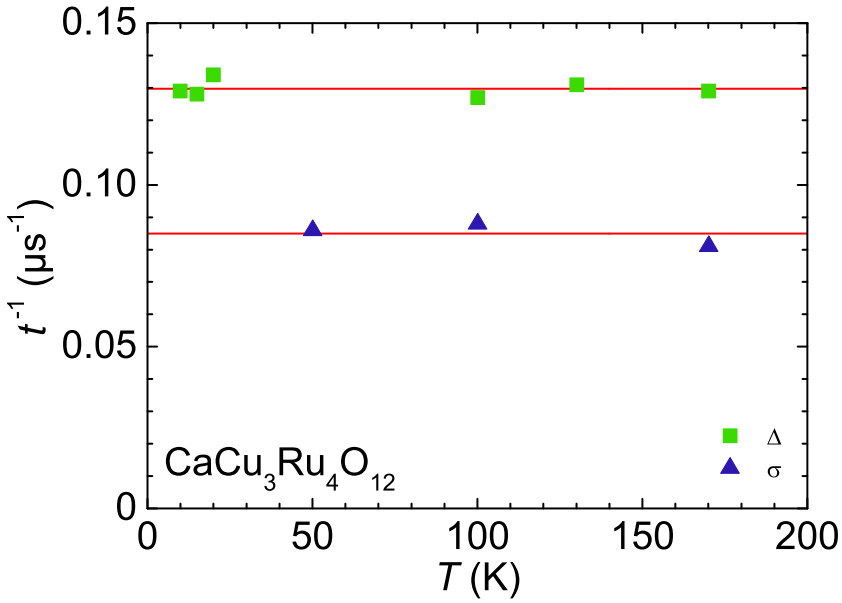

Figure 5.41: Temperature dependent static width Δ derived from the fits to the ZF spectra of $CaCu_3Ru_4O_{12}$ according to a sGKT function and relaxation rate σ of $CaCu_3Ru_4O_{12}$ in weak TF derived from fits with a sGdo pattern. The straight lines are guides for the eye. See text for details.

is most likely a change in the electronic structure which itself again does not affect the muon relaxation effectively.

Fig. 5.40 clearly shows that the ZF spectrum of $PrCu_3Ru_4O_{12}$ at low temperatures (10 K, upper right frame) is markedly different from that at high temperatures (170 K, lower right frame). At 10 K, it does no longer show a pure (static) nuclear relaxation as in the case of $CaCu_3Ru_4O_{12}$ but features a nearly linear decay for the first half of the μSR time window. Such a decay of asymmetry is typical for the case that dynamic interactions on an electronic channel are present, but not dominating. Clearly, this is the coupling of the muon spin to the localized $4f$ moment of the rare-earth ion and as long as there are no correlations among the $4f$ moments (i.e. in the absence of magnetic order), these will fluctuate rapidly (free paramagnetic moments) resulting in a simple exponential decay of asymmetry with rate λ. As this rate is inversely proportional to the fluctuation rate $1/\tau_{4f}$ of the $4f$ moments, it may become quite small in a regime of fast fluctuation (high temperatures). This means that the sGKT relaxation channel through the Cu nuclei is

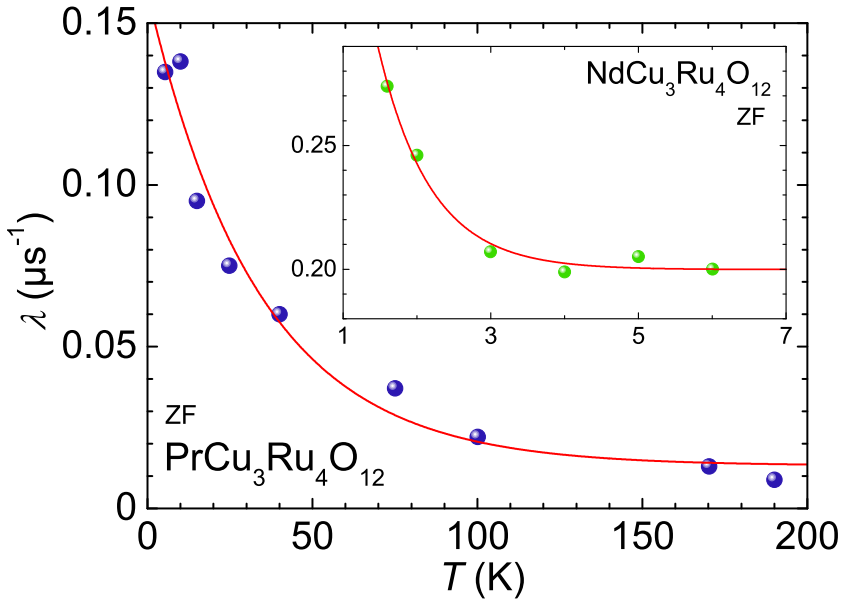

Figure 5.42: Temperature dependent electronic muon relaxation rate λ of $PrCu_3Ru_4O_{12}$ (main frame) and $NdCu_3Ru_4O_{12}$ (inset, different temperature scale) in zero field. The solid lines are fits according to an exponential behavior. See text for details.

no longer negligible and has to be accounted for in a proper fit procedure. In case the two interactions are independent from each other and occur on sufficiently different time scales, then a product of both relaxation functions (electron-nuclear double relaxation) can be applied: $A(t) = A_0 \exp(-\lambda t)\,[2/3\,(1-\Delta^2 t^2)\exp(-\Delta^2 t^2/2) + 1/3]$. As both relaxation rates come out to be small and not very different, the fit procedure was carried out with the following parameters fixed: alpha parameter (0.437), asymmetry ($A_0 = 0.236$) from weak TF data, and a temperature independent static relaxation rate $\Delta = 0.13\,\mu s^{-1}$ (as in the case of $CaCu_3Ru_4O_{12}$). The resulting electronic relaxation rate λ is shown in Fig. 5.42 and has a typical dependence of a coupling between a muon and a free paramagnetic ion: with decreasing temperature also the fluctuation rate of the Pr^{3+} moments decreases leading to a continuous enhancement of the magnitude of λ into a quasi-static spin state at low temperatures. The dependence of λ is relatively smooth which might indicate that the magnetic moment of Pr^{3+} does not change substantially (e.g. by CEF effects) in the temperature range covered.

The situation in $NdCu_3Ru_4O_{12}$ is different. Although its ZF spectra (see Fig. 5.43) also obey an electron-nuclear double relaxation, its relaxation rate seems to level off already at 3 K after a steep decrease when the temperature is increased (see inset in Fig. 5.42). Of course, the small temperature range covered during the experiment limits the relevancy of this statement. Yet, a likely reason for this is the different CEF behavior as Nd^{3+} is a Kramers ion.

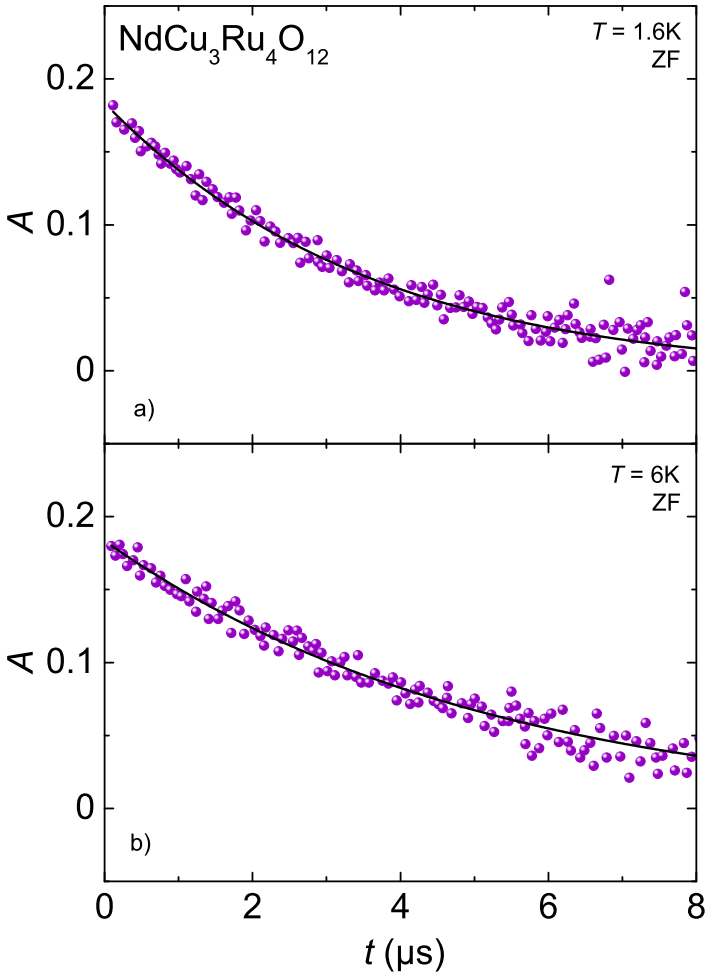

Figure 5.43: Time dependent zero-field asymmetry A of $NdCu_3Ru_4O_{12}$ at 1.6 K (frame a) and 6 K (frame b). The solid lines are fits according to an electron-nuclear double relaxation. See text for details.

6 Conclusion & Outlook

The compounds $A\mathrm{Cu_3Ru_4O_{12}}$ (A = Na, Ca, Sr, La, Pr, Nd) belong to the class of A-site ordered perovskites $AC_3B_4\mathrm{O_{12}}$. The symmetry of the crystal structure is not changed when the compounds are cooled from RT down to 1.6 K. This result can be stated for $A\mathrm{Cu_3Ru_4O_{12}}$ (A = Na, Ca, La, Pr, Nd) whereas no prediction can be made for $\mathrm{SrCu_3Ru_4O_{12}}$ due to the lack of data. While the symmetry is conserved, neutron powder diffraction on $\mathrm{CaCu_3Ru_4O_{12}}$ [62] reveals an anomaly in the temperature dependence of the lattice constant which is not present in the other compounds (again $\mathrm{SrCu_3Ru_4O_{12}}$ is excluded from this statement). This anomaly manifests itself as a small but nonetheless abrupt change in the lattice constant at 154 K while that of the other homologues shows a smooth behavior. The origin of this transition is identified in terms of a valence transition.[62]

The magnetic susceptibility of $A\mathrm{Cu_3Ru_4O_{12}}$ (A = Na, Ca, Sr, La, Pr, Nd) is typical for that of a metallic Pauli-paramagnet with an enhanced susceptibility when compared to a conventional metal. However, the temperature dependence of the susceptibility is markedly different between the respective compounds. $\mathrm{CaCu_3Ru_4O_{12}}$ exhibits a broad maximum in the susceptibility at around 160 K which coincides with the temperature at which the structural anomaly is located. The susceptibility of $\mathrm{NaCu_3Ru_4O_{12}}$ is almost constant down to 100 K, however, with signatures similar to those of the Ca compound, whereas that of $A\mathrm{Cu_3Ru_4O_{12}}$ (A = Sr, La) exhibits a weak temperature dependence with a perfect Curie-Weiss law over a wide temperature range. In the case of $\mathrm{SrCu_3Ru_4O_{12}}$ this dependence is superimposed by a strong signal of the ferromagnetic impurity $\mathrm{SrRuO_3}$ (T_C = 160 K).[175] In the magnetic rare-earth compounds $A\mathrm{Cu_3Ru_4O_{12}}$ (A = Pr, Nd), the crystal field - acting on the rare-earth $4f$-spin - strongly influences the susceptibility leading to deviations from a Curie-Weiss law below $\approx$ 200 K. In general, the resulting Curie-Weiss temperatures have to be interpreted carefully. The complex T-dependence

of the susceptibility of ACu$_3$Ru$_4$O$_{12}$ (A = Na, Ca) makes θ_{CW} very sensitive to the fitting range. More reliable results may be achieved when analyzing susceptibility data toward higher temperatures, i.e. above 400 K. In the case of ACu$_3$Ru$_4$O$_{12}$ (A = Sr, La), the high absolute value of θ_{CW} cannot be ascribed to an unreliable fitting range as the inverse susceptibility follows a perfect linearity. In general, θ_{CW} attains high negative values in the non-magnetic A-site compounds. Taken these values for granted and taking into account that the compounds do not undergo magnetic order at any temperature, such a CW temperature would indicate very strong magnetic frustration or complete moment compensation with a characteristic spin-fluctuation temperature of the order of $T^* = \theta_{\mathrm{CW}}/4$ often found experimentally.[116] For the systems ACu$_3$Ru$_4$O$_{12}$ (A = Ca, La) the latter approach is tolerable as CaCu$_3$Ru$_4$O$_{12}$ shows a characteristic temperature of approximately 200 K [30] whereas the unreasonable high values in ACu$_3$Ru$_4$O$_{12}$ (A = Na, Sr) have to be questioned in terms of such an approach. For the magnetic rare-earth compounds ACu$_3$Ru$_4$O$_{12}$ (A = Pr, Nd), θ_{CW} is reduced to a parameter of the CEF and eludes an interpretation as well.

The resistivity of ACu$_3$Ru$_4$O$_{12}$ (A = Na, Ca, Sr, La, Pr, Nd) is typical for a bad metal with a room temperature value of the order 1 mΩcm. The residual resistance ratio is ≈ 2 for the compounds with trivalent A-site ions (lanthanides), at around 17 for the divalent ones (Ca, Sr), and 55 for the monovalent Na ion. All possess a quadratic T-dependence of the resistivity below ≈ 30 K according to Fermi liquid theory. The field dependence of the resistivity of CaCu$_3$Ru$_4$O$_{12}$ and SrCu$_3$Ru$_4$O$_{12}$ at low temperatures follows Kohler's rule [182, 183] with a quadratic increase with increasing field. At temperatures below ≈ 5 K both a polycrystalline sample of SrCu$_3$Ru$_4$O$_{12}$ and a single crystal of CaCu$_3$Ru$_4$O$_{12}$ show non-Fermi liquid behavior, i.e. deviations from a quadratic T-dependence. For both compounds the resistivity is instead (positively) linear in T and the application of a magnetic field leads to the gradual reestablishment of a Fermi-liquid state. Such an evolution of the resistivity with magnetic field was also found in the heavy-fermion compound YbRh$_2$Si$_2$.[197] Curiously, another CaCu$_3$Ru$_4$O$_{12}$ single crystal shows the signature typical for that of a Kondo system with a resistance minimum at low temperatures followed by a logarithmic divergence and a saturation toward absolute zero. This sample-dependent effect may be due to imperfect crystal growth but could also be related to the closeness of a quantum critical point which is known to have a decisive influence on the material properties by means of slight stoichiometric deviations.

The specific heat of $A\mathrm{Cu_3Ru_4O_{12}}$ (A = Na, Ca, Sr, La, Pr, Nd) follows the predictions of Fermi-liquid theory and is hallmarked by an enhanced Sommerfeld coefficient typical for correlated electron systems. This enhancement is moderate when compared to other heavy-fermion systems - especially f-derived ones - but is still significant with respect to conventional metals. $\mathrm{NaCu_3Ru_4O_{12}}$ exhibits the lowest value ($72\,\mathrm{mJmol^{-1}K^{-2}}$) while $\mathrm{PrCu_3Ru_4O_{12}}$ has the highest one ($294\,\mathrm{mJmol^{-1}K^{-2}}$). Additional specific heat measurements on $\mathrm{CaCu_3Ru_4O_{12}}$ around the temperature of the structural anomaly confirm the effect in terms of a tiny peak with an associated entropy change of $70\,\mathrm{mJmol^{-1}K^{-1}}$. At low temperatures, contributions to the specific heat by CEF effects become observable in $A\mathrm{Cu_3Ru_4O_{12}}$ (A = Pr, Nd). A detailed analysis reveals a broad peak below 5 K for both compounds which can be reasonably described by a Schottky anomaly. The associated entropy gain amounts $\mathrm{R}\ln 2$ in $\mathrm{PrCu_3Ru_4O_{12}}$ and $\mathrm{R}\ln 3$ in $\mathrm{NdCu_3Ru_4O_{12}}$. If now these entropies are identified with the transition from the ground state to the first excited level of the split-up J-manifold of the respective rare-earth ion in a cubic CEF with A-site symmetry $m\bar{3}$ (T_h) [215, 127, 187], this leads to a term scheme with a triplet ground state and an excited triplet in the case of $\mathrm{PrCu_3Ru_4O_{12}}$ and to a doublet ground state and an excited quartet in the case of $\mathrm{NdCu_3Ru_4O_{12}}$. While for the Nd compound this is consistent with the J-manifold diagram of LLW, it is not the case for Pr unless assuming a shift of these triplets to the upper or lower end of the energy scale.

Time-of-flight neutron scattering experiments show no significant inelastic intensity for $\mathrm{CaCu_3Ru_4O_{12}}$ whereas in $\mathrm{PrCu_3Ru_4O_{12}}$ clear signatures of several dispersionless intensities can be observed. These features are most likely related to transitions between the CEF sublevels and correspond to splittings of 41, 92, and 110 K. However, with these values and also taking into account the results of the specific heat measurements, a corresponding term scheme as predicted for $\mathrm{Pr^{3+}}$ in a cubic CEF cannot be established. It is not clear if the reason for this is a more complex splitting or if not all inelastic intensities are really due to transitions within the CEF sublevels. In this context it has to be noted that regarding the formal valences within $A\mathrm{Cu_3Ru_4O_{12}}$ (A = Pr, Nd) and the results from EXAFS [48] and XANES [66] measurements, the presence of a significant amount of $\mathrm{Cu^{+}}$ has to be considered which could lead to a lowering of the CEF symmetry.

Investigations by zero-field and weak transverse field μSR spectroscopy turn out to be insensitive for the confirmation of the structural anomaly at 154 K which means that

this transition takes place without shifting atomic positions significantly. Besides, only an interaction between the muon spin and the nuclear moments of Cu could be detected. The μSR spectra of $A\mathrm{Cu_3Ru_4O_{12}}$ (A = Pr, Nd) are dominated by the interaction with the rare-earth moments, both electronic and nuclear. Therefore, a double-relaxation formalism has to be utilized for fitting. The electronic term shows exponential relaxation - typical for a paramagnet - with a steep increase of the relaxation rate with decreasing temperature.

Both the Kadowaki-Woods [46, 47] and the Wilson [45] ratio localize the copper ruthenates among conventional f-electron based heavy-fermion systems and related d-derived compounds. Apparently, the electronic tuning of the system by changing the valence at the A-site does not weaken the Kondo lattice as the heavy-mass behavior is retained. Taking into account the XANES measurements [66, 77] which identify the ruthenium ions in a tetravalent state, independent of the A-site valence, one can conclude that the Kondo lattice itself is built up by ruthenium ions which are screened by delocalized copper electrons. This places the copper-ruthenates $A\mathrm{Cu_3Ru_4O_{12}}$ (A = Na, Ca, Sr, La, Pr, Nd) among the few d-electron derived systems in which the heavy-mass behavior is caused by the Kondo effect and not by frustration.[216] The non-Fermi liquid properties of the Ca and Sr compound include deviations from a T^2 power law of the resistivity depending on the sample and also a logarithmic divergence of the specific heat with an unresolved upturn in C/T toward lowest temperatures. It is unclear if these two compounds intrinsically are in the proximity to AFM order and at the edge of a zero-temperature quantum phase transition or could be tuned to such one. In this context it has to mentioned that small deviations from the stoichiometry can have a strong influence on the temperature dependence of physical quantities and are typical in canonical heavy-fermion compounds close to a quantum critical point. In both compounds the magnetic field favors the Fermi liquid state, demonstrated by a recovery of the T^2 dependence of the resistivity, a phenomenon also observed in the classic intermetallic $\mathrm{YbRh_2Si_2}$.[197]

The behavior of the magnetic rare-earth compounds (Pr, Nd) due to the crystal field seems to be quite independent of the heavy-fermion formation, i.e. that the magnetism of the rare-earth subsystem can be examined separately. In the Kramers-ion system $\mathrm{NdCu_3Ru_4O_{12}}$ the situation is relatively straightforward. The entropy associated with the lowest Schottky anomaly in the specific heat amounts $\mathrm{R}\ln 3$ and can be identified with a transition from a doublet ground state to an excited quartet state within the

predictions made by standard crystal field theory.[215, 127] Here, on application of a magnetic field, a linear Zeeman effect can be observed for the splitting. In $PrCu_3Ru_4O_{12}$, however, the circumstances are more complicated. Here, the transition in the specific heat with an associated entropy of $R \ln 2$ could be explained by a triplet-triplet pairing of the two lowest multiplets of the Pr^{3+} ion, however, in contradiction to standard theory. A more plausible explanation could be a more complex splitting caused by local defects which lead to a breaking of the $m\bar{3}$ (T_h) CEF symmetry, e.g. by the presence of different species of Cu in terms of Cu^{+} and Cu^{2+}. These come into play during considerations of formal valencies, the evaluation of the susceptibility, and conclusions from EXAFS/XANES/TGA measurements.[48, 66, 77] When additionally taking into account the quadratic field dependence of the splitting of the peak in the specific heat (i.e. a non-linear Zeeman effect), it could also be speculated that the mentioned anomaly might be related to a quadrupolar ordering or quadrupolar Kondo effect. Such effects were found in several cubic Pr-intermetallic compounds recently of which the ground state was identified with the Γ_3 doublet.[206, 207, 208, 209, 210, 211, 212, 213] And indeed, recent systematic investigations on the substitution series $La_{1-x}Pr_xCu_3Ru_4O_{12}$ show a non-cooperative single ion effect independent of the Pr concentration.[217] In order to shed more light on these unresolved problems further sophisticated measurements and analyses are in progress. This might help to solve the question, if we are dealing with collective or single ion effects.

7 Supplemental Material

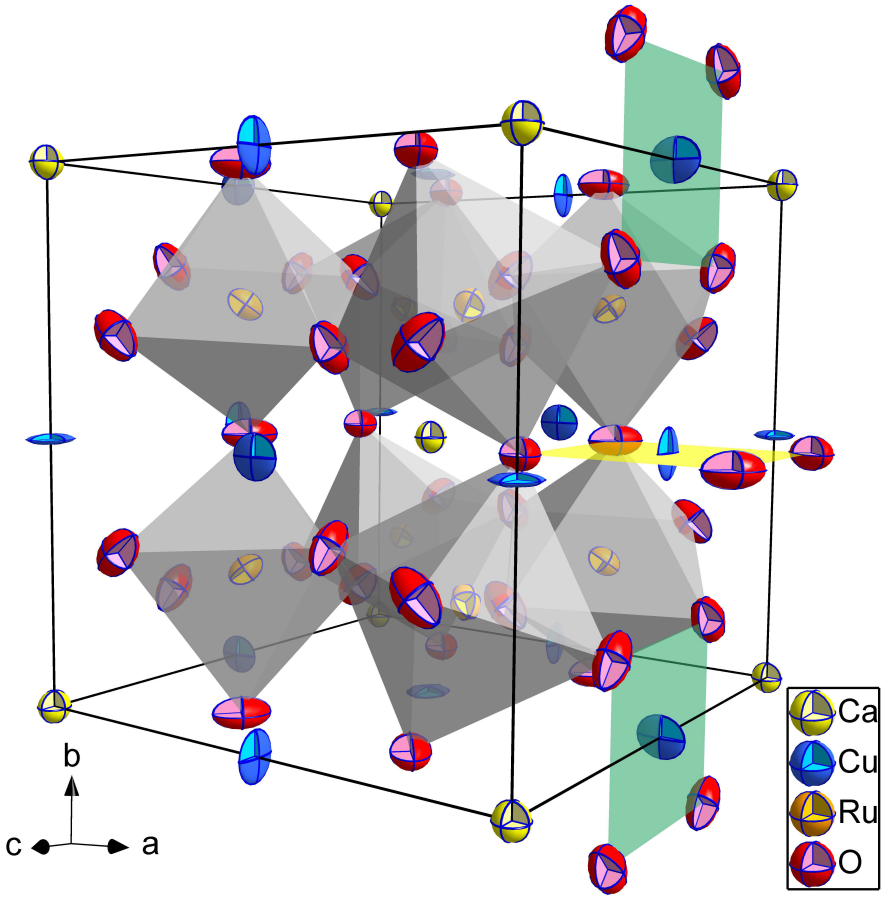

Figure 7.1: Unit cell of $CaCu_3Ru_4O_{12}$ at 254 K derived from NPD including plots of the thermal ellipsoids (99.9% probability level). The octahedra depict the tilted RuO_6 units. On the right cell face, the CuO_4 plaquettes are indicated by yellow/green planes.

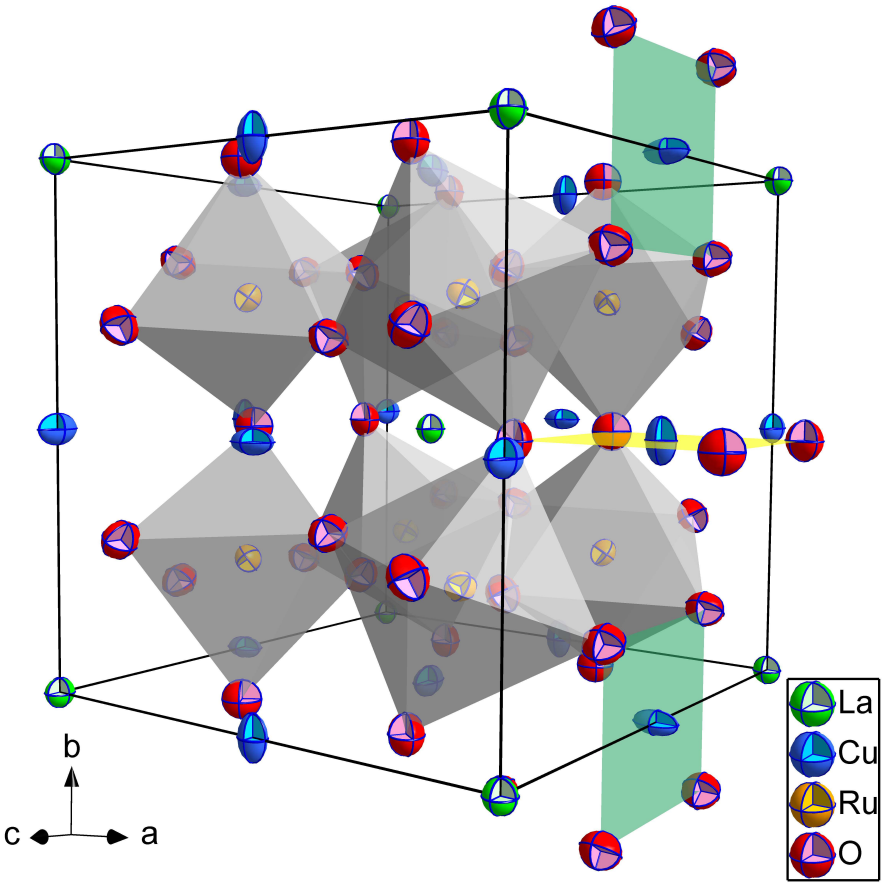

Figure 7.2: Unit cell of $LaCu_3Ru_4O_{12}$ at 175 K derived from NPD including plots of the thermal ellipsoids (99.9% probability level). The octahedra depict the tilted RuO_6 units. On the right cell face, the CuO_4 plaquettes are indicated by yellow/green planes.

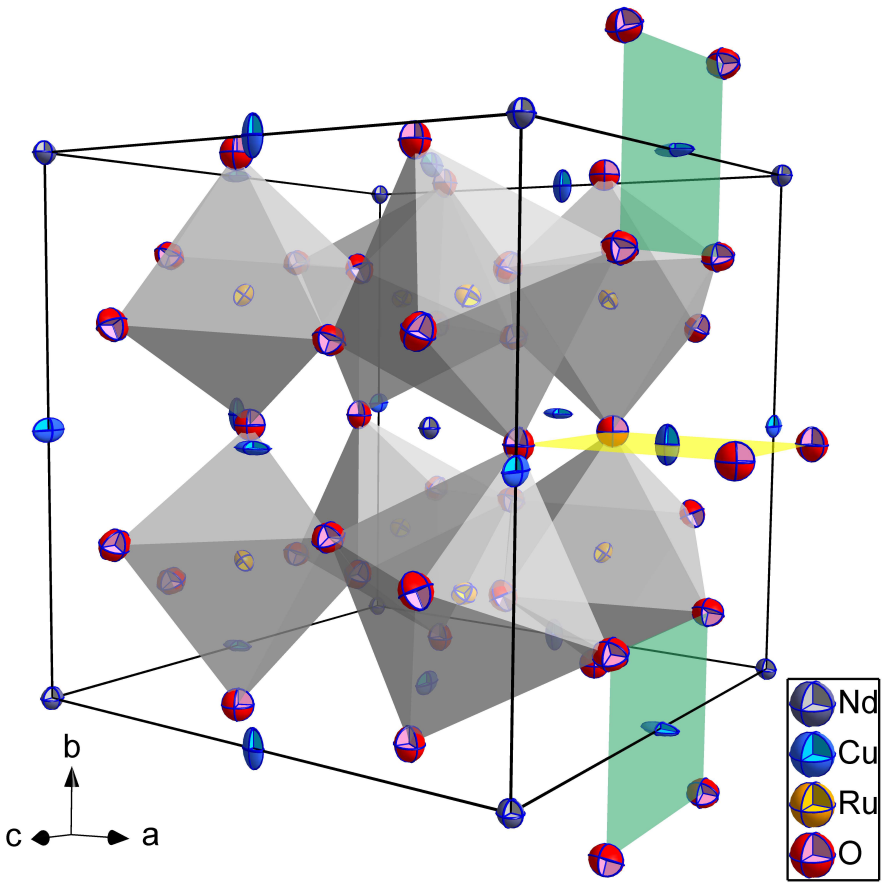

Figure 7.3: Unit cell of $NdCu_3Ru_4O_{12}$ at 175 K derived from NPD including plots of the thermal ellipsoids (99.9% probability level). The octahedra depict the tilted RuO_6 units. On the right cell face, the CuO_4 plaquettes are indicated by yellow/green planes.

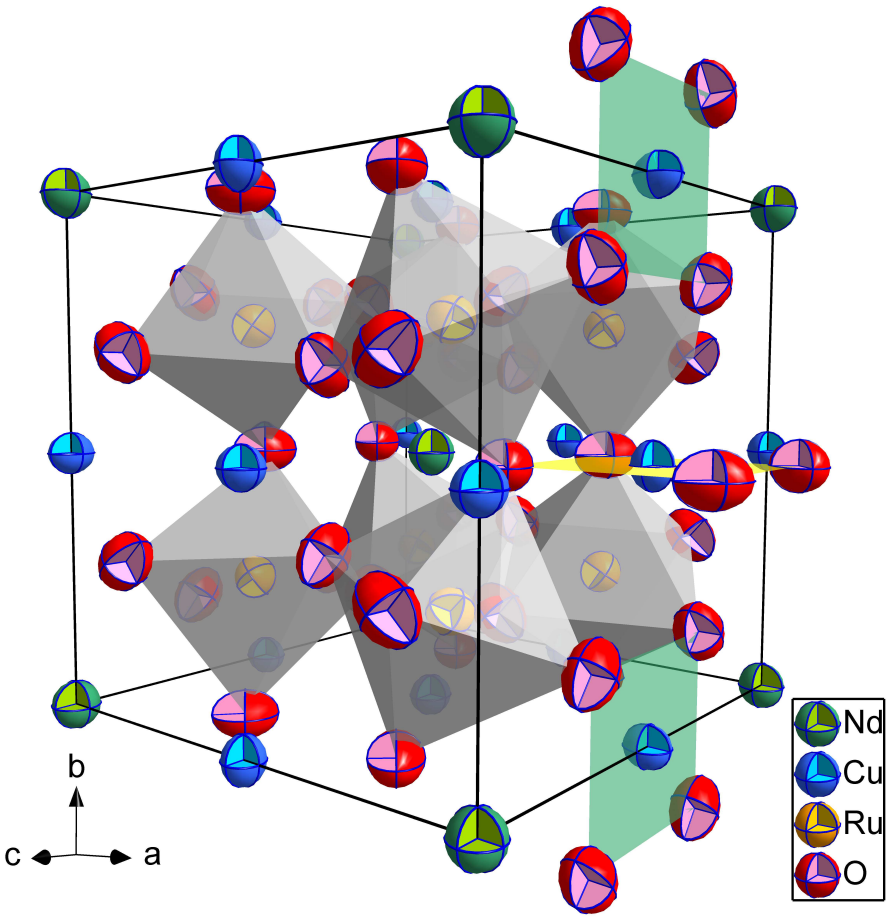

Figure 7.4: Unit cell of $NdCu_3Ru_4O_{12}$ at room temperature derived from XRD including plots of the thermal ellipsoids (99.9% probability level).[42] The octahedra depict the tilted RuO_6 units. On the right cell face, the CuO_4 plaquettes are indicated by yellow/green planes.

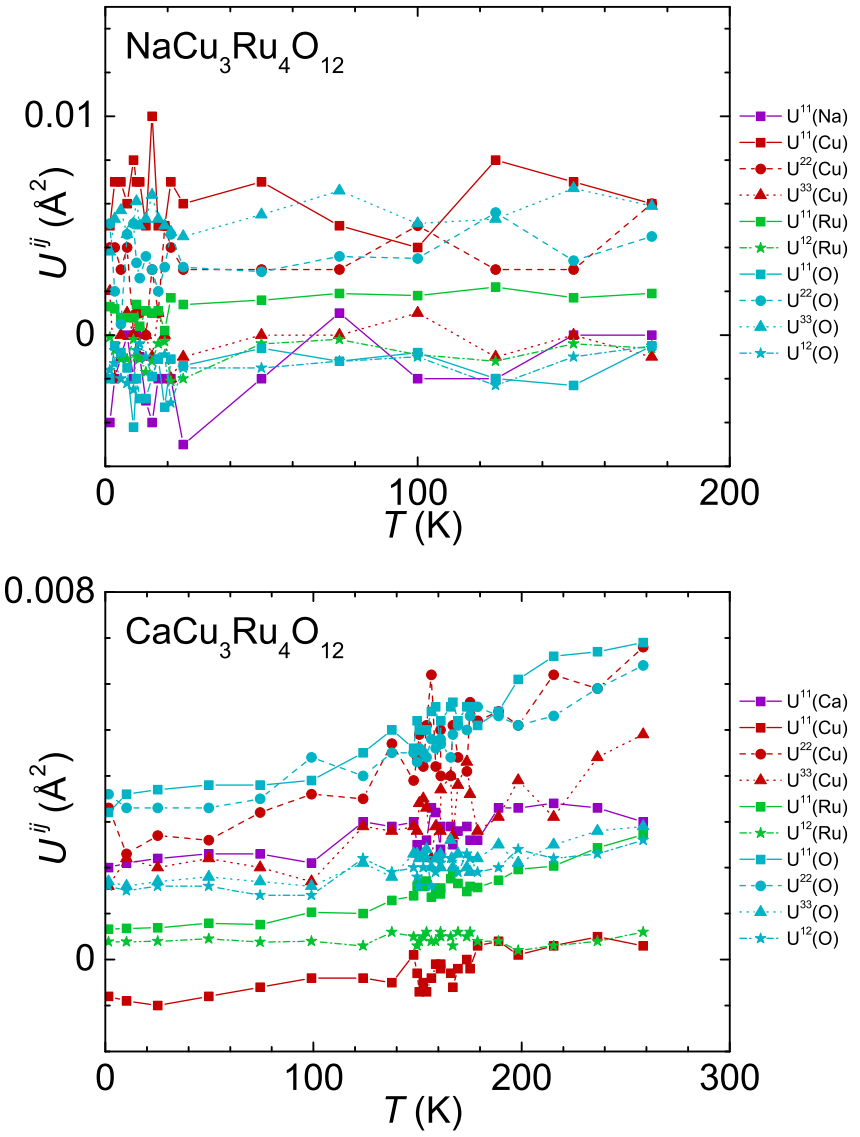

Figure 7.5: Temperature dependent anisotropic displacement factors U^{ij}_{cif} of $NaCu_3Ru_4O_{12}$ (upper frame) and $CaCu_3Ru_4O_{12}$ (lower frame) as resulting from the Rietveld refinement of the NPD measurements. Conventions according to Ref. [174].

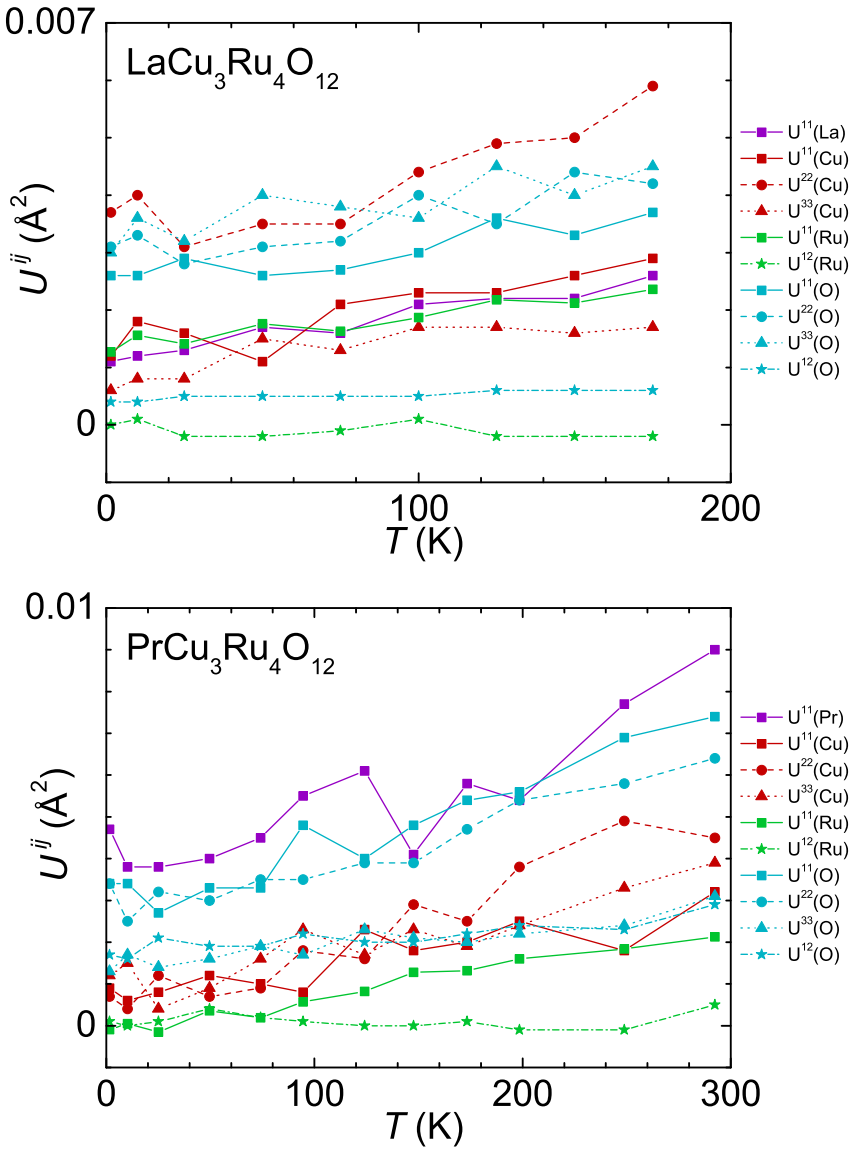

Figure 7.6: Temperature dependent anisotropic displacement factors U_{cif}^{ij} of $LaCu_3Ru_4O_{12}$ (upper frame) and $PrCu_3Ru_4O_{12}$ (lower frame) as resulting from the Rietveld refinement of the NPD measurements. Conventions according to Ref. [174].

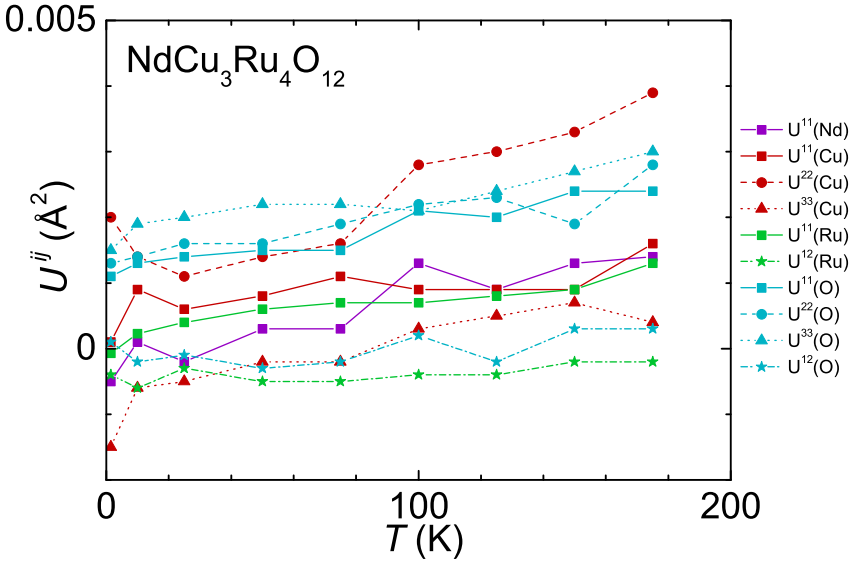

Figure 7.7: Temperature dependent anisotropic displacement factors U^{ij}_{cif} of $NdCu_3Ru_4O_{12}$ as resulting from the Rietveld refinement of the NPD measurements. Conventions according to Ref. [174].

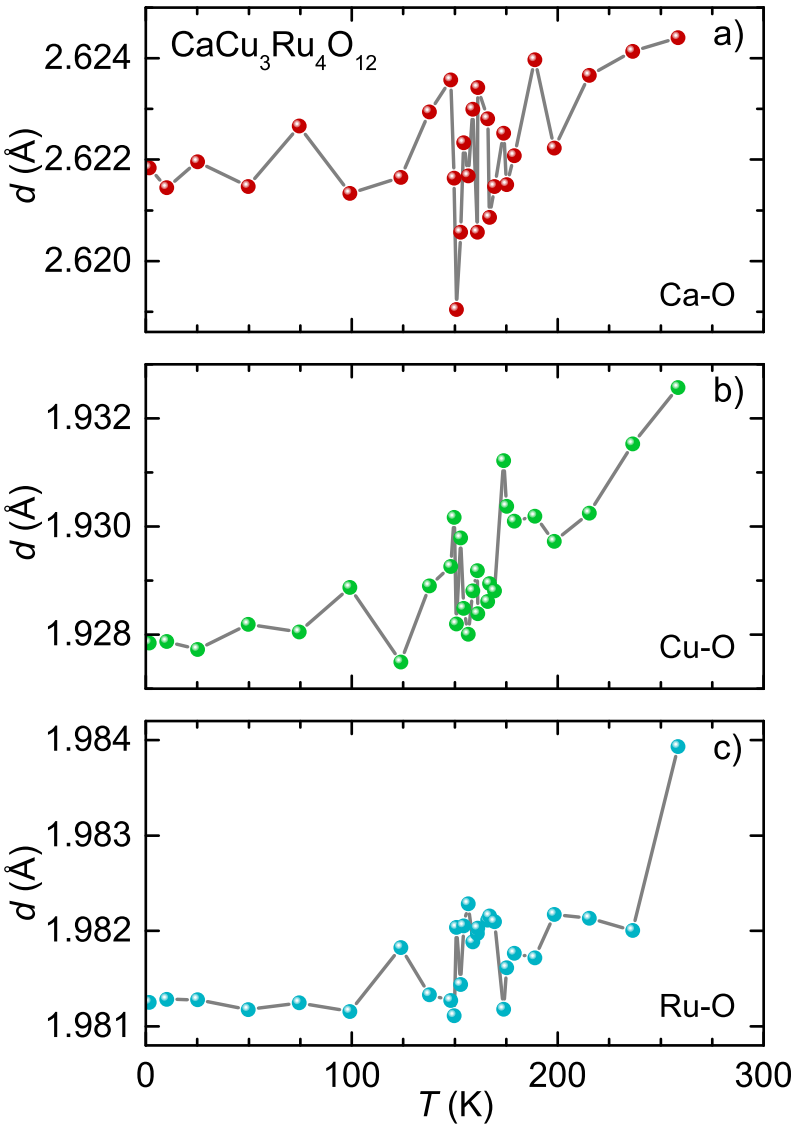

Figure 7.8: Temperature dependent metal-oxygen distances d in $CaCu_3Ru_4O_{12}$ as resulting from the Rietveld refinement of the NPD measurements (frame a: Ca-O, frame b: Cu-O, frame c: Ru-O).

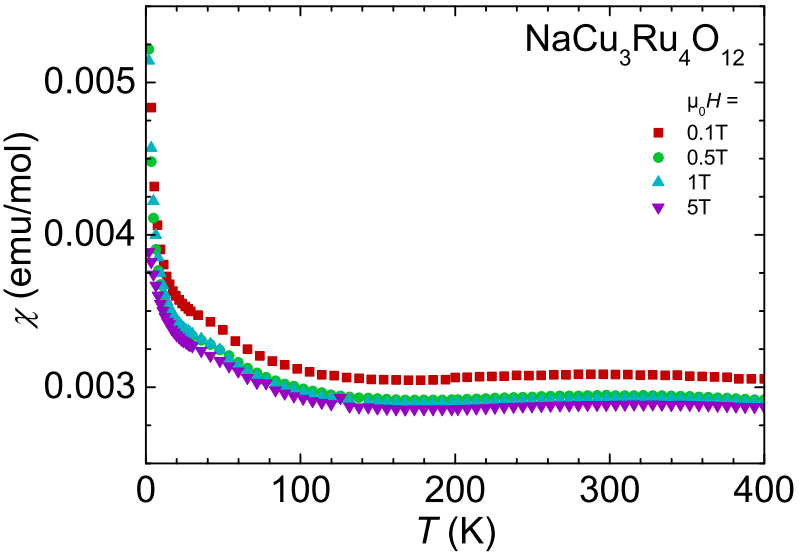

Figure 7.9: Temperature dependent magnetic susceptibility χ of $NaCu_3Ru_4O_{12}$ in various external magnetic fields.

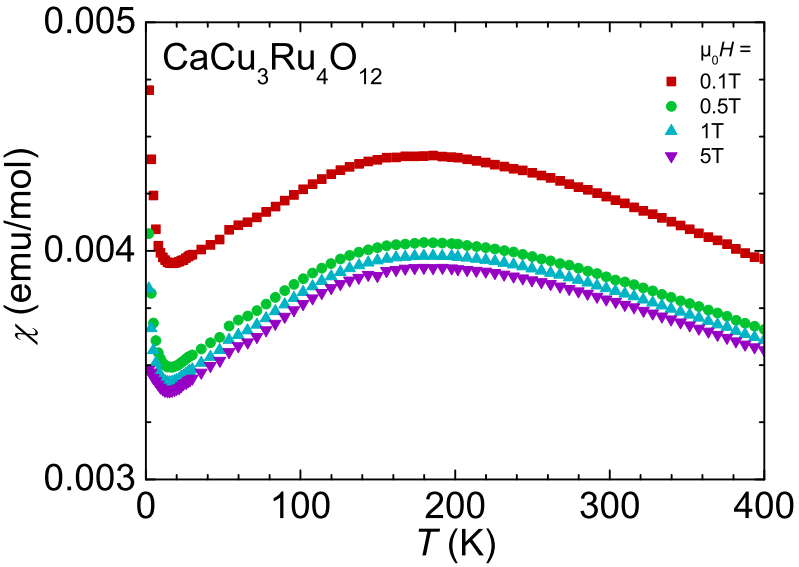

Figure 7.10: Temperature dependent magnetic susceptibility χ of $CaCu_3Ru_4O_{12}$ in various external magnetic fields.

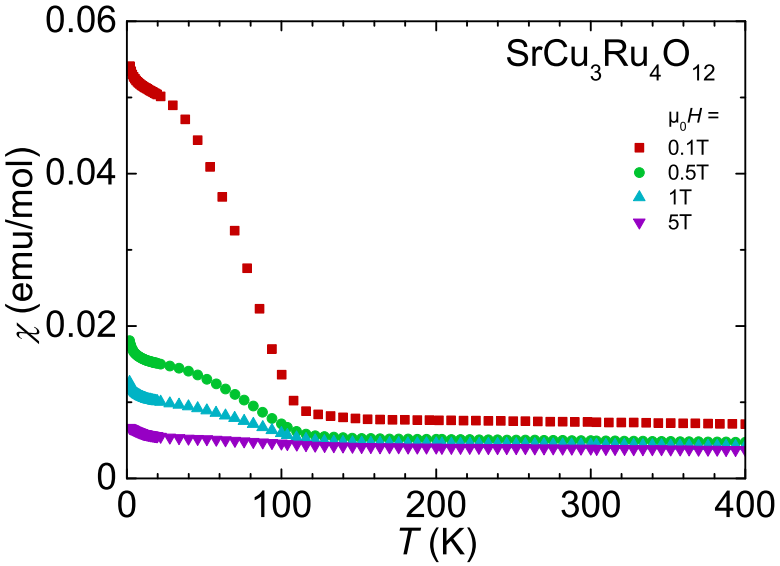

Figure 7.11: Temperature dependent magnetic susceptibility χ of $SrCu_3Ru_4O_{12}$ in various external magnetic fields.

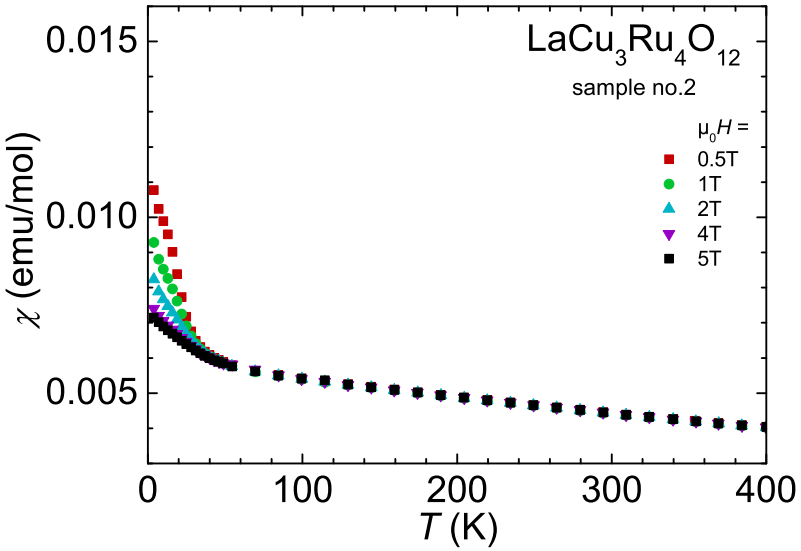

Figure 7.12: Temperature dependent magnetic susceptibility χ of $LaCu_3Ru_4O_{12}$ in various external magnetic fields.

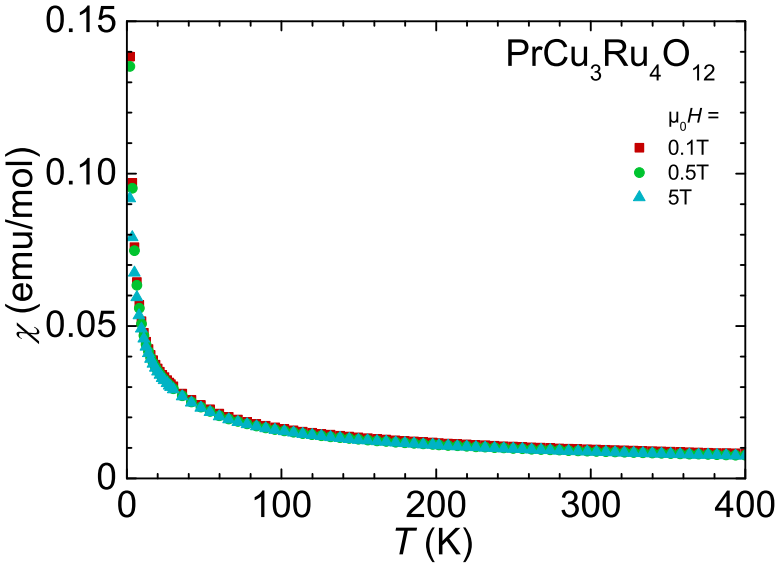

Figure 7.13: Temperature dependent magnetic susceptibility χ of $PrCu_3Ru_4O_{12}$ in various external magnetic fields.

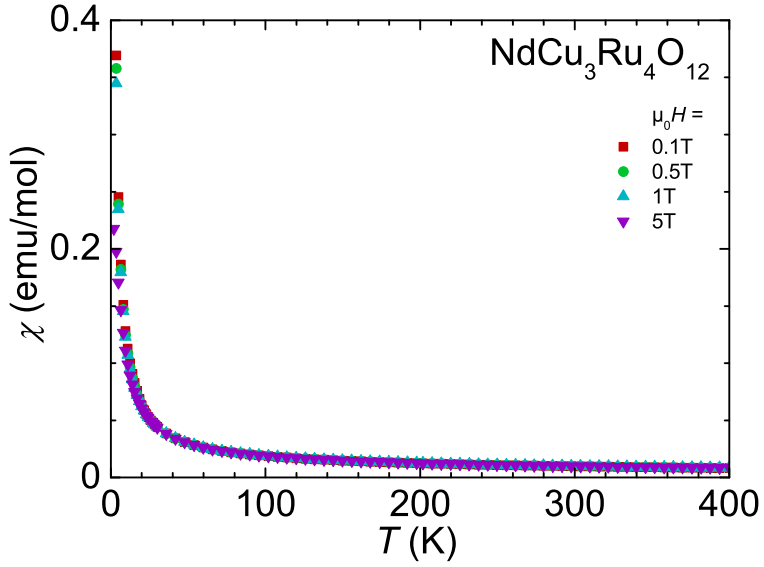

Figure 7.14: Temperature dependent magnetic susceptibility χ of $NdCu_3Ru_4O_{12}$ in various external magnetic fields.

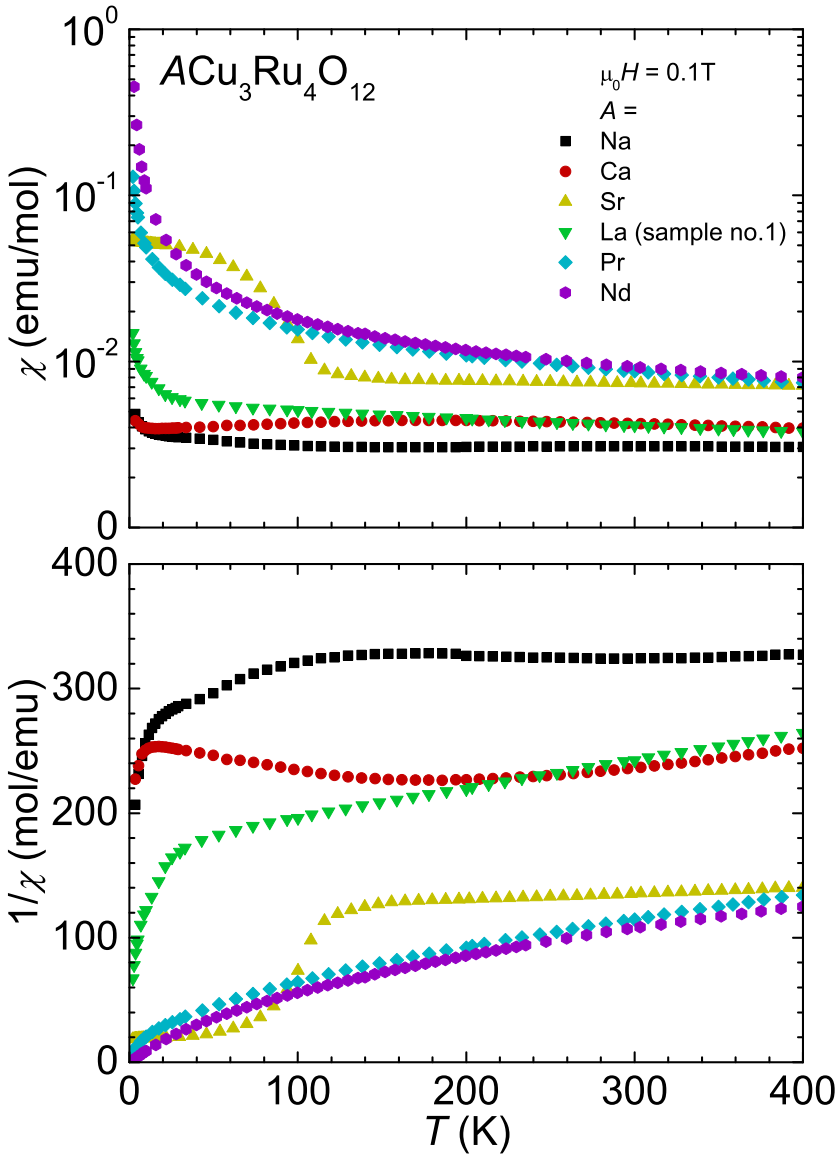

Figure 7.15: Temperature dependent magnetic susceptibility χ (upper frame, semi-logarithmic plot) and its inverse $1/\chi$ (lower frame, linear plot) of $A\mathrm{Cu_3Ru_4O_{12}}$ (A = Na, Ca, Sr, La, Pr, Nd) in an external field of 0.1 T.

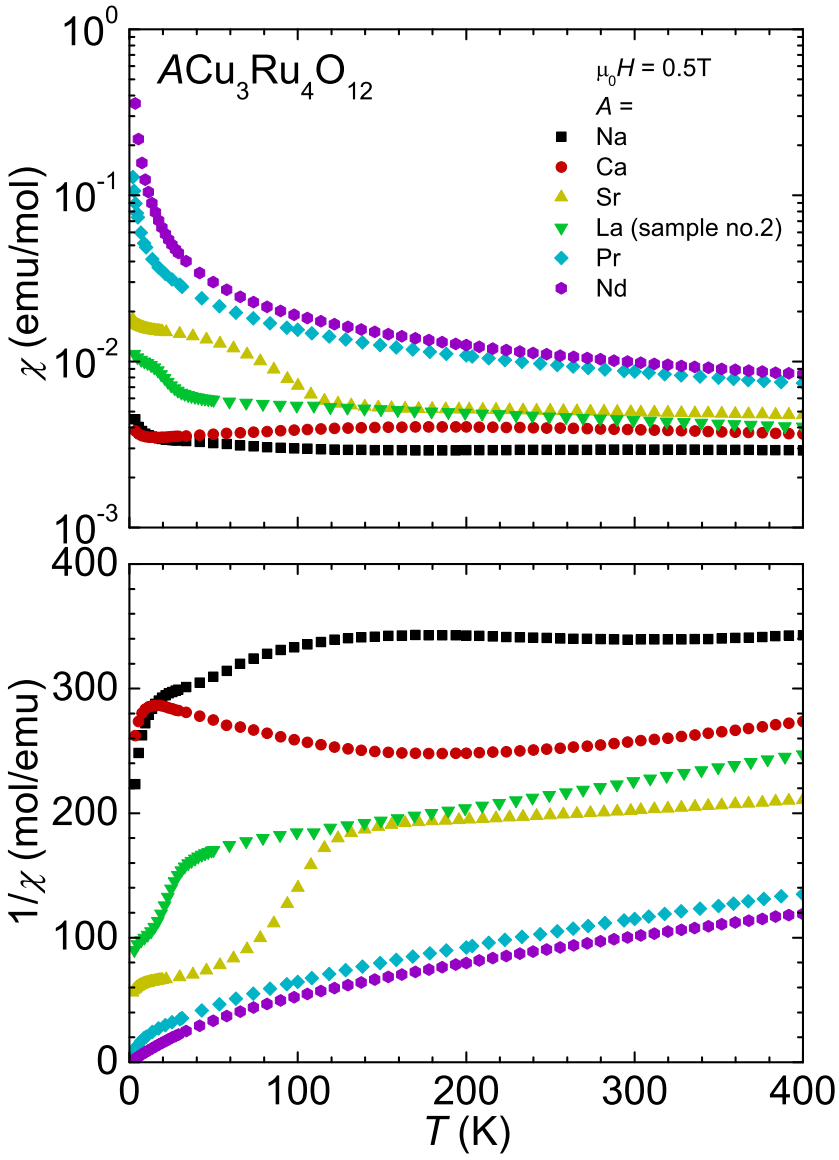

Figure 7.16: Temperature dependent magnetic susceptibility χ (upper frame, semi-logarithmic plot) and its inverse $1/\chi$ (lower frame, linear plot) of $A\mathrm{Cu_3Ru_4O_{12}}$ (A = Na, Ca, Sr, La, Pr, Nd) in an external field of 0.5 T.

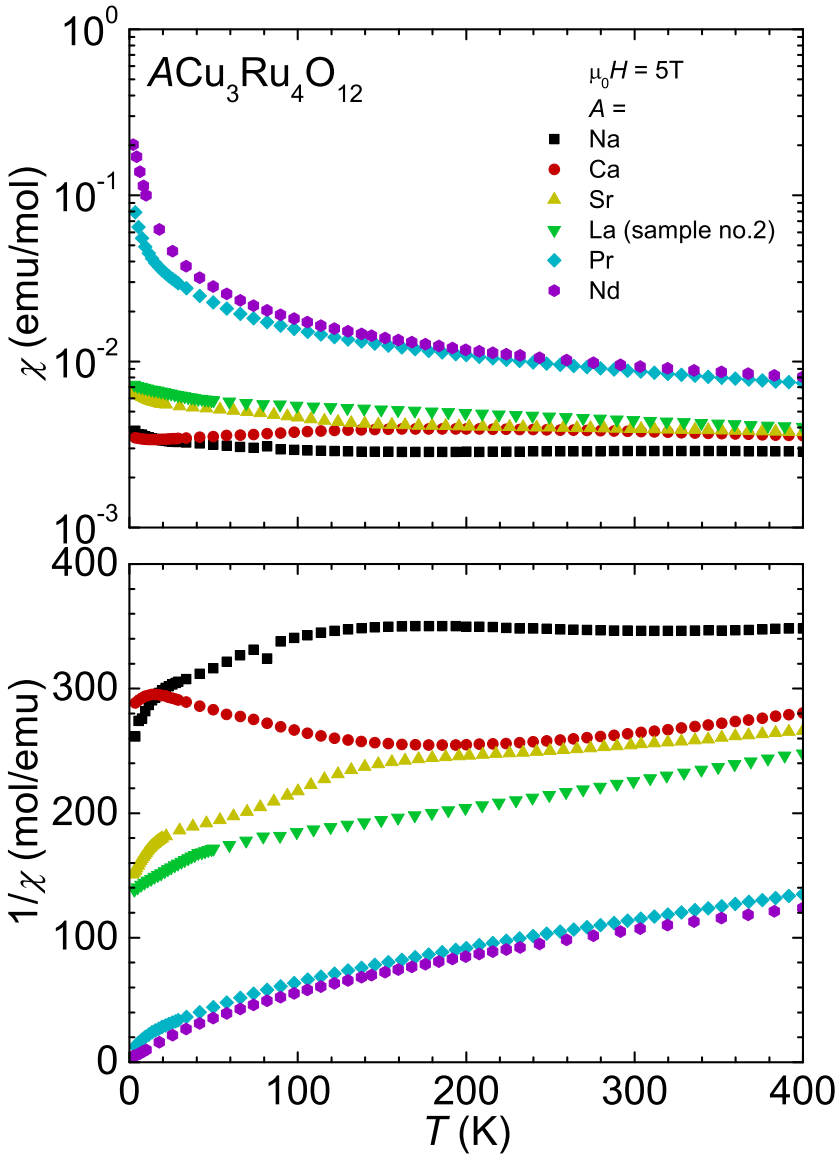

Figure 7.17: Temperature dependent magnetic susceptibility χ (upper frame, semi-logarithmic plot) and its inverse $1/\chi$ (lower frame, linear plot) of $A\mathrm{Cu_3Ru_4O_{12}}$ (A = Na, Ca, Sr, La, Pr, Nd) in an external field of 5 T.

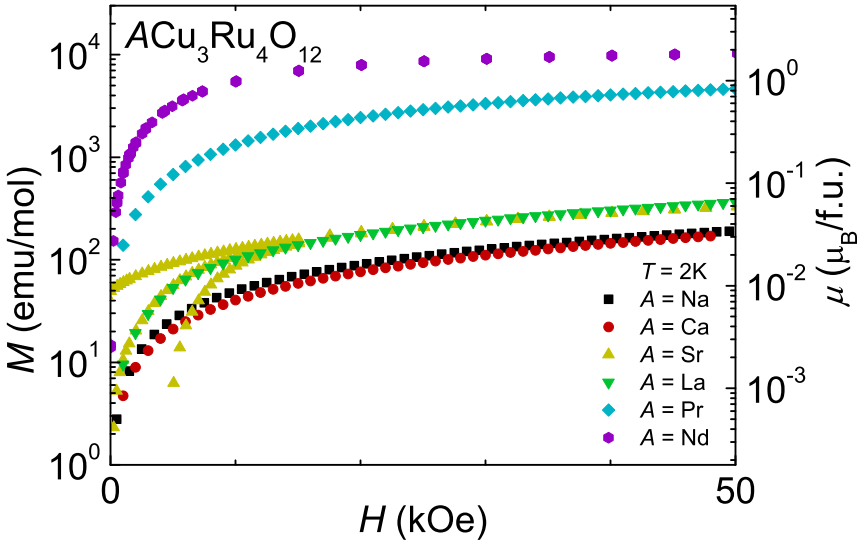

Figure 7.18: Field dependent magnetization M of $A\mathrm{Cu_3Ru_4O_{12}}$ (A = Na, Ca, Sr, La, Pr, Nd) on a semi-logarithmic scale at 2 K in units of emu/mol (left scale) and μ_B/f.u. (right scale).

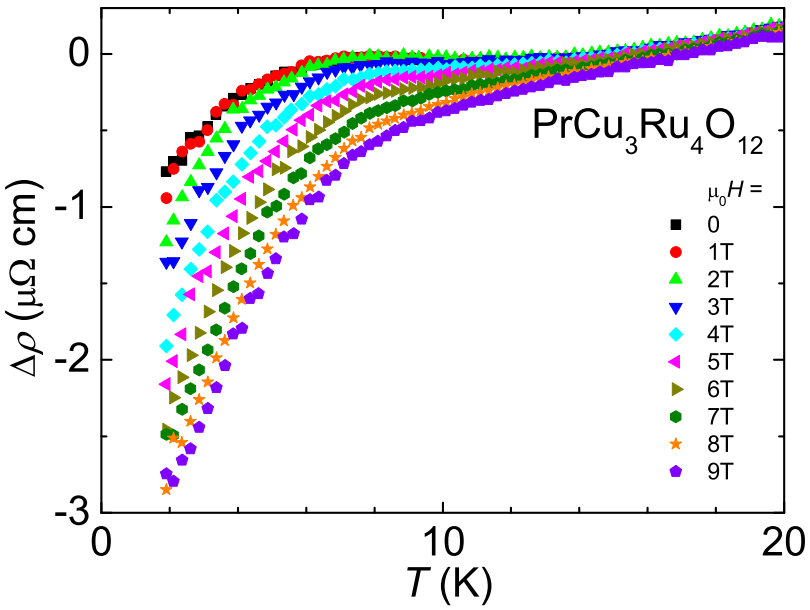

Figure 7.19: Temperature dependent resistivity $\Delta\rho$ of $\mathrm{PrCu_3Ru_4O_{12}}$ in various magnetic fields minus residual resistivity and quadratic contribution as derived from the fit to the zero-field data according to $\rho(T) = \rho_0 + AT^2$.

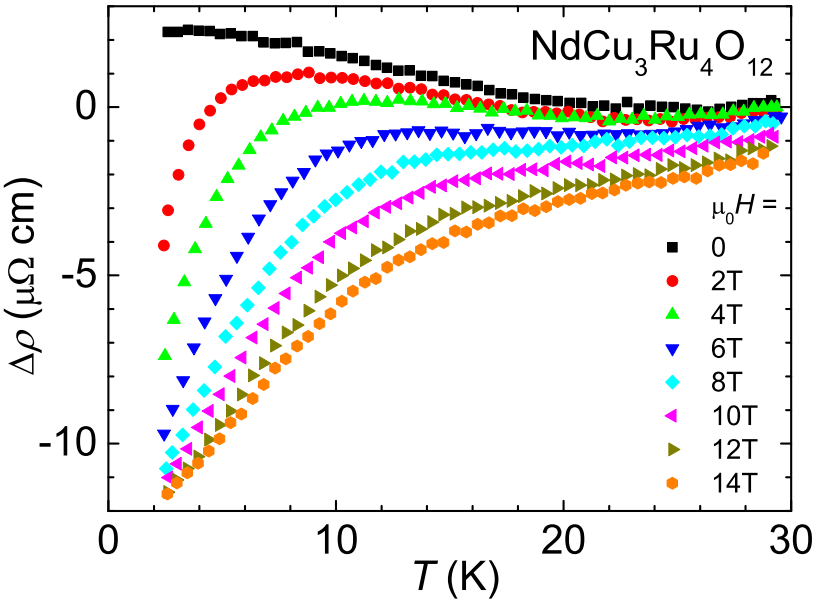

Figure 7.20: Temperature dependent resistivity $\Delta\rho$ of $NdCu_3Ru_4O_{12}$ in various magnetic fields minus residual resistivity and quadratic contribution as derived from the fit to the zero-field data according to $\rho(T) = \rho_0 + AT^2$.

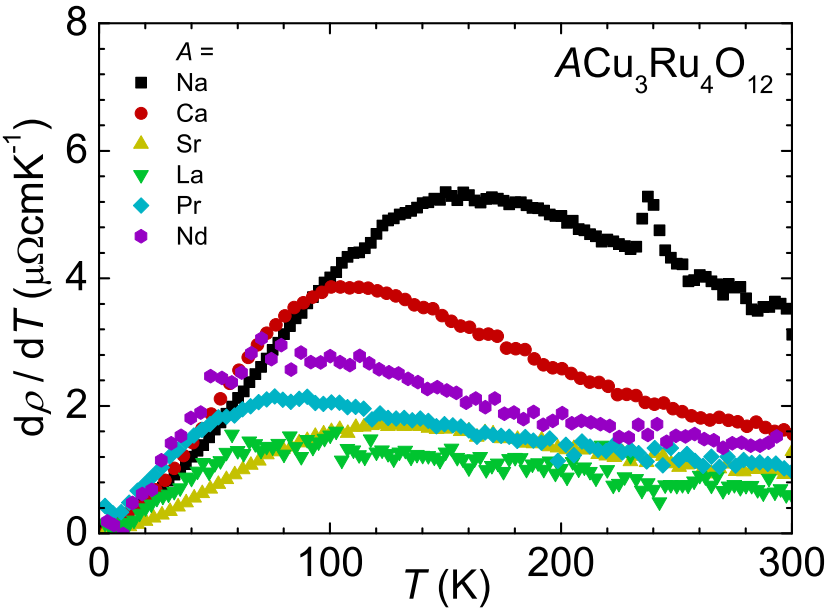

Figure 7.21: Derivative of the resistivity with respect to temperature $d\rho/dT$ of polycrystalline $ACu_3Ru_4O_{12}$ (A = Na, Ca, Sr, La, Pr, Nd) in zero magnetic field (see text for measurement details). A Savitsky-Golay smoothing algorithm [218] is utilized for the data of $NaCu_3Ru_4O_{12}$, $SrCu_3Ru_4O_{12}$, and $LaCu_3Ru_4O_{12}$.

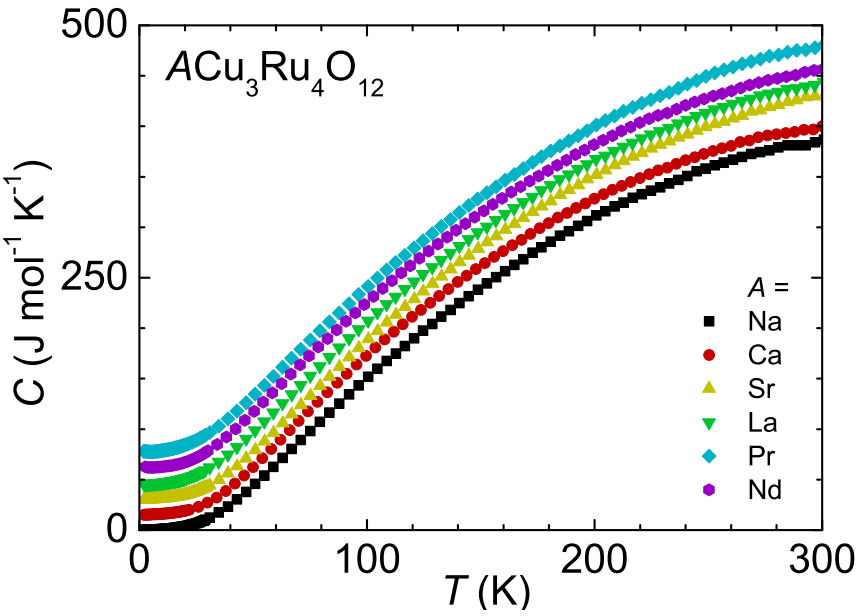

Figure 7.22: Temperature dependent specific heat C of polycrystalline $A\mathrm{Cu_3Ru_4O_{12}}$ (A = Na, Ca, Sr, La, Pr, Nd). The data are shifted for clarity (Ca: +15, Sr: +30, La: +45, Nd: +60, Pr: +75, in units of $\mathrm{Jmol^{-1}K^{-1}}$).

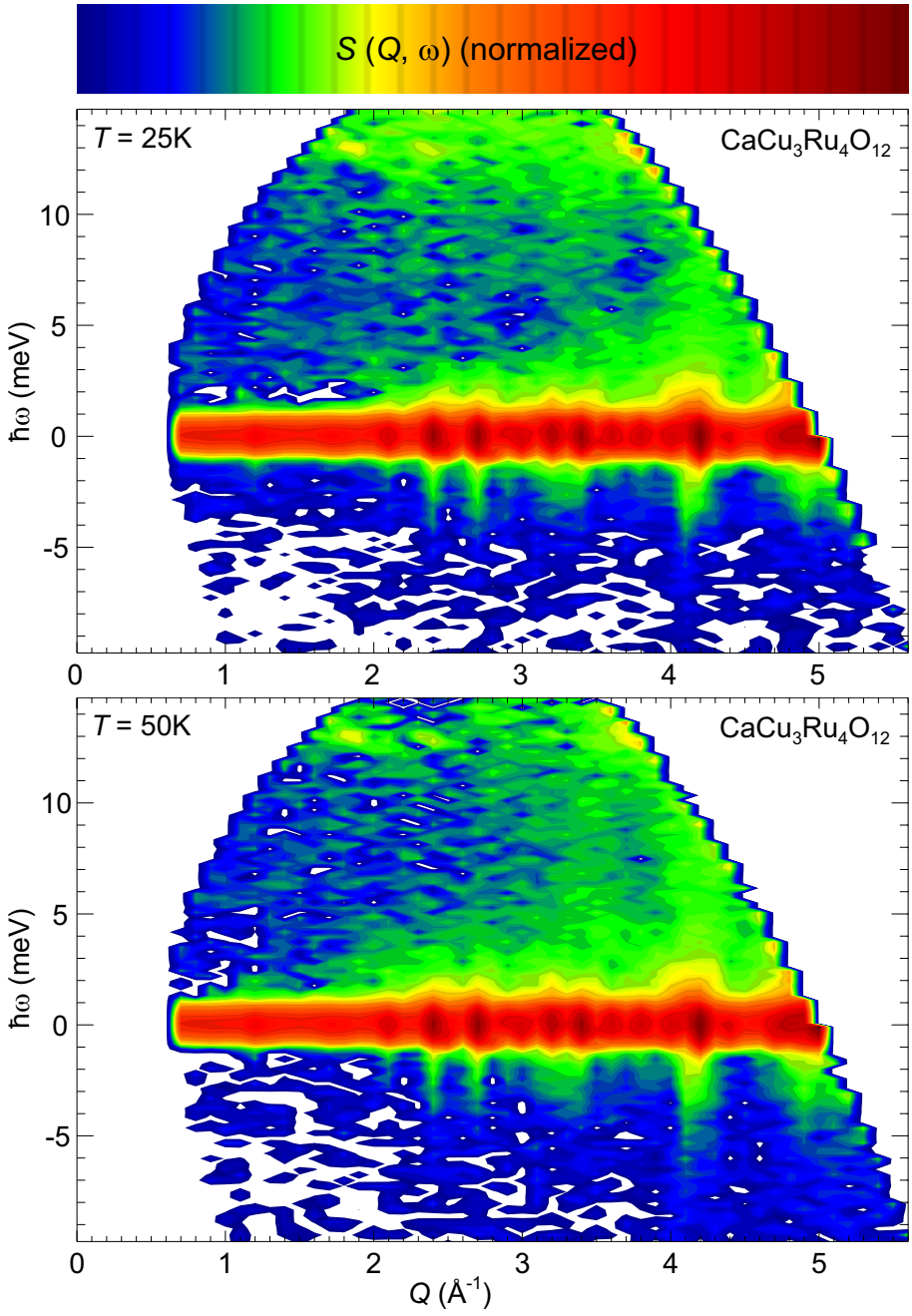

Figure 7.23: Contour plot of the dynamic structure factor $S(Q,\omega)$ of $CaCu_3Ru_4O_{12}$ at 25 K (frame a) and 50 K (frame b). Intensities are shown by a rainbow-color coding on a logarithmic scale to indicate increasing intensities from green via yellow and orange to light red above the background level shown in blue. The red riff around $\hbar\omega \approx 0$ represents elastic incoherent scattering including nuclear Bragg reflections (dark red spots). The area with positive $\hbar\omega$ stands for neutrons loosing energy, negative $\hbar\omega$ means energy gain for neutrons.

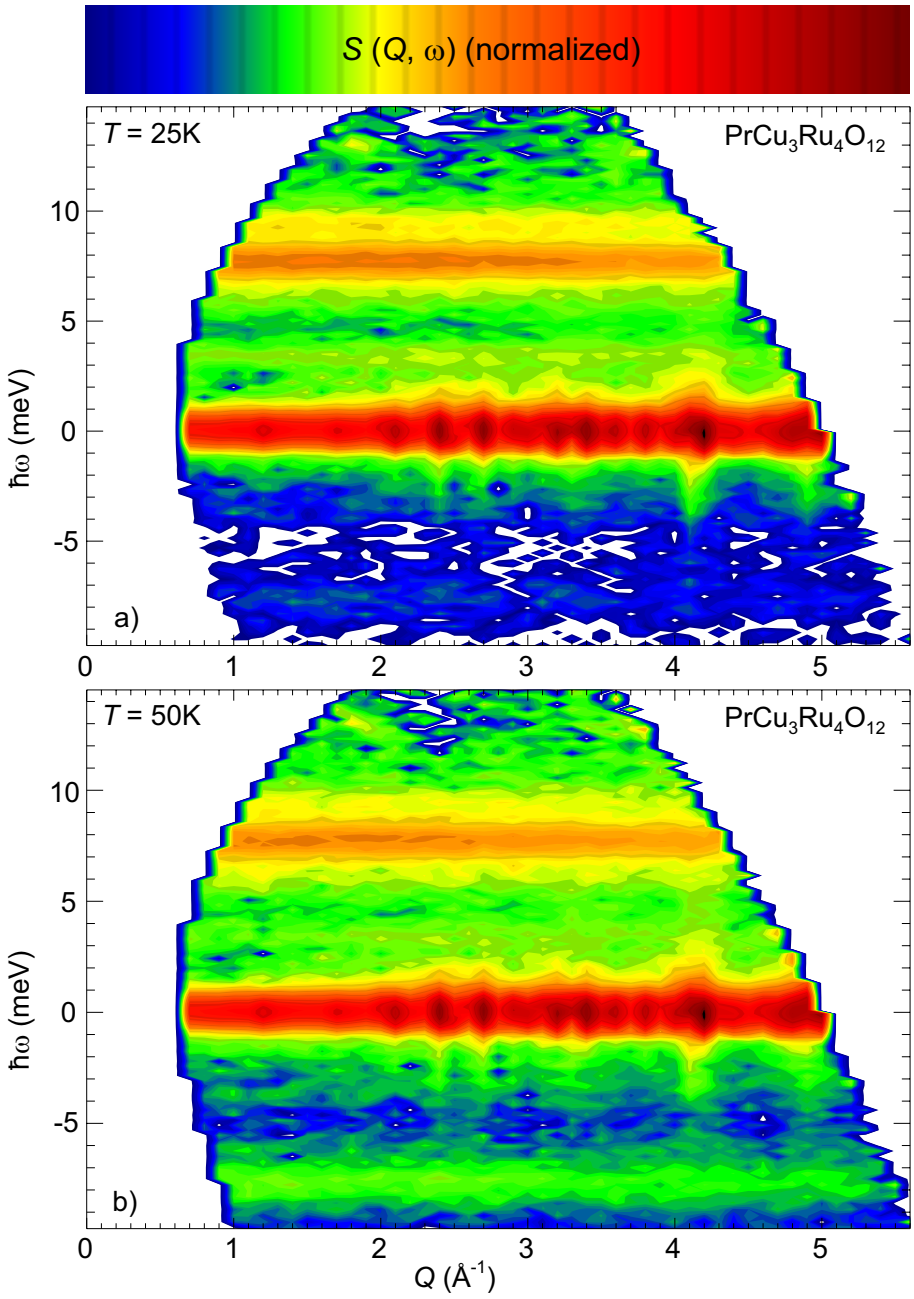

Figure 7.24: Contour plot of the dynamic structure factor $S(Q,\omega)$ of $PrCu_3Ru_4O_{12}$ at 25 K (frame a) and 50 K (frame b). Intensities are shown by a rainbow-color coding on a logarithmic scale to indicate increasing intensities from green via yellow and orange to light red above the background level shown in blue. The red riff around $\hbar\omega \approx 0$ represents elastic incoherent scattering including nuclear Bragg reflections (dark red spots). The area with positive $\hbar\omega$ stands for neutrons loosing energy, negative $\hbar\omega$ means energy gain for neutrons.

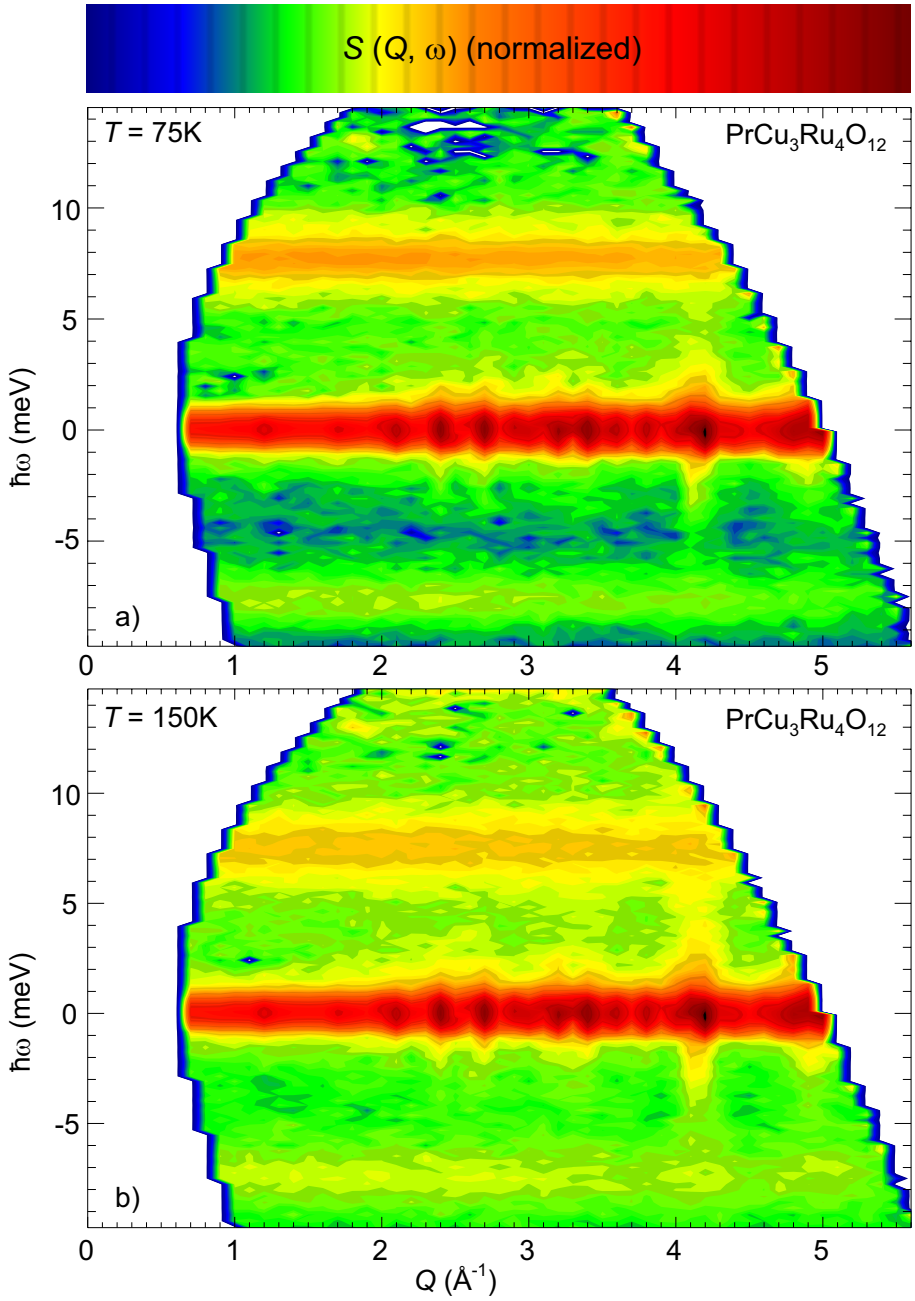

Figure 7.25: Contour plot of the dynamic structure factor $S(Q,\omega)$ of $PrCu_3Ru_4O_{12}$ at 75 K (frame a) and 150 K (frame b). Intensities are shown by a rainbow-color coding on a logarithmic scale to indicate increasing intensities from green via yellow and orange to light red above the background level shown in blue. The red riff around $\hbar\omega \approx 0$ represents elastic incoherent scattering including nuclear Bragg reflections (dark red spots). The area with positive $\hbar\omega$ stands for neutrons loosing energy, negative $\hbar\omega$ means energy gain for neutrons.

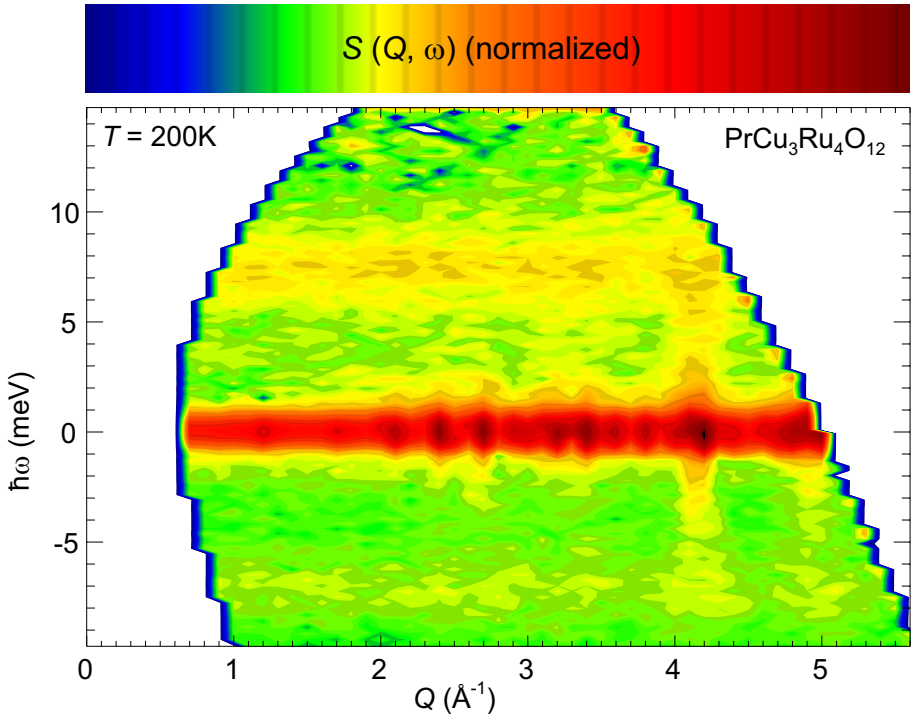

Figure 7.26: Contour plot of the dynamic structure factor $S(Q,\omega)$ of $PrCu_3Ru_4O_{12}$ at 200 K. Intensities are shown by a rainbow-color coding on a logarithmic scale to indicate increasing intensities from green via yellow and orange to light red above the background level shown in blue. The red riff around $\hbar\omega \approx 0$ represents elastic incoherent scattering including nuclear Bragg reflections (dark red spots). The area with positive $\hbar\omega$ stands for neutrons loosing energy, negative $\hbar\omega$ means energy gain for neutrons.

Bibliography

[1] Gustav Rose. Beschreibung einiger neuen Mineralien des Urals. *Annalen der Physik*, 124(12):551–573, 1839.

[2] B. Wul. Dielectric Constants of Some Titanates. *Nature*, 156(3964):480–480, 1945.

[3] A. von Hippel, R. G. Breckenridge, F. G. Chesley, and Laszlo Tisza. High Dielectric Constant Ceramics. *Industrial & Engineering Chemistry*, 38(11):1097–1109, 1946.

[4] R. von Helmolt, J. Wecker, B. Holzapfel, L. Schultz, and K. Samwer. Giant Negative Magnetoresistance in Perovskite like $La_{2/3}Ba_{1/3}MnO_x$ Ferromagnetic Films. *Physical Review Letters*, 71:2331–2333, October 1993.

[5] T. Kimura, T. Goto, H. Shintani, K. Ishizaka, T. Arima, and Y. Tokura. Magnetic Control of Ferroelectric Polarization. *Nature*, 426(6962):55–58, November 2003.

[6] J. H. Haeni, P. Irvin, W. Chang, R. Uecker, P. Reiche, Y. L. Li, S. Choudhury, W. Tian, M. E. Hawley, B. Craigo, A. K. Tagantsev, X. Q. Pan, S. K. Streiffer, L. Q. Chen, S. W. Kirchoefer, J. Levy, and D. G. Schlom. Room-Temperature Ferroelectricity in Strained $SrTiO_3$. *Nature*, 430(7001):758–761, August 2004.

[7] J. G. Bednorz and K. A. Müller. Possible High-T_c Superconductivity in the Ba-La-Cu-O System. *Zeitschrift für Physik B - Condensed Matter*, 64(2):189–193, 1986.

[8] M. K. Wu, J. R. Ashburn, C. J. Torng, P. H. Hor, R. L. Meng, L. Gao, Z. J. Huang, Y. Q. Wang, and C. W. Chu. Superconductivity at 93 K in a New Mixed-Phase Y-Ba-Cu-O Compound System at Ambient Pressure. *Physical Review Letters*, 58:908–910, March 1987.

[9] V. M. Goldschmidt. Die Gesetze der Krystallochemie. *Naturwissenschaften*, 14(21):477–485, 1926.

[10] A. M. Glazer. Classification of Tilted Octahedra in Perovskites. *Acta Crystallographica Section B*, 28(11):3384–3392, November 1972.

[11] P. M. Woodward. Octahedral Tilting in Perovskites. I. Geometrical Considerations. *Acta Crystallographica Section B*, 53(1):32–43, February 1997.

[12] P. M. Woodward. Octahedral Tilting in Perovskites. II. Structure Stabilizing Forces. *Acta Crystallographica Section B*, 53(1):44–66, February 1997.

[13] S. G. Ebbinghaus. On the Structural and Phenomenological Diversity of Perovskites Containing 4*d* and 5*d* Transition Metals. Habilitationsschrift, Universität Augsburg, 2006.

[14] H. A. Jahn and E. Teller. Stability of Polyatomic Molecules in Degenerate Electronic States. I. Orbital Degeneracy. *Proceedings of the Royal Society of London - Series A - Mathematical and Physical Sciences*, 161(905):220–235, July 1937.

[15] U. Schwingenschlögl, V. Eyert, and U. Eckern. Octahedral Tilting in $A\mathrm{Cu_3Ru_4O_{12}}$ (A = Na, Ca, Sr, La, Nd). *Chemical Physics Letters*, 370(5-6):719–724, March 2003.

[16] M. N. Deschizeaux, J. C. Joubert, A. Vegas, A. Collomb, J. Chenavas, and M. Marezio. Synthesis and Crystal Structure of $(\mathrm{ThCu_3})(\mathrm{Mn_2^{3+}Mn_2^{4+}})\mathrm{O_{12}}$, A New Ferrimagnetic Perovskite-Like Compound. *Journal of Solid State Chemistry*, 19(1):45–51, September 1976.

[17] Graham King and Patrick M. Woodward. Cation Ordering in Perovskites. *Journal of Materials Chemistry*, 20(28):5785–5796, 2010.

[18] A. N. Vasil'ev and O. S. Volkova. New functional materials $AC_3B_4\mathrm{O_{12}}$ (Review). *Low Temperature Physics*, 33(11):895–914, 2007.

[19] A. Deschanvres, B. Raveau, and F. Tollemer. Substitution of Copper for a Bivalent Metal in Titanates of Perovskite Type. *Bulletin de la Société Chimique de France*, (11):4077, 1967.

[20] M. Marezio, P. D. Dernier, J. Chenavas, and J. C. Joubert. High Pressure Synthesis and Crystal Structure of $\mathrm{NaMn_7O_{12}}$. *Journal of Solid State Chemistry*, 6(1):16–20, January 1973.

[21] B. Bochu, J. Chenavas, J. C. Joubert, and M. Marezio. High Pressure Synthesis and Crystal Structure of a New Series of Perovskite-Like Compounds $C\mathrm{Mn_7O_{12}}$ (C = Na, Ca, Cd, Sr, La, Nd). *Journal of Solid State Chemistry*, 11(2):88–93, 1974.

[22] B. Bochu, M. N. Deschizeaux, J. C. Joubert, A. Collomb, J. Chenavas, and M. Marezio. Synthèse et Caractérisation d'une Série de Titanates Perowskites Isotypes de $[\mathrm{CaCu_3}](\mathrm{Mn_4})\mathrm{O_{12}}$. *Journal of Solid State Chemistry*, 29(2):291–298, August 1979.

[23] M. A. Subramanian, D. Li, N. Duan, B. A. Reisner, and A. W. Sleight. High Dielectric Constant in $A\mathrm{Cu_3Ti_4O_{12}}$ and $A\mathrm{Cu_3Ti_3FeO_{12}}$ Phases. *Journal of Solid State Chemistry*, 151(2):323–325, May 2000.

[24] C. C. Homes, T. Vogt, S. M. Shapiro, S. Wakimoto, and A. P. Ramirez. Optical Response of High-Dielectric-Constant Perovskite-Related Oxide. *Science*, 293(5530):673–676, July 2001.

[25] P. Lunkenheimer, R. Fichtl, S. G. Ebbinghaus, and A. Loidl. Nonintrinsic Origin of the Colossal Dielectric Constants in $\mathrm{CaCu_3Ti_4O_{12}}$. *Physical Review B*, 70(17):172102, November 2004.

[26] Y. W. Long, N. Hayashi, T. Saito, M. Azuma, S. Muranaka, and Y. Shimakawa. Temperature-Induced A-B Intersite Charge Transfer in an A-Site-Ordered $\mathrm{LaCu_3Fe_4O_{12}}$ Perovskite. *Nature*, 458(7234):60–63, March 2009.

[27] J. Chenavas, J. C. Joubert, M. Marezio, and B. Bochu. The Synthesis and Crystal Structure of $\mathrm{CaCu_3Mn_4O_{12}}$: A New Ferromagnetic-Perovskite-Like Compound. *Journal of Solid State Chemistry*, 14(1):25–32, May 1975.

[28] Z. Zeng, M. Greenblatt, M. A. Subramanian, and M. Croft. Large Low-Field Magnetoresistance in Perovskite-type $\mathrm{CaCu_3Mn_4O_{12}}$ without Double Exchange. *Physical Review Letters*, 82(15):3164–3167, April 1999.

[29] R. Weht and W. E. Pickett. Magnetoelectronic Properties of a Ferrimagnetic Semiconductor: The Hybrid Cupromanganite $\mathrm{CaCu_3Mn_4O_{12}}$. *Physical Review B*, 65(1):014415, January 2002.

[30] W. Kobayashi, I. Terasaki, J. Takeya, I. Tsukada, and Y. Ando. A Novel Heavy-Fermion State in $CaCu_3Ru_4O_{12}$. *Journal of the Physical Society of Japan*, 73:2373–2376, 2004.

[31] S. Kondo, D. C. Johnston, C. A. Swenson, F. Borsa, A. V. Mahajan, L. L. Miller, T. Gu, A. I. Goldman, M. B. Maple, D. A. Gajewski, E. J. Freeman, N. R. Dilley, R. P. Dickey, J. Merrin, K. Kojima, G. M. Luke, Y. J. Uemura, O. Chmaissem, and J. D. Jorgensen. LiV_2O_4: A Heavy Fermion Transition Metal Oxide. *Physical Review Letters*, 78(19):3729–3732, May 1997.

[32] A. Krimmel, A. Loidl, M. Klemm, S. Horn, and H. Schober. Dramatic Change of the Magnetic Response in LiV_2O_4: Possible Heavy Fermion to Itinerant *d*-Metal Transition. *Physical Review Letters*, 82(14):2919–2922, April 1999.

[33] A. P. Ramirez, G. Lawes, D. Li, and M. A. Subramanian. Valence-Electron Transfer and a Metal-Insulator Transition in a Strongly Correlated Perovskite Oxide. *Solid State Communications*, 131(3-4):251–255, July 2004.

[34] R. J. Cava. Schizophrenic Electrons in Ruthenium-Based Oxides. *Dalton Transactions*, pages 2979–2987, 2004.

[35] N. Büttgen, H.-A. Krug von Nidda, W. Kraetschmer, A. Günther, S. Widmann, S. Riegg, A. Krimmel, and A. Loidl. Quantum Criticality in Transition-Metal Oxides. *Journal of Low Temperature Physics*, 161:148–166, 2010.

[36] Y. Maeno, H. Hashimoto, K. Yoshida, S. Nishizaki, T. Fujita, J. G. Bednorz, and F. Lichtenberg. Superconductivity in a Layered Perovskite without Copper. *Nature*, 372(6506):532–534, December 1994.

[37] Andrew Mackenzie and Yoshiteru Maeno. The Superconductivity of Sr_2RuO_4 and the Physics of Spin-Triplet Pairing. *Reviews of Modern Physics*, 75:657–712, May 2003.

[38] F. Steglich, J. Aarts, C. D. Bredl, W. Lieke, D. Meschede, W. Franz, and H. Schafer. Superconductivity in the Presence of Strong Pauli Paramagnetism - $CeCu_2Si_2$. *Physical Review Letters*, 43(25):1892–1896, 1979.

[39] P. Khalifah, K. D. Nelson, R. Jin, Z. Q. Mao, Y. Liu, Q. Huang, X. P. A. Gao, A. P. Ramirez, and R. J. Cava. Non-Fermi-Liquid Behaviour in $La_4Ru_6O_{19}$. *Nature*, 411(6838):669–671, June 2001.

[40] H. von Löhneysen, T. Pietrus, G. Portisch, H. G. Schlager, A. Schröder, M. Sieck, and T. Trappmann. Non-Fermi-Liquid Behavior in a Heavy-Fermion Alloy at a Magnetic Instability. *Physical Review Letters*, 72:3262–3265, May 1994.

[41] M. Labeau, B. Bochu, J. C. Joubert, and J. Chenavas. Synthèse et Caractérisation Cristallographique et Physique d'une Série de Composés $ACu_3Ru_4O_{12}$ de Type Perovskite. *Journal of Solid State Chemistry*, 33:257–261, 1980.

[42] J. Muller, A. Haouzi, C. Laviron, M. Labeau, and J. C. Joubert. Electrical Conductivity and Crystallographic Classification of $NdCu_3Ru_xTi_{4-x}O_{12}$ $(1 \leq x < 4)$ and $Nd_{(2+x)/3}Cu_3Ru_xTi_{4-x}O_{12}$ $(x \leq 1)$. *Materials Research Bulletin*, 21(9):1131–1136, September 1986.

[43] M. A. Subramanian and A. W. Sleight. $ACu_3Ti_4O_{12}$ and $ACu_3Ru_4O_{12}$ Perovskites: High Dielectric Constants and Valence Degeneracy. *Solid State Sciences*, 4:347–351, 2002.

[44] A. Sommerfeld and H. Bethe. Elektronentheorie der Metalle. In *Aufbau der Zusammenhängenden Materie*, volume 24/2 of *Handbuch der Physik*, pages 333–622. Springer Berlin Heidelberg, 1933.

[45] Kenneth G. Wilson. The Renormalization Group: Critical Phenomena and the Kondo Problem. *Reviews of Modern Physics*, 47:773–840, October 1975.

[46] M. Rice. Electron-Electron Scattering in Transition Metals. *Physical Review Letters*, 20:1439–1441, June 1968.

[47] K. Kadowaki and S. B. Woods. Universal Relationship of the Resistivity and Specific-Heat in Heavy-Fermion Compounds. *Solid State Communications*, 58(8):507–509, May 1986.

[48] S. G. Ebbinghaus, A. Weidenkaff, and R. J. Cava. Structural Investigations of $ACu_3Ru_4O_{12}$ (A = Na, Ca, Sr, La, Nd) - A Comparison between XRD-Rietveld and EXAFS Results. *Journal of Solid State Chemistry*, 167(1):126–136, August 2002.

[49] Stefan Riegg. *Relationship between Composition, Crystal Structure, and Physical Properties in Perovskite-Related Ruthenates.* PhD thesis, Mathematisch-Naturwissenschaftlich-Technische Fakultät, Universität Augsburg, Germany, 2014.

[50] P. Hohenberg and W. Kohn. Inhomogeneous Electron Gas. *Physical Review*, 136:B864–B871, November 1964.

[51] W. Kohn and L. J. Sham. Self-Consistent Equations Including Exchange and Correlation Effects. *Physical Review*, 140:A1133–A1138, November 1965.

[52] T. T. Tran, K. Takubo, T. Mizokawa, W. Kobayashi, and I. Terasaki. Electronic Structure of $CaCu_3Ru_4O_{12}$ Studied by X-Ray Photoemission Spectroscopy. *Physical Review B*, 73(19):193105, May 2006.

[53] H. P. Xiang, X. J. Liu, E. Zhao, J. Meng, and Z. J. Wu. First-Principles Study on the Conducting Mechanism of the Heavy-Fermion System $CaCu_3Ru_4O_{12}$. *Physical Review B*, 76(15):155103, October 2007.

[54] W. D. Knight. Nuclear Magnetic Resonance Shift in Metals. *Physical Review*, 76(8):1259–1260, 1949.

[55] H. Kato, T. Tsuruta, T. Nishioka, M. Matsumura, H. Sakai, and S. Kambe. Cu NMR Study in a Heavy-Electron System, $CaCu_3Ru_4O_{12}$. *Journal of Magnetism and Magnetic Materials*, 310(2, Part 1):e51–e53, March 2007.

[56] H. Kato, T. Tsuruta, T. Nishioka, M. Matsumura, H. Sakai, and S. Kambe. A CuNQR Study in a d-Electron Heavy-Fermion System, $CaCu_3Ru_4O_{12}$. *Journal of Physics and Chemistry of Solids*, 68(11):2187–2190, November 2007.

[57] A. Krimmel, A. Günther, W. Kraetschmer, H. Dekinger, N. Büttgen, A. Loidl, S. G. Ebbinghaus, E.-W. Scheidt, and W. Scherer. Non-Fermi-Liquid Behavior in $CaCu_3Ru_4O_{12}$. *Physical Review B*, 78(16):165126, 2008.

[58] Soutarou Tanaka, Nobuhiro Shimazui, Hiroshi Takatsu, Shingo Yonezawa, and Yoshiteru Maeno. Heavy-Mass Behavior of Ordered Perovskites $ACu_3Ru_4O_{12}$ (A = Na, Ca, La). *Journal of the Physical Society of Japan*, 78(2):024706, February 2009.

[59] H. Kato, T. Tsuruta, M. Matsumura, T. Nishioka, H. Sakai, Y. Tokunaga, S. Kambe, and R. E. Walstedt. Temperature-Induced Change in the Magnitude of the Effective Density of States: A NQR/NMR Study of the A-Site-Ordered Perovskite System $CaCu_3Ru_4O_{12}$. *Journal of the Physical Society of Japan*, 78(5):054707, May 2009.

[60] S. Tanaka, H. Takatsu, S. Yonezawa, and Y. Maeno. Suppression of the Mass Enhancement in $CaCu_3Ru_4O_{12}$. *Physical Review B*, 80(3):035113, July 2009.

[61] T. Sudayama, Y. Wakisaka, K. Takubo, T. Mizokawa, W. Kobayashi, I. Terasaki, S. Tanaka, Y. Maeno, M. Arita, H. Namatame, and M. Taniguchi. Bulk-Sensitive Photoemission Study of $ACu_3Ru_4O_{12}$ (A = Ca, Na, and La) with Heavy-Fermion Behavior. *Physical Review B*, 80(7):075113, August 2009.

[62] A. Krimmel, A. Günther, W. Kraetschmer, H. Dekinger, N. Büttgen, V. Eyert, A. Loidl, D. V. Sheptyakov, E.-W. Scheidt, and W. Scherer. Intermediate-Valence Behavior of the Transition-Metal Oxide $CaCu_3Ru_4O_{12}$. *Physical Review B*, 80(12):121101, 2009.

[63] T. Kida, R. Kammuri, S. Yoshii, M. Hagiwara, M. Iwakawa, W. Kobayashi, I. Terasaki, and K. Kindo. High-Field Magnetization and Magnetoresistance of $CaCu_3Ti_{4-x}Ru_xO_{12}$. *Journal of Low Temperature Physics*, 159(1-2):143–146, April 2010.

[64] T. Kida, R. Kammuri, M. Hagiwara, S. Yoshii, W. Kobayashi, M. Iwakawa, and I. Terasaki. High-Field Magnetization and Magnetoresistance of the A-site Ordered Perovskite Oxide $CaCu_3Ti_{4-x}Ru_xO_{12}$ ($0 \leq x \leq 4$). *Physical Review B*, 85(19):195122, May 2012.

[65] I. Tsukada, R. Kammuri, T. Kida, S. Yoshii, T. Takeuchi, M. Hagiwara, M. Iwakawa, W. Kobayashi, and I. Terasaki. Heat Capacity Proportional to T^2 Induced by *Ru* Substitution in $CaCu_3(Ti_{4-x}Ru_x)O_{12}$ ($x \approx 0.5$). *Physical Review B*, 79(5):054430, February 2009.

[66] S. G. Ebbinghaus, S. Riegg, T. Götzfried, and A. Reller. Co-Operative and Frustration Effects in Novel Perovskite-Related Phases. *European Physical Journal - Special Topics*, 180:91–116, January 2010.

[67] M. Mizumaki, T. Mizokawa, A. Agui, S. Tanaka, H. Takatsu, S. Yonezawa, and Y. Maeno. Oxygen Hole State in A-site Ordered Perovskite $A\mathrm{Cu_3Ru_4O_{12}}$ (A = Na, Ca, and La) Probed by Resonant X-ray Emission Spectroscopy. *Journal of the Physical Society of Japan*, 82(2):024709, February 2013.

[68] N. Hollmann, Z. Hu, A. Maignan, A. Günther, L. Y. Jang, A. Tanaka, H. J. Lin, C. T. Chen, P. Thalmeier, and L. H. Tjeng. Correlation Effects in $\mathrm{CaCu_3Ru_4O_{12}}$. *Physical Review B*, 87(15):155122, April 2013.

[69] F. Zhang and T. Rice. Effective Hamiltonian for the Superconducting Cu Oxides. *Physical Review B*, 37:3759–3761, March 1988.

[70] M. A. Subramanian, W. J. Marshall, T. G. Calvarese, and A. W. Sleight. Valence Degeneracy in $\mathrm{CaCu_3Cr_4O_{12}}$. *Journal of Physics and Chemistry of Solids*, 64(9-10):1569–1571, September 2003.

[71] Takashi Mizokawa, Yosuke Morita, Takaaki Sudayama, Kou Takubo, Ikuya Yamada, Masaki Azuma, Mikio Takano, and Yuichi Shimakawa. Metallic Versus Insulating Behavior in the A-site Ordered Perovskite Oxides $A\mathrm{Cu_3Co_4O_{12}}$ (A = Ca and Y) Controlled by Mott and Zhang-Rice Physics. *Physical Review B*, 80:125105, September 2009.

[72] D. Meyers, Swarnakamal Mukherjee, J.-G. Cheng, S. Middey, J.-S. Zhou, J. B. Goodenough, B. A. Gray, J. W. Freeland, T. Saha-Dasgupta, and J. Chakhalian. Zhang-Rice Physics and Anomalous Copper States in A-site Ordered Perovskites. *Scientific Reports*, 3:1834, May 2013.

[73] B. Schmidt, H.-A. Krug von Nidda, S. Riegg, S.G. Ebbinghaus, A. Reller, and A. Loidl. Probing the Metal-to-Insulator Transition in $\mathrm{LaCu_3Ru_xTi_{4-x}O_{12}}$ by Gd-ESR. *Magnetic Resonance in Solids*, 16(2):14210, 2014.

[74] G. M. Kalvius, O. Hartmann, A. Günther, A. Krimmel, A. Loidl, R. Wäppling, K. Sedlak, and R. Scheuermann. A μSR Study of the Ruthenium Perovskites $A\mathrm{Cu_3Ru_4O_{12}}$ with A = Ca, Pr, Nd. *Journal of Physics - Condensed Matter*, 551(1):012015, 2014.

[75] F. Bridges, B. Car, L. Sutton, M. Hoffman-Stapleton, T. Keiber, R. E. Baumbach, M. B. Maple, Z. Henkie, and R. Wawryk. Complex Vibrations in Arsenide Skutterudites and Oxyskutterudites. *Physical Review B*, 91:014109, January 2015.

[76] S. Hébert, R. Daou, and A. Maignan. Thermopower in the Quadruple Perovskite Ruthenates. *Physical Review B*, 91:045106, January 2015.

[77] Stefan Riegg, Armin Reller, Alois Loidl, and Stefan G. Ebbinghaus. Valence Properties of Cu and Ru in Titanium-Substituted $LnCu_3Ru_4O_{12+\delta}$ (Ln = La, Pr, Nd) Investigated by XANES and TGA. *Dalton Transactions*, 44(23):10852–10859, 2015.

[78] F. Steglich, C. D. Bredl, W. Lieke, U. Rauchschwalbe, and G. Sparn. Heavy Fermion Superconductivity. *Physica B*, 126(1-3):82–91, November 1984.

[79] G. R. Stewart. Heavy-Fermion Systems. *Reviews of Modern Physics*, 56(4):755–787, 1984.

[80] N. Grewe and F. Steglich. Heavy Fermions. In K. A. Gschneidner and L. Eyring, editors, *Handbook on the Physics and Chemistry of Rare Earths*, volume 14, chapter 97, pages 343–474. Elsevier Science Publishers B.V., 1991.

[81] Piers Coleman. *Heavy Fermions: Electrons at the Edge of Magnetism*. John Wiley & Sons, Ltd, 2007.

[82] K. Andres, J. E. Graebner, and H. R. Ott. 4f-Virtual-Bound-State Formation in $CeAl_3$ at Low-Temperatures. *Physical Review Letters*, 35(26):1779–1782, 1975.

[83] Hilbert von Löhneysen. Non-Fermi-Liquid Behaviour in the Heavy-Fermion System $CeCu_{6-x}Au_x$. *Journal of Physics - Condensed Matter*, 8(48):9689, 1996.

[84] N. D. Mathur, F. M. Grosche, S. R. Julian, I. R. Walker, D. M. Freye, R. K. W. Haselwimmer, and G. G. Lonzarich. Magnetically Mediated Superconductivity in Heavy Fermion Compounds. *Nature*, 394(6688):39–43, July 1998.

[85] P. Fulde, A. N. Yaresko, A. A. Zvyagin, and Y. Grin. On the Origin of Heavy Quasiparticles in LiV_2O_4. *Europhysics Letters*, 54(6):779, 2001.

[86] H.-A. Krug von Nidda, R. Bulla, N. Büttgen, M. Heinrich, and A. Loidl. Heavy Fermions in Transition Metals and Transition-Metal Oxides. *European Physical Journal B*, 34(4):399–407, August 2003.

[87] K. Pucher, J. Hemberger, F. Mayr, V. Fritsch, A. Loidl, E.-W. Scheidt, S. Klimm, R. Horny, S. Horn, S. Ebbinghaus, A. Reller, and R. Cava. Transport, Magnetic, Thermodynamic, and Optical Properties in Ti-Doped Sr_2RuO_4. *Physical Review B*, 65:104523, March 2002.

[88] M. Minakata and Y. Maeno. Magnetic Ordering in Sr_2RuO_4 Induced by Nonmagnetic Impurities. *Physical Review B*, 63:180504, April 2001.

[89] Jun Kondo. g-Shift and Anomalous Hall Effect in Gadolinium Metals. *Progress of Theoretical Physics*, 28(5):846–856, 1962.

[90] Jun Kondo. Resistance Minimum in Dilute Magnetic Alloys. *Progress of Theoretical Physics*, 32(1):37–49, July 1964.

[91] L. D. Landau. Theory of Fermi-liquids. *Journal of Experimental and Theoretical Physics*, 30:1058, 1956.

[92] L. D. Landau. Oscillations in a Fermi-Liquid. *Journal of Experimental and Theoretical Physics*, 32:59, 1957.

[93] L. D. Landau. On the Theory of the Fermi-Liquid. *Journal of Experimental and Theoretical Physics*, 35:97, 1958.

[94] Hilbert von Löhneysen, Achim Rosch, Matthias Vojta, and Peter Wölfle. Fermi-Liquid Instabilities at Magnetic Quantum Phase Transitions. *Reviews of Modern Physics*, 79(3):1015, August 2007.

[95] A. Schröder, G. Aeppli, R. Coldea, M. Adams, O. Stockert, H. von Löhneysen, E. Bucher, R. Ramazashvili, and P. Coleman. Onset of Antiferromagnetism in Heavy-Fermion Metals. *Nature*, 407(6802):351–355, September 2000.

[96] J. Custers, P. Gegenwart, H. Wilhelm, K. Neumaier, Y. Tokiwa, O. Trovarelli, C. Geibel, F. Steglich, C. Pepin, and P. Coleman. The Break-Up of Heavy Electrons at a Quantum Critical Point. *Nature*, 424(6948):524–527, July 2003.

[97] L. Klein, L. Antognazza, T. H. Geballe, M. R. Beasley, and A. Kapitulnik. Is $CaRuO_3$ a Non-Fermi Liquid Metal? *Physica B*, 259-261:431–432, January 1999.

[98] G. Cao, O. Korneta, S. Chikara, L. E. DeLong, and P. Schlottmann. Non-Fermi-Liquid Behavior in Single-Crystal $CaRuO_3$: Comparison to Ferromagnetic $SrRuO_3$. *Solid State Communications*, 148(7-8):305–309, 2008.

[99] S. A. Grigera, R. S. Perry, A. J. Schofield, M. Chiao, S. R. Julian, G. G. Lonzarich, S. I. Ikeda, Y. Maeno, A. J. Millis, and A. P. Mackenzie. Magnetic Field-Tuned Quantum Criticality in the Metallic Ruthenate $Sr_3Ru_2O_7$. *Science*, 294(5541):329–332, 2001.

[100] K. Kitagawa, K. Ishida, R. Perry, T. Tayama, T. Sakakibara, and Y. Maeno. Metamagnetic Quantum Criticality Revealed by ^{17}O-NMR in the Itinerant Metamagnet $Sr_3Ru_2O_7$. *Physical Review Letters*, 95:127001, September 2005.

[101] P. Gegenwart, F. Weickert, M. Garst, R. S. Perry, and Y. Maeno. Metamagnetic Quantum Criticality in $Sr_3Ru_2O_7$ Studied by Thermal Expansion. *Physical Review Letters*, 96:136402, April 2006.

[102] G. R. Stewart. Non-Fermi-Liquid Behavior in d- and f-Electron Metals. *Reviews of Modern Physics*, 73(4):797–855, October 2001.

[103] P. Limelette, V. Ta Phuoc, F. Gervais, and R. Frésard. ω/T Scaling of the Optical Conductivity in Strongly Correlated Layered Cobalt Oxide. *Physical Review B*, 87:035102, January 2013.

[104] J. Röhler and G. Kaindl. Influence of Pressure on the Inhomogeneous Mixed-Valent State in Eu_3S_4. *Solid State Communications*, 36(12):1055–1057, 1980.

[105] G. Wortmann, E. V. Sampathkumaran, and G. Kaindl. Verwey Transition in Eu_4As_3. *Journal of Magnetism and Magnetic Materials*, 54-57(1):338–340, 1986.

[106] C. M. Varma. Mixed-Valence Compounds. *Reviews of Modern Physics*, 48:219–238, April 1976.

[107] J.M. Robinson. Valence Transitions and Intermediate Valence States in Rare Earth and Actinide Materials. *Physics Reports*, 51(1):1–62, 1979.

[108] J. M. Lawrence, P. S. Riseborough, and R. D. Parks. Valence Fluctuation Phenomena. *Reports on Progress in Physics*, 44(1):1, 1981.

[109] E. V. Sampathkumaran. Intermediate Valence in Rare Earth Systems. *Hyperfine Interactions*, 27(1-4):183–192, 1986.

[110] B. Coqblin and J. R. Schrieffer. Exchange Interaction in Alloys with Cerium Impurities. *Physical Review*, 185:847–853, September 1969.

[111] Ph. Nozieres and A. Blandin. Kondo Effect in Real Metals. *Journal de Physique*, 41(3):193–211, 1980.

[112] H. R. Krishna-murthy, J. W. Wilkins, and K. G. Wilson. Renormalization-Group Approach to the Anderson Model of Dilute Magnetic Alloys. I. Static Properties for the Symmetric Case. *Physical Review B*, 21:1003–1043, February 1980.

[113] H. R. Krishna-murthy, J. W. Wilkins, and K. G. Wilson. Renormalization-Group Approach to the Anderson Model of Dilute Magnetic Alloys. II. Static Properties for the Asymmetric Case. *Physical Review B*, 21:1044–1083, February 1980.

[114] N. Andrei and J. H. Lowenstein. Scales and Scaling in the Kondo Model. *Physical Review Letters*, 46:356–360, February 1981.

[115] A. C. Hewson and J. W. Rasul. Exact High- and Low-Temperature Results for the Coqblin-Schreiffer Model with Applications to YbCuAl. *Journal of Physics C - Solid State Physics*, 16(35):6799, 1983.

[116] A. C. Hewson. *The Kondo Problem to Heavy Fermions*. Cambridge University Press, Cambridge, 1993.

[117] N. Tsujii, K. Yoshimura, and K. Kosuge. Deviation from the Kadowaki-Woods Relation in Yb-based Intermediate-Valence Systems. *Journal of Physics - Condensed Matter*, 15(12):1993–2003, April 2003.

[118] N. E. Hussey. Non-Generality of the Kadowaki-Woods Ratio in Correlated Oxides. *Journal of the Physical Society of Japan*, 74(4):1107–1110, 2005.

[119] N. Tsujii, H. Kontani, and K. Yoshimura. Universality in Heavy Fermion Systems with General Degeneracy. *Physical Review Letters*, 94(5):057201, February 2005.

[120] A. C. Jacko, J. O. Fjærestad, and B. J. Powell. A Unified Explanation of the Kadowaki-Woods Ratio in Strongly Correlated Metals. *Nature Physics*, 5(6):422–425, June 2009.

[121] H. Kröncke, S. Figge, B. M. Epelbaum, and D. Hommel. Determination of the Temperature Dependent Thermal Expansion Coefficients of Bulk AlN by HRXRD. *Acta Physica Polonica A*, 114(5):1193–1200, November 2008. 37th International School on the Physics of Semiconducting Compounds, Jaszowiec, POLAND, JUN 07-13, 2008.

[122] A. Einstein. Die Plancksche Theorie der Strahlung und die Theorie der spezifischen Wärme. *Annalen der Physik*, 327(1):180–190, 1906.

[123] A.-T. Petit and P.-L. Dulong. Recherches sur quelques Points Importants de la Théorie de la Chaleur. *Annales de Chimie et de Physique*, 10:395–413, 1819.

[124] P. Debye. Zur Theorie der Spezifischen Wärmen. *Annalen der Physik*, 344(14):789–839, 1912.

[125] A. Tari. *The Specific Heat of Matter at Low Temperatures*. Imperial College Press, 2003.

[126] E. S. R. Gopal. *Specific Heats at Low Temperatures*. Springer US, 1966.

[127] K. R. Lea, M. J. M. Leask, and W. P. Wolf. The Raising of Angular Momentum Degeneracy of f-Electron Terms by Cubic Crystal Fields. *Journal of Physics and Chemistry of Solids*, 23(10):1381–1405, October 1962.

[128] P. E. Gregers-Hansen, M. Krusius, and G. R. Pickett. Sign of the Nuclear Quadrupole Interaction in Rhenium Metal. *Physical Review Letters*, 27:38–41, July 1971.

[129] C. de la Calle, J. Sanchez-Benitez, F. Barbanson, N. Nemes, M. T. Fernandez-Diaz, and J. A. Alonso. Transition from Pauli-Paramagnetism to Ferromagnetism in $CaCu_3Ru_{4-x}Mn_xO_{12}$ ($0 \leq x \leq 3$) Perovskites. *Journal of Applied Physics*, 109(12):123914, June 2011.

[130] R. D. Schmidt-Whitley, M. Martinez-Clemente, and A. Revcolevschi. Growth and Microstructural Control of Single Crystal Cuprous Oxide Cu_2O. *Journal of Crystal Growth*, 23(2):113–120, 1974.

[131] J. P. Neumann, T. Zhong, and Y. A. Chang. The Cu-O (Copper-Oxygen) System. *Bulletin of Alloy Phase Diagrams*, 5(2):136–140, 1984.

[132] H. M. Rietveld. A Profile Refinement Method for Nuclear and Magnetic Structures. *Journal of Applied Crystallography*, 2(2):65–71, June 1969.

[133] Rudolf Allmann and Arnt Kern. *Röntgenpulverdiffraktometrie: Rechnergestützte Auswertung, Phasenanalyse und Strukturbestimmung.* Clausthaler Tektonische Hefte. Springer, 2nd edition, 2002.

[134] W. L. Bragg. The Diffraction of Short Electromagnetic Waves by a Crystal. *Proceedings of the Cambridge Philosophical Society*, 17:43–57, 1913.

[135] H. P. Klug and L. E. Alexander. *X-Ray Diffraction Procedures: For Polycrystalline and Amorphous Materials.* Wiley Interscience Publication. Wiley, 2nd edition, 1974.

[136] W. H. Miller. *A Treatise on Crystallography.* J. & J. J. Deighton, Cambridge, 1839.

[137] V. K. Pecharsky and P. Y. Zavalij. *Fundamentals of Powder Diffraction and Structural Characterization of Materials.* Springer, 2004.

[138] B. D. Cullity. *Elements of X-Ray Diffraction.* Addison-Wesley, 2nd edition, 1978.

[139] H. Krischner and B. Koppelhuber-Bitschnau. *Röntgenstrukturanalyse und Rietveldmethode: Eine Einführung.* Vieweg, 5th edition, 1994.

[140] Werner Massa. *Kristallstrukturbestimmung.* Teubner, 5th edition, 2007.

[141] J. Rodriguez-Carvajal. Recent Advances in Magnetic Structure Determination by Neutron Powder Diffraction. *Physica B*, 192(1-2):55–69, October 1993.

[142] Louis de Broglie. Recherches sur la Theorie des Quanta. *Annales de Physique*, 3:22, January-February 1925.

[143] G. L. Squires. *Introduction to the Theory of Thermal Neutron Scattering.* Dover books on physics. Dover Publications, 1978.

[144] A. Furrer, J. Mesot, and T. Straessle. *Neutron Scattering in Condensed Matter Physics*. Series on neutron techniques and applications. World Scientific, 2009.

[145] H. Dachs, P. Chieux, P. Coppens, J. B. Hayter, P.-A. Lindgard, D. Petraschek, W. Prandl, H. Rauch, W. Schmatz, and G. Zaccai. *Neutron Diffraction*. Topics in current physics. Springer, 1978.

[146] G. E. Bacon. *Neutron Diffraction*. Monographs on the physics and chemistry of materials. Clarendon Press, 3rd edition, 1975.

[147] H. Mutka. Coupled Time and Space Focusing for Time-of-Flight Inelastic-Scattering. *Nuclear Instruments and Methods in Physics Research - Section A - Accelerators, Spectrometers, Detectors and Associated Equipment*, 338(1):144–150, January 1994. Workshop on Focusing Bragg Optics, Braunschweig, Germany, May 10-11, 1993.

[148] D. Richard, M. Ferrand, and G. J. Kearley. Analysis and Visualisation of Neutron-Scattering Data. *Journal of Neutron Research*, 4(1):33–39, 1996.

[149] Quantum Design, Inc., 11578 Sorrento Valley Rd., San Diego, CA 92121-1311, USA. *Physical Property Measurement System - Hardware Manual*, 3rd edition, 2000.

[150] Quantum Design, Inc., 11578 Sorrento Valley Rd., San Diego, CA 92121-1311, USA. *Physical Property Measurement System - Heat Capacity Option User's Manual*, 11th edition, 2004.

[151] Quantum Design, Inc., 11578 Sorrento Valley Rd., San Diego, CA 92121-1311, USA. *Physical Property Measurement System - Resistivity Option User's Manual*, 2nd edition, 1999.

[152] Quantum Design, Inc., 6325 Lusk Blvd., San Diego, CA 92121, USA. *Physical Property Measurement System - AC Transport Option User's Manual*, 8th edition, 2009.

[153] Quantum Design, Inc., 11578 Sorrento Valley Rd., San Diego, CA 92121, USA. *Magnetic Property Measurement System MPMS XL - Hardware Reference Manual*, 1996.

[154] B. D. Josephson. Possible New Effects in Superconductive Tunnelling. *Physics Letters*, 1(7):251–253, 1962.

[155] C. Enss and S. Hunklinger. *Low-Temperature Physics*. Springer, 2005.

[156] Oxford Instruments Ltd., Scientific Research Division, Old Station Way, Eynsham, Witney, Oxon, OX8 1TL, England. *Teslatron Superconducting Magnet System - Operator's Handbook*, February 1997.

[157] Oxford Instruments Ltd., Scientific Research Division, Old Station Way, Eynsham, Witney, Oxon, OX8 1TL, England. *Magnetic Properties Probe for MagLab and Teslatron*, March 1997.

[158] Frank Pobell. *Matter and Methods at Low Temperatures*. Springer, 3rd edition, 2007.

[159] A. Kent. *Experimental Low Temperature Physics*. MacMillan Physical Science. American Institute of Physics, 1993.

[160] R. Bachmann, R. E. Schwall, H. U. Thomas, R. B. Zubeck, C. N. King, H. C. Kirsch, F. J. Disalvo, T. H. Geballe, K. N. Lee, R. E. Howard, and R. L. Greene. Heat-Capacity Measurements on Small Samples at Low Temperatures. *Review of Scientific Instruments*, 43(2):205, 1972.

[161] Oxford Instruments Ltd., Tubney Woods, Abingdon, Oxon, OX13 5QX, England. *Kelvinox Dilution Refrigerator and Superconducting Magnet System*, July 1997.

[162] Günter Schatz and Alois Weidinger. *Nukleare Festkörperphysik: Kernphysikalische Messmethoden und ihre Anwendungen*. Teubner-Studienbücher : Physik. Teubner, 1992.

[163] A. Schenck. *Muon Spin Rotation Spectroscopy*. Adam Hilger, Ltd., 1985.

[164] T. Hahn, editor. *International Tables for Crystallography*, volume A (Space Group Symmetry). Kluwer Acad. Publ., Dordrecht, 4th edition, 1996.

[165] V. M. Talanov, M. V. Talanov, and V. B. Shirokov. Group-Theoretical Study of Cationic Ordering in Perovskite Structure. *Crystallography Reports*, 59(5):650–661, 2014.

[166] Ralph W. G. Wyckoff. *The Analytical Expression of the Results of the Theory of Space-Groups*. Carnegie Institution of Washington, October 1922.

[167] Ivar Oftedal. XXXIII. Die Kristallstruktur von Skutterudit und Speiskobalt-Chloanthit. *Zeitschrift für Kristallographie - Crystalline Materials*, 66(1):517–546, December 1928.

[168] W. Jeitschko and D. Braun. $LaFe_4P_{12}$ with Filled $CoAs_3$-Type Structure and Isotypic Lanthanoid-Transition Metal Polyphosphides. *Acta Crystallographica Section B*, 33:3401–3406, November 1977.

[169] R. D. Shannon. Revised Effective Ionic Radii and Systematic Studies of Interatomic Distances in Halides and Chalcogenides. *Acta Crystallographica Section A*, 32:751–767, September 1976.

[170] John J. Randall and Roland Ward. The Preparation of Some Ternary Oxides of the Platinum Metals. *Journal of the American Chemical Society*, 81(11):2629–2631, 1959.

[171] M. Labeau, B. Bochu, J. C. Joubert, and J. Chenavas. Synthesis and Crystallographic and Physical Characterization of Compounds $ACu_3Ru_4O_{12}$ of Perovskite-Like Arrangement. *Journal of Solid State Chemistry*, 33(2):257–261, 1980.

[172] W. J. A. Peterse and J. H. Palm. Anisotropic Temperature Factor of Atoms in Special Positions. *Acta Crystallographica*, 20:147–150, 1966.

[173] K. N. Trueblood, H.-B. Bürgi, H. Burzlaff, J. D. Dunitz, C. M. Gramaccioli, H. H. Schulz, U. Shmueli, and S. C. Abrahams. Atomic Dispacement Parameter Nomenclature. Report of a Subcommittee on Atomic Displacement Parameter Nomenclature. *Acta Crystallographica Section A*, 52(5):770–781, September 1996.

[174] R. W. Grosse-Kunstleve and P. D. Adams. On the Handling of Atomic Anisotropic Displacement Parameters. *Journal of Applied Crystallography*, 35(4):477–480, August 2002.

[175] L. Klein, J. S. Dodge, C. H. Ahn, J. W. Reiner, L. Mieville, T. H. Geballe, M. R. Beasley, and A. Kapitulnik. Transport and Magnetization in the Badly Metallic Itinerant Ferromagnet $SrRuO_3$. *Journal of Physics - Condensed Matter*, 8(48):10111, 1996.

[176] T.-W. E. Tsang, K. A. Gschneidner, O. D. McMasters, R. J. Stierman, and S. K. Dhar. Anisotropic Spin Fluctuations in Cubic $CeSn_3$. *Physical Review B*, 29:4185–4188, April 1984.

[177] J. Lawrence. Scaling Behavior near a Valence Instability - Magnetic Susceptibility of $CeIn_{3-x}Sn_x$. *Physical Review B*, 20(9):3770–3782, 1979.

[178] K.-H. Hellwege. *Einführung in die Festkörperphysik*. Springer, 1994.

[179] William G. Penney and Robert Schlapp. The Influence of Crystalline Fields on the Susceptibilities of Salts of Paramagnetic Ions. I. The Rare Earths, Especially Pr and Nd. *Physical Review*, 41(2):194–207, July 1932.

[180] R. J. Birgeneau. Transition Probabilities for f-Electron J-Multiplets in Cubic Crystal Fields. *Journal of Physics and Chemistry of Solids*, 33(1):59–68, January 1972.

[181] P. A. Lee, T. M. Rice, J. W. Serene, L. J. Sham, and J. W. Wilkins. Theories of Heavy-Electron Systems. *Comments on Condensed Matter Physics*, 12:99, 1986.

[182] Max Kohler. Magnetische Widerstandsänderung und Leitfähigkeitstypen. I. *Annalen der Physik*, 440(1-2):89–98, 1949.

[183] Max Kohler. Magnetische Widerstandsänderung und Leitfähigkeitstypen. II. *Annalen der Physik*, 440(1-2):99–107, 1949.

[184] N. Hessel Andersen, P. E. Gregers-Hansen, E. Holm, H. Smith, and O. Vogt. Temperature-Dependent Spin-Disorder Resistivity in a Van Vleck Paramagnet. *Physical Review Letters*, 32(23):1321, June 1974.

[185] A. I. Abou Aly, S. Bakanowski, N. F. Berk, J. E. Crow, and T. Mihalisin. Resistive Behavior in Singlet-Ground-State System $La_{1-x}Pr_xSn_3$. *Physical Review Letters*, 35(20):1387–1390, 1975.

[186] P. Fulde. Selected Crystal-Field Effects in Rare-Earth Systems. *Journal of Applied Physics*, 49(3):1311–1314, 1978.

[187] Katsuhiko Takegahara, Hisatomo Harima, and Akira Yanase. Crystal Electric Fields for Cubic Point Groups. *Journal of the Physical Society of Japan*, 70(5):1190–1193, 2001.

[188] P. Zeeman. The Effect of Magnetisation on the Nature of Light Emitted by a Substance. *Nature*, 55(1424):347, February 1897.

[189] Brian C. Sales. Filled Skutterudites. In K.A. Gschneidner Jr., J.-C. G. Bünzli, and V.K. Pecharsky, editors, *Handbook on the Physics and Chemistry of Rare Earths*, volume 33, pages 1–34. Elsevier, 2003.

[190] Y. Aoki, H. Sugawara, H. Harima, and H. Sato. Novel Kondo Behaviors Realized in the Filled Skutterudite Structure. *Journal of the Physical Society of Japan*, 74(1):209–221, January 2005.

[191] Shotaro Sanada, Yuji Aoki, Hidekazu Aoki, Akihisa Tsuchiya, Daisuke Kikuchi, Hitoshi Sugawara, and Hideyuki Sato. Exotic Heavy-Fermion State in Filled Skutterudite $SmOs_4Sb_{12}$. *Journal of the Physical Society of Japan*, 74(1):246–249, 2005.

[192] M. D. Daybell and W. A. Steyert. Observation of Nagaoka's Bound State for Conduction Electrons in Dilute Magnetic Alloys. *Physical Review Letters*, 18:398–401, March 1967.

[193] J. W. Loram, T. E. Whall, and P. J. Ford. Resistivity of Some CuAuFe Alloys. *Physical Review B*, 2:857–874, August 1970.

[194] Yosuke Nagaoka. Self-Consistent Treatment of Kondo's Effect in Dilute Alloys. *Physical Review*, 138:A1112–A1120, May 1965.

[195] Joel A. Appelbaum and Jun Kondo. Ground-State and Low-Temperature Properties of Paramagnetic Impurities in Metals. *Physical Review Letters*, 19:906–908, October 1967.

[196] R. P. Dickey, M. C. de Andrade, J. Herrmann, M. B. Maple, F. G. Aliev, and R. Villar. Crossover from Non-Fermi-Liquid to Fermi-Liquid Behavior in the Magnetoresistivity of $U_{0.9}Th_{0.1}Be_{13}$. *Physical Review B*, 56:11169–11173, November 1997.

[197] O. Trovarelli, C. Geibel, S. Mederle, C. Langhammer, F. M. Grosche, P. Gegenwart, M. Lang, G. Sparn, and F. Steglich. $YbRh_2Si_2$: Pronounced Non-Fermi-Liquid Effects above a Low-Lying Magnetic Phase Transition. *Physical Review Letters*, 85(3):626, July 2000.

[198] E. J. Freeman, M. C. de Andrade, R. P. Dickey, N. R. Dilley, and M. B. Maple. Non-Fermi-Liquid Behavior and Magnetic Order in the $U_{1-x}Y_xPd_2Al_3$ System. *Physical Review B*, 58:16027–16031, December 1998.

[199] F. Steglich, P. Gegenwart, R. Helfrich, C. Langhammer, P. Hellmann, L. Donnevert, C. Geibel, M. Lang, G. Sparn, W. Assmus, G.R. Stewart, and A. Ochiai. Are Heavy-Fermion Metals Fermi Liquids? *Zeitschrift für Physik B - Condensed Matter*, 103(2):235–242, 1996.

[200] M. C. de Andrade, R. Chau, R. P. Dickey, N. R. Dilley, E. J. Freeman, D. A. Gajewski, and M. B. Maple. Evidence for a Common Physical Description of Non-Fermi-Liquid Behavior in Chemically Substituted f-Electron Systems. *Physical Review Letters*, 81(25):5620–5623, December 1998.

[201] P. Gegenwart, C. Langhammer, C. Geibel, R. Helfrich, M. Lang, G. Sparn, F. Steglich, R. Horn, L. Donnevert, A. Link, and W. Assmus. Breakup of Heavy Fermions on the Brink of Phase A in $CeCu_2Si_2$. *Physical Review Letters*, 81:1501–1504, August 1998.

[202] N. Takeda and M. Ishikawa. Anomalous Magnetic Properties of $CeRu_4Sb_{12}$. *Physica B*, 259-261:92–93, 1999.

[203] R. K. Harris, E. D. Becker, S. M. C. De Menezes, R. Goodfellow, and P. Granger. NMR Nomenclature. Nuclear Spin Properties and Conventions for Chemical Shifts - (IUPAC Recommendations 2001). *Pure and Applied Chemistry*, 73(11):1795–1818, November 2001.

[204] Gladys H. Fuller. Nuclear Spins and Moments. *Journal of Physical and Chemical Reference Data*, 5(4):835–1092, 1976.

[205] U. Walter. Treating Crystal Field Parameters in Lower than Cubic Symmetries. *Journal of Physics and Chemistry of Solids*, 45(4):401–408, 1984.

[206] Takashi Tayama, Toshiro Sakakibara, Kiichiro Kitami, Makoto Yokoyama, Kenichi Tenya, Hiroshi Amitsuka, Dai Aoki, Yoshichika Onuki, and Zbigniew Kletowski. Antiferro-Quadrupolar Ordering and Multipole Interactions in $PrPb_3$. *Journal of the Physical Society of Japan*, 70(1):248–258, 2001.

[207] Osamu Suzuki, Hiroyuki S. Suzuki, Hideaki Kitazawa, Giyuu Kido, Takafumi Ueno, Takashi Yamaguchi, Yuichi Nemoto, and Terutaka Goto. Quadrupolar Kondo Effect in Non-Kramers Doublet System $PrInAg_2$. *Journal of the Physical Society of Japan*, 75(1):013704, 2006.

[208] Akito Sakai and Satoru Nakatsuji. Kondo Effects and Multipolar Order in the Cubic $PrTr_2Al_{20}$ (Tr = Ti, V). *Journal of the Physical Society of Japan*, 80(6):063701, 2011.

[209] N. Nagasawa, T. Onimaru, K. T. Matsumoto, K. Umeo, and T. Takabatake. Nonmagnetic Γ_3 Doublet Ground State in a Caged Compound $PrRh_2Zn_{20}$. *Journal of Physics - Condensed Matter*, 391(1):012051, 2012.

[210] T. Onimaru, K. T. Matsumoto, N. Nagasawa, Y. F. Inoue, K. Umeo, R. Tamura, K. Nishimoto, S. Kittaka, T. Sakakibara, and T. Takabatake. Nonmagnetic Ground States and Phase Transitions in the Caged Compounds PrT_2Zn_{20} (T= Ru, Rh and Ir). *Journal of Physics - Condensed Matter*, 24(29):294207, 2012.

[211] T. Onimaru, N. Nagasawa, K. T. Matsumoto, K. Wakiya, K. Umeo, S. Kittaka, T. Sakakibara, Y. Matsushita, and T. Takabatake. Simultaneous Superconducting and Antiferroquadrupolar Transitions in $PrRh_2Zn_{20}$. *Physical Review B*, 86:184426, November 2012.

[212] Yo Tokunaga, Hironori Sakai, Shinsaku Kambe, Akito Sakai, Satoru Nakatsuji, and Hisatomo Harima. Magnetic Excitations and c -f Hybridization Effect in $PrTi_2Al_{20}$ and PrV_2Al_{20}. *Physical Review B*, 88:085124, August 2013.

[213] Tatsuya Kawae, Mikito Koga, Yoshiaki Sato, Shun Makiyama, Yuji Inagaki, Naoyuki Tateiwa, Tetsuya Fujiwara, Hiroyuki S. Suzuki, and Tetsuo Kitai. Nonlinear Susceptibility Measurement for Quadrupolar Response in a Dilute Γ_3 Non-Kramers Doublet System $Pr_{0.05}La_{0.95}Pb_3$. *Journal of the Physical Society of Japan*, 82(7):073701, 2013.

[214] R. Kubo and T. Toyabe. In R. Blinc, editor, *Magnetic Resonance and Relaxation - Proceedings*, page 810. North-Holland, Amsterdam, 1967.

[215] H. Bethe. Termaufspaltung in Kristallen. *Annalen der Physik*, 395(2):133–208, 1929.

[216] S. Riegg, S. Widmann, A. Günther, B. Meir, S. Wehrmeister, S. Sterz, W. Kraetschmer, S. G. Ebbinghaus, A. Reller, N. Büttgen, H.-A. Krug von Nidda, and A. Loidl. Heavy Fermions, Metal-to-Insulator Transition, and Quantum Criticality in $La_yCu_3Ru_xTi_{4-x}O_{12}$. *European Physical Journal - Special Topics (submitted)*, 2015.

[217] Jean Claude Trabandt. Schwere Fermionen, Korrelationen und Kristallfeld-Effekte in Praseodym-dotiertem $LaCu_3Ru_4O_{12}$, 2015.

[218] Abraham Savitzky and M. J. E. Golay. Smoothing and Differentiation of Data by Simplified Least Squares Procedures. *Analytical Chemistry*, 36(8):1627–1639, 1964.

Acknowledgements

At this place I would like to thank all the people who have made this thesis possible:

- Prof. Dr. Alois Loidl as first referee and for giving me the possibility to make this PhD at the chair of Experimental Physics 5.
- Prof. Dr. Armin Reller as second referee.
- PD Dr. Alexander Krimmel and PD Dr. Hans-Albrecht Krug von Nidda for supervising my thesis.
- Dr. Vladimir Tsurkan, Dana Vieweg, Anna Pimenova, and Thomas Wiedenmann for their experimental support.
- Dr. Ernst-Wilhelm Scheidt for his experimental support and associated evaluations.
- Dr. Stefan Riegg and Prof. Dr. Stefan Ebbinghaus for fruitful discussions and for providing me with samples.
- Dr. Manuel Brando for his experimental support.
- Prof. Dr. Mikhail Eremin for fruitful discussions.
- Prof. Dr. Michael G. Kalvius, Dr. Denis Sheptyakov, and Dr. Hannu Mutka for their support in experiments at the large scale facilities PSI and ILL.
- my bachelor-, master-, diploma- and PhD-colleagues for their scientific support.
- my family.